# The kinetics and mechanics of a dehydrating system and the deformation of porous rock


Thesis submitted in accordance with the requirements of the University of Liverpool for the degree of Doctor of Philosophy by

**John David Bedford**

April 2017

*For my Mum and Dad*

## Abstract

This thesis aims to address two distinct areas of Earth Sciences that are linked by common processes. The first is dehydration reactions at intermediate depths that lead to seismicity, and the second is the mechanics of the deformation of porous sandstones which is important for the development of sub-surface reservoirs.

The breakdown of hydrous minerals in subduction zones is often invoked as the cause of seismicity at intermediate depths (50-200 km). The release of high pressure fluid is thought to reduce effective stress allowing brittle deformation at pressures where instabilities are typically supressed. Pore fluid pressure ($P_f$) evolution is dependent on the feedback between reaction rate, fluid flow and deformation. Reaction generates fluid which, if unable to drain, will lead to an increase in $P_f$. However dehydration reactions are also typically associated with (i) solid volume reduction which produces porosity, enhancing fluid flow and allowing high $P_f$ to dissipate, and (ii) compaction of this pore space that can restrict fluid flow enabling $P_f$ to build up. This thesis aims to constrain the processes that control the reaction rate, and hence the fluid production rate, and also determine the deformation behaviour of the porous reaction product. This is done by investigating experimentally the reaction gypsum → bassanite + $H_2O$.

Reaction processes are investigated by imaging a dehydrating gypsum sample using real time 4D X-ray synchrotron microtomography. The datasets acquired allow the evolving pore structure and connectivity to be analyzed during reaction. The growth of bassanite grains is tracked and the kinetics are shown to be intimately linked to the spatial evolution of porosity. New pores wrap around bassanite grains producing moat-like structures; generating diffusion pathways along which the transport of chemical constituents to the growing grains occurs. As the moats grow in width, diffusion and hence reaction rate slow down. Individual moats become interconnected early in the reaction allowing efficient drainage and dissipation of locally high $P_f$. Identifying the dominant chemical transport pathway is important for modelling of dehydrating systems to constrain better the feedback between reaction, fluid flow and deformation.

The mechanical behaviour of the porous reaction product bassanite is investigated by mapping the yield curve evolution along different loading paths. Yield curves are typically plotted in P-Q space where P is the effective mean stress and Q is the differential stress. They are typically considered to be elliptical in shape with the low pressure side being associated with localized brittle faulting (dilation) and the high pressure side with distributed ductile deformation (compaction). A new stress-probing methodology is used to map in high resolution the yield curve and its evolution with continued deformation. This reveals that the yield curve is not perfectly elliptical with the high pressure side comprised partly of a near vertical limb. The yield curve evolution is dependent on the nature of inelastic strain, with deviatorically compacted samples having considerably larger yield curves than hydrostatically compacted samples of similar porosity. This is associated with the formation of a heterogeneous microstructure during deviatoric loading, showing sets of conjugate shear fractures.

The same stress-probing methodology is applied to two high porosity sandstones to see if the yield curve evolution observed for porous bassanite is applicable. Both sandstones show a similar near vertical limb on the high pressure side of the curve as observed with bassanite. The yield curve evolution for sandstone is also more sensitive to deviatoric loading, like bassanite, although no localized deformation features are observed. The data highlight that future studies of porous rock deformation should consider the effect of the nature of inelastic strain on the mechanical and microstructural evolution of porous rock.

# Contents

# List of Figures and Tables

# Acknowledgments

Firstly I would like to say big thanks to my supervisors, the rock deformation dream team, John Wheeler, Dan Faulkner and Betty Mariani. Over the past three and a half years Wheeler World has provided knowledge, intellectual insight and much entertainment. Whether it be anecdotes about the time he became an overnight celebrity educating millions of television viewers around the world about the swirly rocks of NW Scotland, or sharing his favourite pictures of bad taxidermy in the pub, the laughs are never far away. Dan Faulkner is someone I've always admired, not because of his intellect or scientific prowess, but rather his ability to sustain himself at a week-long conference on little more than two hours sleep a night. One thing I believe Dan has particularly enjoyed about my work is pulling me up on my bad grammar, especially the infamous split infinitives. So this next sentence is just for him. In this thesis I will boldly go where no person has gone before, to further understand dehydration reactions, to better constrain the processes involved and to greatly annoy Prof. Faulkner. Thanks to Betty for being a great 3rd supervisor. Although my project has evolved in a way that hasn't involved Betty as much as either of us would like, she is someone I have learnt a lot from, both in the field during the Almeria trips and in the various lab discussions. On a slightly more serious note, I would like express my sincere gratitude to all my supervisors, I couldn't have asked for a better team and I have certainly learnt many things under their guidance.

Two other people who have played pivotal roles in the research in this thesis are Henri Leclère and Florian Fusseis. Henri was brilliant, especially during the early days of my PhD, when he taught me the basics of experimental work and he'd be the person who I'd go to ask all my stupid questions. I also learnt many French swear words by listening to his mutterings when he'd open the wrong valve on the rig (again!). Meeting Florian at the Gordan Conference (2014) proved to be the best bit of networking I did during my PhD. I will be forever grateful to him for letting us use his experimental cell in the synchrotron beamline at the Advanced Photon Source. The datasets we acquired are superb and I truly believe he's carving out an exciting niche in synchrotron microtomography; a technique I'm convinced will produce many of the big breakthroughs in the geosciences in the next few decades.

The rock deformation lab has been a fantastic place to work over the last few years. But it wouldn't have been the same without Gary, for both technical assistance and friendship. Whether it be golf chat or Simpsons quotes there is always something to

take my mind off work. I also appreciate the patience with the various annoying jobs I have needed help with over the years. There have been many comings and goings from the lab and the rock deformation research group over the course of my PhD. A special mention has to go to my long suffering PhD buddy Mike (aka Mikey). The stories of his latest findings in the deep dark places of the internet provided much lunchtime entertainment. The rest of the group who have been here during my time; Joe G, Cata, Jaslin, Pam, Carolyn, Aurelio, Oshaine, Sabine, Christina, Jake, Rachael and Steve C along with various visitors and masters students make the lab such a vibrant and entertaining place to work.

I have made many other great friends from the rest of the department, there are too many to list and I'd probably embarrass myself by forgetting someone anyway.

I am forever indebted to my parents. They are the ones who have always been there over my entire education, which has now spanned over 20 years. They have provided much encouragement and quite a lot of financial support over the years for which I am incredibly grateful.

Thanks to the rest of my friends and family, most of whom probably haven't had a clue what I've been doing over these last few years or why I've been doing it. "Something to do with gypsum" is quite a good executive summary that I regularly hear. Although, "3 years to learn how a bag of plaster works!" has probably been my favourite.

Finally I must say a big thanks to Debbie. Your support and patience over the course of my PhD has meant a lot and thanks for keeping me well fed, especially over these last few months. I owe you multiple cooked meals!

# 1. Introduction

This introduction will outline the rationale for the work presented in this thesis and introduce the wider context to which it applies. The progression of ideas that arose over the course of this research meant that it evolved to encompass two distinct areas of Earth Sciences that are linked by common processes. The first is dehydration reactions, which are important for the generation of seismicity at intermediate depths in subduction zones. As will be explained later in this introduction, compaction of porosity generated during reaction is important in the evolution of a dehydrating system as a whole. A large part of the research in this thesis is therefore aimed at investigating the compaction of porosity produced during dehydration (Chapter 4). The new findings of this work fuel an interest into the applicability to porous rock deformation in general. Thus the second topic of Earth Sciences that is investigated is the compaction of porous sandstone (Chapter 5), which has implications for the development of hydrocarbon reservoirs. This topic was not initially intended to be investigated at the start of this research; however it became apparent that the findings of chapter 4 needed to be tested for other porous rock types.

The rest of the introduction will be structured as follows. Section 1.1 will highlight the importance of dehydration reactions in nature and why they have been extensively studied in the laboratory. It will also introduce the nature of the problem that this thesis will attempt to address in relation to dehydrating systems. Section 1.2 will introduce the reaction that is used to study dehydrating systems, gypsum → bassanite + $H_2O$, and outline why it is an ideal analogue for higher temperature silicate dehydration reactions. The evolution of a dehydrating system is dependent on the feedback between reaction, fluid flow and deformation. A key concept concerning dehydration reactions is that under most crustal conditions transformations involve a solid volume reduction which generates porosity and enhances the permeability of the system. The overall reaction rate controls the rate at which fluid is released and also how quickly porosity is produced. Chapter 3 investigates the spatiotemporal evolution of porosity during reaction and also the controls on reaction rate. The rate of transformation is underpinned by the mechanisms that facilitate the reaction and these concepts are introduced in section 1.3. It is also important to understand how compaction will reduce the porosity and potentially restrict fluid drainage. Section 1.4 will introduce our current understanding of porous rock deformation and, at this point, the topic of sandstone compaction and its importance for hydrocarbon reservoirs will

be introduced. This is relevant for the work that is presented in chapter 5. Section 1.5 will then outline the structure of the rest of the thesis.

## 1.1. Dehydration reactions

### *1.1.1. The importance of dehydration reactions in nature*

Dehydration reactions occur in nature when hydrous minerals breakdown and release their structurally-bound water, typically during prograde metamorphism. The abundance of hydrous minerals in crustal rocks means that dehydration reactions are common in many metamorphic and tectonic settings. However much of the research into these reactions has been focussed on trying to understand the role of dehydration in subduction zones. This interest is fuelled by the desire to understand the correlation between the depths of thermal breakdown of hydrous minerals, such as serpentine and lawsonite, and the location of intermediate depth earthquakes in a subducting slab (e.g. Peacock, 2001; Hacker et al., 2003; Kita et al., 2006; Nakajima et al., 2009; Abers et al., 2013). It is generally thought that the release of high pressure fluid at depth will reduce the effective stresses acting on the reacting rocks allowing them to deform in a brittle manner at pressures where brittle instabilities involving dilatancy are typically suppressed (Kohlstedt et al., 1995; Hilairet et al., 2007). Intermediate depth earthquakes occur globally in many subduction zones in two distinct layers (Brudzinski et al., 2007), separated by an almost aseismic region up to 40 km thick (Fig. 1.1). The two regions of seismicity are thought to correspond to the breakdown of hydrous minerals in the oceanic crust and mantle respectively. Upper plane earthquakes are likely caused by dehydration reactions associated with the transformation of metabasic rocks to eclogite (Kirby et al., 1996). Lower plane seismicity is thought to be the result of serpentinite dehydration in the oceanic mantle (Peacock, 2001; Seno et al., 2001), which becomes hydrated during flexure of the slab in the outer rise (Garth and Rietbrock, 2014).

Although much of the research on dehydration reactions has focussed on subduction zones, their importance has also been recognized in other tectonic settings. In particular, the influence of reactions on fault zone processes and conversely how fault zone processes might promote reaction has been a subject of wide interest. Hubbert and Rubey (1959) were among the first to recognize a potential need for high

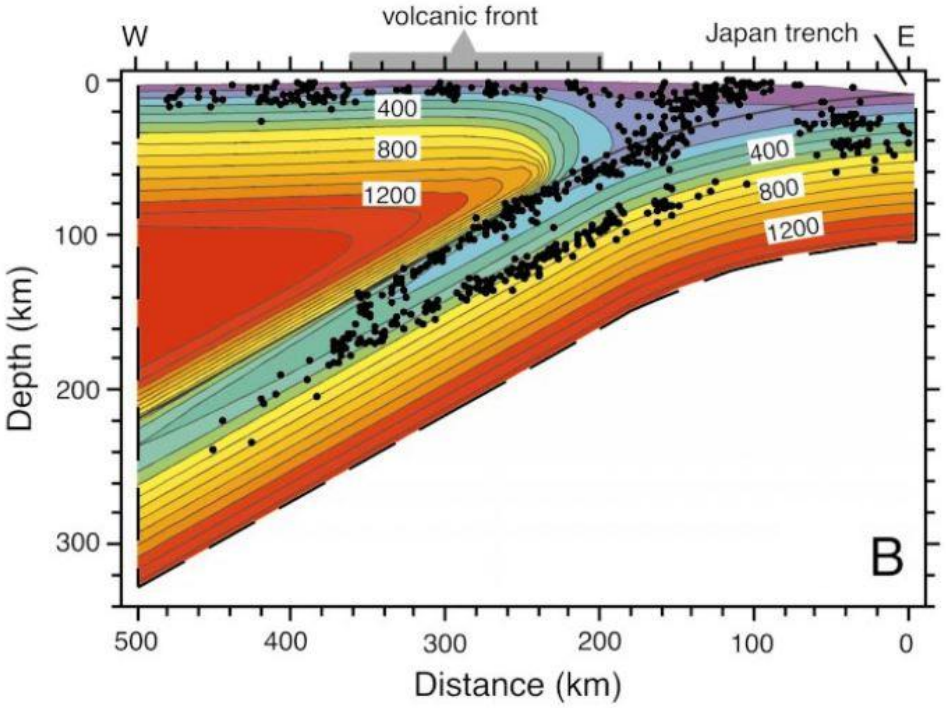


*Figure 1.1 – An example of the double seismic zone seen in a cross section through the northeast Japan Trench showing earthquake hypocenters and calculated thermal structure (from Peacock, 2001).The hypocenters reveal two distinct layers of seismicity in the down-going slab which are thought to correspond to the breakdown of hydrous minerals in the oceanic crust and mantle respectively.*

pore fluid pressures to overcome frictional resistance in order to facilitate large-scale overthrust faulting. They identified compaction of low permeability rocks, in particular clay-rich units, as the predominant mechanism for increasing fluid pressure and thus reducing the effective pressure acting on the thrust plane. The importance of clay rich fault gouges in maintaining fluid pressures in fault zones has also been recognised for strike slip faults (e.g. Faulkner and Rutter, 2001). However a source of this excess fluid into the fault zone is required and in the second part to their seminal study, Rubey and Hubbert (1959) introduce the possibility for thermal decomposition of hydrous minerals as a source of pressurized fluid in low permeability rocks; however it was not until later experimental work that this idea gained momentum. Firstly Raleigh and Paterson (1965) on serpentinite and then Heard and Rubey (1966) on gypsum showed that there is a drastic reduction in strength of the rock as it undergoes dehydration which both studies attribute to a rise in pore fluid pressure. The work of Heard and Rubey (1966) is particularly relevant as evaporites have been recognized to act as detachment horizons in many foreland fold and thrust belts (e.g. Laubscher, 1975;

Marcoux et al., 1987; Jordan and Nuesch, 1989). Therefore dehydration might not just provide a source of fluid into the fault zone; rather it could drastically weaken the deforming rocks and promote the initiation of sliding.

There has also been interest in how active faulting might promote dehydration, specifically by shear heating. As fault slip occurs, the frictional resistance that has to be overcome causes large amounts of energy to be dissipated, primarily in the form of heat. Thus measurements of heat flow across the fault would be expected to show a large anomaly with respect to the surrounding rocks. However low or zero heat flow anomalies have been reported across seismically active faults including the San Andreas Fault (e.g. Lachenbruch and Sass, 1980). Sudden phase changes have been shown to occur as a result of rapid shear heating in both hydrous (Hirose and Bystricky, 2007; Brantut et al., 2011) and carbonate minerals (Han et al., 2007). These types of decomposition reaction are typically endothermic and are thought to be able to buffer the temperature of the fault plane, keeping it relatively low if the reaction occurs rapidly during slip (Sulem and Famin, 2009; Brantut et al., 2010; Brantut et al., 2011). This highlights the interplay that can occur between active deformation and reaction.

The identification of dehydration reactions occurring in many tectonically active settings from subduction zones to strike-slip faults has motivated extensive experimental investigations into the processes involved. It is apparent that an understanding of the interplay between temperature, reaction rate, fluid flow and deformation is required in order to gain insights into how natural dehydrating systems will evolve. This is best achieved through systematic experimental studies into the effects of the different parameters involved during reaction.

### *1.1.2. Experimental investigations of dehydration*

The research in this thesis does not intend to specifically address the problem of brittle instability during dehydration. However this has been the motivation of many previous experimental studies and forms some of the wider implications of this research. These works are therefore summarized in this section before the key concepts of the problem this thesis will investigate are introduced in section 1.1.3.

As mentioned previously, some of the first experimental work on dehydration reactions was by Raleigh and Paterson (1965) and Heard and Rubey (1966) who both show drastic weakening associated with pore pressure build up during reaction. Subsequent work by Murrell and Ismail (1976) on gypsum, partially serpentinized peridotite, serpentinite and chlorite showed similar weakening behaviour when samples were subject to undrained conditions which allow the pore pressure to build up. However in experiments where the pore fluid was drained to the atmosphere the same weakening was not observed. These drained and undrained scenarios represent two end-member drainage conditions; however, in nature the pore pressure evolution will probably be affected by some transient or finite drainage architecture that will evolve during reaction. The development of pore pressures in a dehydrating system is dependent on the reaction, which produces fluid, and permeability evolution which will allow excess $H_2O$ to dissipate. Under most crustal conditions dehydration reactions are associated with a net volume increase (i.e. the volume of the product minerals plus fluid is greater than the initial reactant phases). This means that excess fluid is produced during reaction, which has the potential to create fluid pressures that are greater than hydrostatic. However when considering only the solid components of a dehydration reaction there is typically a solid volume reduction associated with the transformation (i.e. the volume of the product minerals is less than the reactant minerals). This means that porosity is generated by the reaction itself which will in turn increase the permeability and potentially allow the excess fluid to dissipate. Therefore the pore pressure evolution is dependent on the competing processes of fluid and porosity production.

Since the early studies, which showed evidence for dehydration weakening (Raleigh and Paterson, 1965; Heard and Rubey, 1966; Murrell and Ismail, 1976), a large number of investigations have focused on understanding the hydraulic and mechanical feedbacks associated with dehydration. A series of dehydration and deformation tests on gypsum have revealed a transition from weakening to strengthening during reaction (Ko et al., 1995; Olgaard et al., 1995; Ko et al., 1997). Ko et al., (1997) show that there are three stages of fluid expulsion during dehydration of the initially low porosity gypsum: (i) during the early stages fluid is released by the reaction and trapped in isolated pores, allowing the pore pressure to increase, thus reducing the effective pressure and weakening the rock. (ii) As reaction continues the pore network becomes interconnected, high pore pressures dissipate and the sample re-strengthens as the effective pressure increases. (iii) As reaction nears completion

the fluid expulsion slows and the sample is almost totally transformed to the product mineral bassanite which is stronger than the initial gypsum. Therefore the strength evolution of the dehydrating rock is not just dependent on the pore pressure but also the mechanical properties of the product mineral(s). Rutter and Brodie (1988) have shown in serpentinite that weakening can occur by the formation of ultrafine-grained product materials which promotes a change in deformation mechanism to grain-size sensitive flow. Further dehydration and deformation studies on serpentinite have highlighted the role of porosity on influencing the strength of the reacting rocks (Arkwright et al., 2008; Rutter et al., 2009). Rather than just providing a permeable pathway for excess fluids to dissipate, the formation of porosity itself weakens the rock and Rutter et al., (2009) use principles of soil mechanics to demonstrate its importance. Compaction of this newly generated porosity leads to strain hardening, highlighting another mechanism how the behaviour of a dehydrating system can change between weakening and strengthening.

Although these studies have shown that weakening may only be transient during dehydration, it is considered a prerequisite for the initiation of unstable brittle behaviour and earthquake generation. Many studies have observed dehydration embrittlement in the recording of acoustic emissions as well as evidence for localized brittle features in microstructural analysis (e.g. Dobson et al., 2002; Jung et al., 2004; Milsch and Scholz, 2005; Burlini et al., 2009). However despite much documentation of dehydration embrittlement, it remains unclear if this phenomenon will generate seismicity. Some investigations have observed unstable stick-slip instabilities during dehydration (Takahashi et al., 2011; Okazaki and Hirth, 2016) whereas others have documented stable sliding during reaction (Chernak and Hirth, 2011; Gasc et al., 2011; Proctor and Hirth, 2015; Leclère et al., 2016). In those studies that observed instability, it occurred in either the reacting (in lawsonite as shown by Okazaki and Hirth, 2016) or product phase (in olivine as shown by Takahashi et al., 2011). Although Leclère et al., (2016) do not observe instability during gypsum dehydration they do record unstable slip in the product mineral bassanite after reaction has occurred. This is attributed to a switch to velocity weakening behaviour at temperatures above 140 °C, similar to the changes in frictional behaviour observed at the same temperature in anhydrite (Pluymakers et al., 2014). This highlights the importance of understanding the frictional behaviour of all the components of the reacting system and Leclère et al., (2016) produced a flow chart to help identify scenarios when earthquakes might be generated (Fig. 1.2).

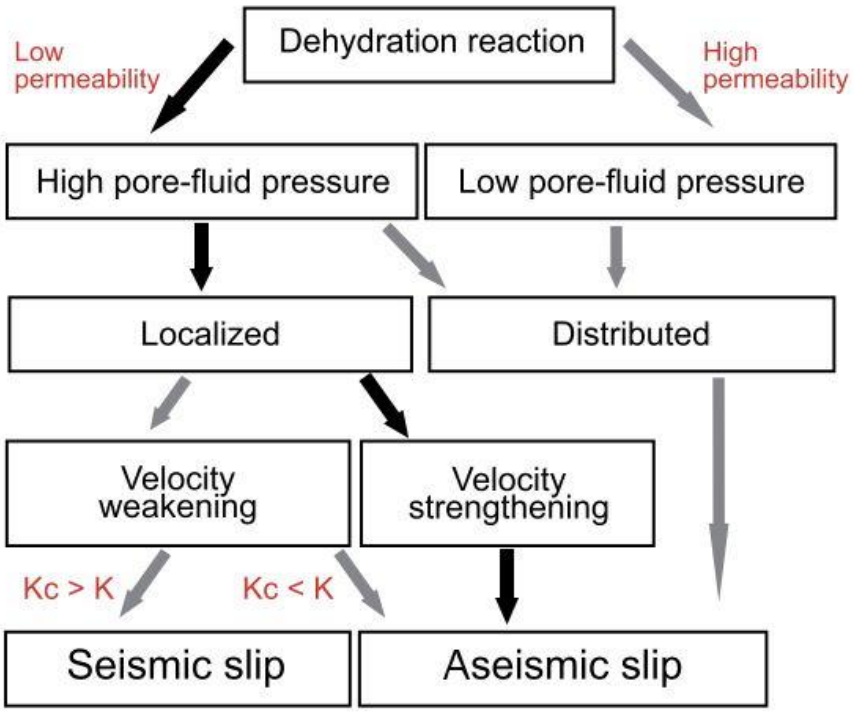


*Figure 1.2 – Flow chart produced by Leclère et al., (2016) summarizing the conditions required to trigger instabilities in a dehydrating system. Localized refers to either the reactant or product phases becoming localized along shear planes associated with the deformation. K refers to the stiffness of the loading system and Kc refers to the critical stiffness value.*

Studies which observe stable slip during dehydration may support the hypothesis that the reacting rocks do not have to be the site of instability in a subduction zone. Rather the expulsion of fluids from the dehydrating system may promote seismicity in the surrounding more brittle rocks (Arkwright et al., 2008; Rutter et al., 2009). Pore pressure pulses have been observed in experiments and dissipate when permeability becomes enhanced enough to allow drainage (e.g. Leclère et al., 2016). A pore pressure pulse could also be driven into the surrounding rocks by compaction of the reaction generated porosity as enhanced drainage reduces the pore pressure in the reacting rocks (Connolly, 1997). However regardless of where instabilities might occur, it is obvious that a more comprehensive knowledge of the hydraulic and mechanical properties of the dehydrating system is required.

### *1.1.3. Nature of the Problem*

It has become apparent from previous experimental work that dehydrating systems are highly complex and can evolve in many different ways depending on the feedbacks between reaction, fluid flow and deformation. The nature of the pore space produced during reaction and its subsequent evolution under elevated pressure and stress will strongly influence the mechanics and fluid flow of the system. An increase in porosity will enhance permeability and allow excess fluid to drain, thus reducing the fluid pressure. This can in turn cause an acceleration of the reaction rate (e.g. Llana-Funez et al., 2012) which will lead to an increase in the porosity production rate. However, as more porosity is produced and fluids are able to drain, the effective pressures will increase and promote compaction. Compaction of the pore space will restrict fluid flow, reduce the effective pressure and potentially slow the reaction rate. Therefore the interplay between porosity generation by reaction and subsequent reduction by compaction will determine the evolution of the whole system.

The importance of these processes is highlighted in the theoretical work of Wong et al., (1997b) who produced the following equation to model the build-up of pore pressure excesses in a dehydrating system:

$$\phi\left(\beta_{\varphi}+\beta_{f}\right)\frac{\partial P'}{\partial t}=\nabla\cdot\left(\frac{k}{\mu}\nabla P'\right)+\dot{\Gamma}-\dot{\Phi} \qquad (1.1)$$

Where:

$\phi$ = porosity

$\beta_{\varphi}$ = pore compressibility

$\beta_{f}$ = fluid compressibility

$P'$ = pore pressure excess

$t$ = time

$k$ = permeability

$\mu$ = viscosity of the fluid

$\dot{\Gamma}$ = reaction rate

$\dot{\Phi}$ = porosity production rate

This equation contains terms for reaction rate and porosity production rate on the right hand side; two important source terms in a dehydrating system (Wong et al.,

1997b). The reaction rate has a positive contribution to the pore pressure excess whereas there is a negative contribution from the porosity production term. Reaction rate has been shown to be strongly associated with fluid pressure (Llana-Funez et al., 2012) which will change as permeability evolves during reaction. It is also dependent on the underlying kinetic processes which facilitate the transformation; however these are very poorly understood as direct observation of metamorphic reactions has been previously impossible. The porosity production rate is dependent on the interaction between the pore space generated by reaction and its subsequent destruction by compaction. A comprehensive understanding of the compaction behaviour of the reacting rocks is therefore paramount in gaining a better knowledge of the overall system evolution. The key concepts and previous work associated with reaction kinetics and the deformation of porous rock is summarized in sections 1.3 and 1.4 respectively.

### *1.1.4. Thesis Aims*

This thesis aims to constrain further the role of porosity in a dehydrating system, in particular its influence on both the reaction rate and the deformability of the reacting rocks. This will be done though experimental investigations using gypsum as analogue material for other hydrous minerals that dehydrate at much higher temperatures in a subduction zone, such as serpentine.

The investigation of kinetic processes in metamorphism has been previously limited by our inability to directly observe reactions in operation, both in nature and in experiment. Recent developments in high-resolution 4D X-ray synchrotron microtomography mean that new experimental setups (e.g. Fusseis et al., 2014) can be utilized to gather mineralogical and microstructural information on geological processes in real time. This includes metamorphic reactions, and the hydrothermal cell designed by Fusseis et al., (2014) allows for gypsum to be heated beyond its dehydration temperature whilst being subjected to realistic crustal pressures. The novel datasets that are gathered using synchrotron X-ray microtomography can provide information on the spatiotemporal evolution of both the porosity and product grains that form during dehydration. These data will be used to analyze the underlying kinetic controls in operation during dehydration and also to understand the influence of pore connectivity on reaction.

There are very few studies on the compaction of porosity generated from dehydration reactions. Much of the previous work on porous rock deformation has been on compaction of reservoir rock, predominantly sandstone (e.g. Wong et al., 1997a). Rutter et al., (2009) attempted to characterize the deformation behaviour of dehydrated serpentinite ($\phi \approx 20\%$) using the concepts of critical state soil mechanics. However no such study has been performed on dehydrated gypsum and this thesis will use similar principles to document the deformation behaviour of the porous product material. In particular the shape and evolution of the yield curve will be analysed under different loading regimes. The thesis will then move away from thinking specifically about dehydration reactions by applying these concepts to the compaction of porous sandstone and considering the implications for porous rock deformation in general.

## 1.2. Gypsum as an analogue material

Gypsum is part of the calcium sulphate system ($CaSO_4$ - $H_2O$) which is comprised of three main minerals:

Gypsum ($CaSO_4 \cdot 2H_2O$)
Bassanite ($CaSO_4 \cdot 0.5H_2O$)
Anhydrite ($CaSO_4$)

These minerals are related by reversible dehydration/hydration reactions. Gypsum and anhydrite are the most abundant evaporite minerals found in nature, with anhydrite typically being formed by the dehydration of gypsum during burial and diagenesis (Murray, 1964):

$$CaSO_4 \cdot 2H_2O \rightarrow CaSO_4 + 2H_2O \quad (1.2)$$

Bassanite is rarely found in evaporitic sequences, but is formed regularly during dehydration of gypsum in the lab:

$$CaSO_4 \cdot 2H_2O \rightarrow CaSO_4 \cdot 0.5H_2O + 1.5H_2O \quad (1.3)$$

The reason for this is that bassanite is a metastable phase at low pressures; but the gypsum to anhydrite dehydration reaction is too sluggish to happen on laboratory timescales therefore bassanite forms instead. The phase diagram (Fig. 1.3) and

solubility data for the Ca-sulphate system further highlight this (Fig. 1.4). When heated at atmospheric pressure, gypsum should dehydrate to form anhydrite at 42 °C. However this reaction is typically bypassed for the more kinetically favourable gypsum-to-bassanite reaction at temperatures above 100 °C (McConnell et al., 1987). The formation of bassanite has been shown to be almost ubiquitous in experimental investigations of gypsum dehydration (Ko et al., 1995; Milsch et al., 2011; Brantut et al., 2012; Llana-Funez et al., 2012; Leclère et al., 2016). If temperature is increased further, anhydrite forms from the dehydration of bassanite (Christensen et al., 2008).

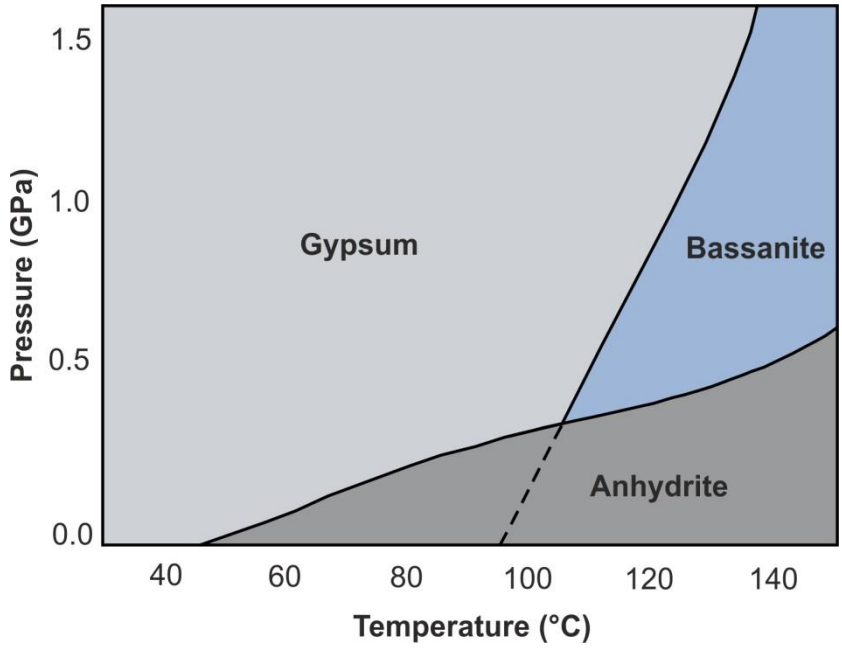


*Figure 1.3 – A phase diagram of the Ca-sulphate system modified from* Mirwald (2008)*. Dashed line represents the conditions where bassanite forms metastably when the gypsum to anhydrite reaction is bypassed.*

Although the minerals in the Ca-sulphate system are related by relatively simple reactions there is some complexity as different polymorphs of bassanite and anhydrite have been identified. There are two distinct morphologies of bassanite; α-bassanite which forms well-formed acicular crystals and β-bassanite which forms 'flaky particles' (Singh and Middendorf, 2007). These different morphologies form under different conditions. When gypsum is dehydrated under a high partial pressure of water vapour α-bassanite forms, whereas β-bassanite is formed by dehydration under

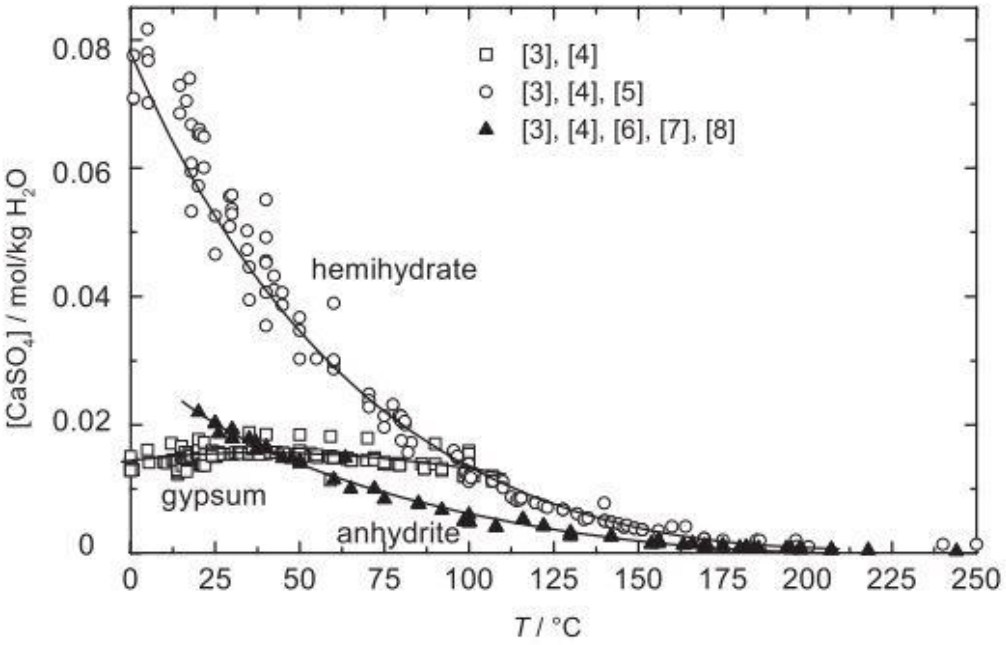


*Figure 1.4 – Collection of literature data on the solubility of gypsum, anhydrite and bassanite in the temperature range 0-200 °C, collated by* Freyer and Voigt (2003).

a low partial pressure of water vapour, i.e. in air or vacuum (Singh and Middendorf, 2007). There are also two phases of anhydrite, which are termed soluble and insoluble anhydrite. Insoluble anhydrite is the form typically found in nature, whereas soluble anhydrite forms from the dehydration of bassanite in the laboratory (Christensen et al., 2008).

Despite the added complexity of the different polymorphs, the relatively simple transformations make gypsum an ideal analogue mineral to study dehydration reactions and the associated processes. The relatively low dehydration temperature (approximately 100 °C) is easier to use in experiment than minerals such as serpentine which requires quite a large overstepping of the reaction boundary to initiate dehydration (e.g. Llana-Funez et al., 2007; Rutter et al., 2009).

## 1.3. Metamorphic reaction kinetics

The study of metamorphism is underpinned by thermodynamics; that a system tends towards a state of minimum energy (e.g. Powell and Holland, 2010). In the case of a chemical system such as the Earth, the Gibbs free energy (Gibbs, 1874) is used to

determine whether a given mineral assemblage will be in equilibrium at specific pressure and temperature conditions. When the Gibbs free energy of the product minerals is less than that of the reactants the reaction may proceed. Thus the Gibbs free energy provides the driving force to initiate a reaction; however it does not determine the kinetic mechanisms that will facilitate the transformation.

There is widespread evidence of disequilibrium in crustal rocks including mineral zoning, coexisting polymorphs and reaction rims (e.g. Carmichael, 1969; Yund, 1997; Carlson, 2002). This shows that although there may be a driving force for a metamorphic reaction, kinetic impediments may prevent thermodynamic equilibrium from being reached. The operative kinetic mechanisms will also determine the overall reaction rate, so it is important to constrain better these processes especially when trying to understand how a dehydrating system might evolve (see equation 1.1.). Kinetic processes that are in operation during a transformation are dependent upon the pathways that chemical components take from detachment at the reactant phase to incorporation into the lattice of the product mineral(s) (e.g. Rubie and Thompson, 1985; Lasaga, 1997; Wheeler, 2014). This makes reaction kinetics inherently more difficult to study than thermodynamics as these pathways are time-dependent (Lasaga, 1997). It has been previously impossible to view chemical pathways in operation, both in nature or traditional experiment, therefore much of our understanding of kinetic processes is inferred from textures that have been preserved in metamorphic rocks after a reaction has ceased (Wheeler, 1991).

There are likely three predominant kinetic processes that can control the reaction rate in a dehydrating system. Firstly nucleation must occur; this is the process of producing a nucleus of a product mineral. Nuclei are angstroms size and the central problem with this step is that a nucleus will have a proportionally high surface area which provides an energy barrier that must be overcome to grow stable grains of the new phase (Wheeler, 1991). Secondly transport of the chemical constituents to the site of the nuclei must occur in order for new grains to grow. The preservation of distinct sedimentary layering in metamorphic rocks up to amphibolite facies (e.g. Carmichael, 1969) suggests that the scales of material transport are typically on the order of mm to cm. It is often assumed, for many reactions, the transport of dissolved solutes during metamorphism occurs through a thin grain-boundary fluid film (Walther and Wood, 1984). However the nature of these fluid films, whether they would permit bulk flow of the fluid containing dissolved solutes or require diffusive processes to facilitate

transport, is poorly understood. Finally interface reactions must occur in order to transfer atoms onto the surface of the growing mineral lattice or to dissolve them from the surface of a reacting material (Lasaga, 1986; Wheeler, 1991). The slowest of these mechanisms, termed the rate-limiting step, will control the overall reaction rate of the mineral transformation (Fisher, 1978). It should be noted that rate of heat input is also an important kinetic process (Fisher, 1978), especially for dehydration reactions which are endothermic.

## 1.4. Deformation of porous rock

### *1.4.1. The deformation of porous sandstone and implications for reservoirs*

As discussed in section 1.1.3, compaction of porosity is important in the evolution of a dehydrating system for generating and maintaining high pore fluid pressures. However much of the interest into porous rock deformation has been aimed at trying to understand the cause of porosity loss from sandstones and siliciclastic sediments, primarily because of the impact on fluid flow and permeability reduction in hydrocarbon reservoirs. During burial, there are two predominant mechanisms that lead to a reduction in porosity: mechanical compaction and chemical lithification. Although chemical processes, such as pressure solution and cementation, may significantly reduce porosity in deep reservoirs, the initial stages of burial are typically dominated by mechanical processes such as grain crushing, pore collapse and localized faulting. These inelastic mechanical processes have important implications for a range of reservoir and geotechnical problems. For example, fluid extraction from a reservoir leads to a reduction in pore pressure, thus increasing the effective pressure (e.g. Teufel et al., 1991), potentially leading to inelastic compaction of the reservoir rock (e.g. Goldsmith, 1989). The consequences of compaction can lead to surface subsidence (e.g. Fredrich et al., 1998; Nagel, 2001) which can be economically severe. For example, 10 ft of subsidence that occurred in the offshore Ekofisk Field during production, required elevation of the steel platforms and a protective barrier to be built around the storage tank at a cost of approximately $1 billion (Sulak, 1991). As well as economic costs, the significant reduction in permeability that potentially results from reservoir compaction (e.g. Goldsmith, 1989; Zhu and Wong, 1997) can have a detrimental effects on the ease at which hydrocarbons can be extracted.

On a smaller scale, the concentration of stresses around wellbores can lead to failure of a well if they exceed the strength of the rock (e.g. Zoback, 2010). If permeability is relatively low, pore pressure drawdown may also be restricted to the near wellbore region causing a perturbation in the local stress field, potentially promoting shear displacement (e.g. Fredrich et al., 1998). Slip on faults may also be induced as a result of fluid injection, for example during $CO_2$ sequestration (e.g. Lucier et al., 2006), which leads to an increase in pore fluid pressure. Knowledge of the occurrence and extent of inelastic deformation along different stress trajectories is therefore an essential aspect of reservoir and geotechnical engineering. This requires a fundamental understanding of the mechanical response and microphysical processes associated with porous rock deformation.

### *1.4.2. Inelastic deformation of porous rock*

When a porous rock is subject to a stress state beyond its elastic yield there will be an instantaneous mechanical response (i.e. compaction or dilation) and, if the rock is left at these conditions for a prolonged period, time-dependent mechanisms such as subcritical crack growth (Atkinson and Meredith, 1981; Atkinson, 1984; Heap et al., 2009) and pressure solution (Rutter, 1976) can lead to further deformation. This thesis will focus on the initial time-independent response of the porous rock to an imposed stress. This is important in a dehydrating system, as well as for hydrocarbon reservoirs, as sudden changes in stress state caused by fluid pressure fluctuations can lead to rapid changes in the deformability of the rock. Subsequent compaction or dilation will then dictate the strength evolution of the system and potentially promote or inhibit instabilities.

The principles of soil mechanics (e.g. Schofield and Wroth, 1968; Wood, 1990) have been widely used to document the deformation of porous rock. In soil mechanics a broadly elliptical yield curve is plotted in P-Q space, where P is the effective mean stress $\left(P = \frac{\sigma_1 + \sigma_2 + \sigma_3}{3} - P_f\right)$ and Q is the differential stress ($Q = \sigma_1 - \sigma_3$). This curve separates the elastic stress states from those where plastic (inelastic) deformation will occur (Fig. 1.5). It should be noted that the term *plastic* does not imply an underlying deformation mechanism, rather, that the deformation proceeds when a yield stress is reached and is permanent, if the load is removed after an amount of plastic strain has been accumulated the rock will not return to its initial starting condition. The nature of

inelastic deformation that a rock experiences when its stress state intersects the yield curve can be broadly separated into two main regimes. At low pressures, the mode of deformation is dilatancy which is typically associated with localized deformation and faulting (e.g. Menendez et al., 1996). At high pressures a rock will experience distributed deformation as it undergoes shear-enhanced compaction (Curran and Carroll, 1979). The compaction of porous rock can also be achieved under a purely hydrostatic stress state (i.e. no differential stress), therefore the yield curve intersects the P-axis at a point that is typically referred to as P*. Empirical data on a range of different porous rock including sandstone (Wong et al., 1997a; Baud et al., 2000b; Cuss et al., 2003b; Baud et al., 2004; Baud et al., 2006; Louis et al., 2009), limestone (Baud et al., 2000a; Vajdova et al., 2004; Baud et al., 2009; Cilona et al., 2014) and volcaniclastics (Zhu et al., 2011) has shown that the yield curves for porous rock are broadly elliptical in shape, in agreement with observations from soil mechanics. These concepts have also been applied to the deformation of porosity formed by the dehydration of serpentinite (Rutter et al., 2009). However there has been no such documentation of the yield curve of dehydrated gypsum.

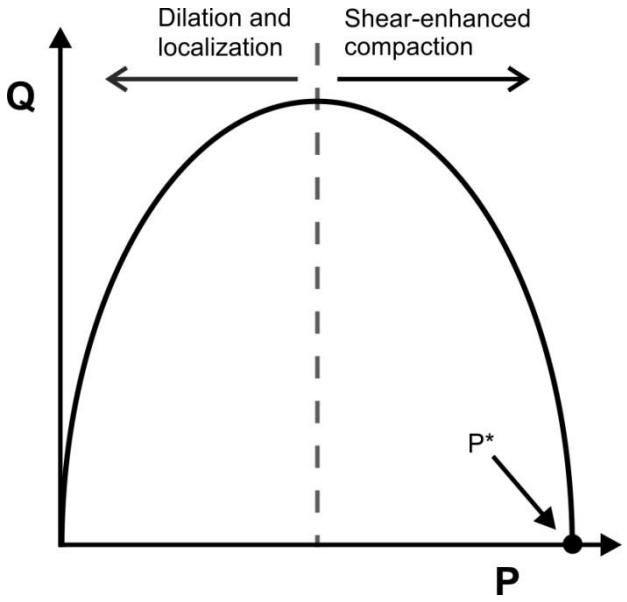


*Figure 1.5 – A schematic diagram of a yield curve which is broadly elliptical in shape. Anywhere inside the curve is in the elastic regime whereas the regions outside the curve represent the stress states where permanent inelastic deformation will occur. The low-pressure side of the curve is associated with dilatancy and localisation. The high-pressure side is associated with shear-enhanced compaction.*

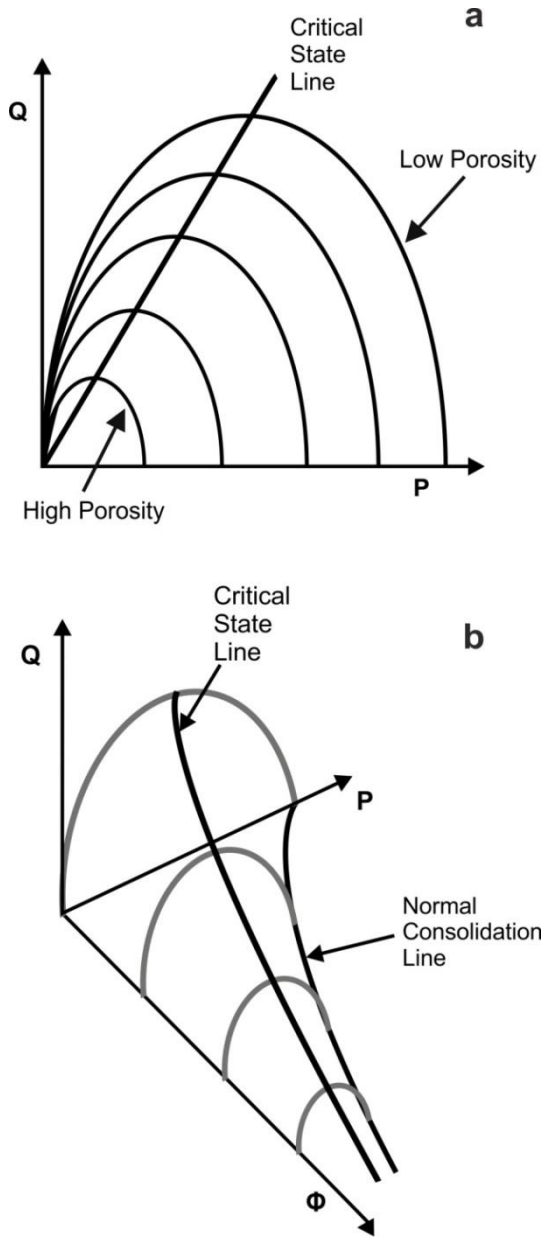


*Figure 1.6 – a) As a porous rock is deformed the subsequent changes in porosity can be represented with a new yield curve. A family of curves can therefore be defined for the different porosities with the most compacted rocks having the largest yield curves. The crests of the curves, which separate regions of dilation from compaction, can be joined by the critical state line. b) These families of curves can be represented in 3D where the third axis is porosity (Φ). The ellipses space out along the porosity axis and their respective P* points can be joined to form the normal consolidation line.*

As a rock accumulates inelastic strain the porosity will either increase or decrease depending on whether the sample is compacting or dilating. A new yield

curve can therefore be defined for this subsequent pore structure. If a rock experiences compaction the porosity will reduce and the yield curve will expand. If the rock undergoes dilation the increase in porosity will cause the yield curve to shrink. A family of yield curves can therefore be plotted for each subsequent yield state (Fig. 1.6a) and the crests, which separate dilation from compaction, can be joined by a line called the *Critical State Line (CSL)*. This can also be visualized in 3D where the third axis represents porosity (Φ). In this diagram (Fig. 1.6b) the ellipses space out along the porosity-axis and their respective P* values form another line called the *Normal Consolidation Line (NCL)*.

The concept of a family of curves, where for a given porosity the shape of the curve remains the same with only the size changing, has been well applied to unconsolidated sediments. A series of complex probing tests on both clay (Graham et al., 1983) and sand (Tatsuoka and Ishihara, 1974; Miura et al., 1984) have revealed the shapes of these families and found that a unique curve shape can be defined for the different materials. However the applicability of this concept to porous rock remains unclear and experimental data on curve evolution is sparse. Some studies have suggested that a unique yield curve shape can be defined for porous rock that is independent of rock type (Wong et al., 1997a; Rutter and Glover, 2012). However the work of Baud et al., (2006) has shown that yield curves do appear evolve in shape with the accumulation of inelastic volumetric strain. Their yield curves do have a large amount of data scatter as a result of sample variability making it difficult to accurately constrain the shape evolution; however they do suggest that a unique curve shape cannot be defined. Alternative models to that of Schofield and Wroth (1968) have been proposed which allow yield curve evolution in response to the accumulation of inelastic strain. The models of Carroll (1991) and DiMaggio and Sandler (1971) allow the yield curve to change shape in response to inelastic volumetric strain; whereas the model of Grueschow and Rudnicki (2005) also considers the effect of inelastic shear strain. In these models the yield curve is not considered to be a single elliptical curve, rather it is comprised of two curves; a low pressure dilational envelope bound on the high pressure side by an elliptical cap. Baud et al., (2006) compared their results to the models of Carroll (1991) and DiMaggio and Sandler (1971) and found these models to have varying amounts of success in approximating the yield curve evolution of different sandstones. This highlights the current uncertainty surrounding the effect of inelastic strain on yield curve evolution for porous rock.

## 1.5. Thesis structure

After this introduction, chapter 2 will describe the experimental set-ups used for the collection of data. This will include a brief summary of the hydrothermal cell used in the synchrotron beamline; however a detailed description of this is beyond the scope of this thesis as the workings of the cell have already been documented by Fusseis et al., (2014). This chapter will also include a detailed description of the workings of the triaxial rig used in the Rock Deformation Laboratory, University of Liverpool. This was used for the collection of data in chapters four and five.

Chapters 3, 4 and 5 present the majority of the original research that was collected for this thesis. These chapters were all written to be stand-alone manuscripts and as such there will be repetition of some key concepts, particularly in the introductions of these chapters. There have been changes to the versions prepared for journal submission, in that the figures and subheadings have all been renumbered for continuity with the rest of the thesis and that the reference sections have all been consolidated into one list at the end of the thesis. All of these chapters include their own abstract and any supplementary material that accompanies the manuscript is included at the end of each chapter. The content of these chapters will be as follows:

- **Chapter 3** presents results on a gypsum dehydration experiment where the sample was constantly imaged in real time using X-ray synchrotron microtomography. This data is then analysed to discuss the implications for the kinetic controls on the reaction.

- **Chapter 4** presents an investigation of the compaction behaviour of the porous dehydration product, bassanite. This chapter has a particular focus on the shape and evolution of the yield curve for the porous material.

- **Chapter 5** presents an investigation into the compaction behaviour of two highly porous sandstones. This is to compare whether the new results found in chapter 4 on porous bassanite have wider implications for porous rock deformation in general.

Chapter 6 provides a summary of the main conclusions found in the previous chapters and relates the work back to the nature of the problem presented in this introduction, by integrating insights concerning chemical aspects of porosity evolution (Ch 3) and mechanical aspects (Chs 4 and 5). Suggestions are then made for further work. This is then followed by a complete reference list for the whole thesis and also by the appendix.

## 1.6 Status of manuscripts and co-author contribution

The status (at the time of thesis submission) of the manuscripts associated with chapters 3, 4 and 5 in this thesis is outlined below. Also detailed is the contribution of each co-author to the manuscripts.

**Chapter 3**: Bedford, J. D., Fusseis, F., Leclère, H., Wheeler, J. and Faulkner D. R., (2017) A 4D view on the evolution of metamorphic dehydration reactions. *Scientific Reports*, **7**.

Submitted: 20th September 2016

Accepted: 26th June 2017

Published: 31st July 2017

*Co-author contribution:*

John Bedford – Principal investigator, primary author, data collection, data analysis

Florian Fusseis – Data collection, data analysis, manuscript review, discussion

Henri Leclère – Data collection, manuscript review, discussion

John Wheeler – Data analysis, manuscript review, discussion

Daniel Faulkner – Manuscript review, discussion

**Chapter 4**: Bedford, J. D., Faulkner D. R., Leclère, H. and Wheeler, J., Deforming porous rock: high-resolution mapping of yield curve evolution and the implications for compaction, dilation and localization. *Journal of Geophysical Research – Solid Earth.*

Submitted: 23rd April 2017

Status: Reviewers comments received, manuscript to be resubmitted after corrections.

*Co-author contribution:*

John Bedford – Principal investigator, primary author, data collection, data analysis

Daniel Faulkner – Experimental design, manuscript review, discussion

Henri Leclère – Manuscript review, discussion

John Wheeler – Manuscript review, discussion

**Chapter 5:** Bedford, J. D., Faulkner D. R., Wheeler, J. and Leclère, H., High-resolution mapping of yield curve shape and evolution for two high porosity sandstones. *Journal of Geophysical Research – Solid Earth*.

Submitted: In preparation

*Co-author contribution:*

John Bedford – Principal investigator, primary author, data collection, data analysis

Daniel Faulkner – Manuscript review, discussion

John Wheeler – Manuscript review, discussion

Henri Leclère – Manuscript review, discussion

# 2. Experimental design

## 2.1. Introduction

The majority of experimental work in this thesis (Chapters 4 and 5) was conducted on high pressure, high temperature triaxial deformation apparatus in the Rock Deformation Laboratory, Department of Earth, Ocean and Ecological Sciences, University of Liverpool. Experimental work was also conducted, in collaboration with Dr. Florian Fusseis (University of Edinburgh), at the Advanced Photon Source synchrotron facility, Argonne National Laboratories, Illinois, USA (Chapter 3). This chapter briefly introduces the experimental cell used at the Advanced Photon Source and then gives a detailed outline of the triaxial deformation apparatus at the University of Liverpool.

## 2.2. Synchrotron X-ray microtomography apparatus

The design of the portable experimental cell that was used for the synchrotron X-ray microtomography dehydration experiments in chapter 4 of this thesis has been comprehensively documented by Fusseis et al., (2014). A detailed description of the equipment is therefore not necessary in this thesis; instead the basic workings are summarized below.

The apparatus is a Hassler-type core holder (Fig. 2.1) which can confine samples up to pressures of 25 MPa and be heated to temperatures of 230°C. The X-ray transparent aluminium pressure vessel can accommodate millimetre sized samples; in our case 2 mm diameter and 5 mm length. It is transparent to a filtered polychromatic beam with peak energy of 65 keV, such as that provided in the A-hutch of Beamline 2BM at the Advanced Photon Source (Fusseis et al., 2014). The confining pressure is applied to the sample by a manual piston screw pump. The sample is inserted into a heatshrink (polyolefin) jacket to ensure it does not come into contact with silicone oil that is used as a confining medium. A pore fluid pressure can be applied to sample and be controlled by two servo-controlled Cetoni high pressure syringe pumps, one

attached to the top of the sample and one to the bottom (Fig. 2.1a). The cell is heated by two knuckle-band heaters which are attached to the end caps on the top and bottom of the vessel. The temperature of the sample is monitored and controlled by a thermocouple that is inserted through the upstream pore pressure pipe so that is positioned just above the top of the sample.

**a)**

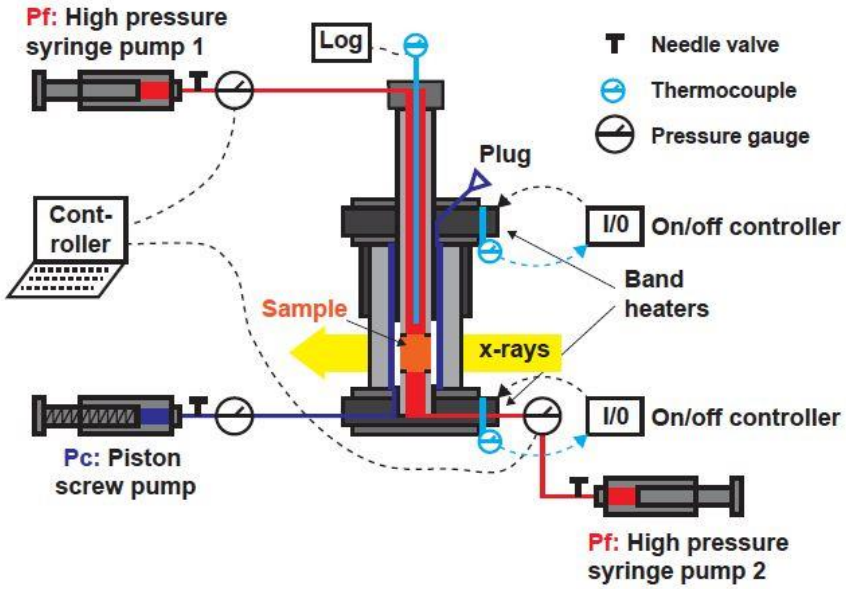


**b)**

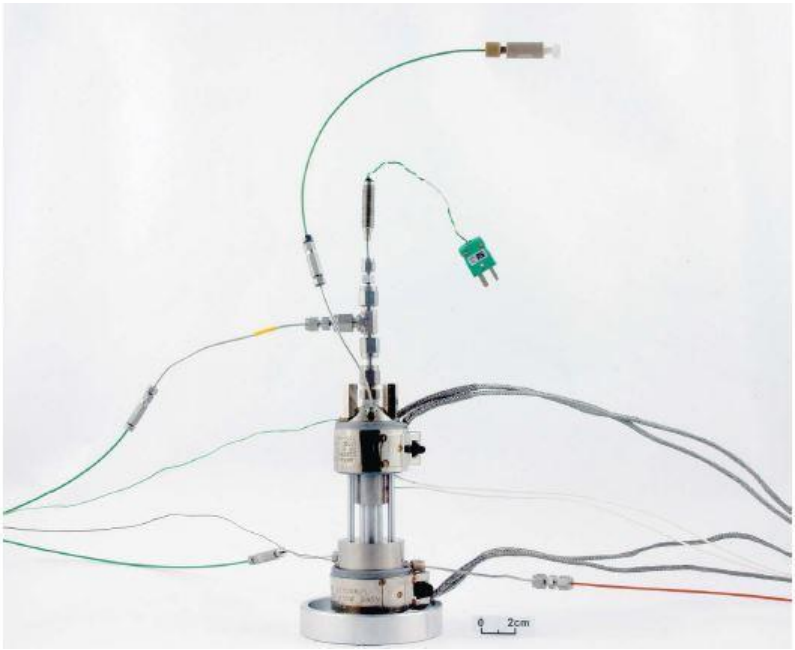

***Figure 2.1 - a)*** *A schematic diagram of the experimental cell and control system used in the synchrotron beamline, modified from Fusseis et al., (2014).* ***b)*** *A photograph of the cell from Fusseis et al., (2014).*

## 2.3. Triaxial deformation apparatus

The basic design of the triaxial deformation apparatus is summarized below. This is followed by more detailed descriptions of the pressure vessel, sample assembly, confining pressure system, pore fluid system, axial loading system and servo-control system. The potential sources of error are then discussed at the end of this section.

### *2.3.1. Basic design*

The triaxial deformation apparatus used in this work is a high pressure, high temperature deformation rig (Fig. 2.2) capable of experiments under conditions of up to 250 MPa confining pressure (approximately equivalent to 10 km depth in the Earth's crust), 200 MPa pore fluid pressure and temperatures of 200°C. A differential load of up to 300 kN can be applied to the sample via an electro-mechanical loading piston. The majority of experiments in this thesis are performed under axisymmetric compression where the greatest principal stress ($\sigma_1$) is increased axially whilst holding the other principal stresses ($\sigma_2$ and $\sigma_3$) equal:

$$\sigma_1 \geq \sigma_2 = \sigma_3$$

Axisymmetric extension tests (where $\sigma_1 = \sigma_2 \geq \sigma_3$) can also be performed, by using an attachment to connect the loading piston to the sample assembly, however these tests were not performed in this study so will not be described in detail (see Faulkner and Armitage, 2013). The apparatus can accommodate 20mm diameter cylindrical samples. The servo-controlled pore fluid system allows for the pore pressure to be controlled at the top and bottom faces of the sample (upstream and downstream). Pipes from the upstream and downstream ends of the sample are connected through to a volumometer with precision of 0.1 $mm^3$. This can be used to monitor relative pore volume change during an experiment. The upstream and downstream reservoirs can be isolated so they are only connected through the sample itself (using valves 3-6 in figure 2.3). This enables permeability measurements to be performed via the transient pulse decay technique (Brace et al. 1968) or the pore pressure oscillation technique (Fischer 1992). The ability to control the confining pressure, pore fluid pressure and axial load allows for experiments where the differential stress and the effective mean stress can be varied independently and hence a range of stress space can be covered.

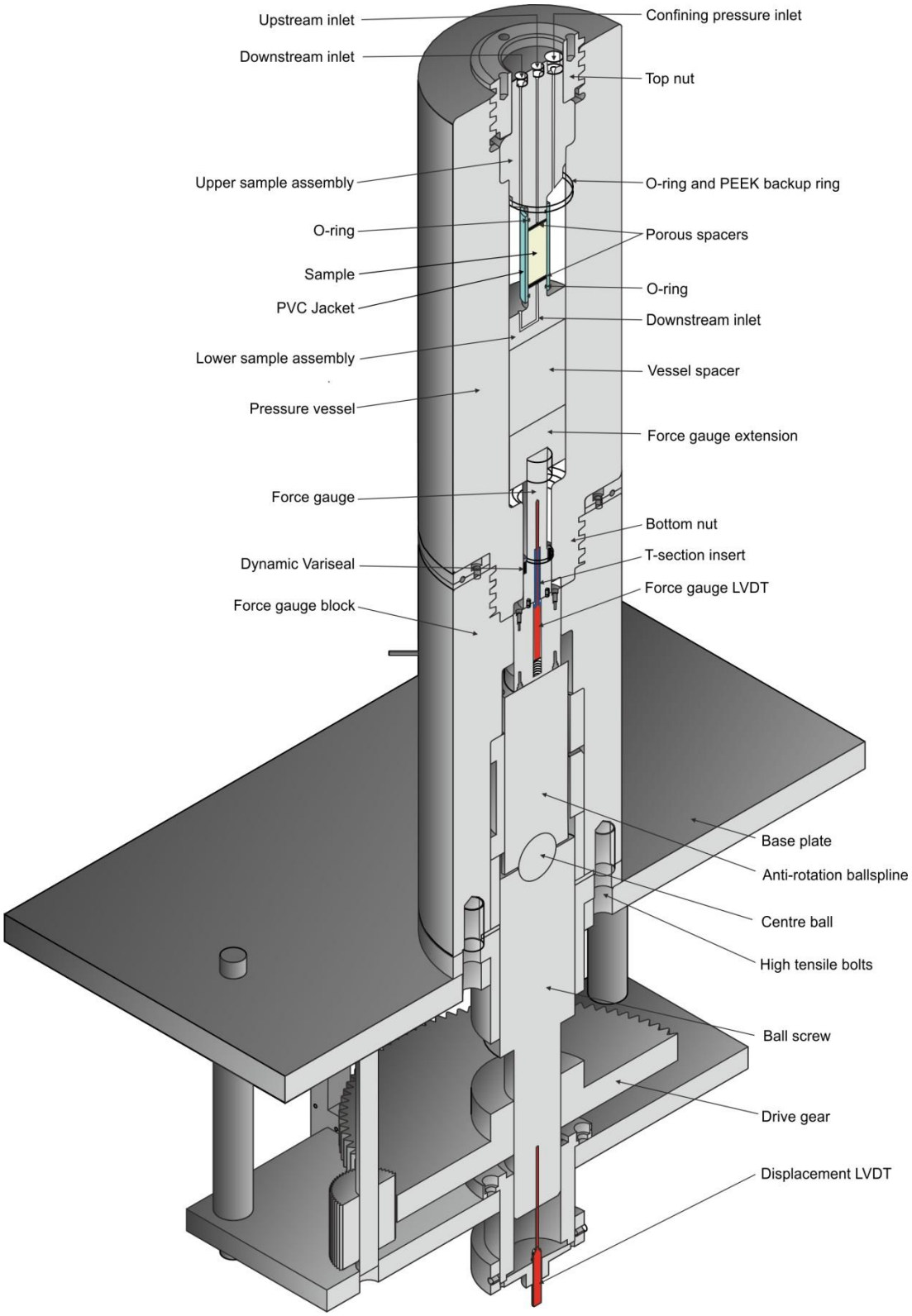


***Figure 2.2*** *- The high pressure triaxial deformation apparatus. Drawn to scale of 1:5.6.*

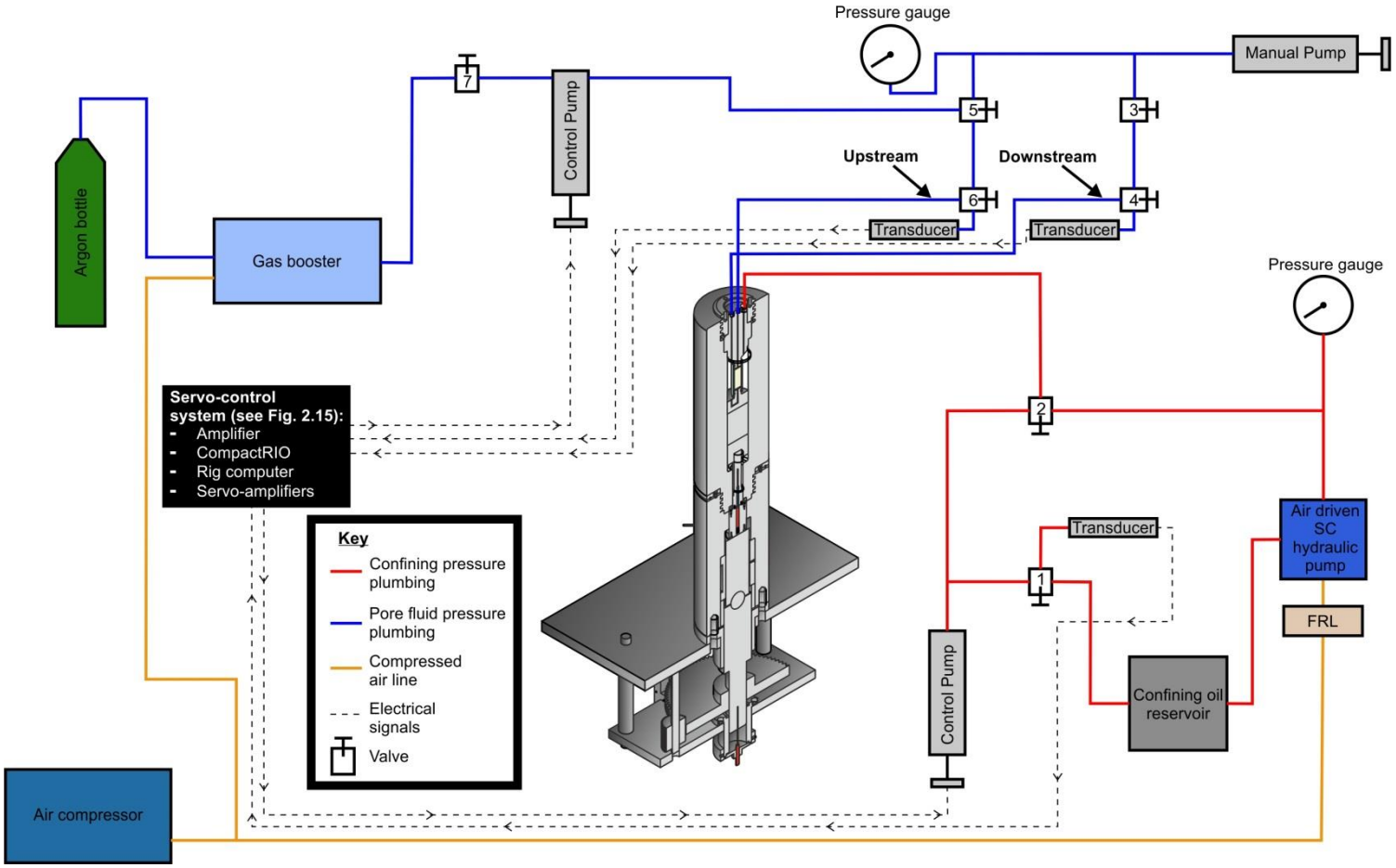


***Figure 2.3*** *- Schematic diagram of the plumbing of the triaxial deformation apparatus.*

### *2.3.2. Pressure vessel and sample assembly*

The cylindrical pressure vessel is made from hot work tool steel, Jessop Saville H.50 (AISI H.13), with an outer diameter of 180 mm and an internal bore of 60 mm. The maximum working pressure of the vessel is 250 MPa, but it has been tested up to 1.5 times the working pressure (375 MPa) according to the High Pressure Safety Code (High Pressure Technology Association, 1975). The pressure vessel sits at the top of the apparatus, above the axial loading column, and the sample assembly is inserted via a top opening (Fig. 2.4). The sample assembly is secured by a threaded top nut (Fig. 2.4c) and is sealed by an o-ring at the top of the sample assembly (Fig. 2.5). This o-ring is supported by a PEEK backup ring to prevent it extruding between the sample assembly and the vessel. The sample assembly is comprised of an upper and lower part with the sample sitting in between (Fig. 2.5). It is designed to accommodate samples of up to 60mm length and 20mm diameter. However samples in this study were typically 50mm in length, consistent with a sample length/diameter ratio of 2.5:1 recommended for tests in uniaxial compression (Paterson and Wong, 2005).

Prior to insertion into the assembly, a sample is placed into a jacket to keep it separate from the confining medium (Fig. 2.6). Jackets are typically made from PVC tubing (19 mm internal diameter), although Viton or copper jackets can be used for tests at elevated temperatures. The jacket seals on the o-rings of the upper and lower parts of the sample assembly when the confining pressure is applied. Pore fluid is introduced to the sample assembly via two thin bore (1.6 mm outer diameter, 0.5 mm internal diameter) high pressure pipes. One pipe is inserted into the centre of the upper sample assembly and supplies fluid to the top of the sample (upstream end). The other pipe passes though the upper sample assembly wraps around the outside of the jacketed sample and is inserted in to the lower sample assembly (Fig. 2.5) to provide fluid to the bottom of the sample (downstream end). Both pipes are secured and sealed by high pressure glands. SIKA-R 1 AX porous 316 stainless steel spacers (Fig. 2.6), with a permeability of $1.3 \times 10^{-13}$ $m^2$, are inserted between the sample and the sample assembly to ensure there is an even distribution of pore fluid across the faces of the sample.

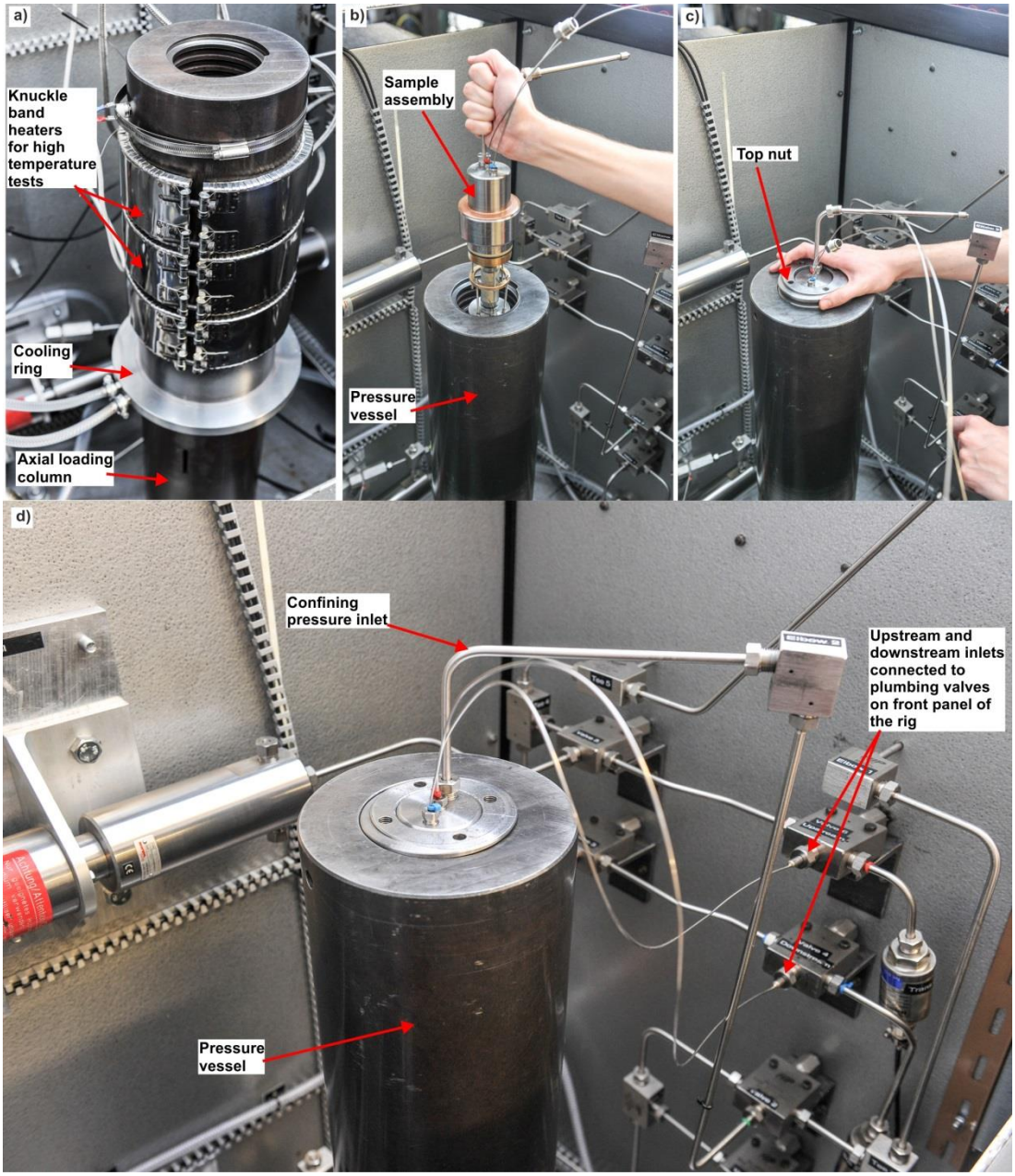


***Figure 2.4 - a)*** *The pressure vessel with external knuckle band furnaces for high-temperature experiments. A cooling ring can be placed between the vessel and the axial loading column to produce a thermal break.* ***b)*** *The sample assembly is inserted via the top opening.* ***c)*** *Sample assembly is secured by the top nut.* ***d)*** *The inlets on the sample assembly for confining and pore pressure are connected to the plumbing of the rig (valves 4 and 6 on Fig. 2.3).*

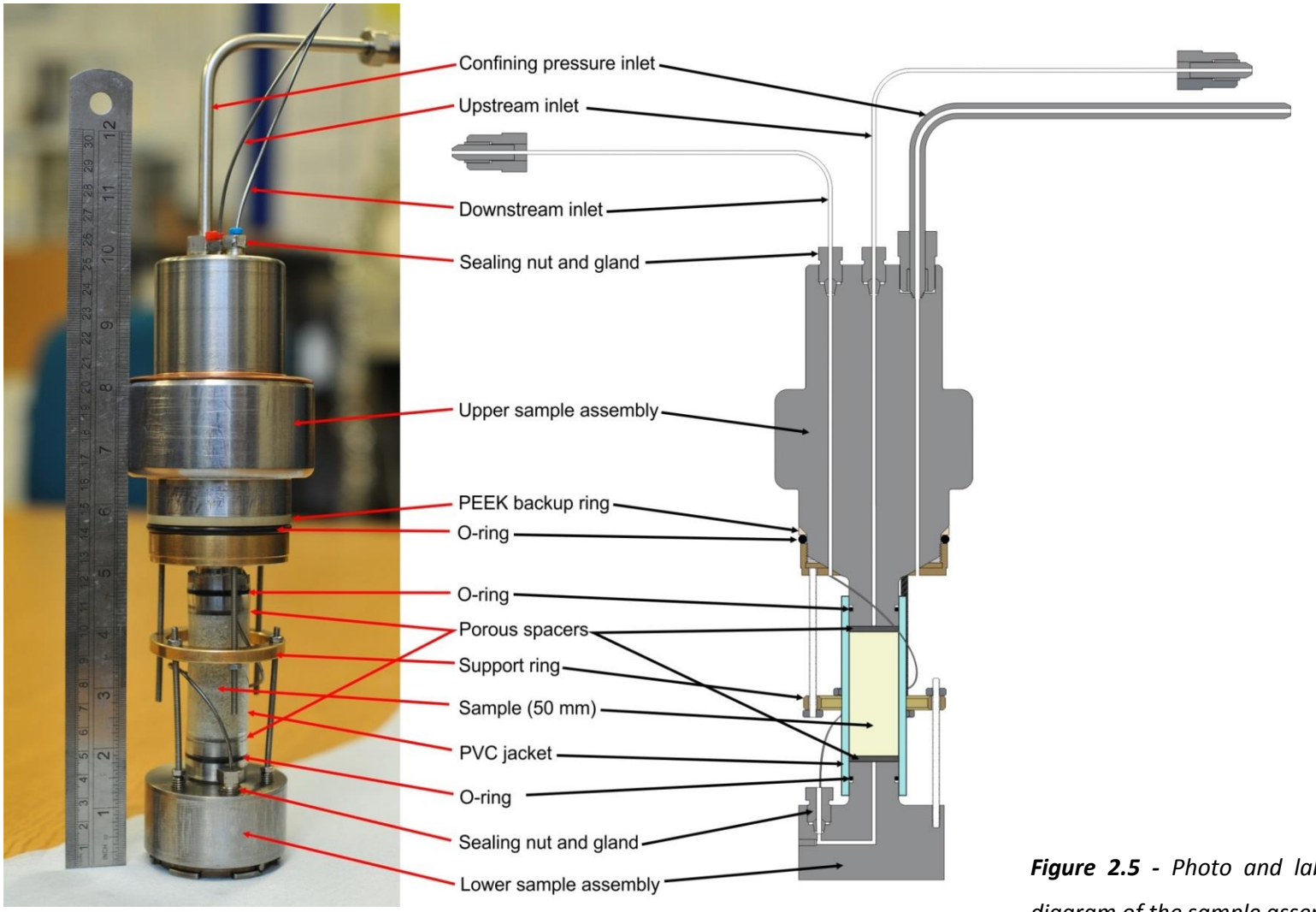


***Figure 2.5*** *- Photo and labelled diagram of the sample assembly.*

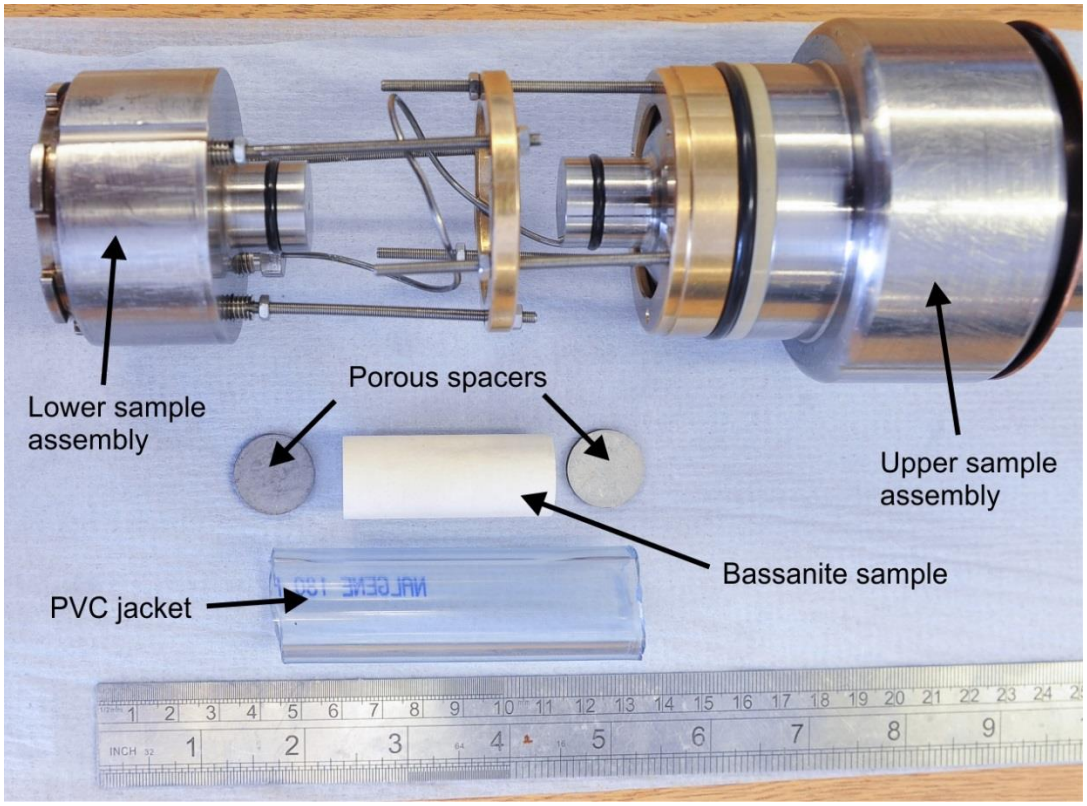


***Figure 2.6 -*** *Sample assembly arrangement with a bassanite sample, PVC jacket and porous disks.*

### *2.3.3. Confining pressure system*

The confining medium used is low viscosity 10 cSt (~0.01 Pa·s) silicone oil which enters the vessel via a pipe at the top of the sample assembly (Fig. 2.5). This is preferred to water to prevent corrosion and prolong the life of the pressure vessel. Pressure is increased by an air-driven SC hydraulic pump which can be isolated from the vessel once the desired pressure is reached (Fig. 2.7). Confining pressure is measured throughout an experiment by a manual gauge and a RDP TJE-type transducer which in our system has a resolution of 0.007 MPa (Fig. 2.8). Pressure can be controlled during an experiment by a Nova Swiss 10cc pump which is connected to the confining pressure system (Fig. 2.9). The pump has been adapted so that it is driven by a servo-controlled motor and gearbox. The full stroke of the pump (limited to 6500 $mm^3$ of oil) will typically change the pressure in the vessel by 20-30 MPa. This is dependent on the starting pressure and also the amount of volume in the vessel taken

up by the sample and the axial piston; if there is a small volume of vessel space occupied by oil then the pump can more efficiently change the pressure. The servo-controlled pump can hold the pressure at a constant value by responding to any change picked up by the transducer and adjusting accordingly. Its primary use is to compensate for pressure changes caused by the movement of the axial piston inside the pressure vessel. The pump can also be used as a volumometer (resolution = 0.1 $mm^3$) to track changes in volumetric strain of the sample as a result of compaction or dilation. The position of the servo-controlled pump is monitored by a linear variable differential transformer (LVDT) attached directly to the piston (Fig. 2.9).

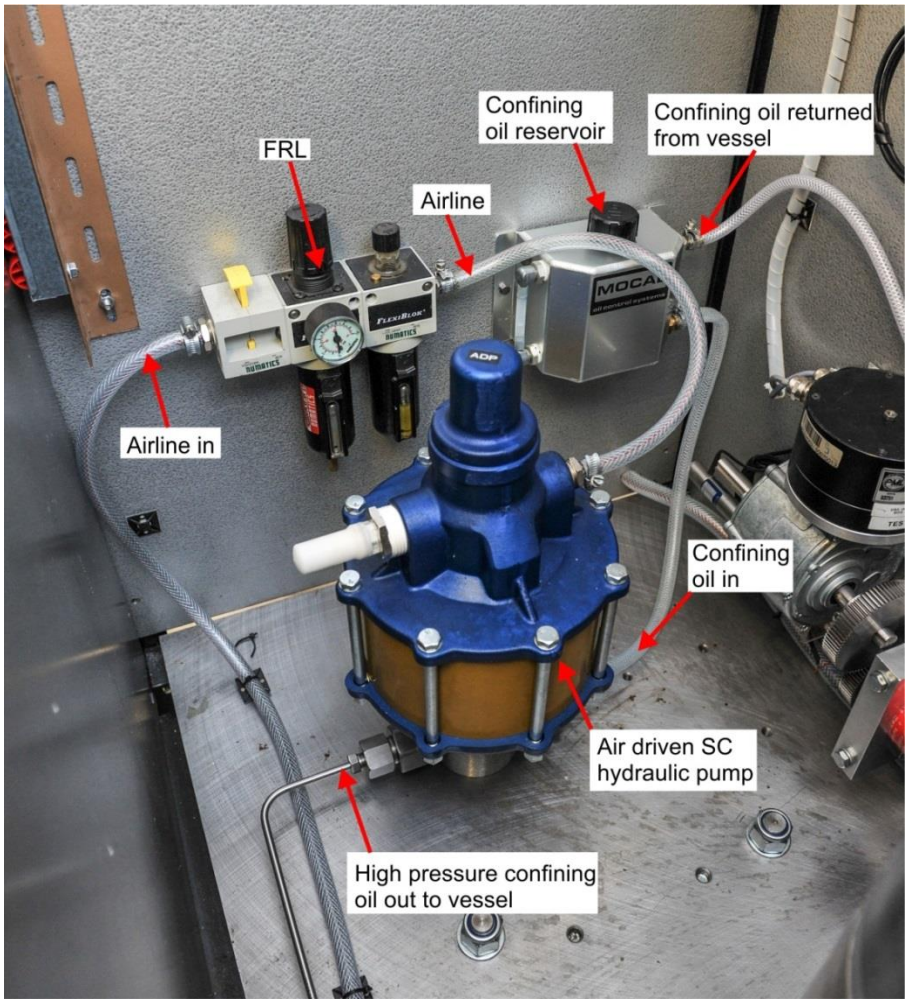


***Figure 2.7*** *- Air-driven SC pump used to increase the confining pressure in the vessel. The air flow into the pump is controlled by a valve on the front of the rig. Air passes through a Filter Regulator Lubricator (FRL) to remove compressor dirt and lubricants from the air stream. Confining oil is stored in a reservoir from where it is transferred to the pump to be pressurized and sent to the vessel.*

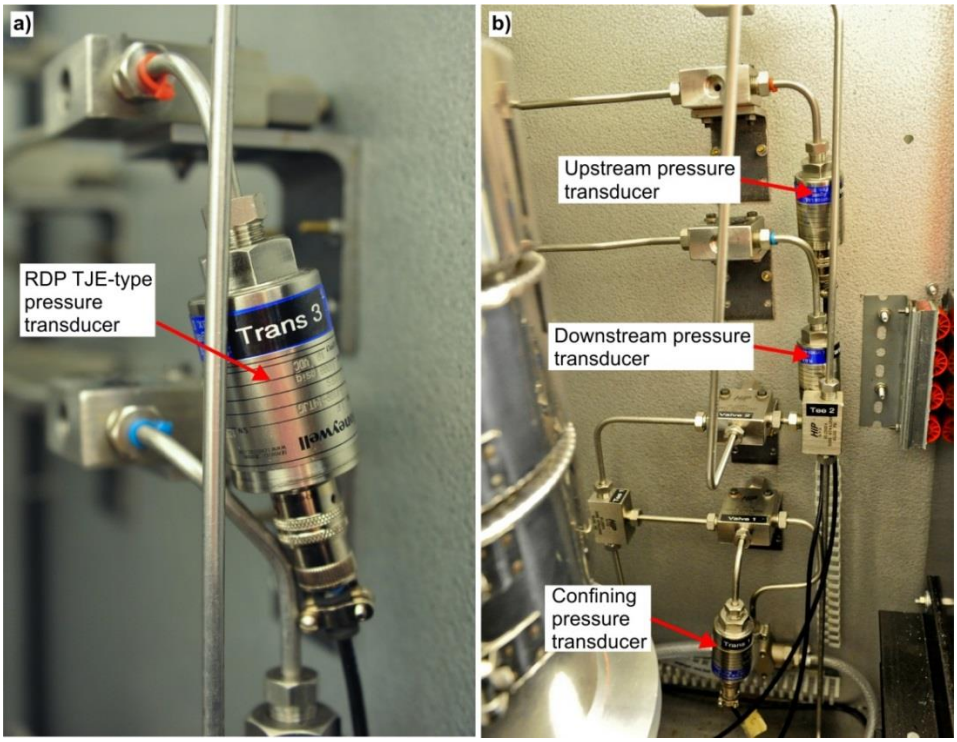


***Figure 2.8*** *– **a)** An RDP TJE-type transducer used to measure the pressure during an experiment. **b)** Pressure transducers are connected to the upstream, downstream and confining pressure systems.*

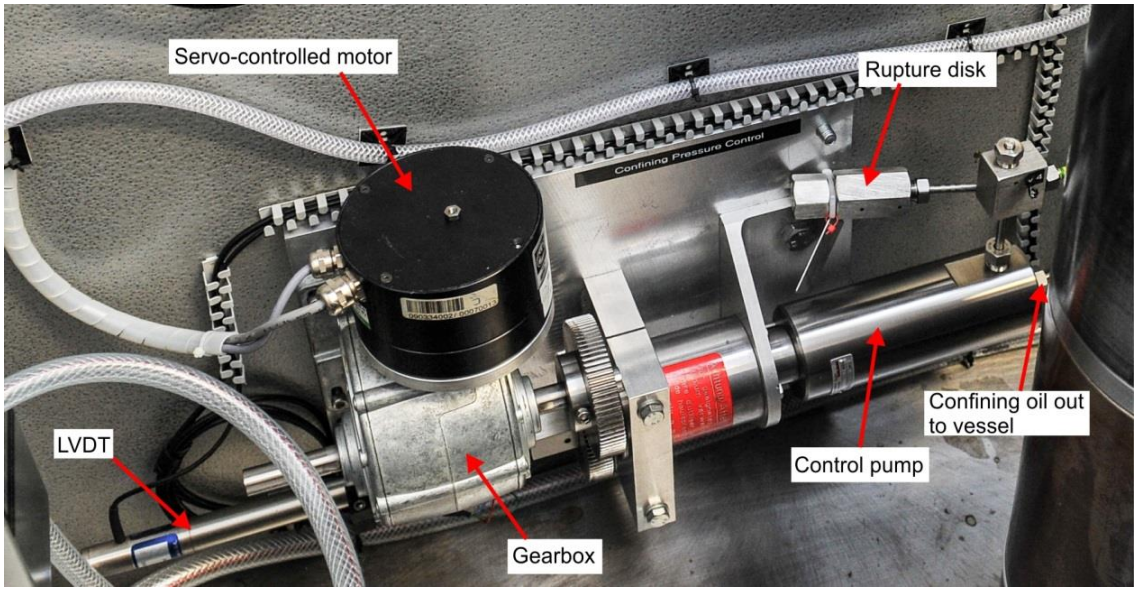


***Figure 2.9*** *– The confining pressure control pump connected to a servomotor and gearbox. The displacement of the pump piston is monitored by an LVDT.*

### *2.3.4. Pore fluid system*

A variety of different pore fluids can be used in the rig. The majority of experiments in this thesis use argon as a pore fluid to prevent hydration of dehydrated gypsum samples. To increase the pressure of argon a Haskel AGT-32/152H gas booster is used (Fig. 2.10). This can also pressurize other gaseous phases that might be used as a pore fluid such as $CO_2$. If the pore fluid is liquid at room pressure and temperature (e.g. $H_2O$) then the gas booster can be disconnected or isolated from the rig and a Nova Swiss hand pump is used to increase the pressure (Fig. 2.14a). The hand pump can also be used to change the pressure of gaseous pore fluids but due to their high compressibility the gas booster is required initially to pressurise the system. The maximum pressure that can be achieved by the gas booster is 120 MPa. Both the Nova Swiss hand pump and the gas booster can be isolated from the system once the desired pressure is reached. Pore fluid pressure is measured by a manual gauge and two RDP transducers (resolution = 0.007 MPa) with one connected to the upstream reservoir and the other to the downstream reservoir (Fig. 2.8).

A servo-controlled Nova Swiss 5cc pump is connected to the upstream reservoir (Fig. 2.11) and can control the pore fluid pressure during an experiment. An LVDT measures the displacement of the piston inside the pump (Fig 2.11). When holding the pressure constant the pump will respond to any changes in pore volume as a sample deforms. Therefore by monitoring the position of the piston the relative pore volume evolution of a sample can be tracked during an experiment (resolution 0.1 $mm^3$). The upstream and downstream reservoirs can be isolated from each other so that they are only connected through the sample itself (Fig. 2.3). This allows for permeability measurements to be performed. The transient pulse decay method (Brace et al., 1968) can be performed by instantaneously increasing the pressure of one reservoir producing a pressure difference across the sample. This is done by building up the pressure behind a valve before opening and closing the valve to release the pressure pulse into the reservoir. The pressure difference then decays at a rate proportional to the permeability of the sample. The pore pressure oscillation technique (Kranz et al., 1990; Fischer, 1992) can also be used by producing a sinusoidal pressure wave with the servo–controlled pump in the upstream reservoir. Permeability is calculated from the amplitude ratio and phase shift between the upstream generated wave and the attenuated downstream signal.

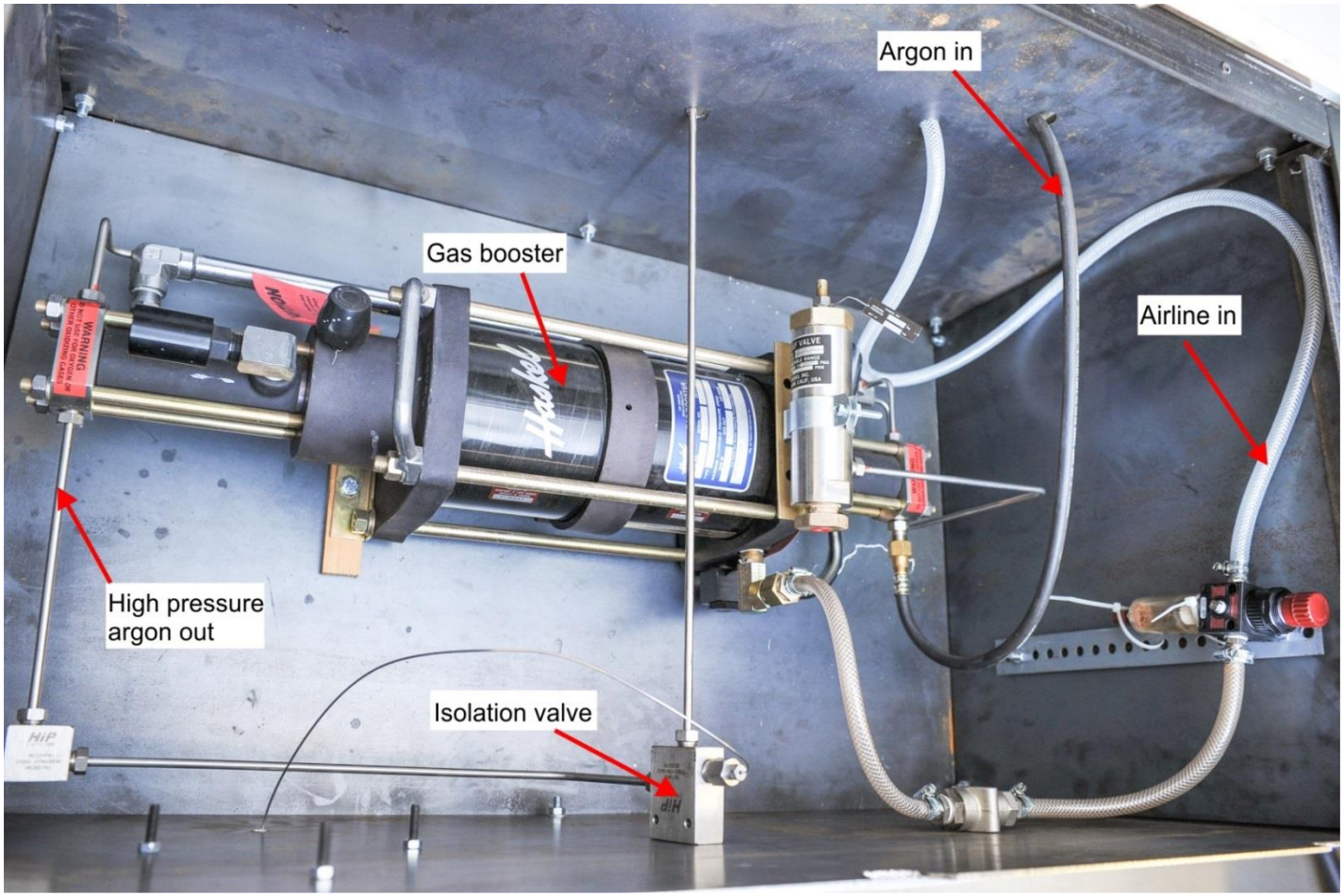


***Figure 2.10*** *– Gas booster used to pressurise gaseous pore fluids (e.g. argon).*

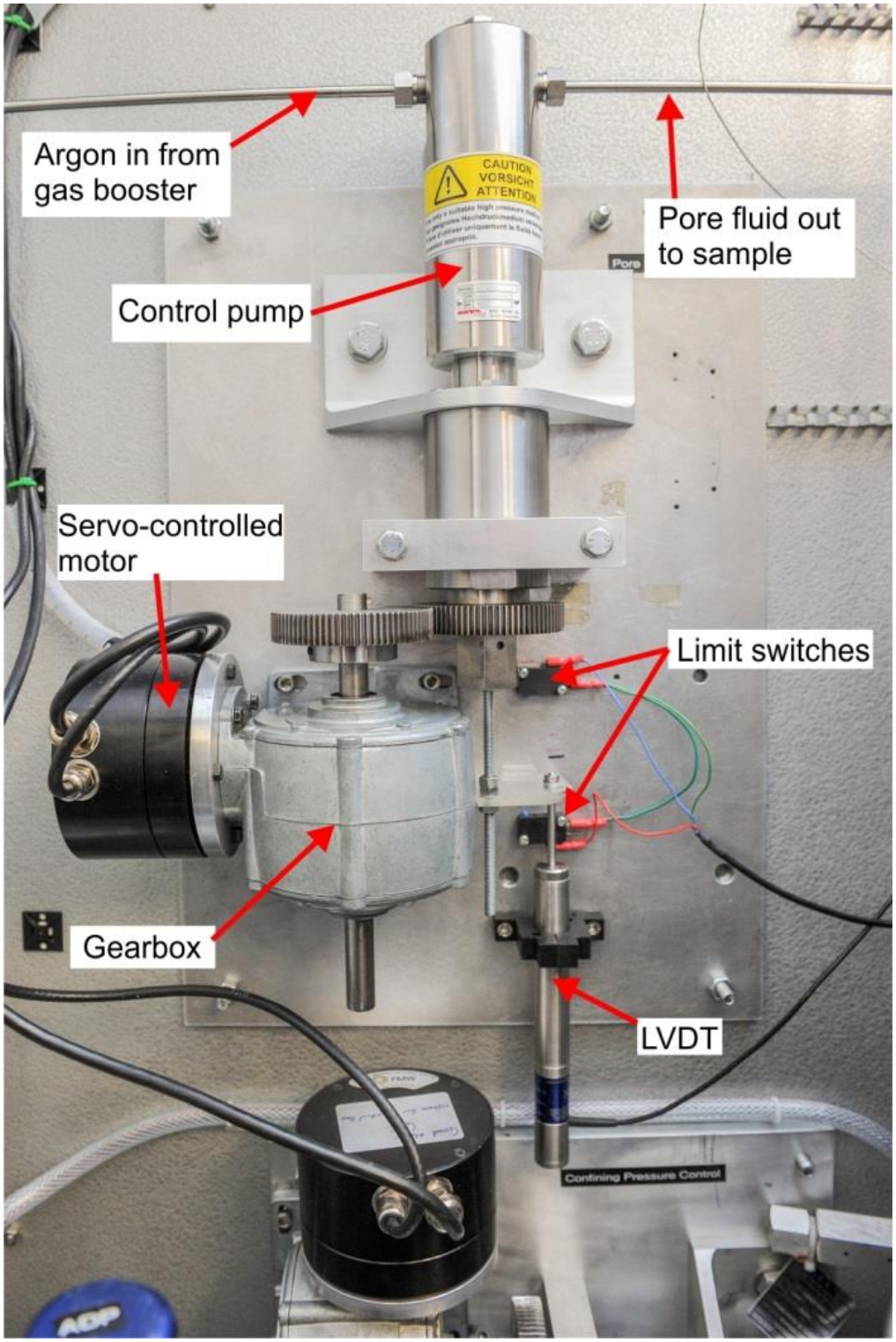


***Figure 2.11*** *– The pore pressure control pump which is connected to a servomotor and gearbox. The argon line from the gas booster enters the rig via the control pump, although this can be disconnected for experiments involving $H_2O$. The displacement of the pumps piston is monitored by an LVDT and limit switches are used to ensure the motor does not drive the pump beyond its full stroke.*

### *2.3.5. Axial loading system and force gauge block*

The axial load is applied by an electromechanical servo-controlled axial piston. The system consists of a force gauge column that protrudes into the base of the pressure vessel and is driven from below by a ball screw actuator. The vessel screws into the force gauge block which is in turn connected to the base plate of the rig by 8 M16 high-tensile (8.8) bolts (Fig. 2.2 and Fig 2.13). A cooling plate can be placed between the vessel and force gauge column so that a thermal break can be created for experiments at elevated temperature (Fig. 2.4a). This minimises the effects of temperature on the force value being measured by the force gauge. The force gauge column seals into the base of the vessel via a dynamic Variseal which is supported by two PEEK backup rings (Fig. 2.12). This prevents confining oil from leaking out the bottom of the vessel. The column comes into contact with base of the sample assembly via the force gauge extension (Fig 2.2). The load applied to the sample is measured by the elastic distortion of the force gauge column. An LVDT is located internally within the column and is supported by a T-section insert (Fig. 2.12). The insert is pushed against an internal shoulder of the column above the level of the dynamic seal. This ensures that any distortion measured by the LVDT is only that above the internal shoulder of the column. Hence, the actively deforming length of the force gauge is above the pressure seal and no correction for seal friction is required. The force gauge column is made from M300 maraging steel which has a yield strength of approximately 2 GPa. The maximum load that ball screw can be subjected to is 500 kN. This is comprised of 300 kN under the maximum differential load as well as 200 kN acting on the ball screw at the highest confining pressure of 250 MPa. A 20 mm diameter sample being subjected to the maximum differential load of 300 kN would therefore experience a maximum differential stress of just less than 1 GPa. This gives a factor of safety of 2 on the force gauge when a sample is under maximum load. The resolution of the force gauge is < 0.03 kN.

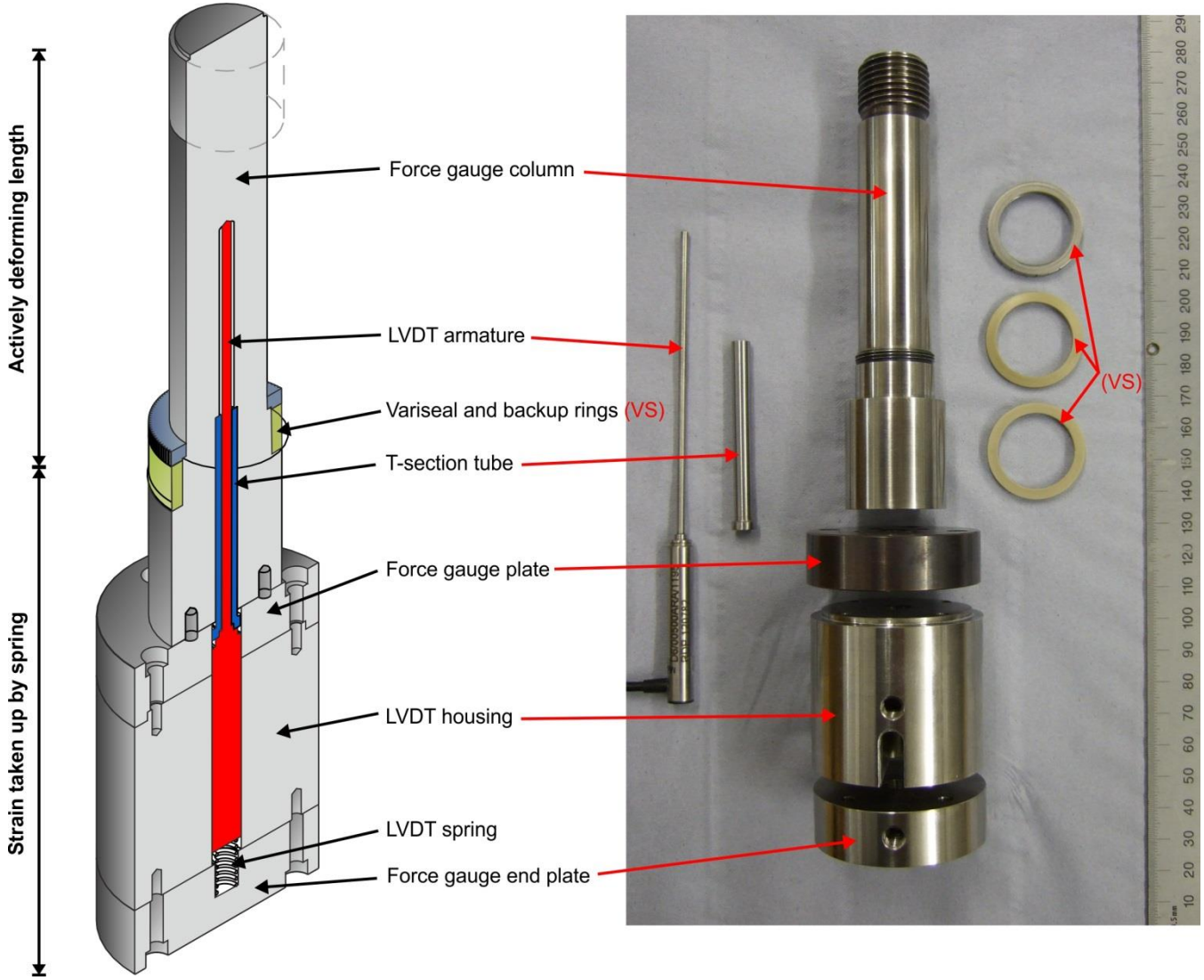


***Figure 2.12*** *– Photo and labelled diagram of the force gauge. VS = dynamic Variseal.*

The force gauge column sits on a high torque anti-rotation THK ballspline which moves along a vertical ball bearing raceway with minimal friction. The base of the spline has a hemispherical seat so that it can couple to the ball screw (Fig 2.2). The ball connection ensures that the load applied from the ball screw remains concentric. The ball screw is able to rotate with low friction under high load, with the threads moving along a recirculating helical ball bearing raceway. The screw is driven by a Printed Motor Works GM12 pancake-type servo motor and gear train (Fig. 2.13). The gear train consists of a Parvalux gearbox with a 115:1 ratio connected in series to a Hydro-mec worm gearbox with a 36:1 ratio. This is in turn connected to the pinion of the main drive gear which has a ratio of 5:1 (Fig. 2.13). The total gear ratio from drive motor to ball screw is 20700:1. The motor has a maximum speed of 3000 rpm which will in turn rotate the drive gear at 0.14 rpm. The lead of the ball screw is 10 mm which gives a maximum displacement rate of 23 $\mu ms^{-1}$. The GM12 motor is capable of supplying a torque of 1.31 Nm which is increased by the gear train to 27117 Nm. The torque required to rotate the ball screw under the maximum load of 500 kN can be calculated by:

$$Torque = \frac{Axial\ Force\ \times\ Lead\ (in\ meters)}{2\pi n}$$

where n is an efficiency factor (typically 0.9, according to http://www.nookindustries.com/LinearLibraryItem/Ballscrew_Torque_Calculations). This equation gives a torque of 885 Nm required to move the ball screw under full load, which is well below the nominal maximum torque of 27117 Nm provided by the gear train.

Axial displacement is measured by an LVDT at the base of the ball screw (Fig. 2.13). To calculate the true sample displacement a correction must be applied to account for the elastic distortion of the loading column. This can be done by using the stiffness of the loading column, which is 180 kN/mm. The correction is slightly non-linear at very low loads (<1 kN), which is likely the result of closure of the various different interfaces along the loading column. A correction is also required to account for the effect of increasing confining pressure on the force value recorded by the force gauge. This is calibrated by measuring how the force changes with increasing confining pressure under zero axial load (see appendix). This linear calibration can then be subtracted from the force value when working at different confining pressures.

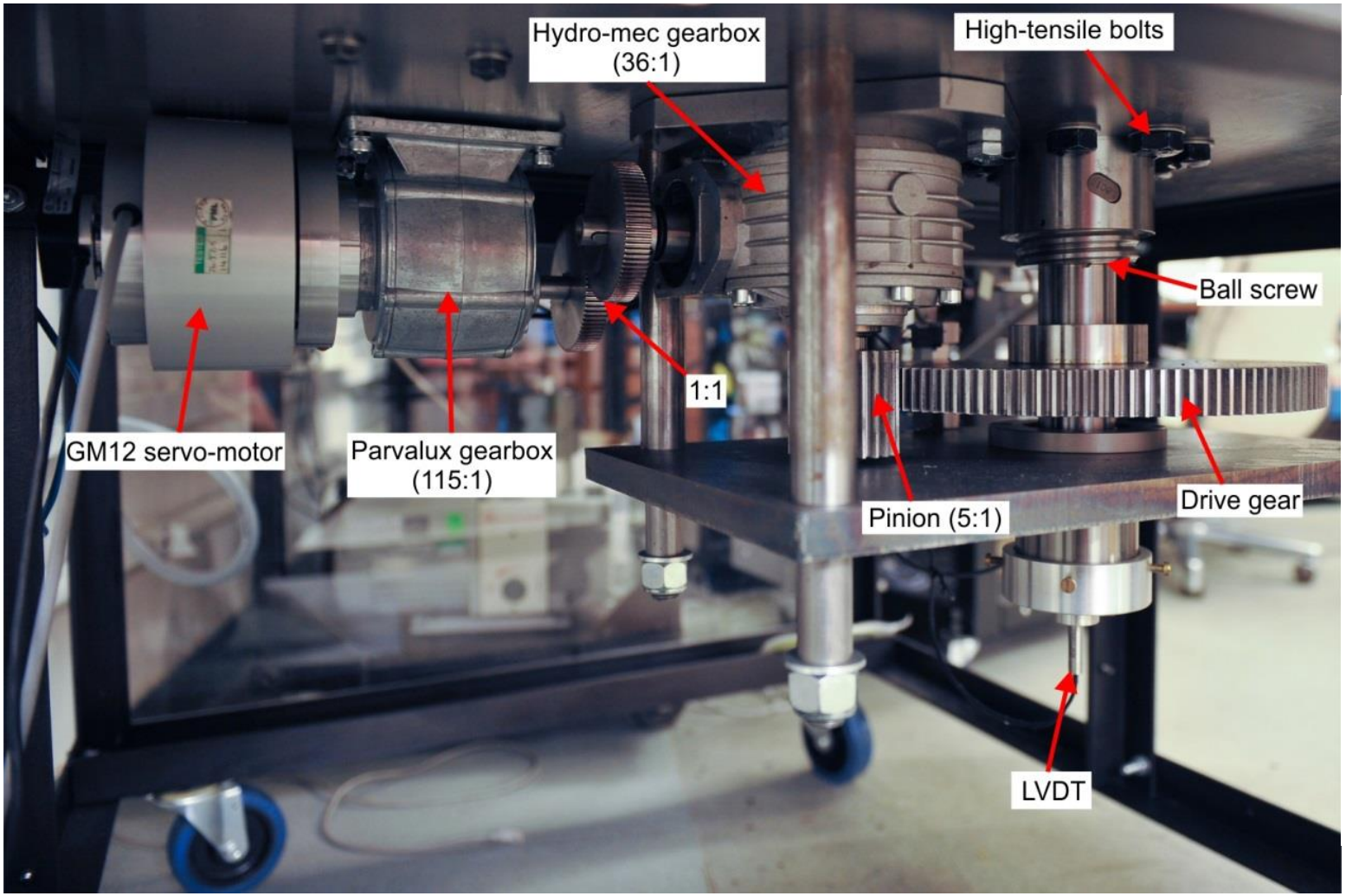


***Figure 2.13*** *– The axial loading system that is attached to the underside of the base plate of the rig. The GM12 drive motor is connected to the gear train which rotates the ball screw. The displacement of the axial loading column is monitored by an LVDT at the base. High-tensile bolts connect the axial loading column above to the base plate of the rig.*

### *2.3.6. Data logging and servo-control system*

Data from the pressure and displacement transducers are logged by a National Instruments CompactRIO (NI 9024) and also by the LabVIEW software on the PC. Before the data is logged, the millivolt signals from the transducers pass through an amplifier to increase them to the ±10V range of the NI-cRIO (Fig. 2.14b). The amplified signals are then sent to the 4-channel, 16-Bit analogue input modules (NI 9215) that are inserted into the chassis of the NI-cRIO (Fig. 2.14c). The working set points (WSPs) of the pore fluid pressure, confining pressure and axial load systems are inputted into the LabVIEW program on the PC. These WSPs are then sent from the PC to the NI-cRIO where a servo loop compares them to the signals being received by the input module (Fig. 2.15). If the input signal does not match the WSP a signal is sent from the NI-cRIO 4-channel, 16-bit analogue voltage output module (NI 9263) to the rig's control boxes which drive the actuators (e.g. pumps or ballscrew) for the pore fluid pressure, confining pressure and axial load systems. The magnitude of this signal is controlled by the PID parameters (Proportional gain, Integral gain, and Derivative gain). The signal that is received by the control boxes is then amplified by a servo amplifier (Fig. 2.14d) to achieve the higher voltage and current required to drive the actuators. The workings of the servo-control system are summarized in figure 2.15.

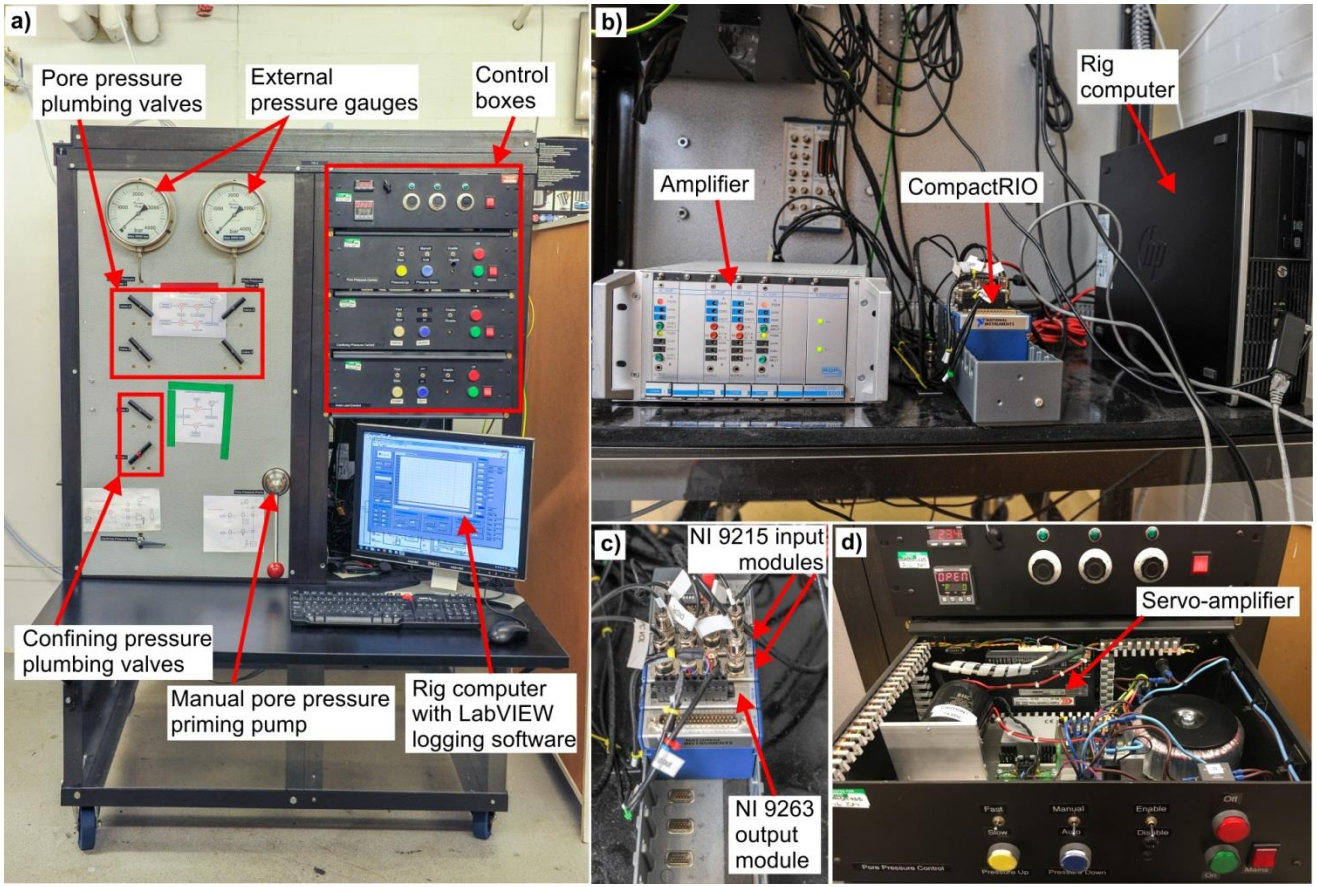


***Figure 2.14 – a)*** *The front of the rig with servo-control boxes, external pressure gauges and manual valves for the confining and pore pressure systems.* ***b)*** *The amplifier, NI-compactRIO and rig computer.* ***c)*** *The NI 9125 input modules and NI 9263 output module are inserted into the chassis of the NI-cRIO.* ***d)*** *Inside the control boxes is a servo-amplifier which sends a high voltage, high current signal to the actuators.*

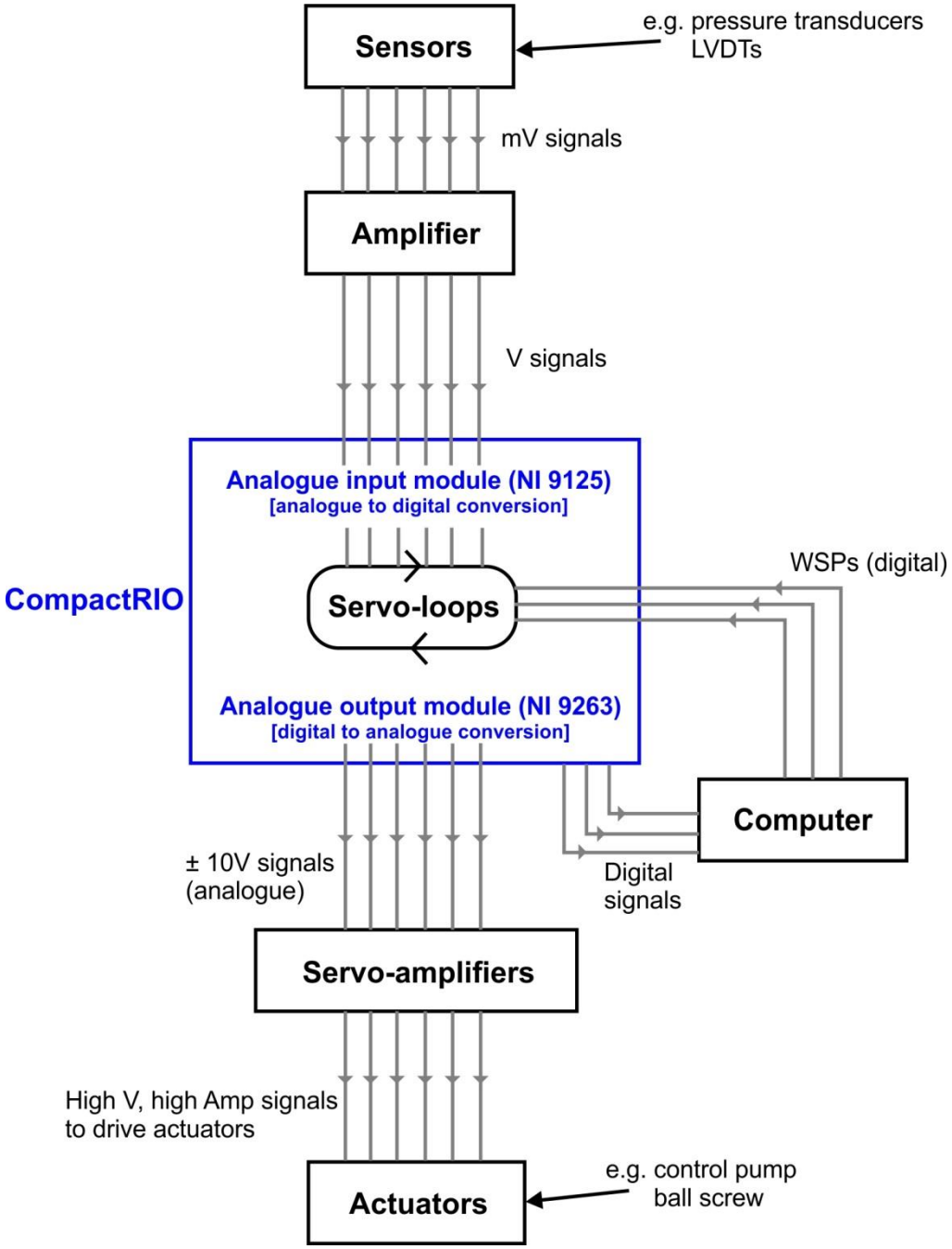


***Figure 2.15*** *– A schematic diagram of the servo-control system.*

### *2.3.7. Potential sources of error and calibration*

The voltages read by the pressure transducers and the distortion of the force gauge measured by the internal LVDT requires calibration against an external pressure gauge and load cell respectively. The displacement of the control pumps on the

confining and pore pressure systems is measured by LVDTs and also requires calibration (see appendix for calibrations). Unavoidable calibration errors will therefore be introduced into any measurement, however their significance can be minimised by careful procedure and repeat calibration. Electrical noise can also produce an error on the output signals but this is typically low in magnitude (< 0.01 MPa on pressure readings) so its effects are minor.

Another source of error is produced by daily temperature fluctuations in the lab which can cause drift on the pressure and force signals as a result of thermal expansion/contraction. This is particularly significant for measurements that are being made over several hours or days. The experiments that are performed in chapters 4 and 5 of this thesis require that a sample is left in the rig over consecutive days making them susceptible to diurnal temperature fluctuations. However the stress probing methodology that is developed in these chapters involves several loading increments that are typically on the order of tens of minutes. The temperature fluctuation over each individual loading increment will therefore be small. To account for long term drift, the force value that is read at the hit-point of each loading increment (where the loading piston comes into contact with the base of the sample assembly) is zeroed in the post-processing of the data.

As mentioned previously, the force is measured by the elastic distortion of the force gauge; this should therefore produce a linear loading versus displacement curve. However there are several interfaces along the loading column (e.g. between the force gauge extension and the vessel spacer, between the spacer and the bottom of the sample assembly, between the sample assembly platen and the sample). This can produce loading curves that are not perfectly linear, especially during the initial loading of the sample when the interfaces are pushed together. This small effect is seen on the apparatus. It is therefore important, when analysing a sample loading curve, to consider what is real sample deformation against what is a machine artefact.

Finally, errors can be produced during sample preparation. Samples that were prepared for testing in this thesis were cored to a diameter of 20 mm and the ends were precision ground to a tolerance of < 0.01 mm. Any inaccuracy in the preparation or measurement of the core plugs can lead to heterogeneous stress distribution across the sample and hence affect the response of the material during deformation. These errors are best reduced by careful procedure during sample preparation.

# 3. A 4D view on the evolution of metamorphic dehydration reactions


## Abstract

Metamorphic reactions influence the evolution of the Earth's crust in a range of tectonic settings. For example hydrous mineral dehydration in a subducting slab can produce fluid overpressures which may trigger seismicity. During reaction the mechanisms of chemical transport, including water expulsion, will dictate the rate of transformation and hence the evolution of physical properties such as fluid pressure. Despite the importance of such processes, direct observation of mineral changes due to chemical transport during metamorphism has been previously impossible both in nature and in experiment. Using time-resolved (4D) synchrotron X-ray microtomography we have imaged a complete metamorphic reaction and show how chemical transport evolves during reaction. We analyse the dehydration of gypsum to form bassanite and H2O which, like most dehydration reactions, produces a solid volume reduction leading to the formation of pore space. This porosity surrounds new bassanite grains producing fluid-filled moats, across which transport of dissolved ions to the growing grains occurs via diffusion. As moats grow in width, diffusion and hence reaction rate slow down. Our results demonstrate how, with new insights into the chemical transport mechanisms, we can move towards a more fundamental understanding of the hydraulic and chemical evolution of natural dehydrating systems.


## 3.1. Introduction

The study of metamorphism is underpinned by thermodynamics; that a system will tend towards a state of minimum energy and reach equilibrium with its environment (Wood and Fraser, 1976; Powell and Holland, 2010). However there is widespread evidence of disequilibrium textures on the sub-millimeter scale in crustal rocks including mineral zoning, coexisting polymorphs and reaction rims (Carmichael, 1969; Yund, 1997; Carlson, 2002). This shows that kinetic impediments often prevent

thermodynamic equilibrium from being reached completely. Knowledge of kinetic processes, such as chemical transport and attachment/detachment of atoms at mineral interfaces, is vital to understand the controls on reaction rate and is also important for characterizing mid-crustal fluid flow as transformations often involve the release of fluids (e.g. dehydration reactions). Dehydration reactions are abundant in the crust during prograde metamorphism, particularly in subduction zone settings where they are thought to play an important role in generating intermediate-depth seismicity (Dobson et al., 2002; Hacker et al., 2003; Jung et al., 2004; Leclère et al., 2016; Okazaki and Hirth, 2016; Incel et al., 2017) and also in returning stored water from the oceanic lithosphere back to the surface (Peacock, 1990; Plümper et al., 2016). If fluids are unable to drain, the resulting high fluid pressures have been previously shown to slow the reaction rate (Llana-Funez et al., 2012), thus the pressure evolution is coupled to the reaction kinetics. The kinetic controls on reaction are dependent upon the pathways (Lasaga, 1997) that chemical components take from detachment at the reactant phase to incorporation into the lattice of the product mineral(s). It is impossible to observe directly these pathways in action in rocks or in traditional experimental setups; therefore our understanding of reaction pathways is limited to disequilibrium textures preserved after reaction (Wheeler, 1991).

The use of 4D synchrotron X-ray microtomography provides new opportunities in the experimental investigation of metamorphism by allowing direct microstructural and mineralogical information to be gathered on the micron scale as a reaction proceeds. We conducted a confined heating experiment to investigate the dehydration of gypsum ($CaSO_4 \bullet 2H_2O$) to form bassanite ($CaSO_4 \bullet 0.5H_2O$) and $H_2O$. The reaction was documented in a 3-dimensional X-ray microtomographic time series dataset (ie. 4D data) using an X-ray transparent hydrothermal cell (Fusseis et al., 2014) that was installed in the microtomography beamline 2BM at the Advanced Photon Source (USA). Gypsum dehydration has proven to be analogous to reactions involving silicate minerals (Olgaard et al., 1995) but is much more suitable for synchrotron study since it completes in hours rather than years and begins at 100 °C, which is much lower than most silicate dehydration reactions (McConnell et al., 1987). The univariant gypsum to bassanite transition is also relatively simple when compared to many silicate dehydration reactions which often involve solid solution series. The fine-grained starting material from Volterra, Italy, has been widely used in studies of dehydration as it is relatively homogeneous with initially low porosities of <1% (Olgaard et al., 1995;

Milsch and Scholz, 2005; Brantut et al., 2012; Fusseis et al., 2012; Leclère et al., 2016). Like most dehydration reactions, the breakdown of gypsum involves a reduction in the solid molar volume, which leads to the formation of porosity (29% when fully dehydrated). However the reaction is associated with a net volume increase as the water produced has a greater volume than the pore space. This means that some water must be expelled, but if that is not possible then the fluid pressure will increase, slowing down the reaction (Llana-Funez et al., 2012). Thus there is a feedback between the mechanisms of reaction and fluid expulsion.

A cylindrical sample (2 mm diameter, 5 mm length) was subject to 9 MPa confining pressure (Pc), 4 MPa pore fluid pressure (Pf) and held at 115 °C for approximately 9 hours. The difference between the two pressures (Pc - Pf = 5 MPa), is small, analogous to the situation in natural dehydrating systems (Wong et al., 1997b). There are no macroscopic differential stresses in this setup; however it is worth noting that anisotropic grain-scale stresses do arise when the confining pressure and fluid pressure are not equal (Wheeler, 1987). Importantly, at the low effective pressure in our experiment there is no pore collapse by compaction and the evolving microstructure is produced by reaction alone. The experiment therefore represents an end member condition; in natural settings compaction may occur if excess fluid is able to drain leading to an increase in effective pressure acting on the reacting rocks. During the experiment, 3-dimensional microtomographic datasets of the entire sample were acquired in 15 minute intervals (see supplementary methods – section 3.3.1). The X-ray microtomographic data have a voxel size of 1.3 μm which is sufficient to image growing grains in detail, and the contrast in absorption allows for segmentation (automatic recognition) of the evolving pore space as it is distinct from the solid phases.

## 3.2. Results and Discussion

Figure 3.1 shows a selection of time sequence micrographs highlighting the evolution of the gypsum and the growing bassanite grains in conjunction with the evolving porosity in the sample (see also Supplementary Movie 3.1 in Appendix IV). The first, relatively isolated, grains of bassanite that we observe appear after approximately 120 minutes, each surrounded by newly formed pore space. Pores initially wrap around bassanite grains forming a fluid-filled, moat-like structure (Fig.

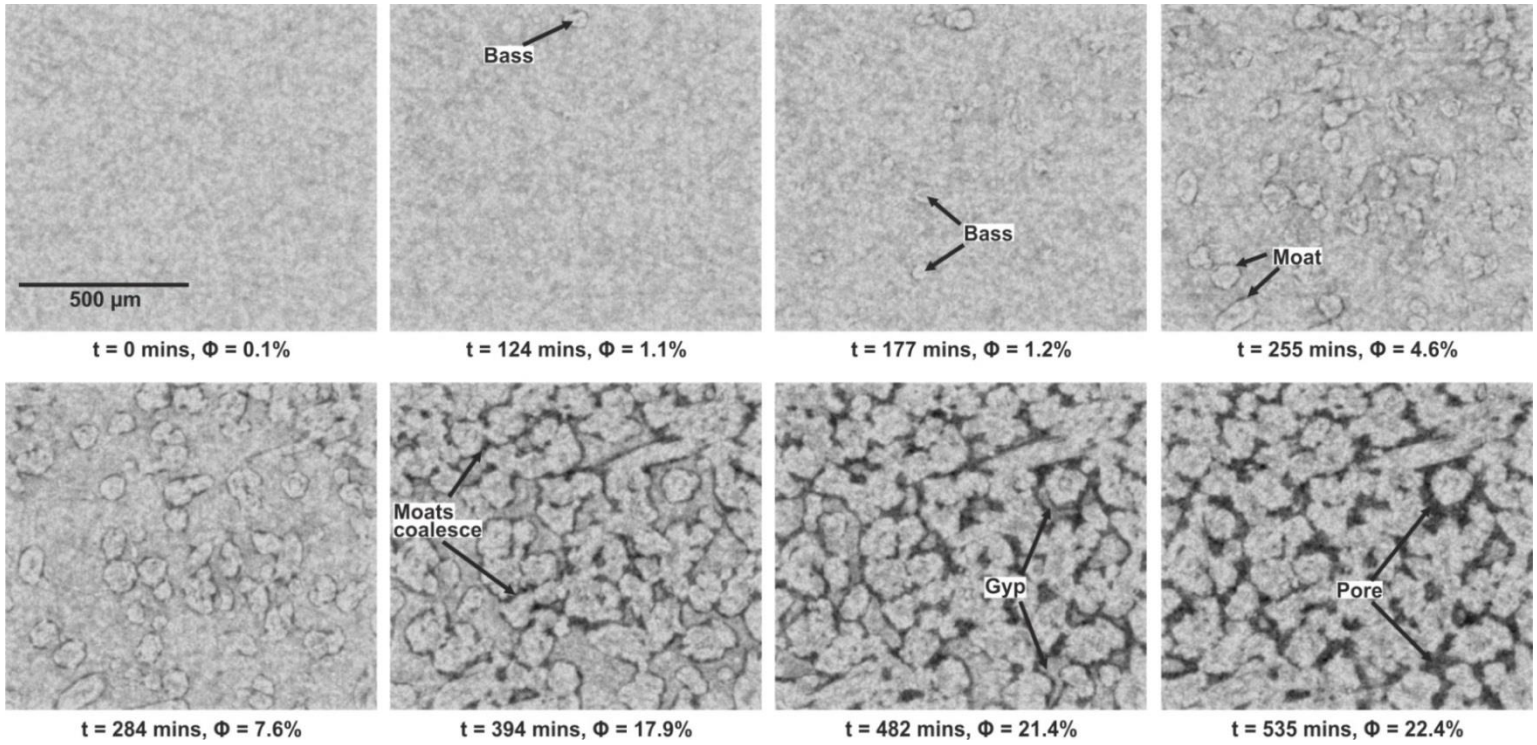


***Figure 3.1*** *- Time-series microtomographic reconstructions of the dehydrating gypsum sample. The first bassanite grains are observed after 124 minutes. The new grains are evenly distributed throughout the sample and grow surrounded by moats of porosity which appear black in the reconstructions. The grains grow larger and the porosity (Φ) increases as the moats get wider. At 394 minutes the grains begin to impinge on each other and the porous moats start to coalesce. By 482 minutes the bassanite grains isolate the remaining pockets of gypsum which is consumed in the reaction and the pores expand into this space.*

3.1). As the reaction continues the grains and pores grow larger until grains begin to impinge on each other and the moats coalesce.

During the experiment the total porosity in the sample increases non-linearly until it begins to settle at just below 25 % after about 450 minutes (see Supplementary Fig. 3.1). Interconnection of individual moats rapidly leads to the formation of a complex pore cluster between 202 and 255 minutes into the experiment. This cluster percolates throughout the entire analyzed subvolume (Fig. 3.2, Supplementary Movie 3.2). Our analysis of the pore size distribution in the sample reveals that, up to 202 minutes, the largest pore cluster accounts for about 20 % of the total porosity. By 255 minutes this value has risen to approximately 81 % (Fig. 3.2, Supplementary Fig. 3.2), showing a dramatic increase in connectivity. The overall porosity in the sample at this time is only 4.6 %, indicating that efficient expulsion of $H_2O$ is achievable after a relatively small amount of reaction. This stage coincides with a consolidation of the pore structure, where small isolated pores are progressively incorporated into a sample-scale drainage architecture (Fig. 3.2, Supplementary Fig. 3.3). A recent study, modelling fluid expulsion during serpentinite dehydration, has shown that early connectivity of the reaction generated porosity is key for initiating fluid channelization in a subducting slab (Plümper et al., 2016), which is thought to be an important mechanism in allowing large-scale fluid expulsion. Our results are in agreement with this finding and therefore have wider implications for the hydraulics of a subduction zone, suggesting that efficient fluid expulsion may be achieved in the initial stages of a dehydration reaction.

In metamorphism, the rate limiting processes are typically considered to be diffusion (Walther and Wood, 1984; Joesten and Fisher, 1988; Yund, 1997), mineral interface reactions (Lasaga and Rye, 1993; Wheeler et al., 2004; Paukert et al., 2012) or combinations of both depending on the length scale (Fisher, 1973). In the case of the gypsum to bassanite transformation, in order for grain growth to occur, bassanite grains require a supply of $Ca^{2+}$ and $SO_4^{2-}$ ions. It is often assumed that the transport of dissolved chemical components during metamorphism occurs through a thin grain-boundary fluid film (Walther and Wood, 1984). However solid volume changes during a transformation produce transient porosity and our datasets show that the transport of ions must occur via diffusion through the wide moats produced by the reaction itself (Fig. 3.3). As the bassanite grains are elongate, we expect the areal growth rate to approximate to the volumetric growth rate. We performed 2D image analysis to

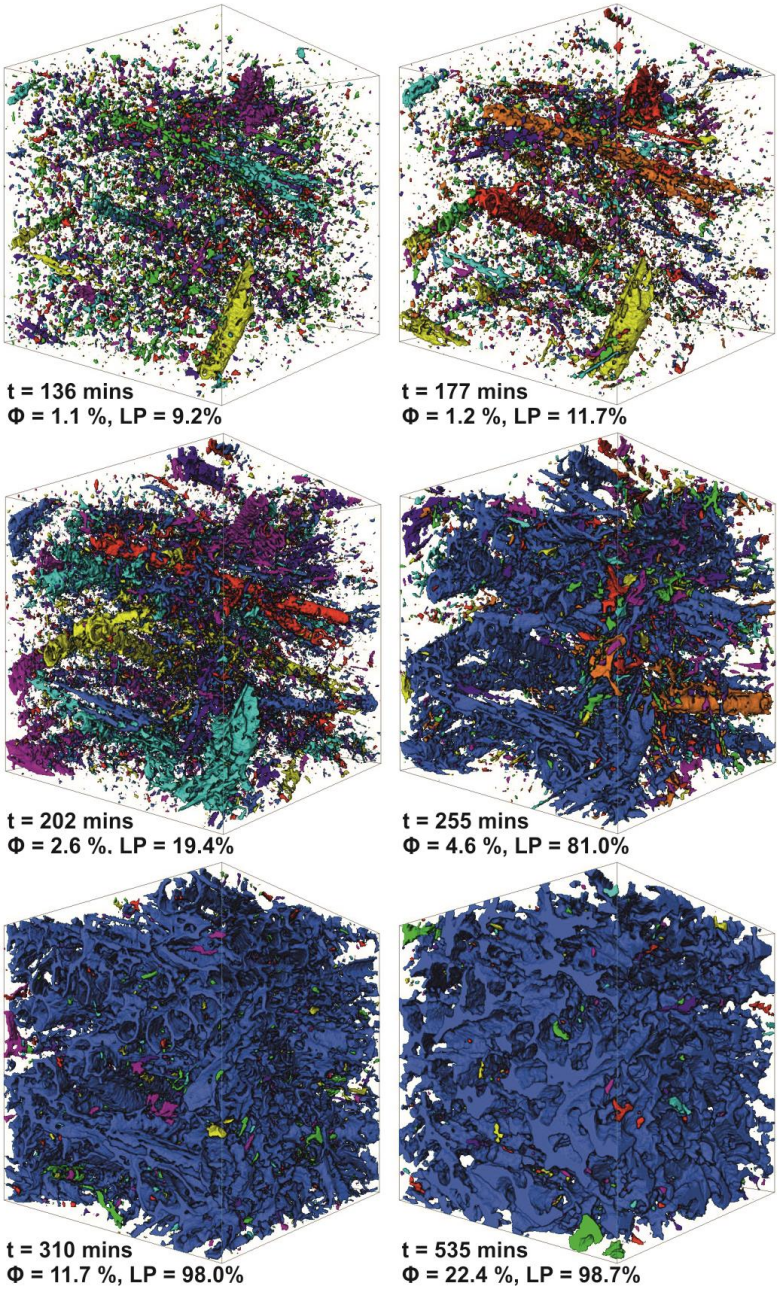


***Figure 3.2*** *- 3-dimensional reconstructions of the pore network with time. Different pore clusters appear in different colours in the reconstructions. The analysed subvolume is a cube with a side length of 975 µm. Until 177 minutes there are thousands of isolated pores, with the largest pore cluster (LP) only comprising 11.7 % of the pore network at this time. By 202 minutes the largest pores are beginning to expand and by 255 minutes most of them are interconnected with the largest pore cluster (which appears blue) comprising 81 % of the total pore network. After 310 minutes this pore cluster dominates the drainage architecture (98%) with only a few isolated small pores remaining.*

measure the areas (A) of the bassanite grains and the grains + moats. Figure 3.4a shows that the ratio of these areas clusters around a central value of approximately 0.71 before the moats coalesce and can no longer be attributed to individual grains. This ratio of 0.71 corresponds exactly to the solid volume change associated with the reaction, indicating that each grain-moat pair is evolving as a closed chemical system with respect to $Ca^{2+}$ and $SO_4^{2-}$, in relative isolation from nearby grains. It also suggests that advection of the dissolved solutes is negligible even though the excess $H_2O$ is able to dissipate away from the site of reaction. The reaction pathway must therefore involve dissolution at the gypsum-moat interface, diffusion across the moat and precipitation at the bassanite-moat interface (Fig. 3.3). Previous experimental work (Llana-Funez et al., 2007) and observations on natural samples (Plümper et al., 2016) have shown similar moat like structures around forsterite grains in partially dehydrated serpentinite, suggesting this reaction pathway may be dominant in many dehydration reactions.

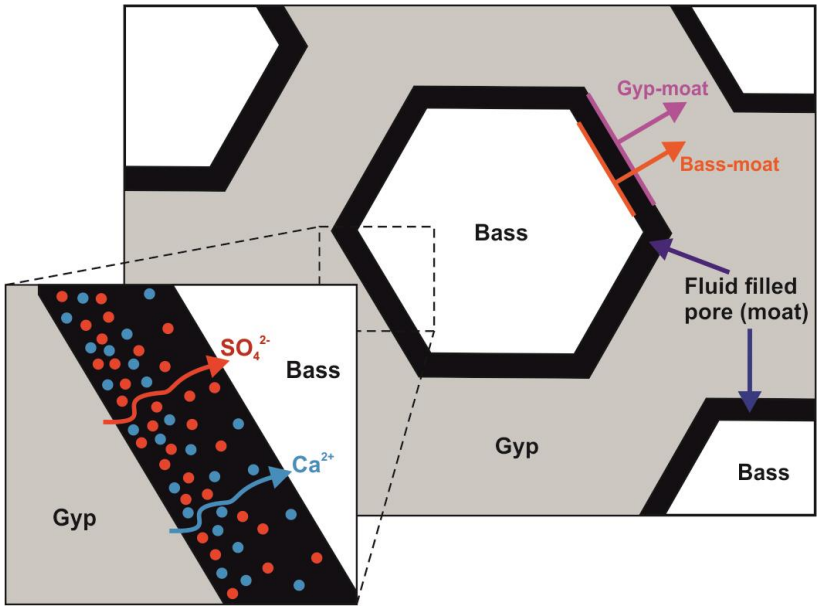


***Figure 3.3*** *- Schematic cartoon of the chemical transport pathways during reaction. For the majority of their growth history bassanite grains grow in relative isolation from nearby grains. Transport of dissolved solutes ($Ca^{2+}$ and $SO_4^{2-}$) occurs via diffusion across the fluid-filled moats surrounding the growing bassanite grains. Also marked are the two interfaces that were measured in the 2D image analysis (Fig. 3.4): the bassanite-moat interface and the gypsum-moat interface. As grains grow both interfaces move away from the grain centre and we are able to track how the area inside these interfaces evolves with time.*

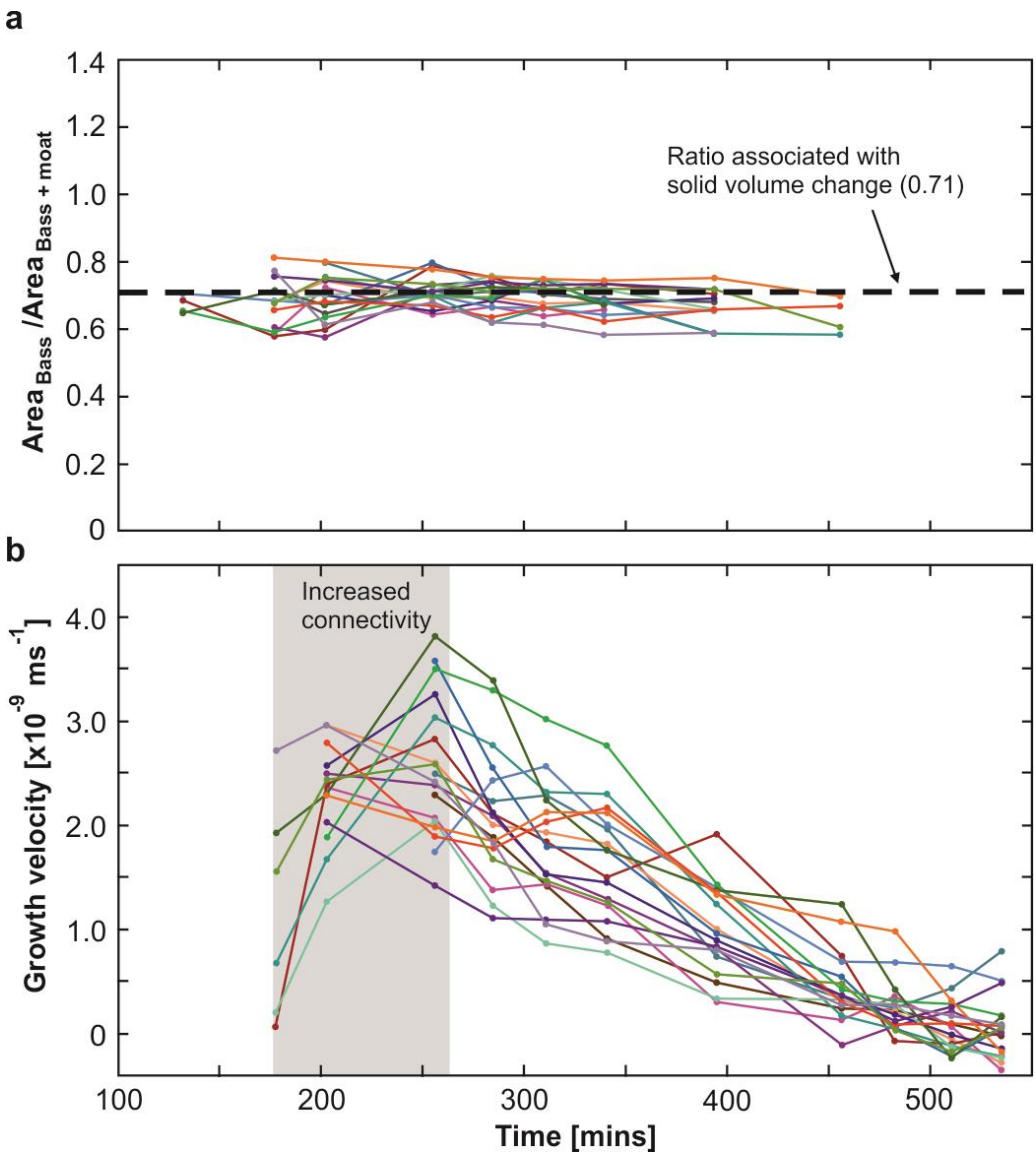


***Figure 3.4*** *- Quantification of the grain areas and growth velocities with time. a) Ratio of the areas between the grain and the grain + moat. Different curves represent individual grains and their associated moats. Values oscillate around a central ratio of 0.71 which is equivalent to the solid volume change associated with the reaction (ie. molar volume of bassanite/molar volume of gypsum = 0.71). Once the moats begin to coalesce they can no longer be associated to a given grain and therefore the ratio can no longer be analysed, hence why the curves do not continue for the duration of the experiment. b) Grain growth velocity curves for individual bassanite grains. The grey shaded area represents the time when the connectivity of the sample dramatically increases. This corresponds to an initial acceleration in growth velocity for the majority of grains. Once the drainage architecture has established itself the growth velocities decrease with time, which is associated with diffusion of solutes across the moats (Fig. 3.3).*

We also derived approximate growth velocities (u) for individual grains from $u = \frac{1}{p}\frac{dA}{dt}$ where $t$ is time, p is the perimeter and A is the area of a given grain. Most grains show an initial increase in velocity until about 250 minutes before an overall deceleration is observed for the majority of their growth history (Fig. 3.4b). The initial growth acceleration is associated with the increasing connectivity of the sample. Prior to the pore network becoming interconnected, locally high pore-fluid pressure in isolated pores hinders the reaction. Previous experimental work on gypsum dehydration has shown that reaction rate is highly dependent on the pore fluid pressure (Llana-Funez et al., 2012). There is a strong agreement between this previous dataset and the reaction rate observed under the experimental conditions of this study (see Supplementary equations and Supplementary Fig. 3.4), highlighting the importance of pore fluid pressure as a rate –controlling parameter. The acceleration in grain growth coincides with the rapid increase in connectivity between 202-255 minutes (Fig. 3.2) because the excess pore fluid pressure, which slows the reaction, is able to dissipate. The subsequent deceleration in growth through time is what would be expected for a diffusional control on reaction, as recently documented for a reaction involving fluid-solid interactions but not dehydration (Jonas et al., 2015). As our moat widths increase, the diffusion distance lengthens causing the growth rates to slow. We calculate a bulk diffusion coefficient of $1.23 \times 10^{-10}$ $m^2/s$ for the transport of chemical components across the moats (see Supplementary equations and Supplementary Fig. 3.5).

On a practical level, these findings show that the solid volume changes that occur as a result of dehydration can create the main pathways to facilitate the mass transport of both hydrous and dissolved chemical components during reaction, albeit on different scales. The new porosity provides a route for excess $H_2O$ to escape in the early stages of the reaction and also generates diffusion gradients along which the dissolved solutes migrate to the growing grains. Identification of the main transport pathway has important implications for the understanding of how reactions will interact with other processes such as deformation, which will no doubt reduce the available pore space and in turn restrict the ability for fluids to be expelled while also reducing the diffusion distances that govern the reaction rate. Knowledge of the kinetic controls on reaction is paramount, particularly for the modelling of dehydrating systems, as they will determine the overall rate of transformation and in turn have implications for the mechanical and hydraulic evolution of the system. We have shown

that the reaction rate can be controlled by both the fluid pressure and the diffusion of dissolved solutes, and that this is determined by the hydraulic properties of the dehydrating rock. Finally, our results can help identify scenarios when seismicity might occur in subduction zones. In our case, if the transient porosity is maintained during reaction, then the early expulsion of fluids and slowing reaction rate suggest that greatest chance of seismicity is early in the reaction rather than at it maximum rate.

## 3.3. Supplementary material

### *3.3.1. Supplementary methods*

#### *3.3.1.1. Sample preparation*

The gypsum samples were cored from a precision ground slab of alabaster. The slab originated from a block of polycrystalline Volterra gypsum which has grain sizes in the range of 10-200 μm (Leclère et al., 2016). Volterra gypsum is considered to be fairly isotropic; however weak shape preferred orientations have been reported (Hildyard et al., 2011). The slab was cut into a 6cm x 6cm square and ground to a thickness of 5mm to a tolerance of 100 μm. Cores, 2 mm in diameter, were drilled from the slab and the ends were lightly hand-ground to remove any roughness produced during coring.

#### *3.3.1.2. Microtomographic data acquisition*

Experiments were conducted at beam line 2BM at the Advanced Photon Source (APS), in the upstream hutch 25 m from the source. There, a polychromatic beam filtered by 35 mm borosilicate glass yielded a photon flux with an energy peak at 65 KeV. A Cooke pco.edge sCMOS camera with 2560×2160 pixels (pixel size 6.5×6.5 μm2) was used in a flying scan mode, where projections are recorded while the sample is continuously rotated (i.e. the stage rotation does not stop in between image acquisitions). The sample-detector distance was kept to 80 mm to minimize phase contrast in the data. For the experiment we used an x-ray transparent Hassler core holder (Fusseis et al., 2014), where the sample was pressurized and heated to 388 K

after an initial reference scan. The camera recorded projections from a 10 μm thick LuAG:Ce single crystal scintillator, magnified through a 5x Mitutoyo long-working distance lens yielding a pixel size of 1.3 μm. Projections were collected with an exposure time of 50 ms while the sample was rotated over 180° with 1.2 °/s. 1500 projections were collected in 150 s. Each time step comprises three individual scans acquired back to back at three different vertical positions to cover the entire sample cylinder. The entire sample was scanned every 15 minutes over a total of 9 hours.

#### *3.3.1.3. Data processing and analysis*

Microtomographic data were reconstructed from the projections using TomoPy (Guersoy et al., 2014). The reconstructed data were processed using the commercial software package Avizo 8.0 and the open source software Fiji (Schindelin et al., 2012). The reconstructed image stacks were cropped (750 x 750 x 750 voxels) and processed to reduce image noise using a non-local means filter. Subsequently, the porosity was segmented from the data in Fiji using the Trainable Weka Segmentation Algorithm (http://imagej.net/Trainable_Weka_Segmentation). The segmented porosity was labelled and analyzed in Avizo to allow for a detailed estimation of porosity and percolation in the time series data. Porosity measurements are based on the segmented datasets and reflect the systematic evolution of the porosity in the sample during reaction.

### *3.3.2. Supplementary equations*

#### *3.3.2.1. Reaction rate is in agreement with a previously determined dependence on pressure and temperature*

Llana-Funez et al., (2012) took a dataset of reaction rates from 35 experiments on gypsum dehydration, using the volume of fluid expelled as a monitor of reaction rate. The maximum rate of fluid expulsion could be used as a measure of reaction rate but, realising that compaction also plays a role in fluid expulsion, they proposed that a reaction rate proxy is more useful:

Reaction rate proxy = (maximum expulsion rate)/(volume expelled at that time)

This idea can applied in the same way to porosity evolution. Because porosity development should scale with fluid expelled, for our new experiment we can calculate the same proxy using:

Reaction rate proxy = (maximum rate of porosity increase)/(porosity at that time)

Smoothing the data of supplementary figure 3.1 we find the maximum rate of porosity increase is 0.1267 %/min when porosity is 10.17 %. Then, converting to $s^{-1}$:

$\log_{10}$(reaction rate proxy) = -3.68

Llana-Funez et al., (2012) made a best fit to their 35 reaction rate proxies, which span 2 order of magnitude:

$\log_{10}(\text{reaction rate proxy}) = -16.9851 + 0.1142\,T - 0.0127\,P_f + 0.0019\,P_c$

So using our experimental parameters of Pc = 9 MPa, Pf = 4 MPa and T = 115 °C, we calculate:

$\log_{10}$(reaction rate proxy) = -3.89

The difference of 0.21 is well within the scatter of residues (measured – calculated) in the Llana-Funez et al., (2012) dataset. Using their Supplementary Table 3, we display the residues in supplementary figure 3.4; the new result is shown in yellow and is not out of place in comparison to the overall scatter.

### *3.3.2.2 Determination of the diffusion coefficient*

For figure 3.4 we required individual grain areas but it was not possible to segment bassanite from gypsum reliably: although the eye can distinguish these two minerals, there is too much overlap in grey scale. So, to analyze grain growth we selected individual grains which could be identified through the time series and measured the areas (A) and perimeters (p) of grains and moats in Fiji. We then calculated average growth and dissolution velocities by from $u = \frac{1}{p}\frac{dA}{dt}$ . This approach

was chosen because it guarantees the correct *average* growth velocity for a particular grain or moat. The net diffusion coefficient quoted in main text was calculated as follows. We assume that the growth rate is controlled by a combination of interface detachment from gypsum, attachment to bassanite and by diffusion leading to a simple quantitative model for rate (Lasaga, 1986). We adapt eqns 9 and 10 from Lasaga (1986) but growth is 2D so there some convergence in chemical flux towards the bassanite. To allow for this we simplify grain and moat shapes to be cylinders. Then diffusive flux will scale with 1/r where r is radial distance from the center line of a bassanite grain. Concentration will be a linear function of ln(r) because its gradient gives the flux. Modifying and rearranging Lasaga (1986) eqns 9 and 10 gives:

$$\frac{1}{u} = \frac{\alpha \ln(\frac{1}{\alpha})}{(1-\alpha)V(C^g - C^b)D} w + \frac{1}{V(C^g - C^b)}\left(\frac{\alpha}{k_g} + \frac{1}{k_b}\right) \qquad \textit{Supp. Eqn. 3.1}$$

Where:

u = bassanite growth speed

V = bassanite molar volume

w = moat width

$C^g$, $C^b$ = concentrations of $CaSO_4$ in solution in equilibrium with gypsum or bassanite

$k_g$, $k_b$ = rate constants for dissolution of gypsum and precipitation of bassanite, assuming rates are linear in over- or undersaturation (m/s)

$\alpha^2$ = (bassanite molar volume)/ (gypsum molar volume) = 0.71

*D* = diffusion coefficient

So, D is derived from the slope s of a best fit line on a 1/u versus w graph:

$$D = \frac{\alpha \ln\left(\frac{1}{\alpha}\right)}{(1-\alpha)} \frac{1}{V(C^g - C^b)s} \qquad \textit{Supp. Eqn. 3.2}$$

We applied this equation to 16 moats. For some moats the correlation coefficient was low so we excluded them; for others the y-axis intercept was negative which is not in accord with supplementary eqn (1) so we excluded these too. We were

left with 6 moats with the data shown in supplementary figure 3.5. Each moat yields an estimate of D and the average is 1.23 $x10^{-10}$ $m^2/s$, the apparent diffusion coefficient of $CaSO_4$. Since the anion and cation have their own diffusion coefficients this is also the harmonic mean of the diffusion coefficients of $Ca^{2+}$ and $SO_4^{2-}$ (Cussler, 1984). For comparison at 1 atm and 25 °C the apparent diffusion coefficient of $CaSO_4$ is 9.11 $x10^{-10}$ $m^2/s$ (Yuan-Hui and Gregory, 1974). We obtain a similar order of magnitude, but we expect the diffusion coefficients to be faster at higher T; the discrepancy may be due to a pressure effect and/or diffusion pathways which are longer than the moat width.

### *3.3.3. Supplementary figures*

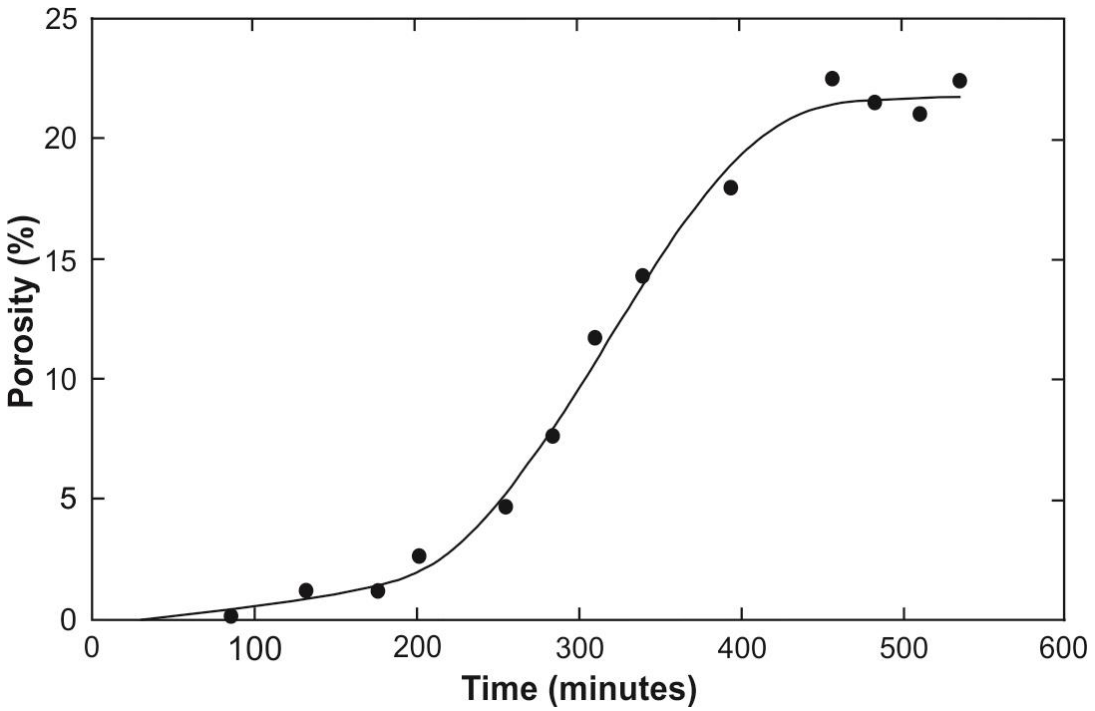


***Supplementary Figure 3.1 -*** *Porosity of the sample over time. Porosity increases non-linearly during the experiment until it settles around 22.5%.*

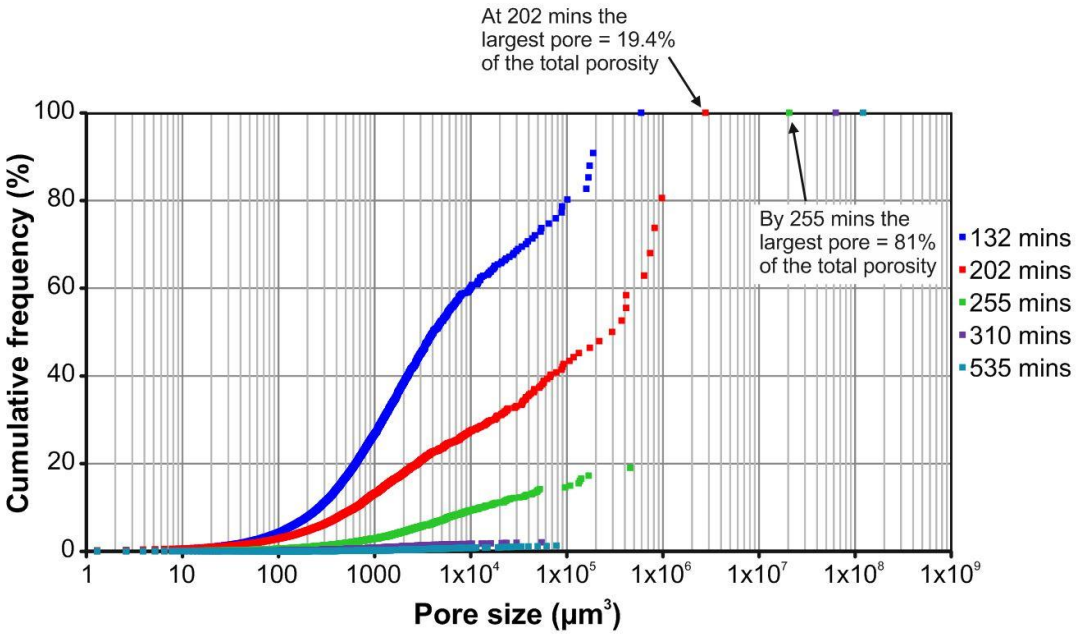


***Supplementary Figure 3.2 -*** *Cumulative pore size frequency distribution over time. After 255 minutes the distribution is dominated by a single cluster of interconnected pores which comprises more than 80% of the total porosity.*

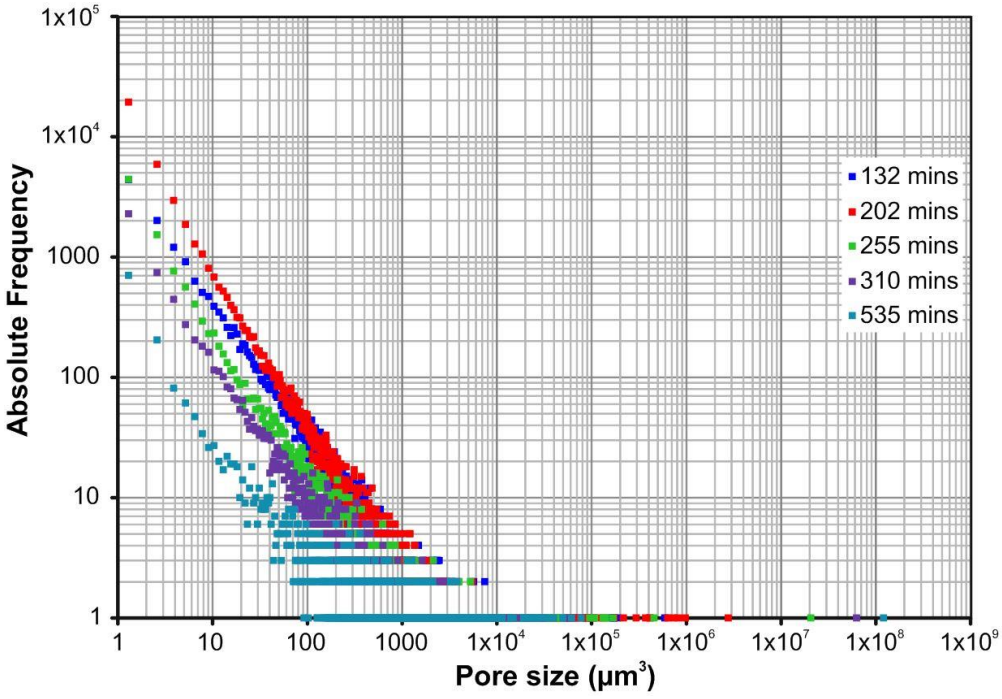


***Supplementary Figure 3.3*** *- Absolute pore size frequency distribution over time. After 202 minutes the amount of small isolated pores drastically reduces as they become incorporated into the large sample-scale drainage architecture.*

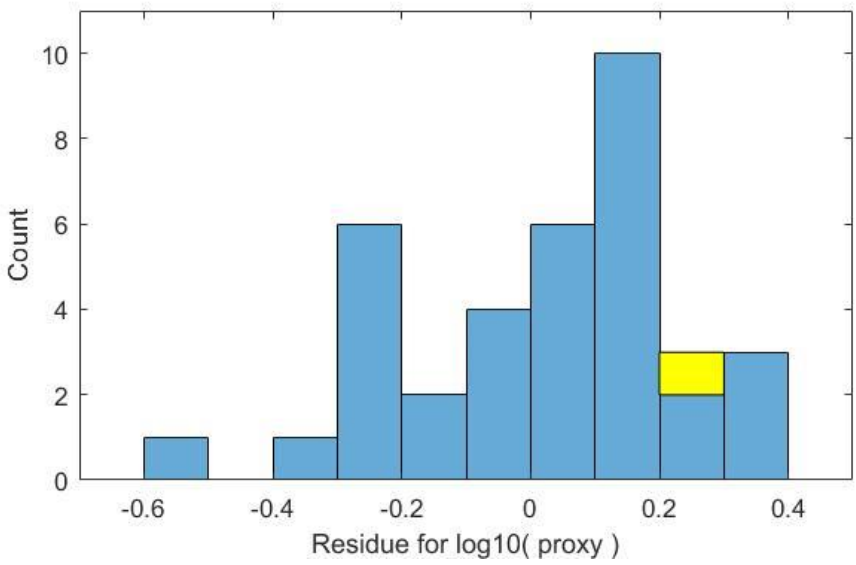


***Supplementary Figure 3.4 -*** *The scatter of residues of the measured minus calculated reaction proxy from the Llana-Funez et al., (2012) dataset. The data from this study is highlighted in yellow and is well within the scatter of residues from the* Llana-Funez et al., (2012) *dataset. See supplementary equations for calculations and further information.*

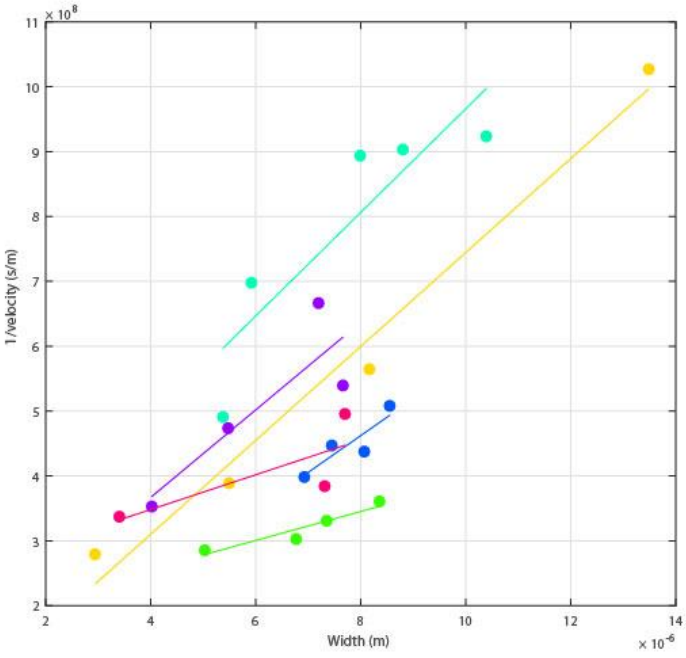


***Supplementary Figure 3.5 -*** *A plot of 1/velocity versus moat width for different grains. The slope of the best fit lines is used to derive the diffusion coefficient (D) in supplementary equation 2.*

# 4. Deforming porous rock: high-resolution mapping of yield curve evolution and the implications for compaction, dilation and localization


## Abstract

The nature of deformation in porous rock is of vital importance for understanding fluid flow in a range of crustal settings. The onset of permanent inelastic strain for porous materials is typically defined by a yield curve that is plotted in P-Q space, where P is the effective mean stress and Q is the differential stress. Empirical studies have shown that these curves are broadly elliptical in shape. We first perform a set of traditional triaxial experiments to document the yield curve of porous bassanite (porosity ≈ 27-28%), a material formed from the dehydration of polycrystalline gypsum. However our data reveal that the yield curve of bassanite is not perfectly elliptical and that the shape of the curve significantly evolves as the material accumulates inelastic strain. We therefore develop a novel methodology to precisely map the yield curve shape and its subsequent evolution for a single sample by a set of stress-probing experiments. These tests show that the high-pressure side of the curve is partly comprised of a near-vertical limb. The evolution of the yield curve is shown to be dependent on the nature of inelastic strain. Bassanite compacted under differential load develops a heterogeneous microstructure and has a yield curve with a peak which is almost double that of an equal porosity sample that has been compacted hydrostatically. The dramatic effect of different loading histories on the strength of porous bassanite highlights the importance of understanding the associated microstructural controls on the nature of deformation in porous rock.


## 4.1. Introduction

Fluids are abundant in the Earth's crust and are of upmost geological importance for a variety of natural and industrial processes, ranging from the transport

of chemical components in metamorphic and hydrothermal systems to the extraction of hydrocarbons from a reservoir. Any fluid phase in the Earth's crust must be stored in some form of available pore space. The nature of this pore space and its evolution in response to tectonic stresses will in turn determine the ability of a rock to transmit fluids. The response can be purely mechanical where the rock will either compact or dilate depending on the stress conditions, or porosity can change as a result of chemical processes, such as pressure solution and cementation. This study will focus on the initial time-independent mechanical response of porous rock to macroscopic stresses; an understanding of which can provide important insights into faulting and fluid flow in porous formations, as well as industrial problems such as borehole stability and reservoir compaction.

As a rock is put under load its initial response is elastic meaning that any deformation is recoverable if the load is removed. The stress-strain relationship in the elastic regime is typically quasi-linear (Fig. 4.1a). However if the stress is increased further, and the yield stress is reached, then the rock will move out of the elastic regime and accumulate permanent plastic (inelastic) strain. It should be noted that the term plastic is used in the mechanical sense and does not imply an underlying deformation mechanism; rather, that the deformation is permanent and if the load is removed after an amount of plastic strain has been accumulated the rock will not return to its initial starting condition. The stress at which the onset of inelastic strain occurs is called the yield point and can be identified by the deviation from linear elastic loading (Fig. 4.1a). Materials that deform by brittle mechanisms (such as compaction and dilation) are pressure-sensitive, meaning that the stress at which yield occurs will vary as the pressure changes. A yield curve can therefore be defined in stress-space to define the locus of points at which yield will occur. For porous materials the yield curve is typically plotted in P-Q space, where P is the effective mean stress $\left(P = \frac{\sigma_1 + \sigma_2 + \sigma_3}{3} - P_f\right)$ and Q is the differential stress($Q = \sigma_1 - \sigma_3$) or the deviatoric stress ($Q = \sigma_1 - P$). Yield can be achieved under a purely hydrostatic stress state (i.e. no differential stress). The curve therefore intersects the P-axis at the pressure where hydrostatic yield is achieved. This point is commonly referred to as P* and marks the onset of grain crushing and pore collapse (Zhang et al., 1990b). Much of our understanding on the yield of porous rock is based on principles from critical state soil mechanics (Schofield and Wroth, 1968). Soil mechanics has shown that yield curves are typically elliptical in shape (Fig. 4.1b) and empirical data on a variety of porous rocks such as sandstone

(Wong et al., 1997a; Baud et al., 2000b; Cuss et al., 2003b; Baud et al., 2004; Baud et al., 2006; Louis et al., 2009), limestone (Baud et al., 2000a; Vajdova et al., 2004; Baud et al., 2009; Cilona et al., 2014), volcaniclastics (Zhu et al., 2011) and dehydrated serpentinite (Rutter et al., 2009) have been in general agreement with broadly elliptical-shaped curves. Therefore if the stress state falls inside the ellipse the rock will be in the elastic regime and any deformation will be recoverable. If the stress conditions are outside the ellipse then the rock will experience some form of inelastic deformation.

The mode of inelastic deformation that a rock experiences at a particular point on the yield curve can be, in its simplest form, separated into two regimes (Fig. 4.1b). At low pressures, the mode of deformation is dilatancy which is typically associated with localized deformation and faulting (e.g. Menéndez et al., 1996). At high pressures a rock will undergo shear-enhanced compaction which is associated with distributed deformation (Curran and Carroll, 1979). This transition from localized dilatancy to distributed compaction is often referred to as the low-temperature brittle-ductile transition in porous rock (e.g. Rutter and Hadizadeh, 1991; Wong and Baud, 2012). As a rock accumulates inelastic strain the porosity will either increase or decrease depending on whether the rock is experiencing dilatancy or compaction. This causes the yield curve to expand or contract depending on the nature of deformation (Fig. 4.1c). A family of elliptical curves can therefore be defined for rocks of different porosity (and/or grain size) or for a single rock undergoing compaction. The crest of each yield curve, which separates dilation from compaction, can be joined by a line called the Critical State Line (CSL). This can also be visualized in 3D where the third axis represents porosity (Φ). In this diagram (Fig. 4.1d) the ellipses space out along the porosity-axis and their respective P* values form another line called the Normal Consolidation Line (NCL) (e.g. Rutter and Brodie, 1995).

The concept of a family of curves, where for a given porosity the shape of the curve remains the same with only the size changing, has been well applied to unconsolidated sediments. A series of complex probing tests on both clay (Graham et al., 1983) and sand (Tatsuoka and Ishihara, 1974; Miura et al., 1984) have revealed the shapes of these families and found that a unique curve shape can be defined for the different materials. However the applicability of this concept to porous rock remains unclear and experimental data on curve evolution is sparse. Alternative models to that of Schofield and Wroth (1968), who consider a family of broadly elliptical shaped yield curves, have been proposed which allow the yield curve shape to evolve with the

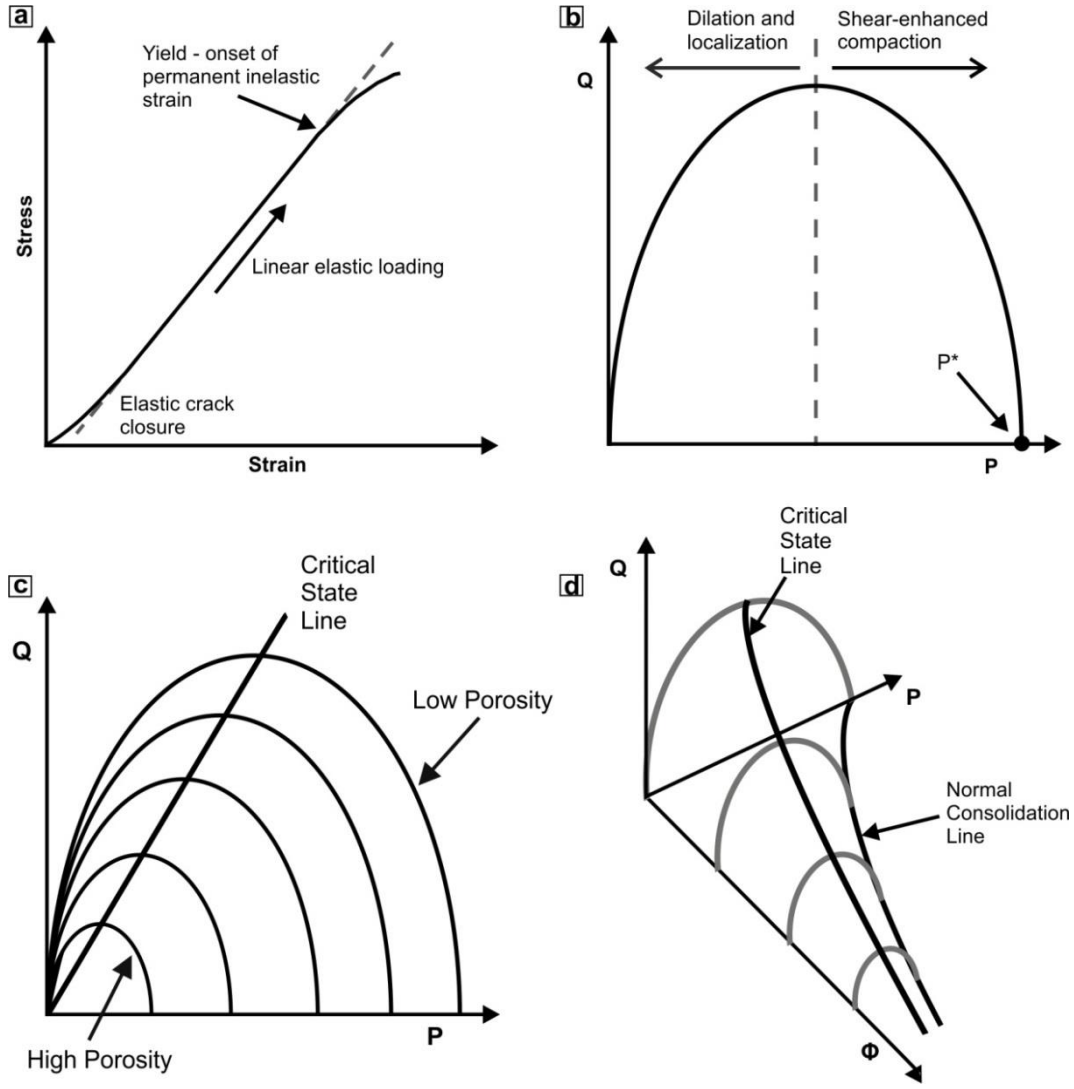


***Figure 4.1 - (a)*** *A typical loading curve for a rock. The initial response is elastic with a quasi-linear stress-strain relationship. At a certain stress the rock will begin to yield as it starts to accumulate inelastic strain. This can be identified by the deviation from linear elastic loading.* ***(b)*** *Yield points can be identified at a range of effective pressures to define a yield curve. The curve is typically thought to be elliptical in shape with the low pressure side being associated with localized dilatant behaviour and the high pressure side with distributed compaction. The point where the curve intersects the effective mean stress axis is referred to as P*.* ***(c)*** *A family of yield curves can be defined for different porosities. The peak of these curves can be joined by the critical state line to separate the regions of dilation from compaction.* ***(d)*** *A 3D representation of the yield envelope where the third axis is porosity (Φ). The ellipses space out along the porosity axis and their respective P* points can be joined to form the normal consolidation line.*

accumulation of inelastic volumetric strain. Rather than a family of elliptical curves both DiMaggio and Sandler (1971) and Carroll (1991) consider the yield envelope to be comprised of two curves; a low pressure dilational envelope bound on the high pressure side by an elliptical cap. This elliptical cap is allowed to change aspect ratio with the accumulation of volumetric strain in the Carroll (1991) model, whereas in DiMaggio and Sandler (1971) the cap remains at a constant aspect ratio as it expands and slides along the P-axis. Baud et al., (2006) have tested yield curve evolution for a range of porous sandstones and found evidence that the compactive side of the curve does evolve with inelastic volumetric strain. They found that models of Carroll (1991) and DiMaggio and Sandler (1971) have varying amounts of success in predicting the yield curve evolution of the different sandstones. However the data of Baud et al., (2006) are subject to a large amount of data scatter as a result of sample variability making it difficult to reliably fit curves to the data in order to monitor their evolution. Other studies have also suggested that the yield curve for porous rock can be constrained to a shape independent of rock type (Wong et al., 1997a; Rutter and Glover, 2012) highlighting the current uncertainty in the importance of yield curve evolution for porous rock.

In this study the compaction behaviour of dehydrated gypsum is tested to see if it fits into a relatively simple critical state model with elliptical yield curves or whether another interpretation is needed. The data are important for understanding the compaction of rocks undergoing solid volume reductions during metamorphic reactions, but also have wider applications to the mechanics of porous rocks in general. Like the majority of devolatilization reactions, the dehydration of gypsum is associated with a large solid volume reduction which generates porosity. It is important to understand the porosity evolution in a dehydrating system because if fluids are not able to drain efficiently then fluid overpressures may develop which could generate earthquakes or slow slip in subduction zone settings (e.g. Hacker et al., 2003; Gao and Wang, 2017). A soil mechanics approach has previously been used to investigate the deformation of porosity created as a result of metamorphic devolatilization reactions (Rutter and Brodie, 1995; Rutter et al., 2009); however a detailed investigation of the compaction behaviour of dehydrated gypsum has been lacking. Gypsum has been widely used to study processes associated with dehydration reactions as it provides an ideal analogue material (e.g. Ko et al., 1997; Fusseis et al., 2012; Llana-Funez et al., 2012; Leclère et al., 2016). The complete dehydration of gypsum, to form the product

mineral bassanite, generates a porosity of 27-28% which is comparable to many of the sandstones used in previous compaction studies (e.g. Cuss et al., 2003b; Fortin et al., 2005). Understanding the compaction of this porosity is important for gaining a better knowledge of the interplay between fluid flow, deformation and reaction during gypsum dehydration.

In this work, traditional triaxial experiments are performed first to try and map the yield surface for porous bassanite similar to that in Figure 4.1d. However, these experiments highlight discrepancies between the compaction behaviour of porous bassanite and the critical state model. This leads us to perform a set of novel stress-probing experiments to try to map precisely the yield curve to explore its true shape and subsequent evolution. This chapter is therefore split into two sections to describe these different sets of experiments. Section 4.2 outlines the initial traditional experiments and the problems with the critical state model before section 4.3 introduces the methodology and results for the novel stress-probing experiments. The implications and wider applications for porous rock deformation are then discussed in section 4.4.

## 4.2. Testing the elliptical Critical State Model for porous bassanite

The type of experiments that are performed to test the elliptical critical state model are traditional triaxial tests, where a suite of samples are loaded to different effective pressures before an axial load is applied and the stress-strain evolution is monitored. In this setup the confining pressure, pore pressure and axial load can all be varied and controlled independently from each other. A more detailed description of the experimental apparatus can be found in Chapter 2 (Fig. 2.2).

### *4.2.1. Sample preparation*

The starting material is natural alabaster gypsum from Volterra, Italy, which has been widely used in a range of studies investigating the dehydration and deformation of gypsum (e.g. Ko et al., 1997; Fusseis et al., 2012; Llana-Funez et al., 2012; Leclère et al., 2016). Volterra gypsum is fine grained (50-200μm), with initial

porosities of <1.5% and is considered to be relatively isotropic; however weak shape-preferred orientations of grains have been reported (Hildyard et al., 2011). Cores (50mm length x 20mm diameter) were drilled in the same orientation from a block of Volterra gypsum and were then precision-ground to square the ends to tolerance (±0.01 mm). Once the gypsum had been cored and squared, samples were placed in an oven where they were left to dehydrate to form bassanite. The oven temperature was set to 80 °C and reaction progress was monitored by measuring the weight loss associated with fluid expulsion (Supplementary Fig. 4.1). Samples would typically take about 30 days to dehydrate completely to form bassanite and they would be left in the oven until they were used for compaction tests to minimize the possibility of rehydration at ambient conditions. Once removed from the oven the samples were left for a few minutes to cool and then the porosity of the dehydrated material was measured using He-pycnometry. All of the reaction was therefore complete prior to insertion into the deformation apparatus.

### *4.2.2. Identification of P**

In order to investigate the nature of the yield curve for porous bassanite it is important to establish first the point at which yield occurs under hydrostatic conditions (P*). After a sample was inserted into the apparatus the confining pressure was increased to 23 MPa and the pore fluid pressure to 20 MPa. Both parameters were increased incrementally to ensure an effective pressure of 3 MPa was never exceeded so that no inelastic compaction occurred. Once these starting conditions were reached, the servo-controlled confining pressure pump was used to increase the confining pressure at a rate of 0.01 MPa/s whilst monitoring the change in pore volume with the pore pressure volumometer (porosity proxy). The pore fluid pressure was held constant at 20 MPa for all tests in this study.

Figure 4.2 shows the results of hydrostatic loading on the porous bassanite samples. A clear deflection in the loading curve, corresponding to the yield point, can be seen at an effective pressure of approximately 6 MPa. Other tests where the load was removed after this point confirm the sample had undergone permanent deformation. This value is much lower than typical P* values for porous sandstones which have comparable porosity to bassanite. For example, Penrith sandstone (Φ =

28%) has a P* of 140-170 MPa (Cuss et al., 2003b) and Bleurswiller sandstone (Φ = 23-25%) has P* values in the range of 135-195 MPa (Fortin et al., 2005; Tembe et al., 2008), highlighting the relative weakness of porous bassanite compared to other rock types. However this means that much of the post-yield behaviour of bassanite is attainable allowing for a large portion of the yield surface to be determined.

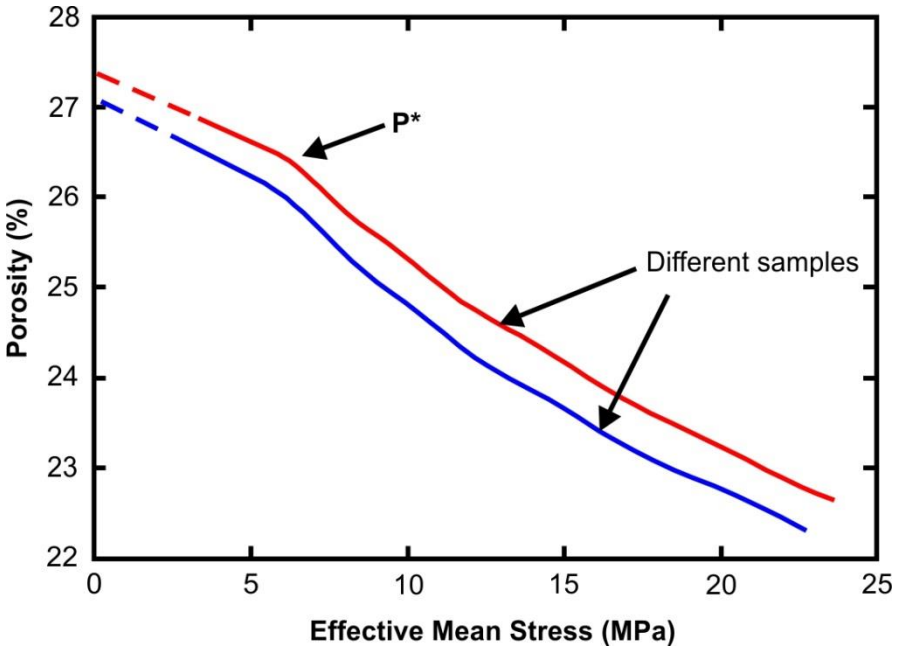


***Figure 4.2 -*** *Hydrostatic loading of porous bassanite. A deflection can be seen at an effective mean stress of 6 MPa marking the onset of permanent inelastic deformation. Dashed lines represent the loading history that is lost as the sample is pressurized to an initial effective stress of 3 MPa; the solid lines are therefore extrapolated back assuming linear elasticity.*

### *4.2.3. Mapping the yield surface*

In order to investigate the nature of yield surface, different samples of bassanite were loaded to different effective pressures before being subjected to axial loading at a constant displacement rate (0.5 μm/s). The starting effective pressures in the tests are higher than the 6 MPa value of P* meaning that they are already sat on the Normal Consolidation Line (NCL) before the axial load is applied (Fig. 4.1d). Therefore,

as a sample is subject to a differential stress, the trajectory in P-Q-Φ space should traverse along the compactive side of the yield surface (the Roscoe surface) towards the critical state line. Thus the shape of the yield surface should be revealed.

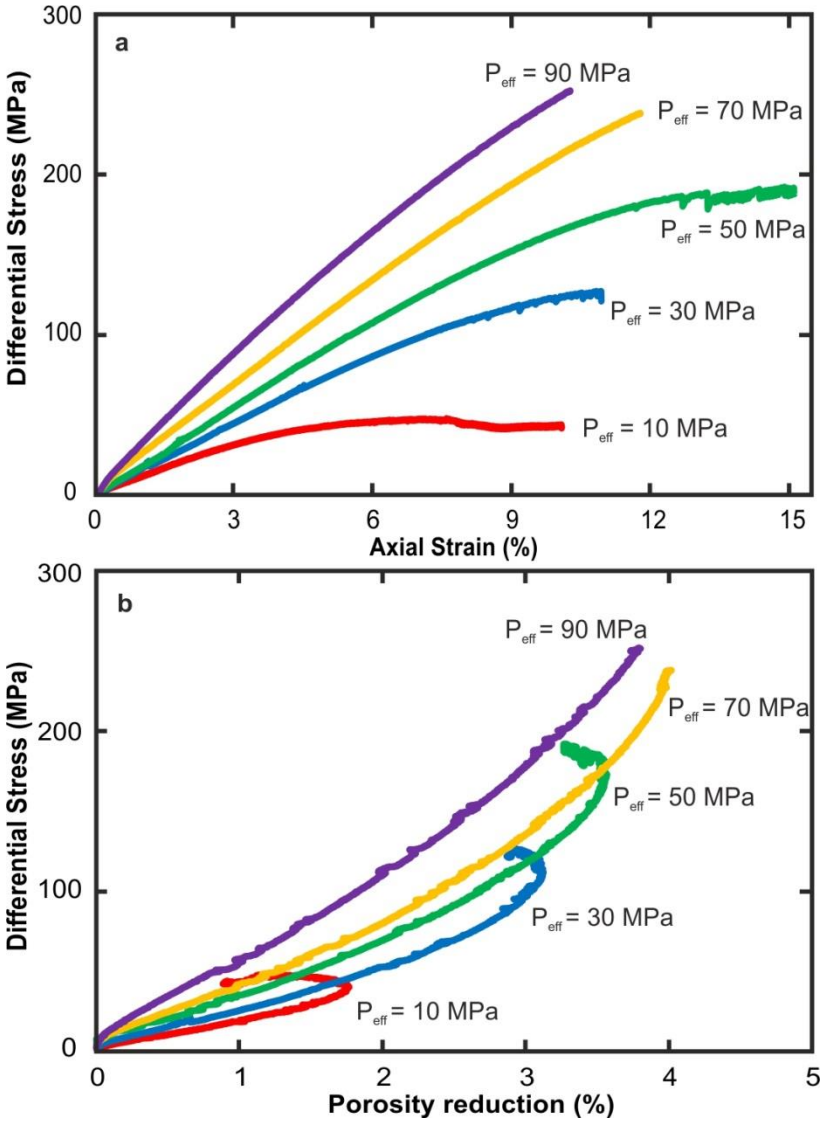


***Figure 4.3*** *- Mechanical data for bassanite samples that were axially loaded at different effective pressures.* ***(a)*** *Stress vs axial strain and* ***(b)*** *stress vs porosity reduction.*

The data from these tests are summarized in Figure 4.3. All samples show initial strain hardening (Fig. 4.3a), which is to be expected when in the compactive regime. As the samples are already sat on the yield surface there are no deflections in

the loading curves that would typically be seen if loading started from the elastic regime inside the yield surface. The majority of strain induced by axial loading is therefore inelastic. Samples which were loaded at the lowest effective pressures (10, 30 and 50 MPa) went through a transition from distributed compaction to localized deformation on a sample-scale shear plane. This is associated with small stress-drops observed in the stress-axial strain data (Fig. 4.3a) and also a switch from compaction to dilation (Fig. 4.3b). Samples that were deformed at higher effective pressures (70 and 90 MPa) only experienced strain hardening and compaction.

### *4.2.4. Implications of the data for the shape of the yield surface*

The data gathered from these tests should provide enough information to map comprehensively the compactive side of the yield envelope. The position of the critical state line should also be revealed by the "hooks" in the porosity data (Fig. 4.3b). These hooks (often referred to as C*') have previously been observed in other studies and represent the change from compaction to dilation (Baud et al., 2000a; Vajdova et al., 2004; Vajdova et al., 2012). However, when the data are plotted in P-Q-Φ space, there are peculiarities in the shape of the yield surface. These peculiarities are most clearly highlighted when the yield surface is observed along the differential (Q) axis and the data are projected down onto the P-Φ plane. In this view, the CSL is expected to lay roughly half way between the NCL and the Φ-axis for elliptical yield curves (Fig. 4.4a). However, we find that that what we interpret as the CSL from the transition from compaction to dilation lies almost directly on top of the NCL, hydrostatic loading data (Fig. 4.4b). This suggests that the compactive side of the yield envelope should therefore be near-vertical. As this contradicts the simple critical state model a new interpretation of the data is required. Two possible explanations could result in the CSL overlying the NCL. Firstly the yield envelope could have an unconventional shape (i.e. not elliptical) which would have its peak overlying P*. Alternatively the yield surface might not be a simple static surface and perhaps it evolves as a sample accumulates permanent inelastic strain as suggested by the models of DiMaggio and Sandler (1971) and Carroll (1991). To test this we need to adopt a different experimental technique to constrain the complete shape of the yield curve after different increments of inelastic strain to identify if there is any evolution.

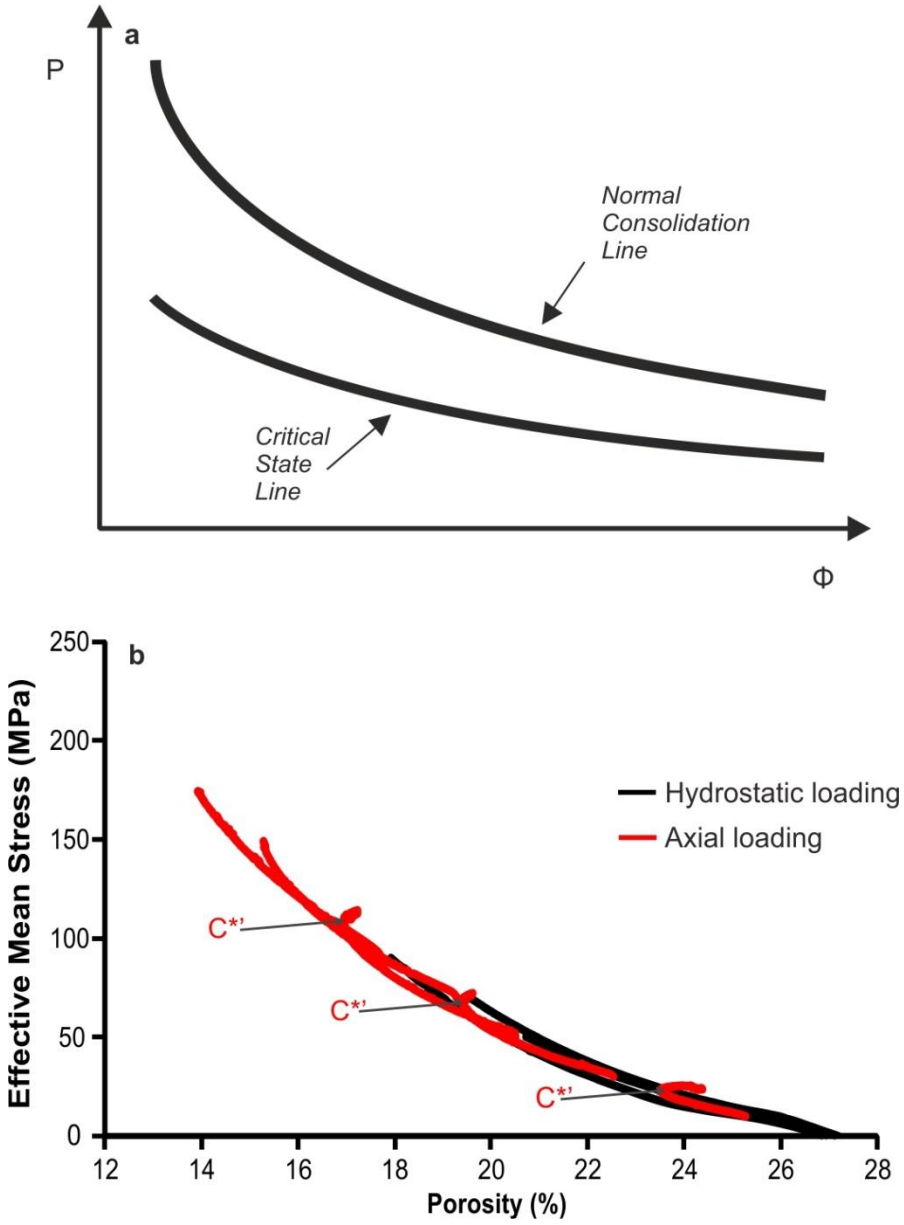


***Figure 4.4 - (a)*** *A schematic projection of a theoretical 3D yield envelope down on to the P-Φ plane. If the critical state line is projected onto this plane, assuming elliptical yield curves, it would be expected to lay half way between the normal consolidation line and the Φ-axis.* ***(b)*** *Mechanical data from the bassanite deformation tests of this study. The axial loading data (red) sits directly on top of hydrostatic data (black). The hooks in the axial loading curves (C*') should mark the location of the critical state line as they represent the switch from compaction to dilation. The position of the hooks directly above the hydrostatic loading data suggests that the critical state line would overly the normal consolidation line which is not expected for elliptical yield curves.*

## 4.3. Investigating the geometry and evolution of the yield surface

In order to investigate the true shape of the yield curve we perform novel experiments to probe a given curve multiple times at different places. To do this a sample is overconsolidated and then the load is reduced to move back into the elastic regime (i.e. inside the yield curve). The sample is then taken to different confining pressures inside the yield curve and axially loaded to yield at each pressure. Using the principle that the yield point can be identified by the deviation from linear elastic loading (Fig. 4.1a), the load is increased until this deviation is observed. Examples of yield identified from axial loading curves can be seen in supplementary figure 4.2. As soon as this deviation is seen, the axial load is immediately removed from the sample to ensure a nominal amount permanent inelastic strain is accumulated. The confining pressure is then changed to a different value and the sample is subjected to another axial loading increment to probe the yield curve at a different point in stress space. All the movement in stress space is therefore inside a given yield envelope in the elastic regime. The only time this is not the case is at the onset of yield itself. Once one yield curve has been probed the sample is overconsolidated further so that the sample sits on another new curve. This new curve is then probed in the same way to investigate if inelastic strain causes the shape to evolve.

To study comprehensively the effects of inelastic strain on the shape of the yield curve, different types of stress paths used to produce overconsolidation need to be considered. In a conventional triaxial experimental setup a sample can experience two types of stress path leading to permanent strain; isotropic loading which produces purely volumetric strain and deviatoric loading which has a component of shear strain. We therefore perform tests to analyse how these two types of loading paths affect the evolution of the yield surface. The first type of test is termed *hydrostatic overconsolidation* where the effects of purely volumetric strain are examined. The second type of test is *deviatoric overconsolidation*, which has a component of shear strain as well as volumetric strain. The experimental procedure and results of each type of test are outlined below.

### *4.3.1. Hydrostatic Overconsolidation*

#### *4.3.1.1. Experimental procedure*

Figure 4.5a shows a schematic summary of the loading path for hydrostatic overconsolidation tests. Initially a sample was loaded hydrostatically beyond P* so that it would experience inelastic volumetric strain and be sat on a new yield envelope at lower porosity. The confining pressure was then decreased in increments; between each increment the sample was axially loaded to probe the shape of the new yield curve. In a triaxial deformation rig a typical axial loading path has a gradient of 3 when plotted in P-Q space. This is because as the axial load ($\sigma_1$) is increased the confining pressure ($\sigma_2$ and $\sigma_3$) is being held constant. Therefore as the differential stress is increased by 1, the effective mean stress increases by $\frac{1}{3}$. As soon as the yield curve is reached (identified by the deviation from linear elastic loading) the axial load is instantly removed and then the confining pressure is reduced further. After the yield curve had been probed over a range of confining pressure increments the pressure was increased again beyond the new P* so the sample reaches another new yield curve. The steps of confining pressure reduction and axial loading were then repeated for this subsequent yield curve. This loading history will therefore map out the family of yield curves that form in response to purely volumetric compaction.

#### *4.3.1.2. Results*

The yield points that were collected during the repeated probing test are collated in figure 4.5b. It can be seen that the use of a single sample has produced minimal data scatter helping to reveal the true shape of the yield curve. Measurements were performed to test the probing technique and ensure that the assumed elastic loading history and incremental yielding does not impose any permanent deformation on the sample. In these tests the yield points were re-examined as the effective pressure was increased back towards P* inside the yield envelope following the first set of measurements. The two sets of yield points (Supplementary Fig. 4.3) are found to be close to each other in stress space suggesting that the elastic probing technique has a minimal effect on the evolution of the sample. Small differences between the yield points could also be explained by hysteresis that might be expected as the pressure is decreased then increased again.

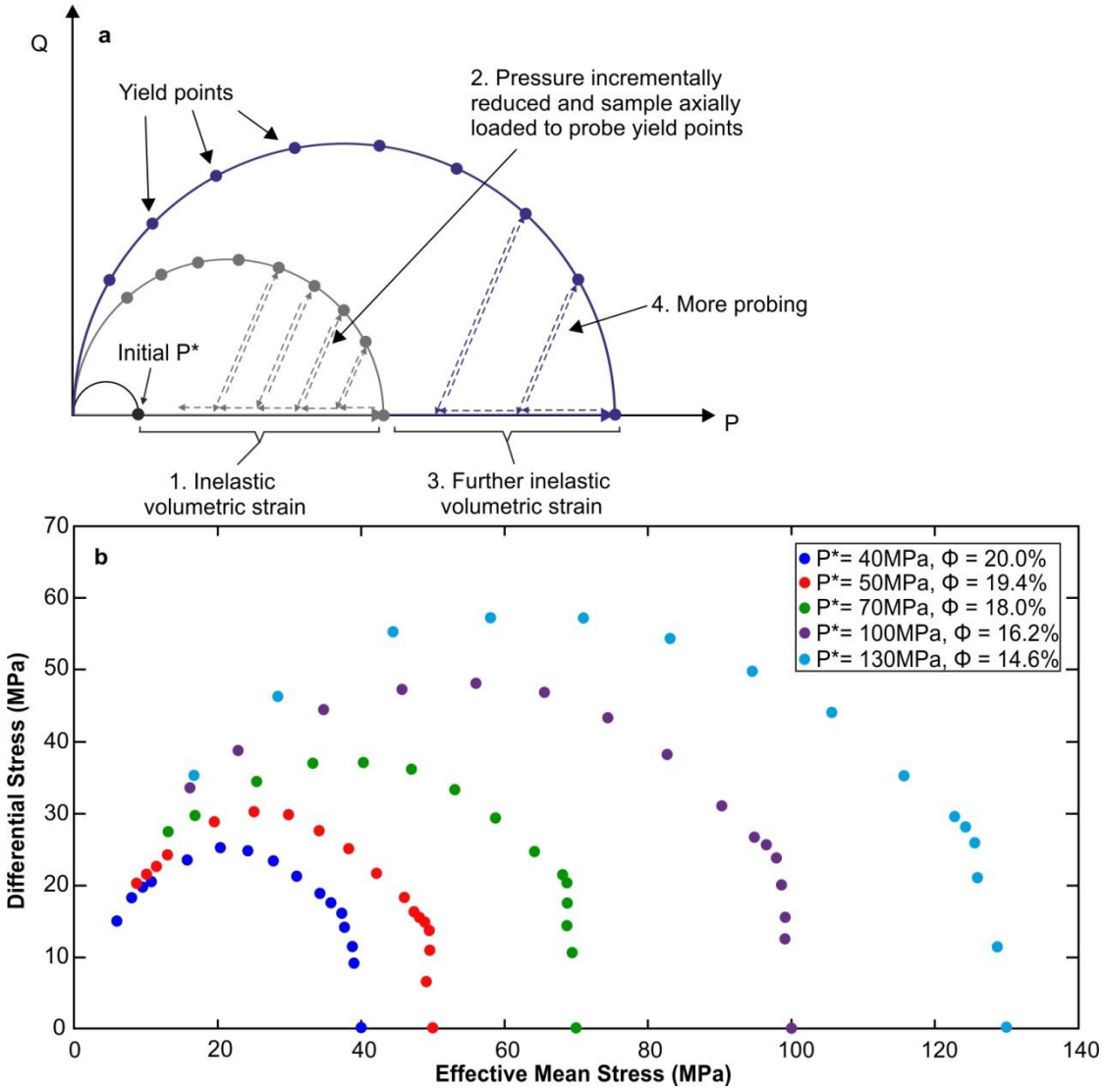


***Figure 4.5 - (a)*** *A schematic summary of the hydrostatic overconsolidation experimental technique. Samples are hydrostatically loaded beyond P* so that inelastic volumetric strain is accumulated and the sample is sat on a new yield curve. The pressure is then incrementally reduced, to move back inside this new curve and the sample subjected to elastic axial loading between each pressure reduction step. The axial load is applied until the deviation from linear elastic loading is observed upon which it is immediately removed. The probing of the yield curve at different pressures reveals its true shape. Once the yield curve is fully probed, the sample is further overconsolidated so that more inelastic volumetric strain is accumulated. The subsequent yield curve is then probed in the same way to determine if there is any shape evolution.* ***(b)*** *Results from the probing technique for a single bassanite sample. The data points reveal that the family of yield curves are partly comprised of the near-vertical limb on the high pressure side.*

On first inspection of the yield curves in figure 4.5b, the shape appears to be broadly elliptical. However the compactive side of the curve is not entirely smooth and consists partly of a near-vertical limb. To compare the shapes of different yield envelopes it is common to normalize curves by dividing them by their respective P* values (e.g. Wong et al., 1997a; Cuss et al., 2003b). If our yield curves do not evolve with increased volumetric strain it would be expected that they all would all plot directly on top of each other when normalized. Figure 4.6 is a plot normalized curves from the hydrostatic overconsolidation tests. It shows that the peak of the curve decreases with respect to P* the more the sample is compacted. This demonstrates that there is not one unique yield curve shape that represents all the yield curves for bassanite and that inelastic volumetric strain has an effect on the overall shape.

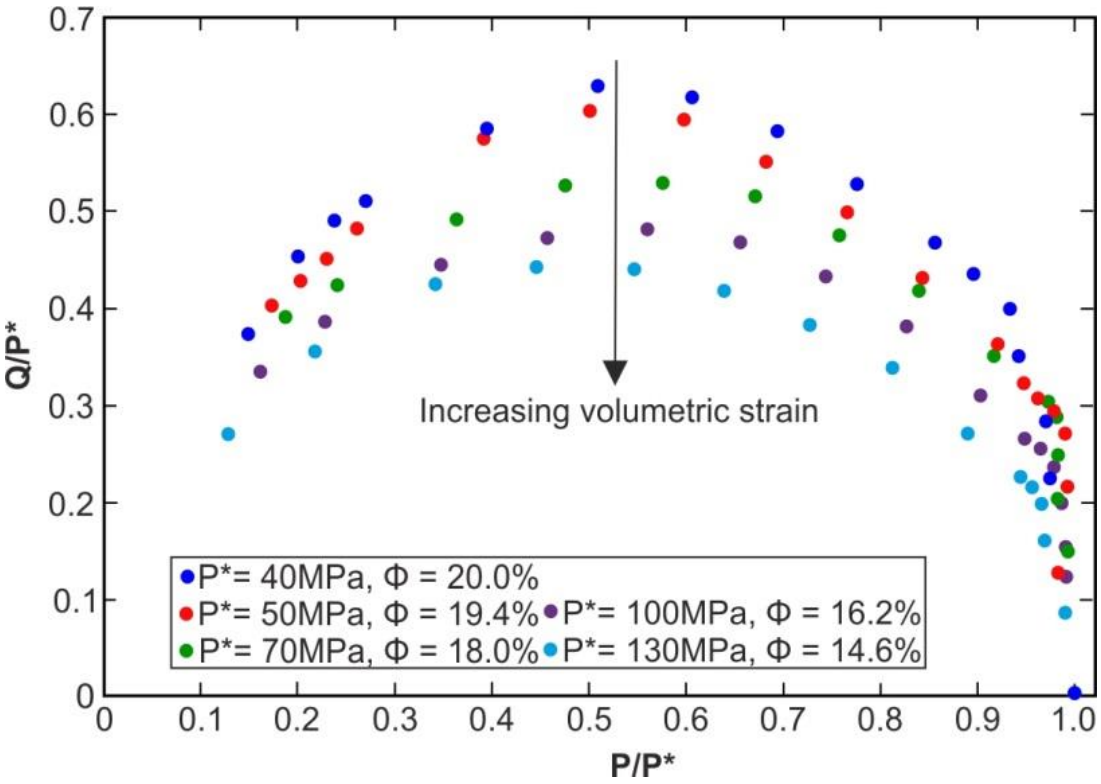


***Figure 4.6 -*** *Normalization of the yield curves from the hydrostatic overconsolidation tests by dividing each curve by its respective P* value. The peak of the curves decreases with respect to P* the more the sample is compacted and volumetric strain accumulated.*

### *4.3.2. Deviatoric Overconsolidation*

#### *4.3.2.1. Experimental procedure*

Tests were also performed to investigate the effect of inelastic deviatoric strain on the shape of the yield curve. The loading history for this type of test is summarized in figure 4.7a. These tests also involved initially loading the sample beyond P*, to an effective pressure of 50 MPa, so that the sample accumulated some inelastic volumetric strain and moved onto a new yield curve. The sample was then loaded axially (displacement rate = 0.5 μm/s) to induce some inelastic deviatoric strain. After a given increment of deviatoric loading, the load was removed and the confining pressure was either increased or decreased incrementally so that the yield curve could be probed. Once the yield curve had been probed the confining pressure was returned to 50 MPa, the value used for the initial axial loading, and the sample subjected to further deviatoric deformation along the same loading path. The loading was then stopped after another increment of inelastic strain had been accumulated and the yield curve was probed again. The sample was deformed along this loading path until 8% inelastic axial displacement was achieved. The shape of the yield curve was tested after every 2% increment of axial displacement along this loading path.

#### *4.3.2.2. Results*

The loading path and yield points from the deviatoric overconsolidation tests are displayed in figure 4.7b. There are less yield points on the compactive side of the yield curves in these tests as P* is not known. The confining pressure was therefore conservatively increased when probing the compactive side of the yield curve to ensure P* was not exceeded hence preventing any further inelastic strain from being accumulated. The obvious feature of these curves is that a near-horizontal ‘plateau’ appears to form on top of the yield curve the more inelastic strain is accumulated. The gradient of this plateau decreases and it flattens off the further along the loading path the sample is taken.

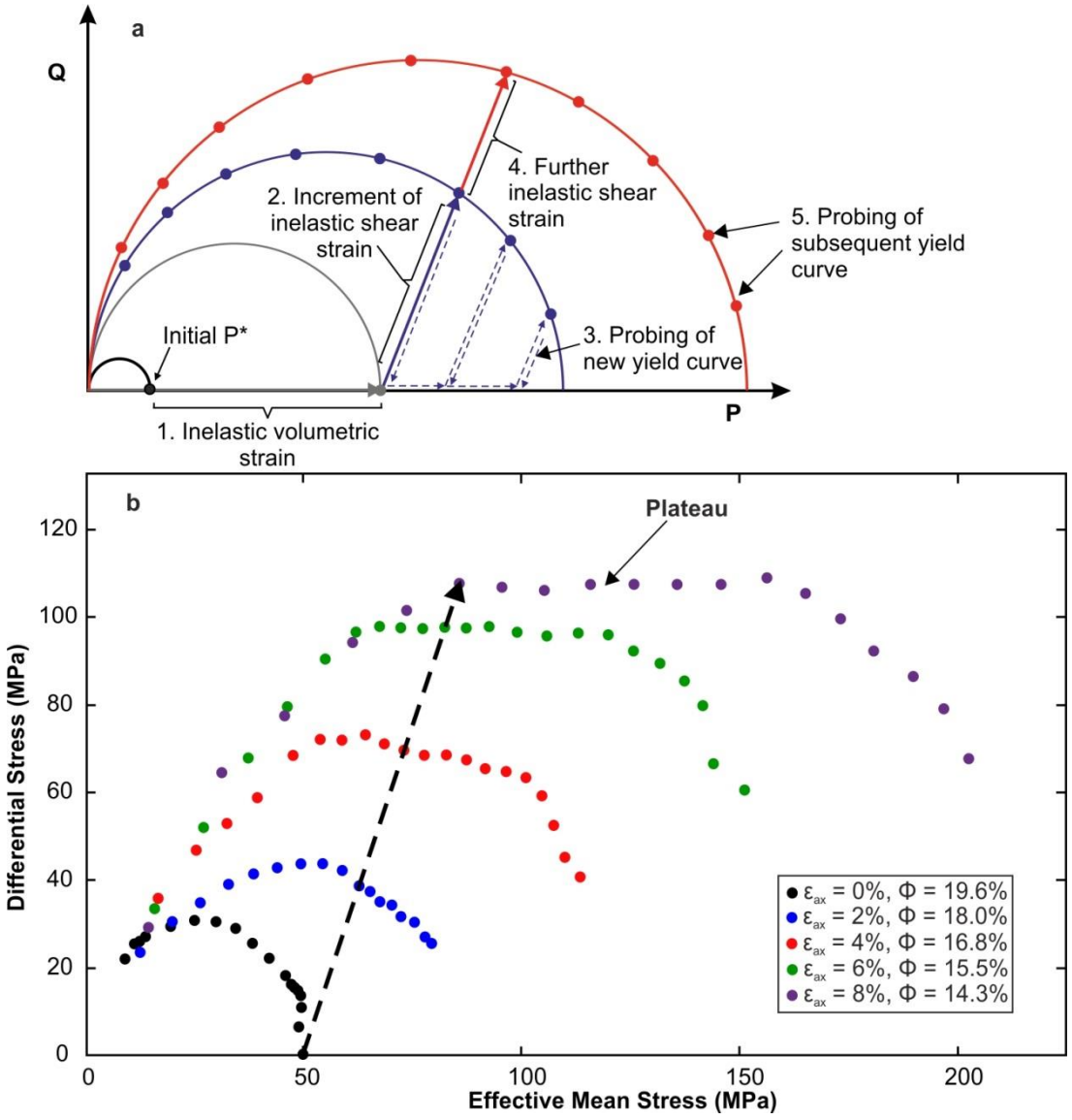


***Figure 4.7 - (a)*** *A schematic summary of the deviatoric overconsolidation experimental technique. Samples are hydrostatically loaded beyond P* and then subject to axial loading to accumulate an increment of inelastic shear strain. The load is then removed and the sample subject to axial probing at different confining pressures. Once the new yield curve has been probed, the sample is further deviatorically overconsolidated along the same loading path so that more inelastic shear strain is accumulated. The subsequent yield curve is then probed in the same way to monitor any shape evolution.* ***(b)*** *Results from the deviatoric overconsolidation tests on a single bassanite sample. The loading path is marked by the black dashed arrow and yield curve was probed every 2% increment of inelastic axial displacement. The data points reveal that the top of the yield curves starts to form a plateau the further along the loading path the sample is taken.*

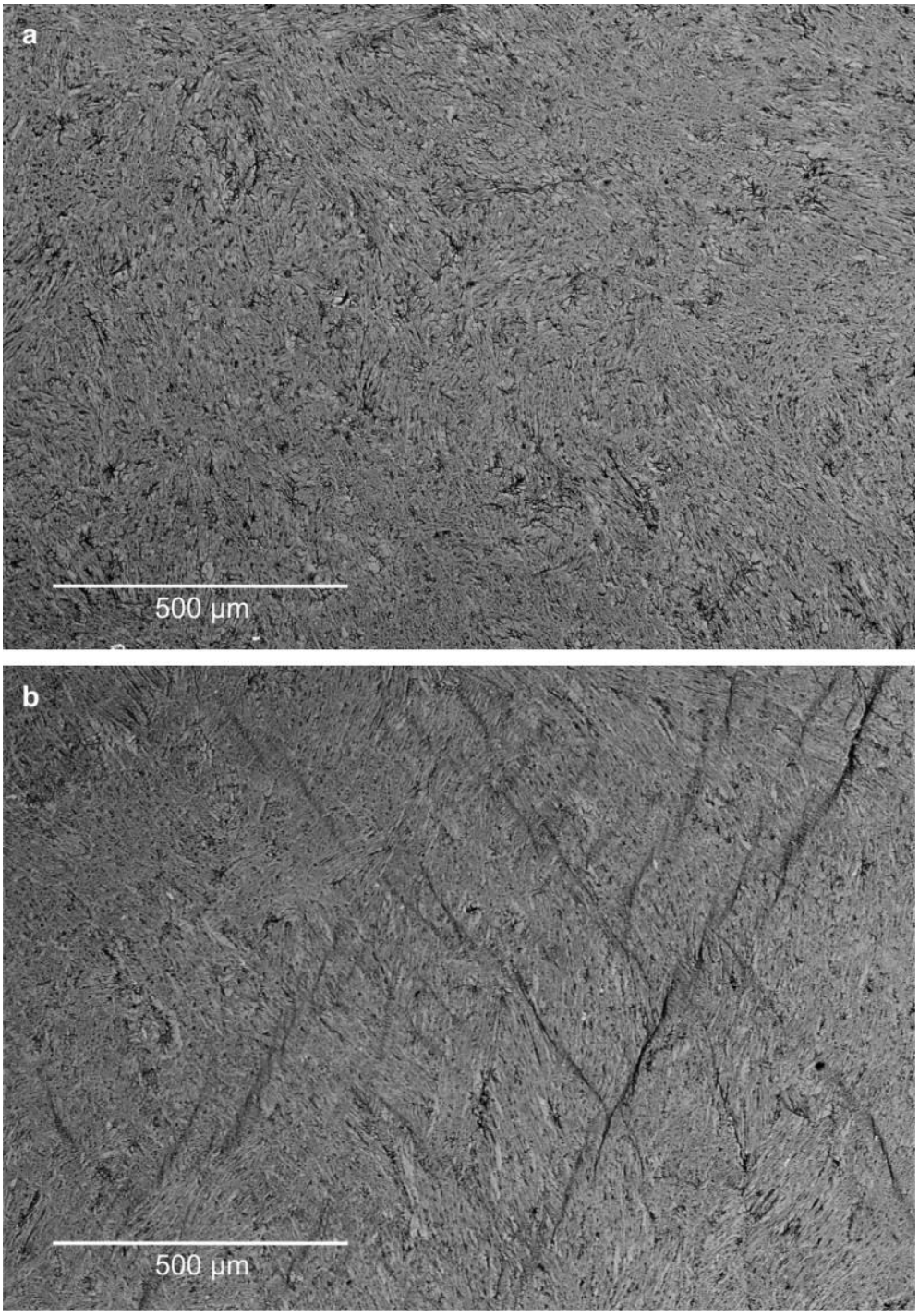


***Figure 4.8 -*** *Back-scatter electron images of deformed bassanite samples.* ***(a)*** *The sample from the hydrostatic overconsolidation experiment which has experienced purely volumetric strain. This sample has deformed by distributed compaction and no localized deformation is observed.* ***(b)*** *The sample from the deviatoric overconsolidation experiment which has been deformed with a component of inelastic shear strain. Deformation has localized onto many conjugate sets of shear bands.*

### *4.3.3. Microstructural analysis*

Figure 4.8 shows backscatter electron images of the hydrostatically and deviatorically overconsolidated samples. The hydrostatically overconsolidated sample appears to have experienced fairly homogeneous deformation. Localized features are not easily identified. The nature of the bassanite grains, which have a platy morphology when formed from the dehydration of gypsum at ambient conditions (Singh and Middendorf, 2007), makes it hard to identify if abundant grain crushing occurred during compaction. The predominant deformation mechanisms are probably a combination of grain rearrangement, grain crushing and pore collapse. The deviatorically overconsolidated sample did localize deformation onto a sample-scale shear band as the strain approached 8%. A backscatter image away from the main shear band (Fig. 4.8b) shows that there is also localized deformation in the body of the sample in the form of multiple conjugate sets of shear bands.

## 4.4. Discussion and implications

It is clear from the initial tests conducted that the critical-state line, in its traditional interpretation as the boundary between compactive and dilatant deformation, is not applicable. Rather, the data suggest that the transition occurs over a region and that within this region both compaction and dilation are occurring within the sample at the same time (e.g. Brace, 1978). Consequently, the subsequent yield curve evolution will be affected by the trade-off between these competing processes. This could potentially make it possible to have a bulk transition from compaction to dilation (shown by the hooks in Fig. 4.4) under stresses that would not be expected from the initial yield condition. Further evidence for this can be seen in the evolving yield curves of the hydrostatic and deviatoric overconsolidation tests which will be discussed below.

### *4.4.1. Yield curve shape and evolution*

Data from both the hydrostatic and deviatoric overconsolidation tests has shown that yield curves are not perfectly elliptical in shape. The hydrostatic overconsolidation experiments have revealed that the compactive side of the curve is

partly comprised of a steep limb. As this part of the curve is near-vertical it suggests that there is a region in P-Q space where yield is insensitive to differential stress. We term this region *shear-insensitive compaction* (Fig. 4.9a). In this region an amount of differential stress needs to be overcome before significant shear-enhanced compaction will occur. Similar steep limbs have also been reported in a study where sandstone samples were axially deformed as pore volume was held constant so that the stress path would traverse along the compactive side of the yield curve (Tembe et al., 2007). An upsurge of acoustic emission activity was recorded by Tembe et al., (2007) as the samples moved from the steep limb to the more traditional curved part of the yield curve which perhaps marks the onset of significant shear-enhanced compaction as we have suggested in this study.

The deviatoric overconsolidation tests have shown that the yield curve develops a plateau as the sample accumulates more inelastic strain. We term this near-horizontal portion of the yield curve *pressure-insensitive deformation* (Fig. 4.9b). In this region we expect that both compaction and dilational processes occur simultaneously and microstructural evidence for this will be discussed below in section 4.4.3. The concept of a critical state line, separating a region of dilation from compaction (Fig. 4.1c), could therefore instead be considered a "critical state zone". The notion of a critical state surface, rather than a line, has previously been suggested in the soil mechanics literature (Wood and Maeda, 2008). The formation of this zone is thought to occur as the grading and material properties of the soil change in response to particle crushing during deformation. Similar processes are in operation during porous rock deformation so it is seems reasonable that a critical state zone could also develop with continued pore collapse and grain crushing.

The shape of the yield curve evolves with inelastic strain in both sets of experiments. As discussed the accumulation of inelastic strain by deviatoric loading leads to the formation of a plateau. Normalization of the hydrostatic overconsolidation data has shown that inelastic volumetric strain also causes the yield curve shape to evolve (Fig. 4.6). It has previously been suggested that the peak of a yield curve scales with P* (Wong et al., 1997a; Cuss et al., 2003b) and that this relationship can be used to define a unique curve independent of rock type (Rutter and Glover, 2012). However the normalized data in figure 4.6 highlights that there is variation in the ratio of Q/P* for the same sample as it accumulates inelastic strain. Although this is not a like with like comparison, as the previous studies were considering the initial yield condition,

the data does suggest that caution should be taken when ascribing a universal yield curve to characterize general porous rock deformation. Particularly as the changing aspect ratio observed in figure 4.6 is likely a result of an evolving microstructure of the bassanite sample. There will undoubtedly be microstructural variations between different porous rocks types making it likely that this will also cause variations in the aspect ratios of the yield curves.

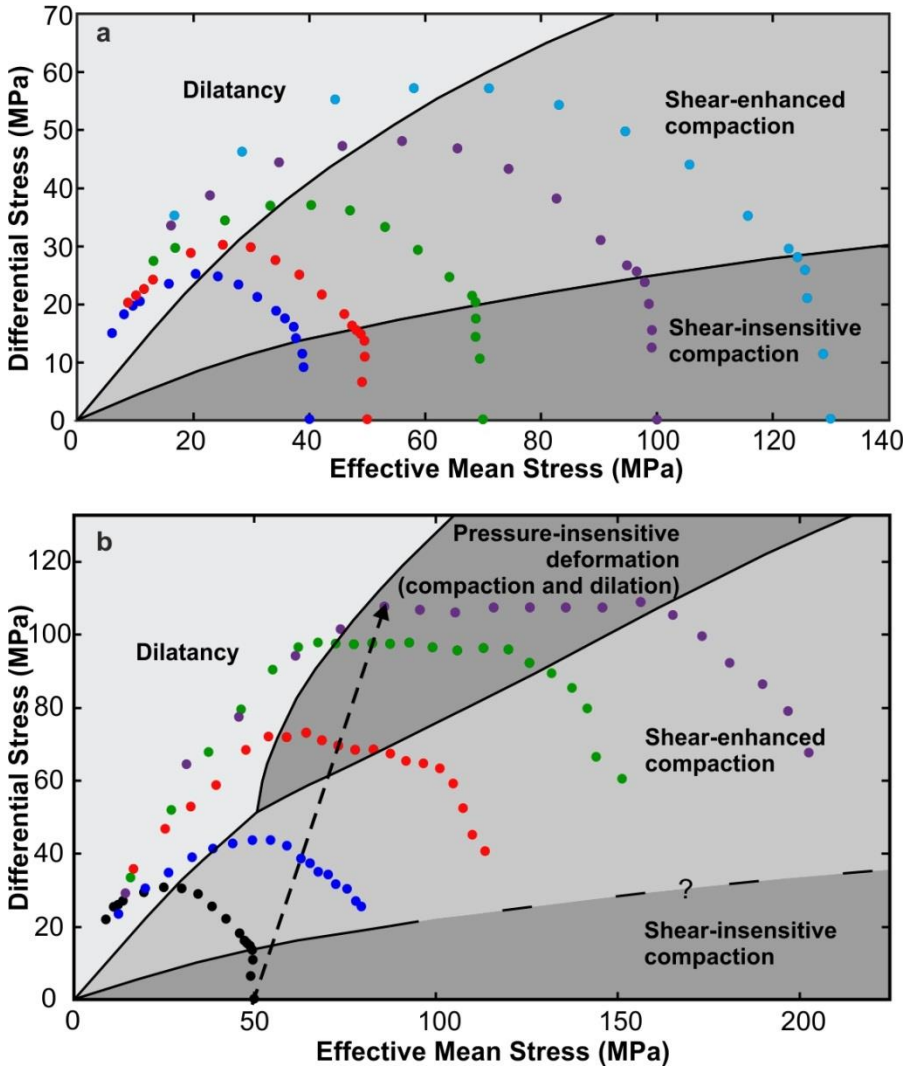


***Figure 4.9 -*** *Interpretation of the yield curves mapped in the hydrostatic and deviatoric overconsolidation experiments.* ***(a)*** *The curves from the hydrostatic overconsolidation tests are partly comprised of a near-vertical limb on the high-pressure side. We term this region shear-insensitive compaction.* ***(b)*** *The curves from the deviatoric overconsolidation tests show the appearance of a sub-horizontal plateau as the sample accumulates more inelastic shear strain. We term this a transitional region of pressure-insensitive deformation which is characterized by simultaneous compaction and dilation.*

The models of DiMaggio and Sandler (1971) and Carroll (1991) both use an evolving elliptical yield 'cap' to model the deformation of porous sandstone with inelastic volumetric strain. In both cases the cap is used to describe the ductile compactive yield in conjunction with a different surface to model brittle (dilational) shear failure. This differs from the critical state model (Schofield and Wroth, 1968) where the cap is part a single yield surface such as that in Figure 4.1b. Baud et al., (2006) have experimentally investigated the effects of inelastic volumetric strain on yield curve evolution for a range of sandstones. They found that the compactive side of the yield curve does evolve as a function of inelastic volumetric strain and that some sandstones appear to fit the DiMaggio and Sandler (1971) model whereas others are better approximated by the Carroll (1991) model. However the data points collected by Baud et al., (2006) use many different samples from the same rock. This produces inevitable data scatter as a result of sample variability which may hide subtleties in the true shape of the curve, such as a steep limb and a region of shear-insensitive compaction. Although the aspect ratios of the yield curves in the hydrostatic overconsolidation experiments of this study do change, neither model would fit particularly well with our data as it does not appear necessary to use different surfaces to model the brittle and ductile parts of the yield curve. Rather, it would be more appropriate to use one curve to describe the regions of dilation and shear-enhanced compaction in conjunction with another curve to describe a region of shear-insensitive compaction.

The study of Baud et al., (2006) aside, there is a lack of previous experimental data on the effects of inelastic shear strain on yield curve evolution. Grueschow and Rudnicki (2005) incorporate the effects of inelastic shear strain into their constitutive model, which also considers the effects of inelastic volumetric strain. In this model, inelastic shear strain should cause the peak of the yield curve to expand relative to hydrostatic yield point (P*). The combination of hydrostatic overconsolidation and deviatoric overconsolidation tests in this study provides, for the first time, the opportunity to analyse yield curve evolution and compare the effects of purely inelastic volumetric strain (i.e. hydrostatic overconsolidation) against loading with a component of inelastic shear strain (i.e. deviatoric overconsolidation).

### *4.4.2. Effect of hydrostatic vs deviatoric strain*

As the P* for the deviatoric overconsolidation yield curves (Fig. 4.7b) is not known we cannot normalize the data in the same way as for the hydrostatic overconsolidation tests (Fig. 4.6). However we can compare curves of similar porosity from the different sets of tests to look at the how the peaks compare. Figure 4.10a compares the hydrostatically overconsolidated sample at a P* of 70 MPa to the deviatorically overconsolidated sample with an axial strain of 2%. Both these samples have been inelastically compacted to a porosity of 18.0% so should provide a direct comparison between the effects of inelastic hydrostatic vs deviatoric strain. There is a small difference between the curves with the peak of the deviatorically overconsolidated sample being slightly higher (~5 MPa). However the difference is minimal and could easily be a result of sample variability. Figure 4.10b compares the hydrostatically overconsolidated sample at a P* of 130 MPa with the deviatorically overconsolidated sample to an axial strain of 8%. These samples have similar porosities of 14.6% and 14.3% respectively, so again should provide a useful comparison between the effects of inelastic hydrostatic vs deviatoric strain. In this case, ignoring the change in yield curve shape and appearance of a plateau, the peak of the deviatorically overconsolidated sample is almost double that of the hydrostatically overconsolidated sample. This indicates that there is a drastic effect of inelastic shear strain and anisotropic loading on the evolution of the yield curve, as predicted by Grueschow and Rudnicki (2005).

The evolution observed under deviatoric loading can also help explain the peculiarities observed in the initial set of experiments where the CSL appears to overlie the NCL (Fig. 4.4). Figure 4.10b shows the plateau that has developed during deviatoric loading sitting directly above the P* of the hydrostatically loaded sample. This is exactly the same phenomenon as that seen in figure 4.4 if the CSL is now considered to be a critical state zone rather than a line. However in reality the P* of the deviatorically overconsolidated sample has also evolved as the yield curve had expanded. Therefore the NCL will migrate as the sample is subject to deviatoric loading, as is schematically shown in figure 4.10c. Thus the peculiarities of figure 4.4 are predominantly a result of yield curve evolution in response to inelastic shear strain.

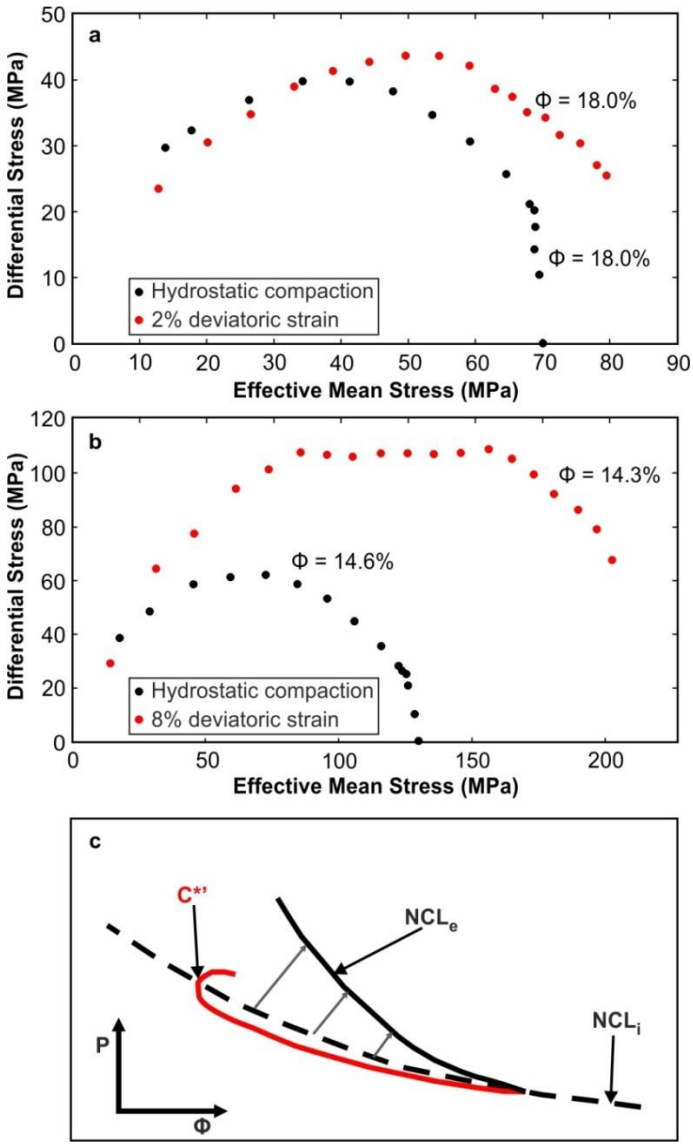


***Figure 4.10*** *- Comparison of similar porosity yield curves deformed by hydrostatic overconsolidation vs deviatoric overconsolidation.* ***(a)*** *The red curve has experienced 2% inelastic deviatoric strain whereas the black curve has been deformed by hydrostatic compaction. There is a small difference between the curves although this could be as a result of sample variability.* ***(b)*** *The red curve has experienced 8% inelastic deviatoric strain and the black curve has been deformed by purely hydrostatic compaction. There is a large difference in the yield curve size with the deviatorically overconsolidated curve having a peak which is almost double that of the hydrostatically compacted sample.* ***(c)*** *Schematic diagram to show the evolution of the NCL during deviatoric loading. The hooks (C*') in the loading curve (red) overlie the initial normal consolidation line ($NCL_i$) as seen in figure 4.4. However in reality the normal consolidation line evolves ($NCL_e$) as the yield curve expands during deviatoric loading.*

As well as a marked difference in the relative sizes of the yield cures between the hydrostatically and deviatorically consolidated samples, there is also a significant difference in the microstructural evolution. The accumulation of purely volumetric strain leads to homogenous compaction (Fig. 4.8a); whereas the development of conjugate shear bands as a result of deviatoric loading produces a significant heterogeneity in the microstructure. Although the complex nature of the pore network is difficult to quantify for this material, a recent study has shown that significant strength anisotropy can be produced by different pore geometries (Bubeck et al., 2017). The importance of other microstructural parameters such as the orientation of intergranular grain contacts has also been shown to produce mechanical anisotropy in porous rock (Louis et al., 2009). Another study into the compaction behaviour of porous andesite has attributed the duality of porosity (i.e. cracks and pores) to explain the unusually linear shaped yield envelopes that were observed (Heap et al., 2015). Therefore microstructure and pore geometry is of upmost importance in determining the mechanical response of a porous rock and if this evolves significantly during accumulation of inelastic shear strain, as in our experiments, this could produce a considerable change in the shape of the yield curve. Models for porous rock deformation typically consider porosity as the only microstructural parameter, however it appears that a much more comprehensive understanding pore and grain geometry is required to understand fully the nature of yield and subsequent strength evolution.

### *4.4.3. Potential implications for localization*

By definition a yield curve should only identify the positions in stress space where a rock will begin to undergo permanent plastic deformation. However the majority of plasticity models also specify the nature of inelastic deformation after yield has occurred. The models of Schofield and Wroth (1968), DiMaggio and Sandler (1971) and Carroll (1991) all state that the inelastic strain should be dilatational on the low pressure side of the yield surface and compactive on the high pressure side; as simply displayed in figure 4.1b. This is based on the assumption of an *associated flow* law (often referred to as the *normality* condition). At a given position in stress space where yielding will occur, the accompanying plastic strain will be comprised by some inelastic volumetric strain $\delta\varepsilon^{p}$ and some inelastic shear strain $\delta\varepsilon^{q}$ (Wood, 1991). The

magnitudes of these components can be drawn parallel to the P and Q axes respectively to define a *strain increment vector* (Fig. 4.11a). Vectors can be defined at all positions in P-Q space where yield occurs. Orthogonal lines can then be drawn at the base of each vector and joined to define a surface called the *plastic potential surface* (Hobbs et al., 1990). Associated flow requires that the yield curve and plastic potential surface are coincident such that the strain increment vector is always perpendicular to the yield surface (Fig. 4.11b). This means that on the low pressure side of the yield curve the component of inelastic volumetric strain is negative (i.e. dilation) whereas on the high pressure side it is positive (i.e. compaction). Despite its simplicity, experimental results have shown that associated flow is not always applicable and the mode of deformation does not always coincide with the yield curve. For example studies have shown that shear-enhanced compaction can occur on the low pressure side of the yield curve where the gradient is positive and typically associated with dilation (Wong et al., 2001; Baud et al., 2006). However the greatest disadvantage in associated flow appears to be in its ability to predict localization of deformation. In associated flow, localization should only occur in conditions of strain softening (Hobbs et al., 1990) which typically accompanies dilation. However localized deformation has been found under high pressure conditions, which should suppress instabilities and promote distributed deformation, in studies of both porous (Hirth and Tullis, 1989; Zhang et al., 1990a; Wong et al., 1992) and crystalline rock (Byerlee and Brace, 1969). It has therefore been suggested that the deformation of porous rock would be better approximated by a *non-associated flow* law (or non-normality), to describe the conditions where homogeneous deformation is able to bifurcate and form localized bands, with homogeneous deformation continuing outside the band (e.g. Rudnicki and Rice, 1975). Non-associated flow occurs where the yield curve and the plastic potential surface do not coincide so that the strain increment vector is no longer orthogonal to the yield curve (Fig. 4.11c). For a model that allows non-associated flow it is necessary that it involves a plastic potential function with additional constitutive parameters that are separate to the yield condition. Separating the mode of plastic strain from the yield condition therefore allows scenarios where localized deformation can occur under conditions where distributed shear-enhanced compaction would typically be expected.

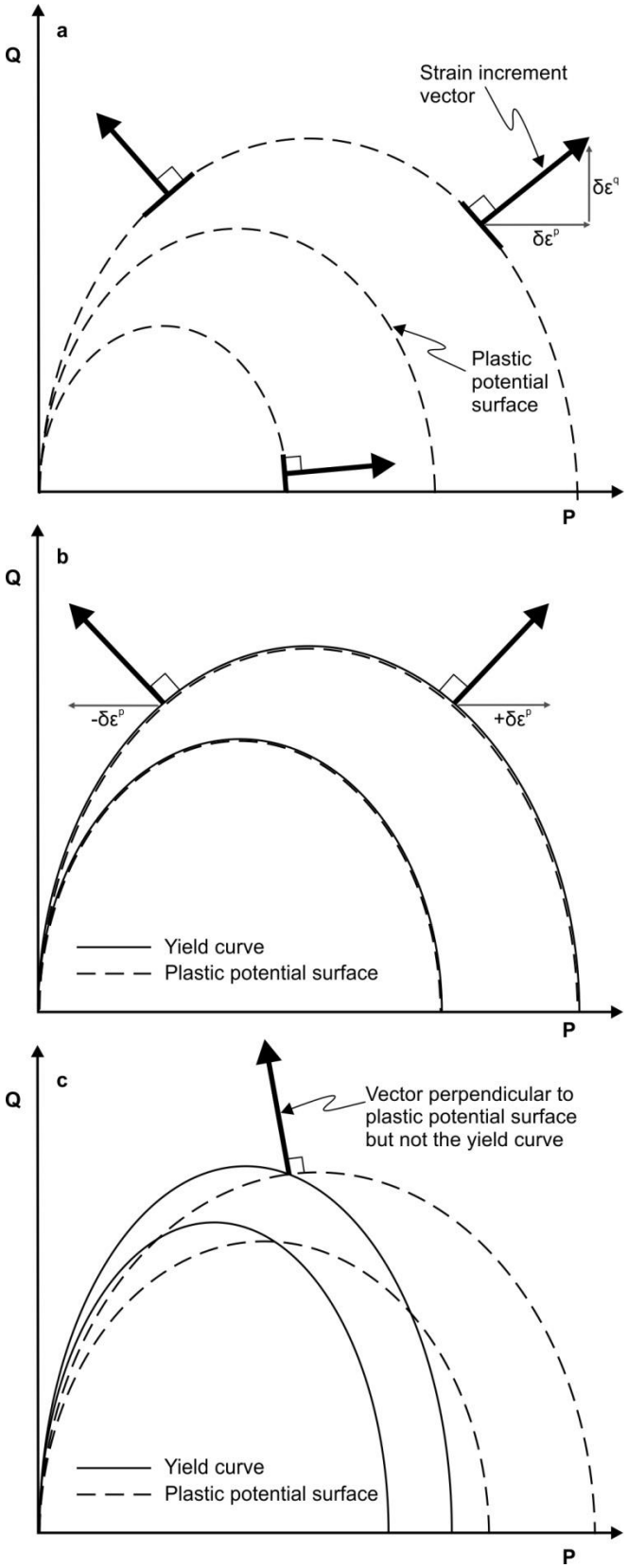


***Figure 4.11 - (a)*** *Strain increment vectors can be defined for every point in stress space where plastic deformation will occur. Each vector is comprised of some inelastic volumetric strain ($\delta\varepsilon^p$) and some inelastic shear strain ($\delta\varepsilon^q$). An orthogonal line can be drawn at the base of each vector and these can be joined to form families of plastic potential surfaces.* ***(b)*** *A schematic example of associated flow where the yield curve and the plastic potential surfaces coincide such that the strain increment vector is always perpendicular to the yield curve.* ***(c)*** *A schematic example of non-associated flow where the yield curves and plastic potential surfaces do not coincide. The strain increment vector is therefore no longer perpendicular to the yield curve, allowing for conditions where dilational deformation can occur on the high pressure side of the yield curve.*

Although non-associated flow provides a framework to explain the occurrence of localization, these constitutive models are not without limitation. There are many

different types of localized features that can occur in porous rocks including shear (Mair et al., 2000), dilational (Du Bernard et al., 2002) and compaction bands (Mollema and Antonellini, 1996; Olsson and Holcomb, 2000). A theoretical predication of the type of localized feature is provided by Issen and Rudnicki (2000) based on the plastic constitutive parameters of Rudnicki and Rice (1975). However significant discrepancies are found between theoretical predictions and the observed mode of localization in experiment (Wong et al., 2001; Baud et al., 2006). This is attributed to the constitutive model, which is based on non-associated flow, not being able to capture the different damage mechanisms in operation during porous rock deformation. The complex interplay between pore collapse, grain crushing and the growth of microcracks will probably be strongly influenced by the local microstructure such as pore geometry and the nature of grain contacts. The microstructural properties of the rock will in turn affect its localization behaviour. For example it has been previously shown that compaction band formation is highly sensitive to grain size distribution (Cheung et al., 2012).

In our initial experiments to test the critical state model (Fig. 4.3), we observed strain localization and a switch from compaction to dilation in the experiments at the lowest effective pressures of 10, 30 and 50 MPa. This manifested itself as sample-scale shear band with many sets of conjugate shear bands being found in the bulk of the sample away from the main localized feature (Fig. 4.12a). However in the tests at the highest effective pressures (70 and 90 MPa) the mechanical data suggest that the samples only experienced homogeneous shear-enhanced compaction. Even in these samples, less well developed localized shear bands begun to form (Fig 4.12b). In section 4.4.1 we hypothesized that as a sample accumulates inelastic deviatoric strain, a region of pressure-insensitive deformation develops where both compaction and dilation can occur together (Fig. 4.9b). The mechanical data from the high-pressure tests in figure 4.3 suggest homogeneous compaction is occurring, whereas the microstructures display evidence for dilation in the form of high-angle shear fractures (Fig. 4.12b). Perhaps the yield curves of these samples have evolved in a way similar to figure 4.9b and a transition zone has formed at the peak of the curve allowing both compaction and dilation to occur simultaneously in different parts of the sample. This could also explain how localization might be initiated under conditions where it would not typically be expected, potentially without needing to invoke a non-associated flow law. It has been suggested in previous work that compaction bands also form at the

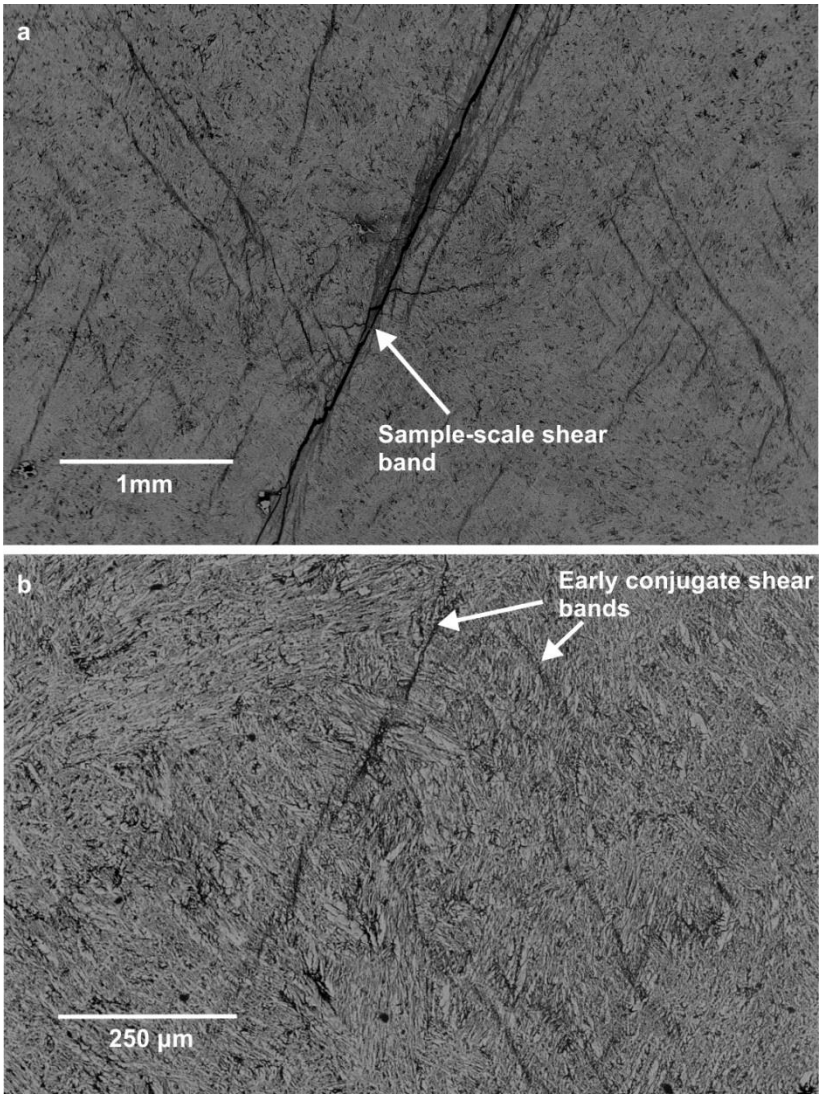


***Figure 4.12 -*** *Back scatter electron images of samples used to initially test the critical state model for porous bassanite (section 4.2).* ***(a)*** *Sample deformed at an effective pressure of 10 MPa. Mechanical data for this sample indicates a switch from compaction to dilation during its loading history (Fig. 4.3b). Deformation localized onto sample-scale shear band and there are also many sets of high-angle conjugate away from this main feature in the bulk of the sample.* ***(b)*** *Sample deformed at an effective mean stress of 90 MPa. Mechanical data shows that bulk response of the sample is strain hardening and compaction. However the microstructure reveals evidence of the early stages of localization in the form of conjugate shear bands.*

transition region between brittle and ductile deformation in porous rock (Wong et al., 2001). The yield curve evolution in response to inelastic shear strain could therefore be influential in the localization behaviour of the rock. It would also be important if non-associated flow is invoked, as the constitutive internal friction parameter, $\mu$, of Rudnicki and Rice (1975) is determined in experiments from the slope of the yield curve in P-Q space which evolves as inelastic shear strain is accumulated (Fig. 4.7b). However, irrespective of whether an associated or non-associated flow law is most applicable, it is apparent that the evolution of the microstructure in response to different inelastic loading histories strongly controls the strength properties and subsequent deformation of the rock.

## 4.5. Conclusions

A series of deformation experiments were performed on porous bassanite to investigate the shape and evolution its yield curve. The curve was found to not be perfectly elliptical in shape as often assumed by critical state soil mechanics. Rather, the high pressure compactive side of the curve is partly comprised of near vertical limb which implies there is a region in P-Q space where the deformation is insensitive to shear stress.

The yield curve shape evolves in response to both inelastic volumetric strain and inelastic shear strain. Samples of the same porosity but with different deformation histories show significant differences in strength. Those that have experienced anisotropic loading with a large component of inelastic shear strain have a yield curve with a peak that is considerably higher than those that have deformed under hydrostatic conditions and accumulated purely volumetric strain. This is a result of a drastic change in the microstructure as the sample begins to localize deformation and form many sets of conjugate shear bands in response to inelastic shear strain. A region that we term pressure-insensitive compaction forms at the peak of the yield curve as the sample deforms along the typical stress trajectory of an axisymmetric compression test. In this region separating the brittle and ductile parts of the yield curve, both compactive and dilational processes occur together which could help explain previously reported occurrences of localized deformation under conditions which would typically be associated with distributed shear-enhanced compaction. An

evolving yield curve is also important to understand for any future models that allow non-associated flow as this can have implications for the constitutive parameters that describe the plastic deformation. Future studies should consider the effects of inelastic shear strain on the evolution of yield curves for a range of porous rocks. It is also important to try and constrain what microstructural parameters control the shape and evolution of yield curves and the implications of this for the onset of localized deformation.

## 4.6. Supplementary figures

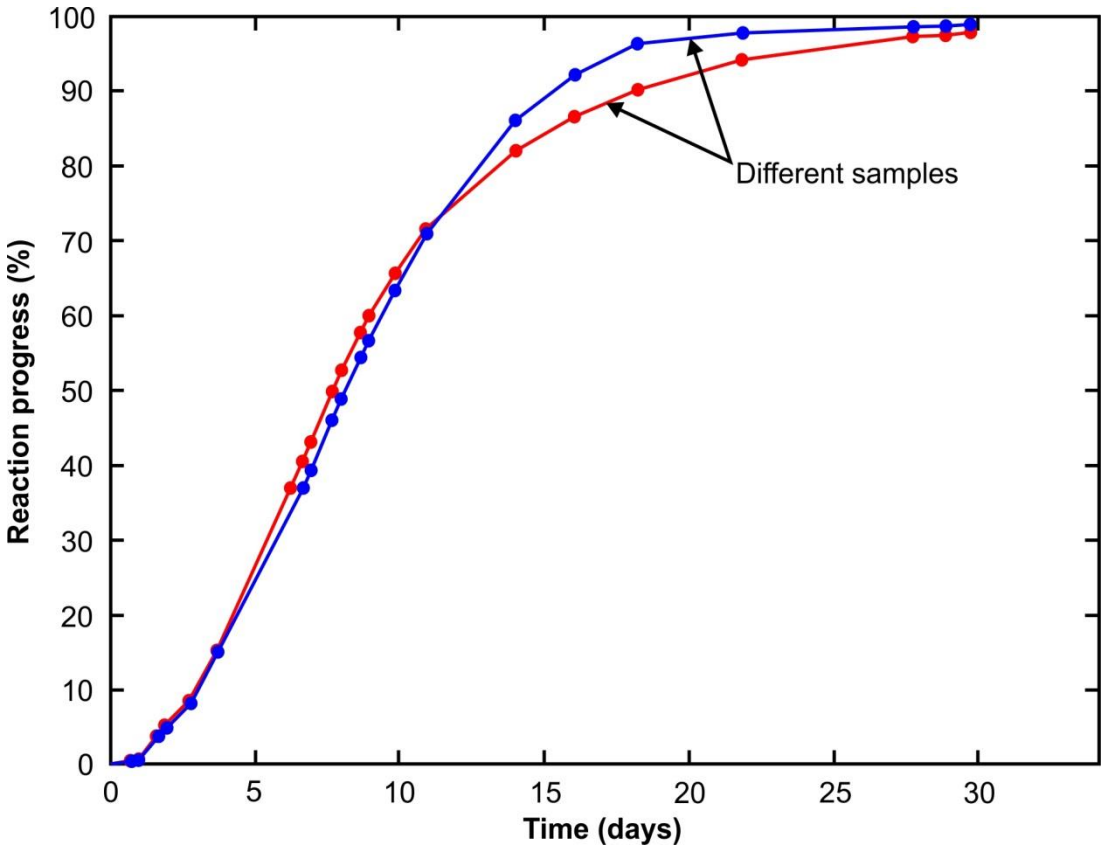


**Supplementary Figure 4.1 -** Gypsum dehydration progress versus time. The reaction progress was calculated by monitoring the weight loss of the gypsum cores. After approximately 30 days the gypsum had undergone complete dehydration to form bassanite.

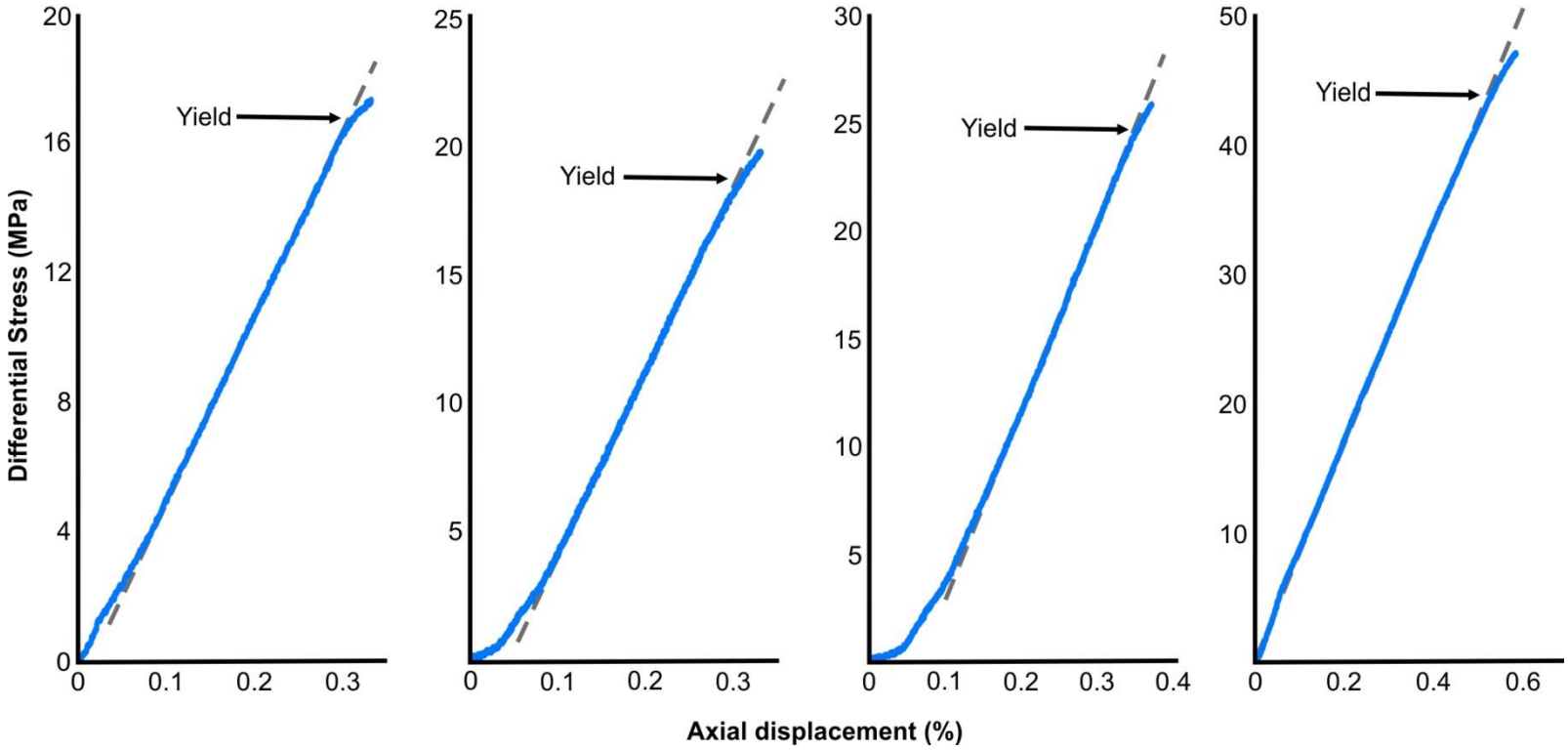


**Supplementary Figure 4.2** - Examples of the loading curves from the stress-probing technique. Yield can be identified by the deviation from linear elastic loading marked by the dashed lines. As soon as yield is identified the load is removed to ensure no permanent deformation is accumulated.

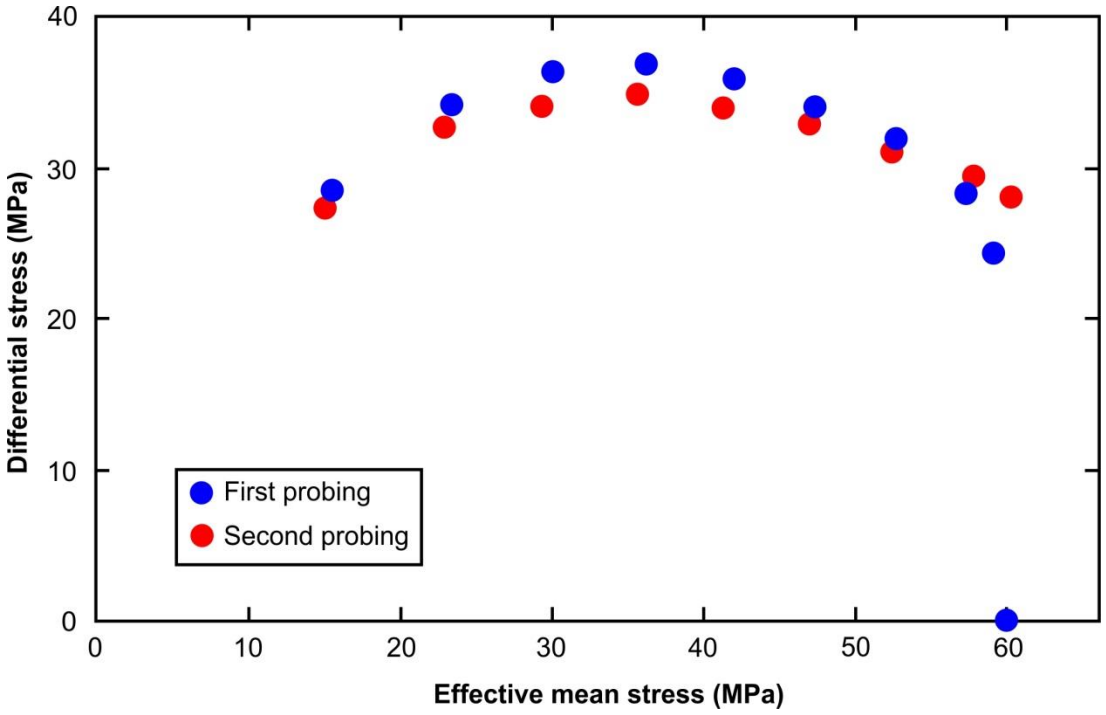


**Supplementary Figure 4.3 -** To ensure the elastic loading history and incremental yield does not impose any permanent deformation on the sample, preliminary tests were performed where the yield points were re-examined. In this test the sample was probed, as normal, as the confining pressure was incrementally reduced (blue). The sample was then re-probed (red) as the confining pressure was increased back towards P*. The difference between the two sets of yield points is small suggesting the loading history has minimal effect on the evolution of the sample.

# 5. High-resolution mapping of yield curve shape and evolution for two high porosity sandstones


## Abstract

The onset of permanent inelastic deformation for porous rock is typically defined by a yield curve plotted in P-Q space, where P is the effective mean stress and Q is the differential stress. Sandstones usually have broadly elliptical shaped yield curves, with the low pressure side of the ellipse associated with localized brittle faulting (dilation) and the high pressure side with distributed ductile deformation (compaction). However recent works have shown that these curves might not be perfectly elliptical and that there is significant evolution in shape with continued deformation. We therefore use a stress-probing methodology to map in high resolution the yield curve shape for Boise and Idaho Gray sandstones and also investigate curve evolution with increasing deformation. The data reveal yield curves with a much flatter geometry than previously recorded for porous sandstone and that the compactive side of the curve is partly comprised of a near vertical limb. The yield curve evolution is found to be strongly dependent on the nature of inelastic strain. Samples that were compacted under a deviatoric load, with a component of inelastic shear strain, were found to have yield curves with peaks that are approximately 50% higher than similar porosity samples that were hydrostatically compacted (i.e. purely volumetric strain). Increased shear strain also leads to the formation of a plateau at the peak of the yield curve as samples deform along the deviatoric loading path. These results have important implications for understanding how the strength of porous rock evolves along different stress paths, including during fluid extraction from hydrocarbon reservoirs where the stress state is rarely isotropic.


## 5.1. Introduction

There is widespread interest in the cause of porosity loss from sandstones and siliciclastic sediments, primarily because of the impact on fluid flow and permeability reduction in hydrocarbon reservoirs. During burial, sandstones predominantly lose

their primary porosity by mechanical and/or chemical compaction. Although chemical compaction, particularly through pressure solution and cementation, may significantly reduce fluid flow in deep reservoirs, the initial stages of burial are typically dominated by mechanical processes such as grain rearrangement, grain crushing, pore collapse and localized faulting. Understanding the nature of porous rock deformation is important for both natural and geotechnical problems including faulting and deformation band formation (Aydin and Johnson, 1978; Antonellini et al., 1994; Griffiths et al., 2016), borehole stability (Cuss et al., 2003a; Dresen et al., 2010) and reservoir subsidence and compaction (Fisher et al., 1999; Nagel, 2001; Makowitz and Milliken, 2003).

The mechanical response of a porous rock or sediment to a compressive load can be broadly separated into two regimes. At low effective pressures, inelastic deformation is associated with dilatancy and localized faulting. Under higher effective pressures the deformation transitions into a regime of cataclastic flow and distributed compaction. This transition from localized to distributed deformation is often referred to as the low temperature brittle to ductile transition (e.g. Rutter and Hadizadeh, 1991; Wong and Baud, 2012). Numerous laboratory studies have investigated these different modes of deformation in porous rock and attempted to map their occurrence in stress space. This is typically done by plotting a yield curve in P-Q space, where P is the effective mean stress $\left(P = \frac{\sigma_1 + \sigma_2 + \sigma_3}{3} - P_f\right)$ and Q is either the differential stress ($Q = \sigma_1 - \sigma_3$) or the deviatoric stress ($Q = \sigma_1 - P$). The yield curve separates regions of elastic deformation (i.e. recoverable) from regions of plastic deformation (i.e. inelastic/permanent). It should be noted that the term plastic is used in the mechanical sense and does not imply an underlying deformation mechanism. A family of subsequent yield curves can also be defined for the rock as porosity changes during the accumulation of permanent inelastic strain (Fig. 5.1). Hence, as yield curves are used to predict the conditions under which a porous rock will permanently deform, an understanding of the precise nature of the curve and it evolution are of key importance.

Traditionally yield curves have been mapped by performing a suite of axisymmetric compression tests where multiple samples of a given rock type are axially loaded under different effective pressures. This has been done on a variety of different porous rocks including sandstone (Wong et al., 1997a; Baud et al., 2000b; Cuss et al., 2003b; Baud et al., 2004; Baud et al., 2006; Louis et al., 2009), limestone

(Baud et al., 2000a; Vajdova et al., 2004; Baud et al., 2009; Cilona et al., 2014), volcanic rocks (Zhu et al., 2011) and dehydrated serpentinite (Rutter et al., 2009). These tests have revealed that most yield curves have a broadly elliptical shape with the low pressure side of the curve associated with dilatancy and the high pressure side with compaction (Fig. 5.1a). As yield of porous rock can be achieved under purely hydrostatic stress, the yield curve intersects the P-axis at the pressure where hydrostatic yield occurs. This point is commonly referred to as P* and marks the onset of pore collapse and grain crushing (Zhang et al., 1990b). These yield curves have many similarities with those that have been mapped for unconsolidated sediments and many of the concepts of porous rock deformation are based on the principles of critical state soil mechanics (e.g. Schofield and Wroth, 1968; Wood, 1991).

Traditional investigations, using axisymmetric compression tests, have provided many insights in to the general shape of yield curves and the nature of deformation in porous rock. However the use of multiple samples produces inevitable data scatter, which can be substantial, making it difficult to constrain the true shape of the curve. More recently, new methodologies have been developed to try and map precisely yield curves of single samples. Tembe et al., (2007) performed a series of modified undrained tests on two sandstones to map the compactive side of their yield curves. As a sample was axially loaded, they held the pore volume constant by adjusting the confining pressure to compensate for changes in volume during loading. Assuming negligible inelastic strain, the stress path in P-Q space should therefore trace out the compactive side of the yield curve starting from P*. The results of Tembe et al., (2007) reveal the part of yield curve near to P* is steeper than would be expected for a smooth elliptical curve. They also record an upsurge of acoustic emissions, which they interpret as the onset of significant inelastic strain, as the sample transitions from the near vertical limb to the more traditional curved part of the yield curve. Bedford et al., (in review) have also attempted to map in high resolution the yield curve of a single sample by performing a series of stress probing overconsolidation experiments. They use porous bassanite, a material formed by the dehydration of gypsum, and compact it beyond its yield point so that the sample sits on a new yield curve. The pressure is then incrementally reduced to return the sample to the elastic regime and the sample is axially loaded over a range of effective pressures to probe the yield curve at different stress states. From this probing technique they also find that the compactive side of the yield curve is comprised partly of a steep near-vertical limb. The results of Tembe

et al., (2007) and Bedford et al., (in review) suggest that the traditional concept of elliptical yield curves is an oversimplification which requires modification to incorporate a steep compactive limb (Fig. 5.1a). Bedford et al., (in review) term this a region of "shear-insensitive compaction" as the near vertical part of the curve implies that yield is almost independent of differential stress in this region.

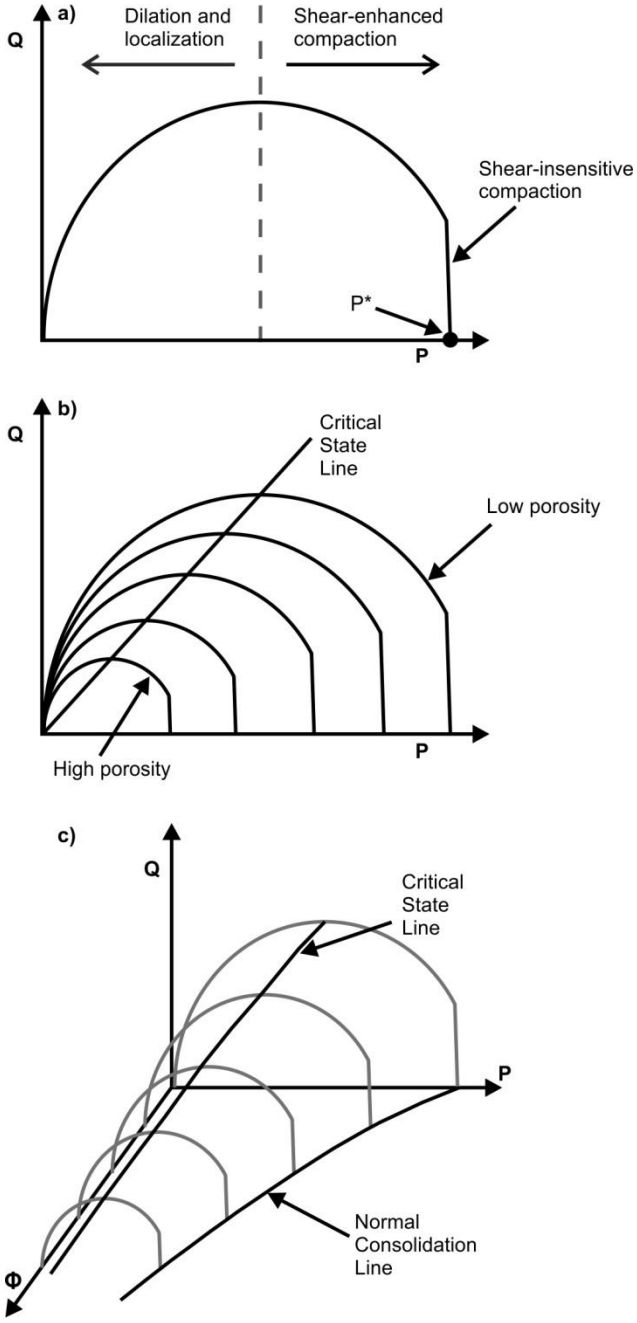


***Figure 5.1*** *- A schematic illustration of yield curves plotted in P-Q space.* ***a)*** *Yield curves for porous sandstone are broadly elliptical in shape with the low pressure side associated with dilatancy and the high pressure side with compaction. The point where the curve intersects the effective mean stress axis is referred to as P*. Recent works have shown that region of the yield curve in the vicinity of P* is near-vertical and associated with shear-insensitive compaction.* ***b)*** *A family of yield curves can be defined for different porosities. The peak of these curves is joined by the critical state line (CSL) to separate the regions of dilation from compaction.* ***c)*** *A 3D representation of the yield envelope where the third axis is porosity (Φ). The yield curves space out along the porosity axis and their respective P* points are joined by the normal consolidation line (NCL).*

As well as a yield function, that identifies the stress conditions at which the onset of inelastic strain will occur, a comprehensive description of porous rock deformation also requires a work hardening rule which describes how the yield function changes as inelastic strain is accumulated (Paterson and Wong, 2005). During deformation, the porosity will either increase or decrease as a result of compaction or dilation. This will cause the yield curve to either expand or contract. A family of yield curves can therefore be defined to represent all the subsequent changes in porosity (Fig. 5.1b). Traditionally the crests of these curves are joined by the critical state line (CSL) which separates regions of dilation from compaction. The family of curves can also be visualized in 3D where the third axis is porosity (or porosity multiplied by the grain size) and the yield curves space out along this axis (Fig. 5.1c). The respective P* values of the different yield curves can then be joined by the normal consolidation line (NCL). In the theory of critical state soil mechanics, isotropic hardening is assumed which produces a successive family of yield curves that symmetrically expand with compaction (Schofield and Wroth, 1968). Therefore this family has a universal shape that does not evolve with deformation. The yield curves in the family can be compared by dividing each curve by its respective P* value. This normalization technique has also been used to compare yield curves of different rock types (e.g. Wong et al., 1997a; Cuss et al., 2003b). However experimental studies have begun to show that the concept of a family, with unique curve shape, does not adequately describe porous rock deformation and that significant yield curve evolution occurs with the accumulation of inelastic strain (Baud et al., 2006; Bedford et al., in review). Alternative models to critical state soil mechanics have been proposed which allow the yield curve to evolve as porosity increases or decreases with the accumulation of inelastic volumetric strain (e.g. DiMaggio and Sandler, 1971; Carroll, 1991). The model of Grueschow and Rudnicki (2005) also allows the yield curve to evolve under a differential load where the sample will also accumulate a component of inelastic shear strain. However it is apparent that more empirical data are needed to constrain better the effects of different types of inelastic strain on yield curve evolution.

The study of Bedford et al., (in review), to the best of our knowledge, is the first to document the effects of both inelastic volumetric strain and inelastic shear strain on yield curve evolution. This was done on porous bassanite, a material comprised of relatively weak platy grains. They performed a series of overconsolidation tests under different hydrostatic and deviatoric loading paths and found that a sample compacted

under a deviatoric load (i.e. with a component of shear strain) had a yield curve with a peak that is almost double that of an equal porosity sample that had been hydrostatically compacted (i.e. purely volumetric strain). The difference in yield curve shape is qualitatively attributed to the heterogeneous microstructure and formation of multiple sets of conjugate shear bands that developed during deviatoric loading, highlighting the importance of understanding microstructural controls on rock strength. Bedford et al., (in review) also document the formation of a plateau on top the yield curve during deviatoric loading, suggesting the critical state line is actually a zone rather than a line. They suggest that compactional and dilational processes occur together at all yield states and that the traditional regions of the yield curve associated with compaction or dilation (Fig. 5.1) represent where one is more dominant than the other; however in this plateaued region they become almost balanced. The development of a transitional zone between the regions of bulk dilatant and bulk compactant deformation could have important implications for understanding the conditions that lead to localized deformation. It has generally been assumed that strain localization would only occur in the dilatant (brittle) regime, in the form of shear fractures, and that it would be inhibited in the compactant (ductile) regime. However many studies have reported localized compaction bands in the field (Mollema and Antonellini, 1996; Fossen et al., 2011; Ballas et al., 2013), in experiment (Olsson and Holcomb, 2000; Wong et al., 2001; Baud et al., 2004; Fortin et al., 2006; Tembe et al., 2008; Baud et al., 2015) and also in theoretical predictions (Issen and Rudnicki, 2000; Grueschow and Rudnicki, 2005). Wong et al., (2001) show that these localized compactional features are associated with stress states in the transitional regime between brittle faulting and ductile cataclastic flow. Thus understanding the evolution of yield curves in this region could help elucidate the deformation modes.

In this study we apply the stress probing methodology of Bedford et al., (in review) to test if the yield behaviour and subsequent evolution they observe for porous bassanite is applicable to sandstone, which is comprised of stronger more equant grains. We therefore map in high resolution the yield curves of two highly porous sandstones. The post yield evolution of the curves is investigated in response to both hydrostatic and deviatoric loading and the associated microstructures from these different loading histories are analysed.

## 5.2. Methods

### *5.2.1 Experimental materials*

The two porous sandstones used in this study are Boise and Idaho Gray sandstone. Blocks of both rock type were purchased from Kocurek Industries Inc. (USA). A petrophysical description of the rocks is provided in Table 5.1. In order to investigate post yield evolution, it is important the sandstones are relatively weak so that they will yield well with the limits of the deformation apparatus to allow for them to be inelastically overconsolidated. Boise sandstone was chosen for this investigation because of the relatively low P* values (42-105 MPa) that have previously been reported for this rock type (Zhang et al., 1990b; Zhang et al., 1990c; David et al., 1994; Wong et al., 1997a; Baud et al., 2000b; Cheung et al., 2012). The differences in these P* values are attributed to variations in porosity (25-35 %) and grain size (0.28-0.46 mm radius) between the different blocks used in previous experimental investigations. In this study, initial porosities were determined using He-pycnometry and Boise sandstone was found to have a starting porosity of 37.6 % (average of 5 measured samples) which is the highest that has been reported for this rock type. Idaho Gray sandstone was chosen because of its similar petrophysical properties to Boise sandstone which is a good indication that it should also have a relatively low P*, allowing for the post yield evolution to be investigated. There are some slight differences in that Idaho Gray sandstone has a lower measured starting porosity of 36.2 %, a slightly coarser grain size and is slightly more quartz rich than Boise sandstone (see Table 5.1).

| Sandstone | Porosity (%) | Grain size (mm) | Modal analysis |
|---|---|---|---|
| Boise | 37.6 ± 1.0 | 0.5 ± 0.3 | quartz 47%, plagioclase 29%, K-feldspar 17%, muscovite 2%, biotite 1%, clays 3%, others 1% |
| Idaho Gray | 36.2 ± 0.5 | 0.7 ± 0.2 | quartz 53%, plagioclase 26%, K-feldspar 17%, muscovite 1%, biotite 1%, clays 2%, others <1% |

***Table 5.1****. Petrophysical description of the sandstones investigated in this study*

Cores (50 mm length x 20 mm diameter) were drilled perpendicular to bedding from both blocks and these cores were then precision ground to square the ends to tolerance (± 0.01 mm). The porosity would then be measured in the He-pycnometer before the core is placed into a 2.5 mm wall thickness PVC jacket prior to insertion in to the deformation apparatus.

### *5.2.2. The deformation apparatus*

The triaxial apparatus used (see chapter 2, Fig. 2.2) was designed and built in the University of Liverpool and is capable of experiments under conditions of up to 250 MPa confining pressure, 200 MPa pore fluid pressure and a 300 kN differential load. The confining pressure and pore pressure are servo-controlled and can be measured to resolution of better than 0.01 MPa. The servo-controlled pore pressure pump can also be used as a volumometer to monitor changes in pore volume to a resolution of 0.1 $mm^3$. The pore fluid used in this study is argon as it is chemically inert, which was chosen to minimize the effects of any time-dependent stress corrosion cracking (e.g. Atkinson and Meredith, 1981; Atkinson, 1984; Heap et al., 2009). The axial load is generated by a servo-controlled electromechanical piston and is monitored by an internal force gauge with a resolution of better than 0.03 kN.

### *5.2.3. The experimental procedure*

In order to investigate the shape and evolution of the yield curves of the porous sandstones we perform a series of stress-probing tests similar to those by Bedford et al., (in review) on porous bassanite. These experiments allow for the yield curve of a single sample to be mapped in high resolution. This is done by overconsolidating a sample (i.e. compact it beyond its yield point) so that it is positioned on a new yield curve before reducing the load to move back into the elastic regime (i.e. inside the new yield curve). The sample is then taken to different confining pressures inside the yield curve where it is axially loaded until yield is achieved. Yield is recognized by the deviation from quasi-linear elastic loading (Fig. 5.2) and the load is increased until this deviation is observed. At this point the axial load is immediately removed from the

sample to ensure no permanent inelastic strain is accumulated. The confining pressure is then changed to a different value inside the yield curve and the stress-probing procedure is repeated; this is done over a range of confining pressures until the yield curve has been mapped. All the movement in stress space is therefore inside a given yield envelope in the elastic regime; the only time this is not the case is at the onset of yield itself. Bedford et al., (in review) show that the probing technique causes minimal inelastic damage to the sample allowing the curve to probed multiple times at different effective pressures. Once a yield curve has been mapped the sample is overconsolidated further so that is sits on another new yield curve to see if there is any evolution as a result of increased inelastic strain. Bedford et al., (in review) have shown that yield curve evolution is strongly dependent on the nature of inelastic strain accumulated. We therefore investigate two overconsolidation pathways, hydrostatic overconsolidation and deviatoric overconsolidation, to analyse the effects of inelastic volumetric versus inelastic shear strain. These different tests are outlined below.

#### *5.2.3.1. Hydrostatic overconsolidation*

Figure 5.2a shows a schematic summary of the loading path for the hydrostatic overconsolidation tests. Initially a sample is loaded hydrostatically beyond P* so that it accumulates inelastic volumetric strain and is sat on a new yield envelope. The confining pressure is then incrementally decreased so that stress state is returned to the elastic regime inside the new yield curve. Between each increment of confining pressure reduction the sample is axially loaded until yield is achieved to probe the shape of the new yield curve. As soon as yield is reached, identified by the deviation from linear elastic loading, the axial load is immediately removed and then the confining pressure is incrementally reduced. Once a yield curve has been probed over a range of confining pressure increments the pressure is increased again beyond the new P* so that the sample is sat on another new yield curve. The procedure of incremental confining pressure reduction and axial loading is then repeated for this subsequent yield curve. This loading history therefore maps out the family of yield curves associated with the accumulation of purely volumetric strain.

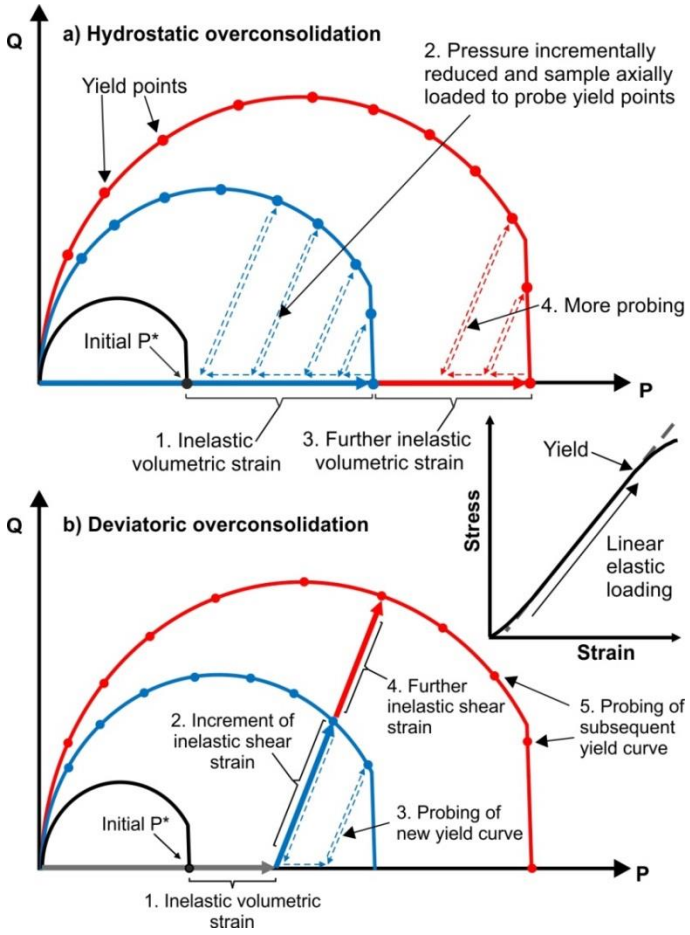


***Figure 5.2 - a)*** *A schematic summary of the hydrostatic overconsolidation experimental technique. Samples are hydrostatically loaded beyond P* so that inelastic volumetric strain is accumulated and the sample is sat on a new yield curve. The pressure is then incrementally reduced, to move back inside this new curve and the sample subjected to elastic axial loading between each pressure reduction step. The axial load is applied until the deviation from linear elastic loading is observed (inset) upon which it is immediately removed. Once the yield curve is fully probed, the sample is further overconsolidated so that more inelastic volumetric strain is accumulated. The subsequent yield curve is then probed in the same way to determine if there is any shape evolution.* ***b)*** *A schematic summary of the deviatoric overconsolidation experimental technique. The sample is hydrostatically loaded beyond P* and then subject to axial loading to accumulate an increment of inelastic shear strain. The load is then removed and the sample subject to axial probing at different confining pressures. Once the new yield curve has been probed, the sample is further deviatorically overconsolidated along the same loading path so that more inelastic shear strain is accumulated. The subsequent yield curve is then probed in the same to monitor any shape evolution.*

*5.2.3.2. Deviatoric overconsolidation*

The second type of overconsolidation test that can be performed in a traditional triaxial configuration is deviatoric overconsolidation. These tests have a component of inelastic shear strain as well as volumetric strain; the loading history is summarized in figure 5.2b. Initially a sample is loaded beyond P* so that it is sat on the yield envelope before being axially loaded to induce some inelastic deviatoric strain. After a given increment of deviatoric loading, the load is removed and the confining pressure is incrementally increased or decreased so that the yield curve can be probed. After a yield curve has been probed the confining pressure is returned to the value used for the initial axial loading and the sample is further deformed along the same loading path. The loading is then stopped again after another increment of inelastic deviatoric strain has been accumulated and the probing procedure is repeated. Samples were deformed along this loading path until 10% axial displacement was achieved. The yield curve of a given sample was probed every 2% increment of inelastic axial displacement.

*5.2.3.3. Validation tests*

As will be discussed in sections 5.3 and 5.4, the overconsolidation tests reveal that the peaks of the yield curves for these highly porous sandstones is much lower than has been previously reported for other porous rocks. However the majority of previous works have focussed on the initial yield curve for a particular porous rock whereas we have analysed the post yield evolution. As the samples in the overconsolidation tests are initially loaded beyond P*, information is lost on the initial yield condition of the sandstones. To test whether there is difference in the shape of the initial and post yield curves, a series of validation tests were performed. These tests are based on the traditional method of determining a yield curve by axially loading multiple samples at different pressures below P*. This produces data scatter as a result of sample variability, as each point corresponds to an individual sample, but it does provide a constraint on the shape of the initial yield curve.

### *5.2.4. Microstructural analysis*

Upon removal from the deformation apparatus, samples were prepared for microstructural analysis. Samples were vacuum impregnated with epoxy resin whilst still in their PVC jackets to ensure no material was lost. After impregnation, samples were cut and this surface was then re-impregnated to ensure resin fills all the pore space. The samples were then polished ready for imaging in the scanning electron microscope (SEM). Backscatter electron images (BSE) were acquired using a Philips XL30 SEM.

## 5.3. Mechanical and microstructural results

Prior to the overconsolidation tests, the initial P* for the different sandstones was determined by increasing the effective mean stress while monitoring the relative pore volume change with the volumometer. Examples of porosity evolution with increasing pressure are presented in figure 5.3 with a clear deflection in the curves marking P* and the onset of inelastic compaction. There is some sample variability in the pressure that P* occurs, however typical values are 37-48 MPa for Boise sandstone and 54-59 MPa for Idaho Gray sandstone (range determined from 3 samples per rock type).

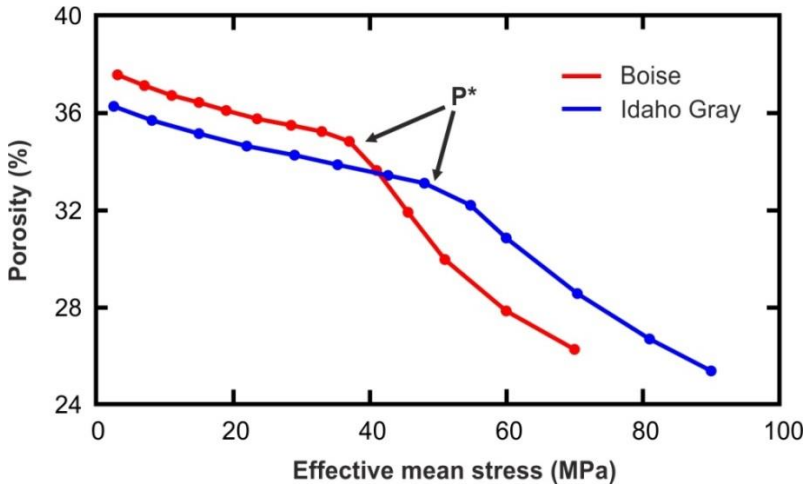


***Figure 5.3 -*** *The evolution of porosity with increasing effective mean stress for the different sandstones. Clear deflections in the loading curves mark P* and the onset of permanent compaction.*

### *5.3.1. Hydrostatic overconsolidation results*

Yield curves from the hydrostatic overconsolidation tests are presented in figure 5.4. The data show that the curves of both sandstones are very similar with a broadly elliptical shape, albeit a shallow one. The compactive side of the yield curves are also comprised partly of near-vertical limb in the vicinity of P*, similar to those reported by Bedford et al., (in review) and Tembe et al., (2007). As mentioned, validation experiments were performed to test the position of the initial yield curve and assess whether the shallowness is a result of post-yield evolution. The initial yield points lie within the families of post-yield curves for both sandstones suggesting there is not a major transition to a flatter yield curve as a result of post-yield inelastic strain. There is one outlier in the initial yield points, for Idaho Gray at low pressure, which is likely a result of sample variability. This highlights the difficulty in trying to constrain accurately the yield curve shape from the traditional methodology of performing numerous triaxial tests on multiple samples. The overconsolidation stress-probing procedure produces a high-resolution yield curve which has minimal data scatter.

To test whether there is evolution in the family of yield curve as result of increasing inelastic volumetric strain, the curves can be normalized by dividing each member of the family by its respective P* value (Fig. 5.5). This normalization technique has been used previously to compare yield curves from different rock types (e.g. Wong et al., 1997a; Cuss et al., 2003b). The normalized data for both sandstones reveal that there is only minor evolution of the yield curves in response to increasing volumetric strain. The yield curves appear to expand slightly on the compactive side. Normalization of the yield curves further highlights the flattened shape of the yield curves. The peaks of the curves have a Q/P* ratio of 0.22-0.3. This is substantially lower than values that have been previously reported for other sandstones which typically have Q/P* ratios in the range of 0.5-0.7 (e.g. Wong et al., 1997a).

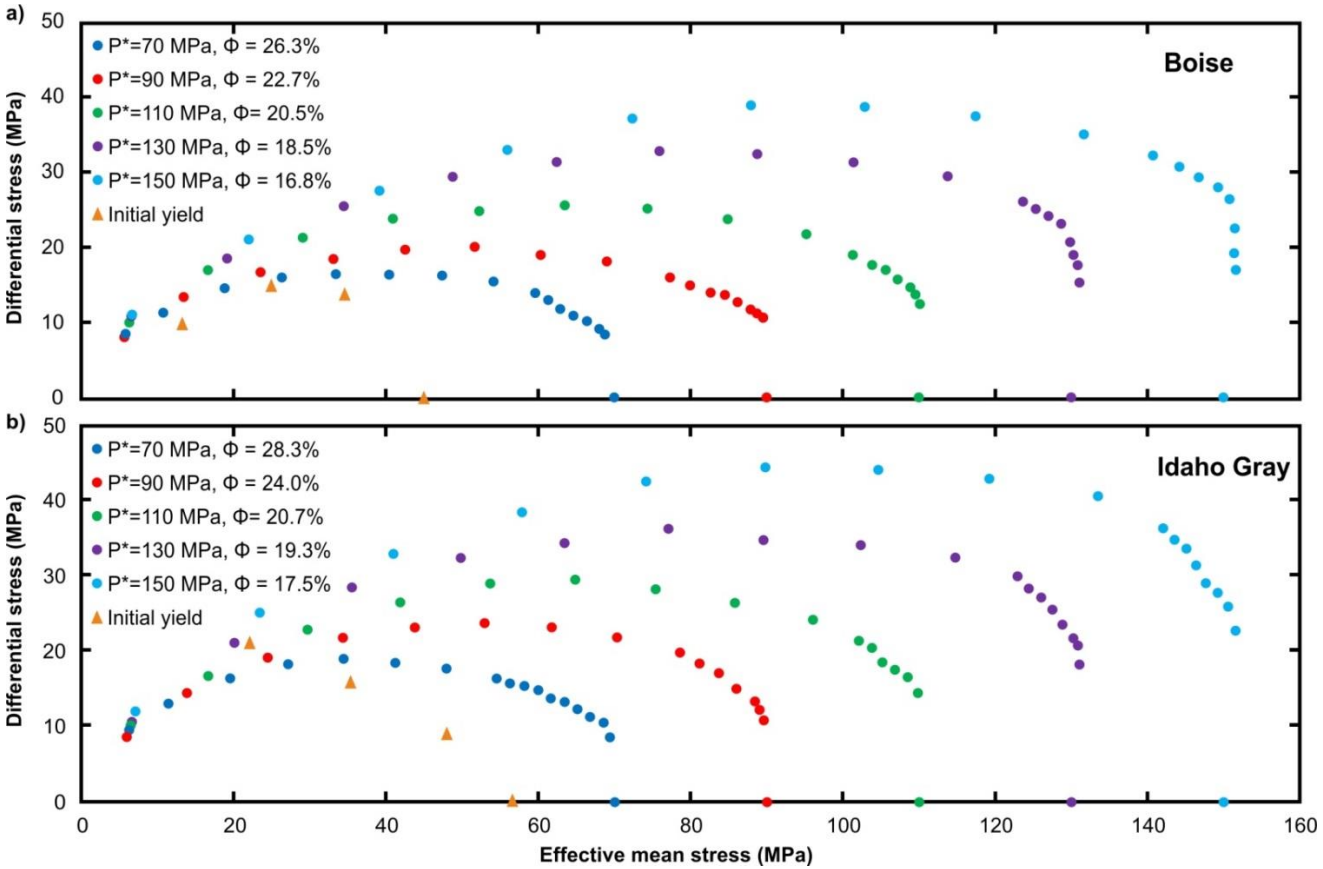


***Figure 5.4 -*** *Yield curves from the hydrostatic overconsolidation tests on* ***a)*** *Boise and* ***b)*** *Idaho Gray sandstones. The data points reveal a family of shallow yield curves which are partly comprised of a near-vertical limb on the high pressure side. Initial yield points from the validation tests are included.*

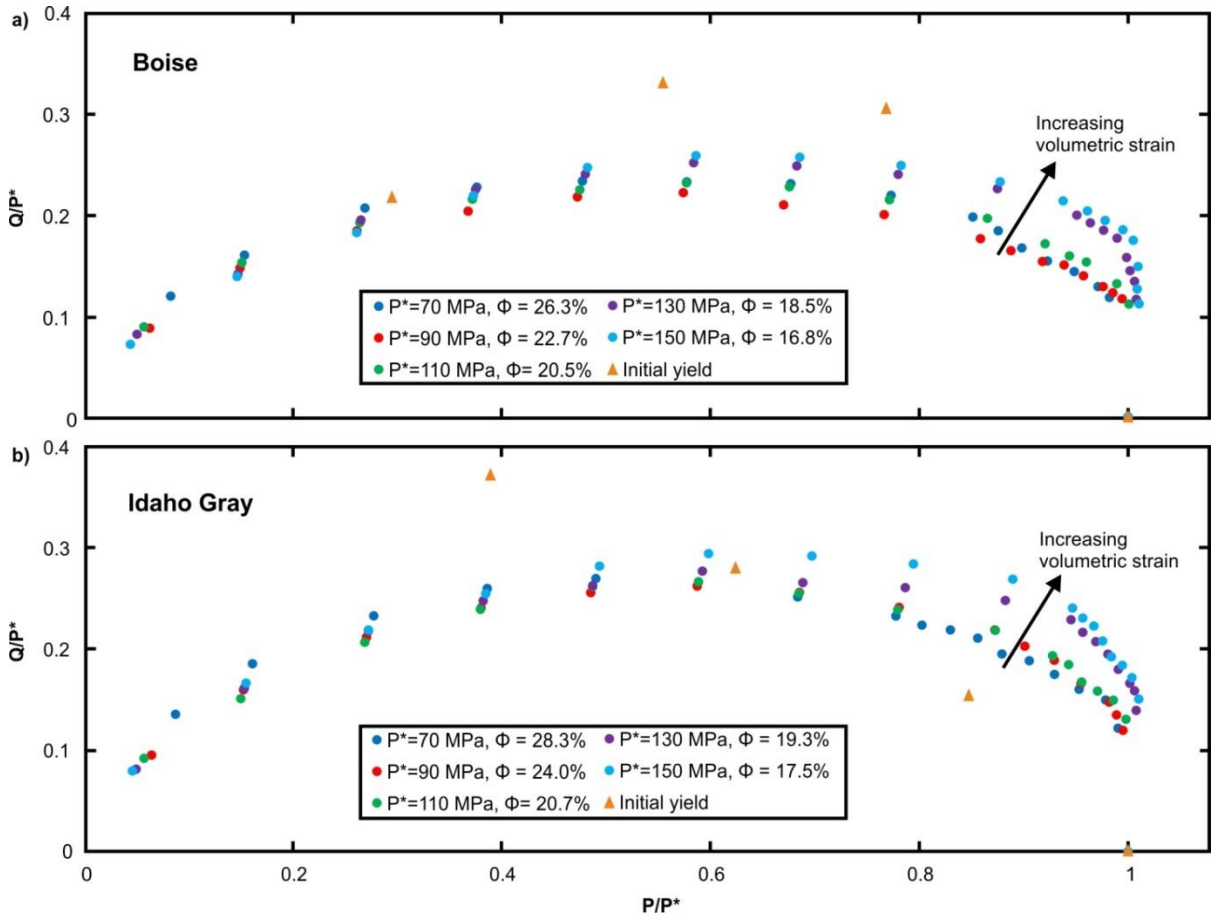


***Figure 5.5 -*** *Normalization of the yield curves from the hydrostatic overconsolidation tests by dividing each curve by its respective P* value. There is a slight expansion of the compactive side of the yield curves with increasing volumetric strain.*

### *5.3.2. Deviatoric overconsolidation results*

Yield curves from the deviatoric overconsolidation tests are presented in figure 5.6 with the dashed arrow marking the loading trajectory along which the sample was deformed. There are fewer points on the compactive side of the yield curves as P* is no longer known as soon as an increment of inelastic deviatoric strain is accumulated. P* cannot be identified by stress-probing as the effective mean stress needs to be increased considerably beyond P* before it can be recognised, causing inelastic deformation of the sample that is not a result of the deviatoric loading path. Therefore the confining pressure was conservatively increased during the stress-probing procedure to ensure the new P* was not exceeded. The yield curve evolution along the deviatoric loading path is similar for both sandstones, with the curves expanding in height and width with increasing inelastic deviatoric strain. Continued deformation also leads to the development of a plateau at the peak of the yield curves, similar to those reported by Bedford et al., (in review) for porous bassanite. Therefore the transition between dominantly dilatant and compactive behaviour, which is typically considered to be the critical state line (Fig. 5.1b), develops into a broad zone rather than a line. The lack of P* data means that the deviatoric overconsolidation yield curves cannot be normalized in the same way as the hydrostatic overconsolidation curves. However yield curve evolution in response to deviatoric strain can be analysed by comparing with the hydrostatic overconsolidation tests.

### *5.3.3. Hydrostatic versus deviatoric strain*

As the hydrostatic overconsolidation tests involve purely inelastic volumetric strain, any differences in the yield curve evolution during deviatoric overconsolidation is likely a result of inelastic shear strain. Comparisons can therefore be made between yield curves from the different test type where samples have been compacted to a similar porosity. Figure 5.7a compares yield curves of a Boise sandstone sample that has been hydrostatically compacted to a P* of 90 MPa with a sample that has experienced 2% inelastic deviatoric loading. These samples have similar porosities of 22.7% and 23.3% respectively so should provide a useful comparison of the effects of inelastic volumetric versus shear strain. The deviatorically overconsolidated sample has a slightly larger yield curve; however the difference is small and we cannot rule out

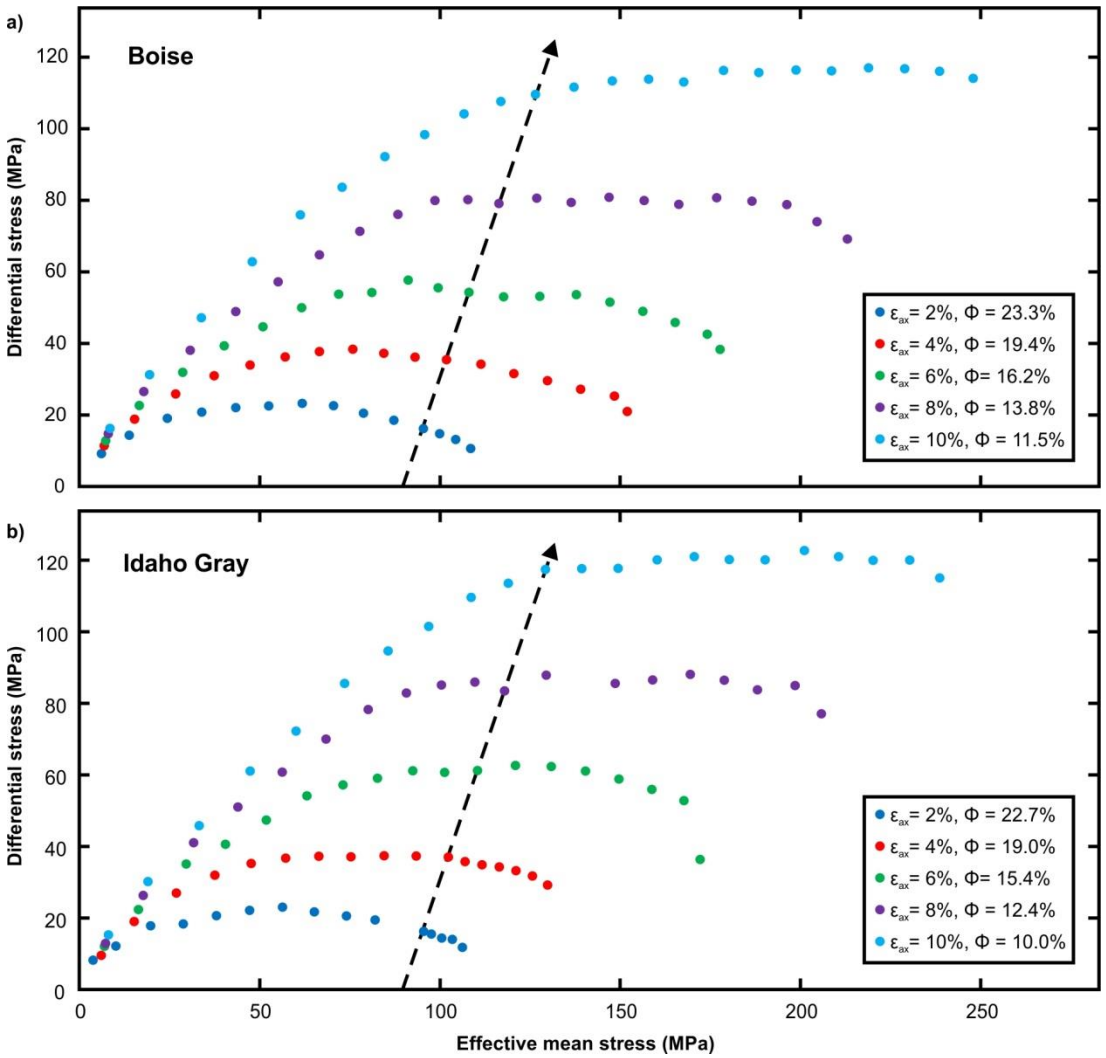


***Figure 5.6 -*** *Yield curves from the deviatoric overconsolidation tests on* ***a)*** *Boise and* ***b)*** *Idaho Gray sandstones. The loading path is marked by the black dashed arrow and yield curve was probed every 2% increment of inelastic axial displacement. The data points reveal that a plateau starts to form at the top of the yield curves further along the loading path the sample is taken.*

the effect of sample variability. Figure 5.7b compares yield curves of the same samples after more inelastic strain has been accumulated. The hydrostatically overconsolidated sample has now been compacted to a P* of 150 MPa and the deviatorically overconsolidated sample to an axial displacement of 6%. The porosities are now 16.8% and 16.2% respectively, so again represent a comparable amount of inelastic compaction. However the difference between the yield curves is much more significant with the peak of the deviatorically deformed sample being approximately 50% higher

than the hydrostatically compacted sample. This highlights that inelastic shear strain has a substantial effect on the relative size of the yield curve for sandstone and that this is dependent of the amount of shear strain that has been accumulated.

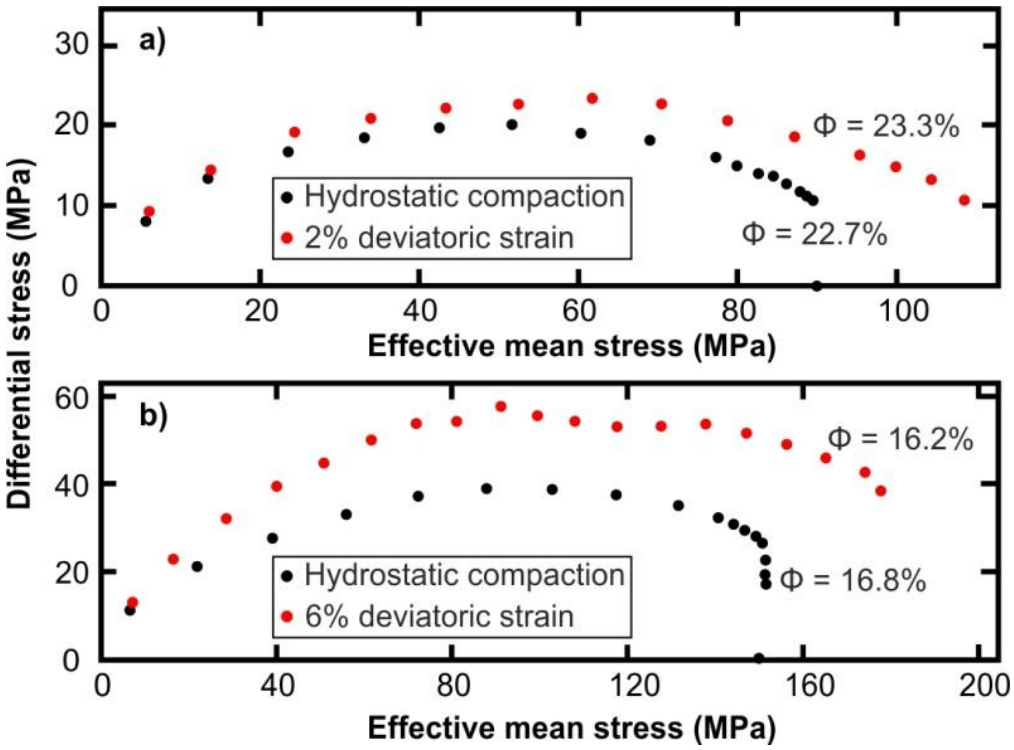


***Figure 5.7 -*** *Comparison of similar porosity yield curves for Boise sandstone deformed by hydrostatic overconsolidation vs deviatoric overconsolidation.* ***a)*** *The red curve has experienced 2% inelastic deviatoric strain whereas the black curve has been deformed by hydrostatic compaction. There is a small difference between the curves although this could be as a result of sample variability.* ***b)*** *The red curve has experienced 6% inelastic deviatoric strain and the black curve has been deformed by purely hydrostatic compaction. There is about a 50% increase in the peak of the deviatorically overconsolidated sample with respect to the hydrostatically overconsolidated sample.*

### *5.3.4. Microstructure*

Undeformed samples of both sandstones show that the majority of quartz and feldspar grains have relatively few microcracks and fractures (Fig. 5.8a and b).

Samples that have been deformed by both hydrostatic (to 150 MPa) and deviatoric (to 10% axial displacement) overconsolidation show deformation by distributed cataclastic flow (Fig. 5.8c-f). This is dominated by intragranular cracking that leads to grain crushing and pore collapse. Intragranular cracking has been shown previously to be the dominant hydrostatic and triaxial compaction mechanism at the onset of yield in siliciclastic rocks (Wong and Baud, 2012). The deviatorically overconsolidated samples were compacted to a lower porosity and hence show more intense deformation (Fig. 5.8e and f). Cataclasis and grain crushing leads to the formation of a poorly sorted fine grained deformation product (in the order of a few microns) which anastomoses around large intact relict grains. It is likely that a large amount of the post-yield deformation can be accommodated by grain rearrangement in this finer grained material after it has formed, which probably leads to the preservation of large relict grains. No obvious localization features or any sample-scale structure is observed in either the hydrostatically or deviatorically deformed samples.

It has been documented in previous studies on sandstone compaction that grain crushing is facilitated by Hertzian fractures that radiate from impinging grain contacts because of local stress concentrations (e.g. Zhang et al., 1990b; Menéndez et al., 1996; Fortin et al., 2007). Similar Hertzian fractures are seen in these sandstones (Fig. 5.9a and b) with intragranular cracks propagating across larger grains of quartz and feldspar, ultimately leading to grain crushing and pore collapse. Mica grains that were trapped between quartz and feldspar grains deform via grain kinking and cleavage cracking (Fig. 5.9c).

To investigate if microstructural anisotropy develops during deviatoric loading, the orientation of microfractures was measured along horizontal transects across the BSE images of the deformed samples. All BSE images were acquired with $\sigma_1$ vertical with respect to the image. The orientation data show that for a hydrostatically overconsolidated sample the fractures are orientated fairly randomly (Fig. 5.10a), which is consistent with Hertzian fractures radiating from grain contacts in an isotropic stress field. However for the deviatorically overconsolidated sample there is a preferred orientation of fractures aligned at an angle of ±40° to $\sigma_1$ (Fig. 5.10b) suggesting a microstructural anisotropy develops during deviatoric compaction.

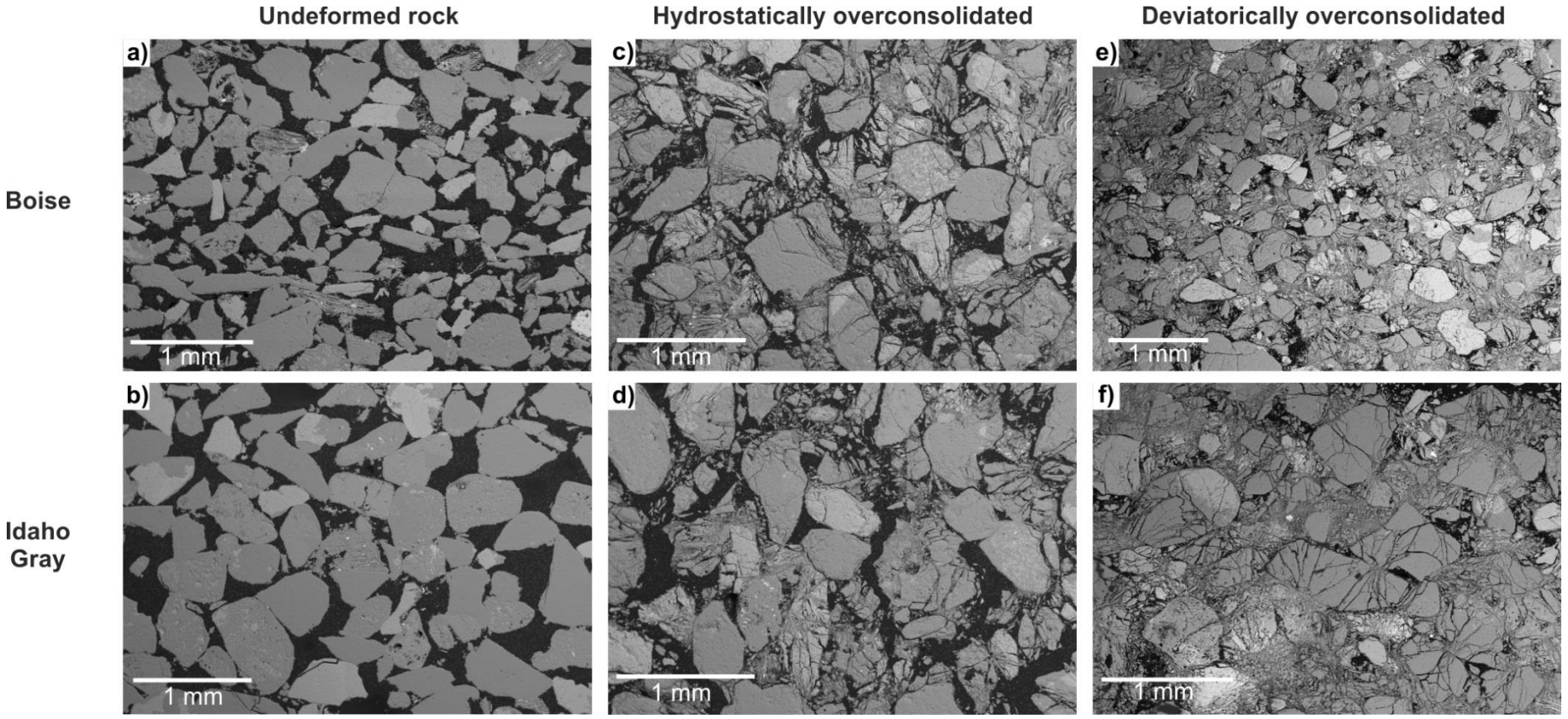


***Figure 5.8 -*** *Back-scatter electron images of the Boise and Idaho Gray sandstones.* ***a)*** *and* ***b)*** *show images of the undeformed samples.* ***c)*** *and* ***d)*** *show samples that have been hydrostatically overconsolidated with evidence for grain crushing.* ***e)*** *and* ***f)*** *show deviatorically overconsolidated samples with fine grained deformation product anastomosing around relict large grains.*

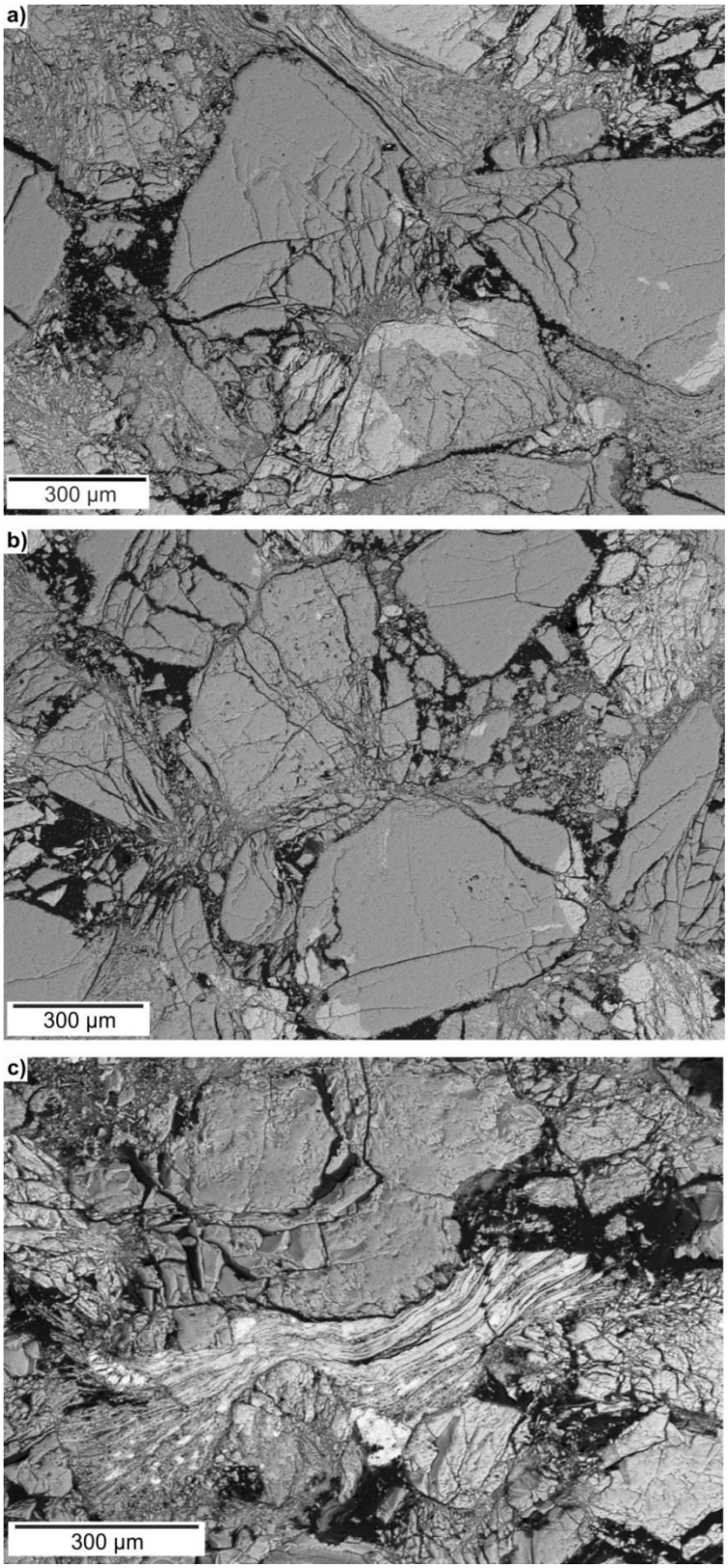


***Figure 5.9 - a)*** *and* ***b)*** *Quartz and feldspar grains deform by grain crushing which is facilitated by Hertzian fractures propagating from grain contacts.* ***c)*** *Mica grains deform by grain kinking and become pinched between quartz and feldspar grains.*

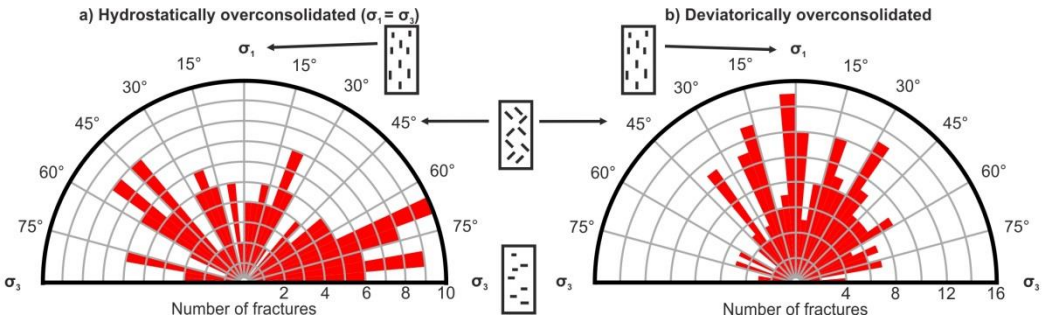


***Figure 5.10 -*** *Rose diagrams of microfracture orientation from* ***a)*** *hydrostatically overconsolidated and* ***b)*** *deviatorically overconsolidated samples of Idaho Gray sandstone. The hydrostatically deformed sample shows a distributed set of fracture orientations. The deviatorically deformed sample has fractures that a preferentially aligned with their long axis ±40° from* $\sigma_1$.

## 5.4. Discussion

A stand out feature from both sets of overconsolidation tests is that the yield curves have a very flat geometry in comparison to previous studies. Wong et al., (1997a) suggested that normalized yield curves should have a peak Q/P* ratio in the range of 0.5-0.7, however normalized curves of the sandstones in this study have a peak Q/P* ratio of approximately 0.3 (Fig. 5.5), further highlighting their eccentricity. Both Boise and Idaho Gray sandstones have porosities that are higher than any of the sandstones reported by Wong et al., (1997a) and are therefore probably more comparable with loose or poorly lithified sands. However normalized data for loose sand (e.g. Miura et al., 1984; Crawford et al., 2004; Nguyen et al., 2014) also typically fall in between the bounds proposed by Wong et al., (1997a). The similarities between loose sand and lithified sandstone, rules out the strength of grain contacts as the reason for the flatter yield curves of this study. Crawford et al., (2004) systematically investigated the effects of sand textural characteristics on yield curve shape. They found that Ottawa Sand, which is consists of coarse (approx. 1 mm) well-rounded grains of quartz, had a relatively shallow yield curve and was the only sand that when normalized plotted below the lower bound of Wong et al., (1997a), with a Q/P* ratio of just below 0.4. Both Boise and Idaho Gray sandstones have a similar coarse grain size to Ottawa Sand and consist of subrounded to subangular grains, which could potentially explain the similar flatter yield curves observed for these rock types. One

major difference between the sandstones of this study and many investigations of loose sands is the modal composition. Ottawa sand and many of the other loose sands that have been studied are predominantly comprised of quartz whereas both Boise and Idaho Gray sandstone are only about 50% quartz with a large amount of feldspar and other minerals. It has been suggested that mineralogy can affect the magnitude of yield curves. For example Bleurswiller sandstone has a high abundance of minerals other than quartz (feldspar, mica, oxides) and its compactive yield stresses are lower, by approximately a factor of 5, than Bentheim sandstone which is similar porosity but comprised almost entirely of quartz (95%) (Tembe et al., 2008). However the peak Q/P* ratios of these sandstones are broadly similar (approximately 0.45 for Bleurswiller and 0.53 for Bentheim) and it remains uncertain whether composition also leads to systematic variation in yield curve shape as well as size. Perhaps the flatter yield curves observed for Boise and Idaho Gray sandstones are a combined result of both texture and mineralogy. Irrespective of the reason for the eccentric yield curves, the data suggest that caution should be taken when generalizing yield envelopes (e.g. Wong et al., 1997a; Zhang et al., 2000; Rutter and Glover, 2012) and that the previously ascribed bounds for normalized yield data could be extended to incorporate flatter yield curves, particularly for overconsolidated porous rocks.

As well as the yield curves having a flattened geometry the data show that there is evolution in shape with continued deformation. The hydrostatic overconsolidation tests reveal a slight expansion of the compactive side of the yield curve with increased volumetric strain (Fig. 5.5). This type of evolution is similar to that predicted by the yield cap models of DiMaggio and Sandler (1971) and Carroll (1991). Unlike the traditional critical state model (Schofield and Wroth, 1968), which assumes one elliptical curve that can be scaled to encompass the entire yield criterion (e.g. Fig. 5.1), these models separate the yield criterion into two curves that individually describe the regions of compactive and dilatant deformation. Compactive yield is defined by an elliptical cap at high pressure, which is bounded by a separate low pressure dilational envelope. This compactive cap can then evolve with the accumulation of volumetric strain. Baud et al., (2006) have tested the yield curve evolution of different sandstones against these models and found that they have some success in approximating the theoretical evolution in experiments. However the data of Baud et al., (2006) are subject to a large amount of data scatter as a result of using multiple samples to document the yield curve, making it difficult to fit well-constrained curves in order to

monitor their evolution. Despite there being some yield curve evolution as a result of volumetric strain in this study, it is minor and the majority of the curves appears to fit well to a single smooth ellipse, apart from the steep limb on the compactive side. It therefore does not seem sensible to decouple the dilatant and compactive sections of the yield curve as in the models of DiMaggio and Sandler (1971) and Carroll (1991). Rather, it would be more appropriate to have a single ellipse, to incorporate the regions of dilation and shear-enhanced compaction, which is intersected by a near-vertical curve extending upwards from P*. Bedford et al., (in review) described this near-vertical section of the yield curve as a region of "shear-insensitive compaction" and a similar region can be defined for Boise and Idaho Gray sandstones (Fig. 5.11a).

Although the yield curve evolution of Boise and Idaho Gray sandstones to increasing volumetric strain is relatively minor, the response to inelastic shear strain is more significant. It is observed in the deviatoric overconsolidation tests that a plateau forms at the peak of the yield curve as more inelastic shear strain is accumulated (Fig. 5.6). This is similar to plateaus observed by Bedford et al., (in review) on porous bassanite. They termed this region "pressure insensitive deformation", which is associated with an equal contribution of both compactive and dilational processes occurring simultaneously in this region (Fig. 5.11b). It is known that during deformation of porous rock that both compaction and dilation occur together (e.g. Brace, 1978). During compaction of siliciclastic rocks, grain crushing is facilitated by Hertzian fractures propagating across individual grains (Fig. 5.9) which involves the opening of voids and hence dilatancy on the scale of the grain. As these fractures break grains into smaller fragments, the fragments can rearrange themselves and collapse into adjacent pores thus reducing the porosity on the sample scale. As a sample experiences further compaction and porosity is reduced, there becomes less space available for grain rearrangement and therefore dilatancy can become a more dominant process in the behaviour of the bulk sample. The formation of a plateau likely arises when compactive and dilational mechanisms reach a similar order, as a sample deforms along the deviatoric loading path (Fig. 5.11b). The critical state model, where the yield ellipse can be divided into a dilatant low pressure side and a compactive high pressure side separated by the critical state line (Fig. 5.1), is therefore an oversimplification. Rather, the CSL develops into a critical state zone instead of a line and the deformation modes likely occur as a spectrum of dilation to compaction around the yield curve rather than as discrete zones. Wood and Maeda (2008) have also

suggested that a critical state zone can develop during sand deformation as the grading and particle size of the sand changes in response to particle crushing.

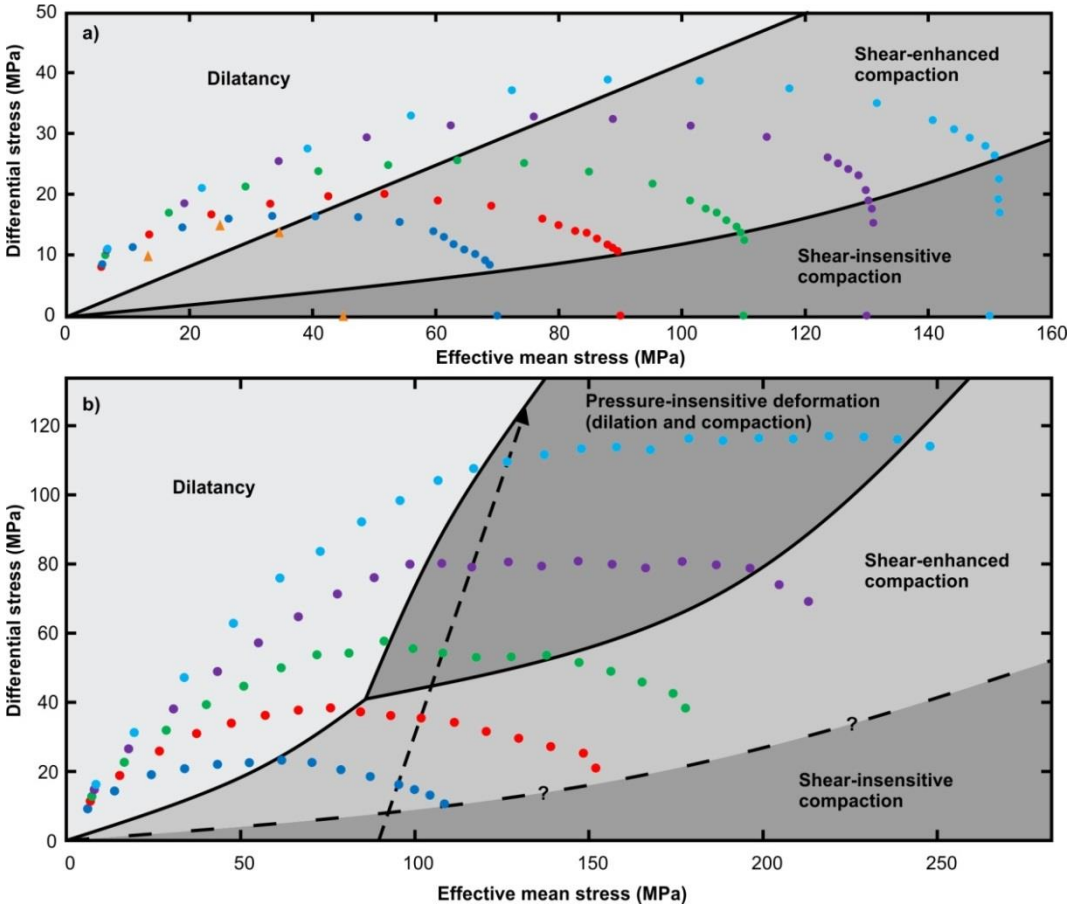


***Figure 5.11 -*** *Interpretation of the yield curves mapped in the hydrostatic and deviatoric overconsolidation experiments.* ***a)*** *The curves from the hydrostatic overconsolidation tests are partly comprised of a near-vertical limb on the high-pressure side which defines a region of shear-insensitive compaction.* ***b)*** *The curves from the deviatoric overconsolidation tests show the appearance of a sub-horizontal plateau as the sample accumulates more inelastic shear strain. This marks a transitional region of pressure-insensitive deformation which is characterized by simultaneous compaction and dilation processes.*

Bedford et al., (in review) suggest that the interplay of compaction and dilation in this region of pressure insensitive deformation could help facilitate localized

deformation. During the deformation of bassanite they observe that a strongly heterogeneous microstructure develops in the form of many localized conjugate shear bands. Although no obvious localization features have formed during the deformation of Boise and Idaho Gray sandstones (Fig. 5.8e and f), the development of a region of pressure insensitive deformation on the yield curve has still occurred. The reason for a lack of localization could be because of the non-uniform grain size distribution that develops during deformation, with fine grained material anastomosing around large relict grains (Fig. 5.8). Cheung et al., (2012) have suggested that a uniform grain size distribution favours the development of localized compaction bands. However we cannot discount that shear localization might have occurred if the sample had been further deformed along the same loading path (e.g. Wong et al., 1992).

As well as changes in yield curve shape that occur during deformation, it is important to consider how different stress paths affect the relative magnitude of the yield curves. Figure 5.7 highlights that the accumulation of inelastic shear strain along the deviatoric loading path produces a yield curve with a peak that is considerably higher than a similar porosity sample that has been hydrostatically compacted. Similar behaviour was documented by Bedford et al., (in review) which they attributed to the development of a heterogeneous microstructure and conjugate shear bands. Although there is no obvious structure that develops in the Boise and Idaho Gray sandstones it is likely that the reason for the difference in yield curve magnitude is microstructural anisotropy that develops along the deviatoric loading path. Wu et al., (2000) have shown that a significant anisotropy in intragranular and intergranular fractures, with a preferred orientation parallel to the maximum principal stress ($\sigma_1$), develops during dilatancy. Therefore if dilatancy is becoming a more dominant process along the deviatoric loading path, a similar anisotropy may develop in Boise and Idaho Gray sandstones. Figure 5.10b shows that there is a preferential alignment of microfractures with respect to $\sigma_1$ in the deviatorically overconsolidated sample, similar to the observations of Wu et al., (2000). This could produce mechanical anisotropy that would explain the observed differences in yield curve magnitude. Recent works have highlighted the importance of pore geometry and orientation on rock strength (Bubeck et al., 2017; Griffiths et al., 2017). It seems clear that a universal model for yield, based on porosity and/or grain size (e.g. Fig. 5.1) is an oversimplification and more effort needs to be directed towards factors that influence the evolution of yield curves with inelastic strain. Evolution of sandstone strength and microstructure under different

loading conditions has important implications for reservoir production. For example, depletion-induced compaction can lead to changes in the stress state which will in turn affect the deformation behaviour of the reservoir. It is often assumed that reservoir compaction follows a uniaxial stress path, however studies have shown that during production stress states can evolve and actually the rock is rarely at purely uniaxial conditions (e.g. Rhett and Teufel, 1992; Hettema et al., 2000).

## 5.5. Conclusions

A series of stress-probing experiments were performed on Boise and Idaho Gray sandstones to investigate the shape and evolution of their yield curves. The yield curves were found to have broadly elliptical geometry, albeit a much flatterer one than typically associated with porous sandstone (Wong et al., 1997a). This is likely a result of the textural and mineralogical characteristics of the sandstones we studied. The compactive side of the yield curves is partly comprised of a near-vertical limb in the vicinity of P* in agreement with previous studies (Tembe et al., 2007; Bedford et al., in review).

The evolution of the yield curves with work hardening is dependent on the nature of inelastic strain. Hydrostatically overconsolidated samples, experiencing purely volumetric strain, showed only minor yield curve evolution with a slight expansion of the compactive side of the curve. However samples that were deviatorically overconsolidated, with a component of inelastic shear strain, displayed a much more significant yield curve evolution. A plateau forms at the peak of the curve with continued deviatoric loading, likely as a result of dilational deformation becoming more important in the bulk behaviour of the sample. Deformation is predominantly accommodated by grain crushing which reduces grain size allowing the pore space to be filled. Deviatoric deformation produces yield curves which are greater in magnitude than similar porosity samples that have been hydrostatically compacted. This is likely a result of microstructural anisotropy that develops along the deviatoric loading path because of the preferential closure of fractures orientated with their long axis perpendicular to the maximum principal stress. Future work should consider the effects of inelastic shear strain on yield curve evolution and rock strength. It is also important to better constrain the microphysical controls on yield curve shape as the

results of this study have shown that sandstones can have curves with a much more eccentric shape than previously reported.

# 6. Summary and suggestions for future work

The nature of the problem and thesis aims was outlined in chapter 1. Chapters 3, 4 and 5 were presented as individual pieces of work and in this chapter the main findings of these works will be summarized and related back to the nature of the problem outlined in chapter 1. The wider context of this work, for both dehydrating systems and porous rock deformation, will then be discussed and suggestions will be made to show how this work can guide future studies.

## 6.1. Summary of results

In chapter 1 it was stated that evolution of a dehydrating system is dependent on the feedbacks between reaction, fluid flow and deformation. The importance of the interactions between these different parameters is highlighted in equation 1.1 which can be used to model the build-up of pore pressure excesses in dehydrating systems (Wong et al., 1997b), an important prerequisite for dehydration embrittlement. In this equation there are terms for reaction rate ($\dot{\Gamma}$) and porosity production rate ($\dot{\Phi}$) and it was the processes that influence these parameters that were to be the focus of this thesis. Both terms are strongly interlinked and the evolution of one will have feedbacks for the other. The reaction rate term is dependent on reaction temperature, the fluid pressure evolution (e.g. Llana-Funez et al., 2012) and the underlying kinetic processes that facilitate the reaction. The porosity production rate term is dependent on the competing processes of porosity produced as a result of solid volume reduction during reaction (linked to $\dot{\Gamma}$) and the destruction of porosity by deformation. Compaction of porosity will in turn restrict the dissipation of excess fluid pressures and hence feedback on the reaction rate.

In chapter 3 the reaction rate term was explored by performing a gypsum dehydration experiment whilst imaging the sample using 4D X-ray synchrotron microtomography. This technique provided a real-time microstructural record of the spatiotemporal evolution of porosity and product grains allowing for kinetic processes to be elucidated. It was found that the predominant chemical transport pathway during reaction is controlled by the spatial relationship between new porosity and product grains. As the pores wrap around the bassanite grains to form moat-like structures, the

chemical transport of dissolved solutes ($Ca^{2+}$ and $SO_4^{2-}$) must involve diffusion across these moats. This chemical transport pathway is one that has not been widely acknowledged in previous studies, with transport often thought to occur through a thin grain boundary fluid film (e.g. Walther and Wood, 1984) however it will be key in controlling the overall reaction rate, especially at low effective pressures where the porosity is maintained. At higher pressures, if porosity collapses, this transport pathway may manifest itself through a thin grain boundary film. As the newly formed moats are integral to the chemical transport, the overall reaction rate is intimately linked to the connectivity of this porosity and fluid flow in the sample. In the early stages of reaction, when pores are isolated, the reaction rate is buffered by locally high fluid pressures in these pores. As connectivity increases, the high pore fluid pressures dissipate and the growth velocity of individual bassanite grains accelerates. Once the pore fluid pressure in the pores becomes in equilibrium with the externally controlled pore fluid pressure of the experiment, the reaction rate is then controlled by the diffusion of $Ca^{2+}$ and $SO_4^{2-}$ ions. During this stage, as the moats grow in width the diffusion distance lengthens and hence the reaction rate slows. Identification of the main chemical transport pathway and the underlying kinetic processes in operation during reaction is key for modelling dehydrating systems and, for example, could be fed directly into the reaction rate term ($\dot{\Gamma}$) of Wong et al., (1997b). If pore connectivity is low and local fluid pressures are high then pore fluid pressure controls the reaction rate (e.g. Llana-Funez et al., 2012). If a connected pore network is established and local pore pressures can equilibrate then chemical transport (i.e. diffusion) dominates. Hence the reaction rate term will evolve with the permeability of the system. This leads into the work of chapter 4 as deformation of the reaction produced porosity will affect fluid flow and also influence the reaction rate.

In chapter 4 the deformation behaviour of the porous reaction product (bassanite) was investigated, with a focus on the instantaneous mechanical deformation that occurs at the onset of yield. This chapter tested the applicability of critical state soil mechanics, which assumes elliptical shaped yield curves in P-Q space, to the deformation of porous bassanite. It was found that the yield curves of bassanite are not perfectly elliptical and the high pressure side of the curve, which is typically associated with distributed shear-enhanced compaction, is actually almost vertical in the vicinity of P* (the hydrostatic yield point). This suggests that the region encompassed by this steep limb is associated with shear-insensitive compaction as the

deformation should be independent of differential stress in this region. The shape of the yield curve also evolves with continued inelastic strain and this is dependent on the nature of inelastic strain. Samples that are hydrostatically compacted (i.e. purely volumetric strain) have yield curves that have a peak Q/P* ratio that decreases with increasing volumetric strain. This is the opposite effect to deformation under a deviatoric load (i.e. with a component of inelastic shear strain) which causes an expansion of the yield curves with increased strain. A bassanite sample that has been deviatorically overconsolidated to an axial displacement of 8% has a yield curve with a peak that is almost double that of a similar porosity sample that has been hydrostatically overconsolidated. This highlights that inelastic shear strain is a key parameter in determining yield curve evolution. The differences in mechanical response are related to differences in microstructural evolution along different stress trajectories. Hydrostatically compacted samples deform by homogeneous compaction whereas deviatorically compacted samples ultimately localize deformation on to multiple sets of conjugate intergranular shear fractures. The formation of a plateau at the peak of the yield curve also occurs along the deviatoric loading path, forming a transitional zone of pressure-insensitive deformation. This zone is found between the regions of compaction and dilation, which is traditionally thought to be the location of the critical state line in critical state soil mechanics. In this critical state zone it is likely that compactive and dilational processes occur simultaneously and are almost balanced, which could help promote localized deformation.

The results from chapter 4 show that the deformation behaviour of porous rock is complex and strongly dependent on microstructure. The simple yield criterion of critical state soil mechanics, based on porosity and/or grain size, is an oversimplification and more work needs to be done to constrain the microstructural controls on yield and its subsequent evolution. The mapped yield curves in chapter 4 provide a first-order approximation of the instantaneous mechanical deformation of porous bassanite along different loading paths. However a better understanding the fundamental microphysical controls on porous deformation is needed before a universal yield curve theory could be applied to a dehydrating system. To get a complete understanding of the porosity production rate term ($\dot{\Phi}$) of Wong et al., (1997b) this would also need to incorporate time-dependent compaction mechanisms (e.g. pressure solution and subcritical crack growth). In chapter 5 the controls on yield curve evolution for porous rock were explored further using two high porosity

sandstones to see if the observations on porous bassanite are applicable to other rock types.

The yield curves of the porous sandstones are found to have a similar steep limb in the vicinity of P* as was observed for bassanite. However a major difference is that the yield curves have a much shallower geometry than those mapped for bassanite and also than previously reported yield curves for other sandstones (e.g. Wong et al., 1997a). This could be a result of the petrophysical properties of the sandstones studied in chapter 5, which are comprised of relatively coarse subrounded grains and well as being mineralogical immature with only about 50% quartz. However a more systematic study of the effect of grain shape, grain size and mineralogy is required to confirm this. Yield curve evolution for the porous sandstones, like bassanite, is dependent on the nature of inelastic strain. During hydrostatic compaction (purely volumetric strain) the changes are minor, with a slight expansion of the compactive side of the curve. Note that this is the opposite effect observed during hydrostatic compaction of bassanite, which could be because of different grain morphologies which result in different compaction mechanisms and hence different yield curve evolution. Sandstone deformation during hydrostatic compaction is dominated by grain crushing, whereas the platy grains of bassanite deform by grain rearrangement. During deviatoric loading, with a component of shear strain, the yield curve expands similar to that of porous bassanite. Comparison of yield curves along the different loading trajectories shows that a deviatorically compacted sandstone sample (to 6% axial displacement) has a peak that is 50% higher than a similar porosity hydrostatically compacted sample. The formation of a plateau at the peak of the curve also occurs during deviatoric compaction of sandstone. However no localized features were observed in the microstructure; rather there is a preferential alignment of microfractures orientated parallel to the maximum principal stress, which likely causes the difference in yield curve magnitude.

Which attributes of porous rock promote localized deformation is a big unanswered question. It is complicated further by there being different types of localized deformation band that can occur including dilation (Du Bernard et al., 2002), shear (Mair et al., 2000) and compaction bands (Olsson and Holcomb, 2000). Theoretical studies have tried to constrain the conditions that lead to each type of localized feature (e.g. Issen and Rudnicki, 2000), however there is disagreement between theory and experimental result (Wong et al., 2001; Baud et al., 2006). In

general, if localization is going to occur, the type of localized feature is related to the stress state the rock is at. Under low effective pressures dilational and dilational-shear bands are favoured. With increasing effective pressure compactional-shear and compaction bands form, until at even higher effective pressures distributed (non-localized) compaction occurs (Fossen et al., 2007). This transition from dilational bands to distributed compaction, with increasing effective pressure, is shown schematically in relation to a traditional yield curve in figure 6.1a. With increasing pressure, the angle of the localized feature with respect to the maximum principal

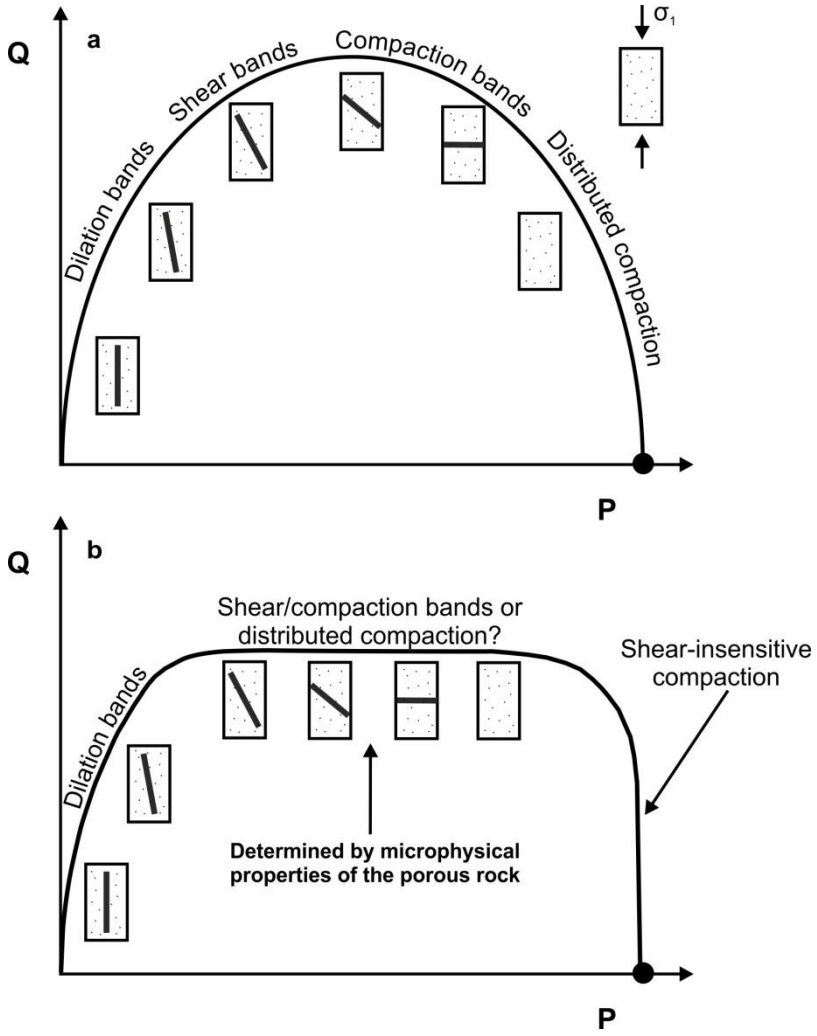


***Figure 6.1 – a)*** *A schematic diagram to show where different types of localization features would be expected to occur in relation to a traditional elliptical yield envelope. The angle of the band increases with respect to* $\sigma_1$ *with increasing effective mean stress.* ***b)*** *A schematic diagram of a yield curve that has evolved to form a broad transitional region at its peak. In this region there is range of possible deformation feature that could form and this is determined by the underlying microphysical properties of the rock.*

stress direction ($\sigma_1$) also increases. Previous experimental work has shown that shear and compaction localization occur near the peak of the yield curve (Olsson and Holcomb, 2000; Wong et al., 2001; Baud et al., 2004). However identification of a plateau forming at the peak of the yield curve in chapters 4 and 5 could help explain why our understanding of localization is poorly constrained. In this transitional zone, where compaction and dilatancy occur simultaneously, the nature of deformation is undetermined by the stress state alone. For porous bassanite shear bands formed in this region, whereas the porous sandstones displayed distributed compaction. The underlying microphysical properties of the rock will control the nature of deformation in this region (Fig. 6.1b). These include grain size, grain shape, pore geometry, nature of grain contacts, grain size distribution, mineralogy and mineralogical sorting. Cheung et al., (2012) showed that grain size distribution can influence localization behaviour; however the exact influence of different microphysical properties on the localization behaviour of porous rock is poorly constrained.

The investigations of yield curve evolution for both porous bassanite and sandstone have revealed some key conclusions that are applicable to both rock types. These are summarized below:

- The high pressure side of the yield curve is comprised partly of near vertical limb in the vicinity of P*.

- There is not a universal yield criterion, based on porosity and grain size alone, that can be applied to porous rock deformation in general.

- There is significant yield curve evolution as inelastic strain is accumulated (work hardening rule) and this is dependent on the nature of inelastic strain along different loading paths.

- The accumulation of inelastic shear strain along a deviatoric loading path produces a yield curve that is significantly greater in magnitude than similar porosity rocks that have been hydrostatically compacted.

- A plateau forms at the peak of the yield curve during continued deformation along a deviatoric loading path.

- It should be reiterated that porous rock deformation involves competition between compactional and dilational processes that occur simultaneously. Although this has been previously recognised (e.g. Brace, 1978; Mitchell and Faulkner, 2008) it is not always explicitly stated in studies of porous rock deformation.

## 6.2. Implications for dehydrating systems

In chapter 1 it was highlighted that much of the research into dehydration reactions has been aimed at trying to understand better the correlation between the depths at which hydrous minerals breakdown in a subducting slab and the occurrence of intermediate depth earthquakes. If dehydration embrittlement is the cause of unstable slip in these settings then weakening as a result of high pore fluid pressures is a prerequisite. The identification in chapter 3 that, under low effective pressure, pore connectivity is enhanced early in the reaction suggests that seismicity would be most likely to occur in these early stages prior to the establishment of an efficient drainage network. The early drainage of isolated pores observed in chapter 3 may support alternative hypotheses other than elevated pore pressure for the link between dehydration reactions and intermediate depth seismicity. This includes the idea that brittle deformation may be promoted by changes in frictional properties as a result of mineralogical transformations (e.g. Leclère et al., 2016) or the formation of fine-grained reaction products (e.g. Incel et al., 2017). It may also support the hypothesis that the site of reaction does not have to be the site of seismicity (Arkwright et al., 2008; Rutter et al., 2009; Leclère et al., 2016). The relatively quick enhancement of permeability could promote pore pressure pulses (e.g. *Leclère et al.*, 2016) that may cause embrittlement in neighbouring rocks. Pulses could also be driven by compaction of reaction generated porosity as the effective pressure increases with pore connectivity (Connolly, 1997).

Dehydration at higher effective pressure will promote compaction as the stress conditions intersect the yield curve of the dehydrating material. Compaction could also play a potentially important role in subduction zone seismicity. Firstly it will reduce the pore connectivity in the dehydrating rock, enabling the maintenance of locally high pore fluid pressures which could promote weakening and instability. Secondly it has

been shown in chapter 4 that localized deformation can occur during compaction along deviatoric loading paths. Localization is also an important prerequisite for the initiation of instabilities and it has been shown previously that dehydration products can preferentially form along localized deformation features (Leclère et al., 2016). In chapters 4 and 5 it was observed that there is mechanical and microstructural evolution of porous rock along deviatoric loading paths. This was reflected in the yield curve evolution and the formation of a plateau at the peak of the curve. The formation of a critical state zone, where both compaction and dilation are almost balanced, could promote the formation of localized shear bands which may ultimately experience unstable slip (Fig 6.1b). Previous work has suggested that localization in porous rock is promoted by a uniform grain size distribution (Cheung et al., 2012). The grain size of metamorphic rocks is dependent on the kinetic processes of nucleation and crystal growth (Philpotts and Ague, 2009). If nucleation is the dominant kinetic process and continuous throughout crystal growth then a range of grain sizes will result. If nucleation of new grains occurs at a similar time and crystal growth dominates the reaction rate a more uniform grain size distribution will result. In chapter 3 it was shown that during dehydration, reaction rate is controlled by diffusion of chemical components to the growing grains which favours a uniform grain size distribution. If the kinetics of dehydrating systems generates a uniform grain size distribution this may promote localization during subsequent deformation. Thus kinetics will control the microphysical properties of the dehydrating rock which may in turn determine the nature of deformation in dehydrating systems.

## 6.3. Implications for sandstone reservoirs

There has been much interest in sandstone compaction because of the implications for reservoir and geotechnical engineering. Yield curves provide a constraint on the conditions as which the onset of inelastic mechanical deformation will occur. This information can be used in conjunction with reservoir stress data to predict how much extraction can occur prior to inelastic compaction initiating (e.g. Chan and Zoback, 2002). Ideally this would be complimented by permeability data to identify how quickly the reservoir-scale stress field would respond to extraction through a wellbore. This would help identify whether significant stress perturbations might occur in the vicinity of the wellbore that could potentially trigger a breakout or

initiate faulting in neighbouring rock. Identification, in chapter 5, of sandstone yield curves that are much flatter than previously recognised implies that inelastic compaction may be initiated under lower stresses than previously thought. This is particularly relevant for wellbore stability because the flatness of the curve means that only a small stress perturbation, leading to an increase in differential stress, would be needed to cause yielding of the reservoir rock.

Identification of significantly evolving yield curves, where the evolution is dependent on the stress path, is important for understanding the long term evolution of the stress field and inelastic deformation in a reservoir. Significant variations in the stress history, and hence stress path in P-Q space, can occur during production of a reservoir (e.g. Hettema et al., 2000). The stress trajectory will also be different for extraction of hydrocarbons than it would be for fluid injection, for example during $CO_2$ sequestration. Therefore different parts of the yield curve will be intersected depending on the nature of the engineering. These different stress paths will lead to different microstructural evolution as inelastic strain is accumulated and hence differences in the rock strength.

## 6.4. Suggestions for future studies

Identification of the chemical transport pathways during dehydration reactions is important for understanding the kinetic controls on reaction and the evolution of the system as a whole. The study in chapter 3 is the first of its kind, where a microstructural record of the reaction products through time allows for the kinetic processes to be constrained. It therefore only scratches the surface with regard to understanding the underlying kinetics for dehydrating systems and metamorphic transformations in general. Diffusion of chemical constituents across reaction generated porosity is the dominant pathway during gypsum dehydration but it is yet to be established how important this is for the dehydration of other hydrous minerals. Llana-Funez et al., (2007) acquired micrographs of partially dehydrated serpentinite that show moat-like structures wrapping around forsterite grains, similar to those observed around bassanite during gypsum dehydration. This suggests that the same reaction pathway is in operation during serpentinite dehydration, however future studies should investigate if it has the same control on grain growth velocity as it does

for gypsum dehydration or whether other kinetic mechanisms control the overall reaction rate. It is also important to investigate how the kinetic processes will interact with the other parameters associated with dehydration reactions under different pressure and temperature conditions. For example dehydration at higher confining pressure will lead to compaction of the pore space which will in turn restrict fluid flow and shorten the distances required for chemical transport.

Future studies into porous rock deformation should investigate more thoroughly the microstructural and petrophysical characteristics of porous rock that cause differences in yield curve shape. Crawford et al., (2004) have shown that variations in yield curve aspect ratio can occur in loose sand based on grain size and grain shape, however more systematic investigations are needed that also incorporate the effect of different mineralogies. A better understanding of the underlying microphysical controls on yield curve shape will help to relate yield curve evolution with the microstructures that develop along different stress paths. Further studies should consider the effects of inelastic shear strain along different deviatoric loading trajectories; this will help to understand how yield curve evolution may differ between fluid extraction and injection in a reservoir. Finally more investigations are needed into what controls localization during porous rock deformation. Important questions to address in regard to this problem include, (i) what microphysical properties of the rock are important for localization, (ii) does a broad transitional zone form at the peak of the yield curve for other porous rocks and along different stress paths, (iii) can localization only be explained by non-associated flow.

# 7. References

Abers, G.A., Nakajima, J., van Keken, P.E., Kita, S., and Hacker, B.R., 2013, Thermal-petrological controls on the location of earthquakes within subducting plates: Earth and Planetary Science Letters, v. 369, p. 178–187, doi: 10.1016/j.epsl.2013.03.022.

Antonellini, M.A., Aydin, A., and Pollard, D.D., 1994, Microstructure of deformation bands in porous sandstones at Arches National Park, Utah: Journal of Structural Geology, v. 16, no. 7, p. 941–959.

Arkwright, J.C., Rutter, E.H., Brodie, K.H., and Llana-Funez, S., 2008, Role of porosity and dehydration reaction on the deformation of hot-pressed serpentinite aggregates: Journal of the Geological Society, v. 165, p. 639–649, doi: 10.1144/0016-76492007-119.

Atkinson, B.K., 1984, Subcritical Crack Growth in Geological Materials: Journal of Geophysical Research, v. 89, no. 10, p. 4077–4114, doi: 10.1029/JB089iB06p04077.

Atkinson, B.K., and Meredith, P.G., 1981, Stress corrosion cracking of quartz: a note on the influence of chemical environment: Tectonophysics, v. 77, p. T1–T11, doi: 10.1016/0040-1951(81)90157-8.

Aydin, A., and Johnson, A.M., 1978, Development of faults as zones of deformation bands and as slip surfaces in sandstone: Pure and Applied Geophysics PAGEOPH, v. 116, no. 4–5, p. 931–942, doi: 10.1007/BF00876547.

Ballas, G., Soliva, R., Sizun, J.P., Fossen, H., Benedicto, A., and Skurtveit, E., 2013, Shear-enhanced compaction bands formed at shallow burial conditions; implications for fluid flow (Provence, France): Journal of Structural Geology, v. 47, p. 3–15, doi: 10.1016/j.jsg.2012.11.008.

Baud, P., Klein, E., and Wong, T., 2004, Compaction localization in porous sandstones: spatial evolution of damage and acoustic emission activity: Journal of Structural Geology, v. 26, no. 4, p. 603–624, doi: 10.1016/j.jsg.2003.09.002.

Baud, P., Reuschle, T., Ji, Y.T., Cheung, C.S.N., and Wong, T.F., 2015, Mechanical compaction and strain localization in Bleurswiller sandstone: Journal of Geophysical Research-Solid Earth, v. 120, no. 9, p. 6501–6522, doi: 10.1002/2015jb012192.

Baud, P., Schubnel, A., and Wong, T., 2000a, Dilatancy, compaction, and failure mode in Solnhofen limestone: Journal of Geophysical Research: Solid Earth, v. 105, no. B8, p. 19289–19303, doi: 10.1029/2000jb900133.

Baud, P., Vajdova, V., and Wong, T.F., 2006, Shear-enhanced compaction and strain localization: Inelastic deformation and constitutive modeling of four porous sandstones: Journal of Geophysical Research: Solid Earth, v. 111, no. 12, p. B12401, doi: 10.1029/2005JB004101.

Baud, P., Vinciguerra, S., David, C., Cavallo, A., Walker, E., and Reuschlé, T., 2009, Compaction and Failure in High Porosity Carbonates: Mechanical Data and Microstructural Observations: Pure and Applied Geophysics, v. 166, no. 5–7, p. 869–898, doi: 10.1007/s00024-009-0493-2.

Baud, P., Zhu, W., and Wong, T., 2000b, Failure mode and weakening effect of water on sandstone: Journal of Geophysical Research: Solid Earth, v. 105, no. B7, p. 16371–16389, doi: 10.1029/2000jb900087.

Bedford, J.D., Faulkner, D.R., Leclère, H., and Wheeler, J., In review, Deforming porous rock: high-resolution mapping of yield curve evolution and the implications for compaction, dilation and localization: Journal of Geophysical Research - Solid Earth.

Du Bernard, X., Eichhubl, P., and Aydin, A., 2002, Dilation bands: A new form of localized failure in granular media: Geophysical Research Letters, v. 29, no. 24, p. 24–29, doi: 10.1029/2002gl015966.

Brace, W.F., 1978, Volume changes during fracture and frictional sliding: A review: Pure and Applied Geophysics PAGEOPH, v. 116, no. 4–5, p. 603–614, doi: 10.1007/BF00876527.

Brace, W.F., Walsh, J.B., and Frangos, W.T., 1968, Permeability of granite under high

pressure: Journal of Geophysical Research, v. 73, no. 6, p. 2225–2236, doi: 10.1029/JB073i006p02225.

Brantut, N., Han, R., Shimamoto, T., Findling, N., and Schubnel, A., 2011, Fast slip with inhibited temperature rise due to mineral dehydration: Evidence from experiments on gypsum: Geology, v. 39, no. 1, p. 59–62, doi: 10.1130/g31424.1.

Brantut, N., Schubnel, A., Corvisier, J., and Sarout, J., 2010, Thermochemical pressurization of faults during coseismic slip: Journal of Geophysical Research-Solid Earth, v. 115, p. B05313, doi: 10.1029/2009JB006533.

Brantut, N., Schubnel, A., David, E.C., Héripré, E., Guéguen, Y., and Dimanov, A., 2012, Dehydration-induced damage and deformation in gypsum and implications for subduction zone processes: Journal of Geophysical Research: Solid Earth, v. 117, no. 3, p. B03205, doi: 10.1029/2011JB008730.

Brudzinski, M.R., Thurber, C.H., Hacker, B.R., and Engdahl, E.R., 2007, Global prevalence of double Benioff zones: Science, v. 316, no. 5830, p. 1472–1474, doi: 10.1126/science.1139204.

Bubeck, A., Walker, R.J., Healy, D., Dobbs, M., and Holwell, D.A., 2017, Pore geometry as a control on rock strength: Earth and Planetary Science Letters, v. 457, p. 38–48, doi: 10.1016/j.epsl.2016.09.050.

Burlini, L., Di Toro, G., and Meredith, P., 2009, Seismic tremor in subduction zones: Rock physics evidence: Geophysical Research Letters, v. 36, no. 8, p. L08305, doi: 10.1029/2009GL037735.

Byerlee, J.D., and Brace, W.F., 1969, High-pressure mechanical instability in rocks: Science, v. 164, no. 3880, p. 713–715, doi: 10.1126/science.164.3880.713.

Carlson, W.D., 2002, Scales of disequilibrium and rates of equilibration during metamorphism: American Mineralogist, v. 87, no. 2–3, p. 185–204.

Carmichael, D.M., 1969, On the mechanism of prograde metamorphic reactions in quartz-bearing pelitic rocks: Contributions to Mineralogy and Petrology, v. 20, no. 3, p. 244–267, doi: 10.1007/bf00377479.

Carroll, M.M., 1991, A critical state plasticity theory for porous reservoir rock: Recent Advances in Mechanics of Structured Continua, v. 117, p. 1–8.

Chan, A.W., and Zoback, M.D., 2002, Deformation Analysis in Reservoir Space (DARS): A Simple Formalism for Prediction of Reservoir Deformation With Depletion, *in* SPE 78174 - SPE/ISRM Rock Mechanics Conference, Society of Petroleum Engineers, Irving, TX.

Chernak, L.J., and Hirth, G., 2011, Syndeformational antigorite dehydration produces stable fault slip: Geology, v. 39, no. 9, p. 847–850, doi: 10.1130/g31919.1.

Cheung, C.S.N., Baud, P., and Wong, T., 2012, Effect of grain size distribution on the development of compaction localization in porous sandstone: Geophysical Research Letters, v. 39, no. L21302, doi: 10.1029/2012gl053739.

Christensen, A.N., Olesen, M., Cerenius, Y., and Jensen, T.R., 2008, Formation and Transformation of Five Different Phases in the $CaSO_4$–$H_2O$ System: Crystal Structure of the Subhydrate β-$CaSO_4$·$0.5H_2O$ and Soluble Anhydrite $CaSO_4$: Chemistry of Materials, v. 20, no. 6, p. 2124–2132, doi: 10.1021/cm7027542.

Cilona, A., Faulkner, D.R., Tondi, E., Agosta, F., Mancini, L., Rustichelli, A., Baud, P., and Vinciguerra, S., 2014, The effects of rock heterogeneity on compaction localization in porous carbonates: Journal of Structural Geology, v. 67, p. 75–93, doi: 10.1016/j.jsg.2014.07.008.

Connolly, J.A.D., 1997, Devolatilization-generated fluid pressure and deformation-propagated fluid flow during prograde regional metamorphism: Journal of Geophysical Research-Solid Earth, v. 102, no. B8, p. 18149–18173, doi: 10.1029/97jb00731.

Crawford, B.R., Gooch, M.J.J., and Webb, D.W., 2004, Textural controls on constitutive behavior on unconsolidated sands: micromechanics and cap plasticity: 6th North America Rock Mechanics Symposium, v. 4, no. 611, p. 12.

Curran, J.H., and Carroll, M.M., 1979, Shear stress enhancement of void compaction: Journal of Geophysical Research, v. 84, no. B3, p. 1105–1112, doi: 10.1029/JB084iB03p01105.

Cuss, R.J., Rutter, E.H., and Holloway, R.F., 2003a, Experimental observations of the mechanics of borehole failure in porous sandstone: International Journal of Rock Mechanics and Mining Sciences, v. 40, p. 747–761, doi: 10.1016/S1365-1609(03)00068-6.

Cuss, R.J., Rutter, E.H., and Holloway, R.F., 2003b, The application of critical state soil mechanics to the mechanical behaviour of porous sandstones: International Journal of Rock Mechanics and Mining Sciences, v. 40, no. 6, p. 847–862, doi: 10.1016/s1365-1609(03)00053-4.

Cussler, E.L., 1984, Diffusion: Mass transfer in fluid systems: Cambridge University Press.

David, C., Wong, T.-F., Zhu, W., and Zhang, J., 1994, Laboratory measurement of compaction-induced permeability change in porous rocks: Implications for the generation and maintenance of pore pressure excess in the crust: Pure and Applied Geophysics PAGEOPH, v. 143, no. 1–3, p. 425–456, doi: 10.1007/bf00874337.

DiMaggio, F.L., and Sandler, I.S., 1971, Material model for granular soils: Journal of Engineering Mechanics, p. 935–950.

Dobson, D.P., Meredith, P.G., and Boon, S.A., 2002, Simulation of subduction zone seismicity by dehydration of serpentine: Science, v. 298, no. 5597, p. 1407–1410, doi: 10.1126/science.1075390.

Dresen, G., Stanchits, S., and Rybacki, E., 2010, Borehole breakout evolution through acoustic emission location analysis: International Journal of Rock Mechanics and Mining Sciences, v. 47, no. 3, p. 426–435, doi: 10.1016/j.ijrmms.2009.12.010.

Faulkner, D.R., and Armitage, P.J., 2013, The effect of tectonic environment on permeability development around faults and in the brittle crust: Earth and Planetary Science Letters, v. 375, p. 71–77, doi: 10.1016/j.epsl.2013.05.006.

Faulkner, D.R., and Rutter, E.H., 2001, Can the maintenance of overpressured fluids in large strike-slip fault zones explain their apparent weakness? Geology, v. 29, no. 6, p. 503–506, doi: 10.1130/0091-7613(2001)029<0503:ctmoof>2.0.co;2.

Fischer, G.J., 1992, The determination of permeability and storage capacity: Pore pressure oscillation method, *in* Evans, B. and Wong, T.F. eds., Fault Mechanics and Transport Properties of Rocks, Academic Press Ltd, p. 187–211.

Fisher, G., 1973, Nonequilibrium thermodynamics as a model for diffusion-controlled metamorphic processes: American Journal of Science, v. 273, p. 897–924, doi: 10.2475/ajs.273.10.897.

Fisher, G.W., 1978, Rate laws in metamorphism: Geochimica et Cosmochimica Acta, v. 42, no. 7, p. 1035-, doi: 10.1016/0016-7037(78)90292-2.

Fisher, Q.J., Casey, M., Clennell, M. Ben, and Knipe, R.J., 1999, Mechanical compaction of deeply buried sandstones of the North Sea: Marine and Petroleum Geology, v. 16, no. 7, p. 605–618, doi: 10.1016/S0264-8172(99)00044-6.

Fortin, J., Gueguen, Y., and Schubnel, A., 2007, Effects of pore collapse and grain crushing on ultrasonic velocities and Vp/Vs: Journal of Geophysical Research-Solid Earth, v. 112, no. B08207, doi: 10.1029/2005jb004005.

Fortin, J., Schubnel, A., and Gueguen, Y., 2005, Elastic wave velocities and permeability evolution during compaction of Bleurswiller sandstone: International Journal of Rock Mechanics and Mining Sciences, v. 42, no. 7–8, p. 873–889, doi: 10.1016/j.ijrmms.2005.05.002.

Fortin, J., Stanchits, S., Dresen, G., and Gueguen, Y., 2006, Acoustic emission and velocities associated with the formation of compaction bands in sandstone: Journal of Geophysical Research-Solid Earth, v. 111, no. B10, doi: 10.1029/2005jb003854.

Fossen, H., Schultz, R.A., Shipton, Z.K., and Mair, K., 2007, Deformation bands in sandstone: a review: Journal of the Geological Society, London, v. 164, p. 755–769, doi: 10.1144/0016-76492006-036.

Fossen, H., Schultz, R.A., and Torabi, A., 2011, Conditions and implications for compaction band formation in the Navajo Sandstone, Utah: Journal of Structural Geology, v. 33, no. 10, p. 1477–1490, doi: 10.1016/j.jsg.2011.08.001.

Fredrich, J.T., Deitrick, G.L., Arguello, J.G., and DeRouffignac, E.P., 1998, Reservoir Compaction , Surface Subsidence , and Casing Damage : A Geomechanics Approach to Mitigation and Reservoir Management, *in* Eurock - Rock Mechanics in Petroleum Engineering, SPE/ISRM, p. 403–412.

Freyer, D., and Voigt, W., 2003, Crystallization and phase stability of CaSO4 and CaSO4-based salts: Monatshefte Fur Chemie, v. 134, no. 5, p. 693–719, doi: 10.1007/s00706-003-0590-3.

Fusseis, F., Schrank, C., Liu, J., Karrech, A., Llana-Fúnez, S., Xiao, X., and Regenauer-Lieb, K., 2012, Pore formation during dehydration of a polycrystalline gypsum sample observed and quantified in a time-series synchrotron X-ray micro-tomography experiment: Solid Earth, v. 3, no. 1, p. 71–86, doi: 10.5194/se-3-71-2012.

Fusseis, F., Steeb, H., Xiao, X., Zhu, W., Butler, I.B., Elphick, S., and Maeder, U., 2014, A low-cost X-ray-transparent experimental cell for synchrotron-based X-ray microtomography studies under geological reservoir conditions: Journal of Synchrotron Radiation, v. 21, p. 251–253, doi: 10.1107/s1600577513026969.

Gao, X., and Wang, K., 2017, Rheological separation of the megathrust seismogenic zone and episodic tremor and slip: Nature, v. 543, p. 416–419, doi: 10.1038/nature21389.

Garth, T., and Rietbrock, A., 2014, Order of magnitude increase in subducted H2O due to hydrated normal faults within the Wadati-Benioff zone: Geology, v. 42, no. 3, p. 207–210, doi: 10.1130/g34730.1.

Gasc, J., Schubnel, A., Brunet, F., Guillon, S., Mueller, H.J., and Lathe, C., 2011, Simultaneous acoustic emissions monitoring and synchrotron X-ray diffraction at high pressure and temperature: Calibration and application to serpentinite dehydration: Physics of the Earth and Planetary Interiors, v. 189, no. 3–4, p. 121–133, doi: 10.1016/j.pepi.2011.08.003.

Gibbs, J.W., 1874, On the equilibrium of heterogeneous substances: Connecticut Academy of Arts and Sciences Transactions, v. 3, p. 108–248.

Goldsmith, A.S., 1989, Permeability decline and compressibility in sandstone reservoir

rocks, *in* Maury, V. and Fourmaintraux, D. eds., Rock at Great Depth, Balkema, Rotterdam, p. 923–928.

Graham, J., Noonan, M.L., and Lew, K. V, 1983, Yield states and stress–strain relationships in a natural plastic clay: Canadian Geotechnical Journal, v. 20, no. 3, p. 502–516, doi: 10.1139/t83-058.

Griffiths, J., Faulkner, D.R., Edwards, A.P., and Worden, R.H., 2016, Deformation band development as a function of intrinsic host-rock properties in Triassic Sherwood Sandstone: Geological Society, London, Special Publications, v. 435, p. 1–16, doi: 10.1144/SP435.11.

Griffiths, L., Heap, M.J., Xu, T., Chen, C., and Baud, P., 2017, The influence of pore geometry and orientation on the strength and stiffness of porous rock: Journal of Structural Geology, v. 96, p. 149–160, doi: 10.1016/j.jsg.2017.02.006.

Grueschow, E., and Rudnicki, J.W., 2005, Elliptic yield cap constitutive modeling for high porosity sandstone: International Journal of Solids and Structures, v. 42, no. 16–17, p. 4574–4587, doi: 10.1016/j.ijsolstr.2005.02.001.

Guersoy, D., De Carlo, F., Xiao, X., and Jacobsen, C., 2014, TomoPy: a framework for the analysis of synchrotron tomographic data: Journal of Synchrotron Radiation, v. 21, p. 1188–1193, doi: 10.1107/s1600577514013939.

Hacker, B.R., Peacock, S.M., Abers, G.A., and Holloway, S.D., 2003, Subduction factory 2. Are intermediate-depth earthquakes in subducting slabs linked to metamorphic dehydration reactions? Journal of Geophysical Research: Solid Earth, v. 108, no. B1, doi: 10.1029/2001jb001129.

Han, R., Shimamoto, T., Hirose, T., Ree, J.H., and Ando, J., 2007, Ultralow friction of carbonate faults caused by thermal decomposition: Science, v. 316, no. 5826, p. 878–881, doi: 10.1126/science.1139763.

Heap, M.J., Baud, P., Meredith, P.G., Bell, A.F., and Main, I.G., 2009, Time-dependent brittle creep in Darley Dale sandstone: Journal of Geophysical Research-Solid Earth, v. 114, no. B07203, doi: 10.1029/2008jb006212.

Heap, M.J., Farquharson, J.I., Baud, P., Lavallee, Y., and Reuschle, T., 2015, Fracture and compaction of andesite in a volcanic edifice: Bulletin of Volcanology, v. 77, no. 6, p. 55, doi: 10.1007/s00445-015-0938-7.

Heard, H.C., and Rubey, W.W., 1966, Tectonic Implications of Gypsum Dehydration: Geological Society of America Bulletin, v. 77, no. 7, p. 741–760, doi: Doi 10.1130/0016-7606(1966)77[741:Tiogd]2.0.Co;2.

Hettema, M.H.H., Schutjens, P.M.T.M., Verboom, B.J.M., and Gussinklo, H.J., 2000, Production-Induced Compaction of a Sandstone Reservoir: The Strong Influence of Stress Path: SPE Reservoir Evaluation & Engineering, v. 3, no. 4, p. 342–347, doi: 10.2118/65410-pa.

Hilairet, N., Reynard, B., Wang, Y.B., Daniel, I., Merkel, S., Nishiyama, N., and Petitgirard, S., 2007, High-pressure creep of serpentine, interseismic deformation, and initiation of subduction: Science, v. 318, no. 5858, p. 1910–1913, doi: 10.1126/science.1148494.

Hildyard, R.C., Llana-fúnez, S., Wheeler, J., Faulkner, D.R., and Prior, D.J., 2011, Electron backscatter diffraction (EBSD) analysis of bassanite transformation textures and crystal structure produced from experimentally deformed and dehydrated gypsum: Journal of Petrology, v. 52, no. 5, p. 839–856, doi: 10.1093/petrology/egr004.

Hirose, T., and Bystricky, M., 2007, Extreme dynamic weakening of faults during dehydration by coseismic shear heating: Geophysical Research Letters, v. 34, no. 14, doi: 10.1029/2007gl030049.

Hirth, G., and Tullis, J., 1989, The effects of pressure and porosity on the micromechanics of the brittle-ductile transition in quartzite: Journal of Geophysical Research, v. 94, no. B12, p. 17825, doi: 10.1029/JB094iB12p17825.

Hobbs, B.E., Muhlhaus, H.-B., and Ord, A., 1990, Instability, softening and localization of deformation, *in* Knipe, R.J. and Rutter, E.H. eds., Deformation Mechanisms, Rheology and Tectonics, Geological Society Special Publication, p. 143–165.

Hubbert, M.K., and Rubey, W.W., 1959, Role of Fluid Pressure in Mechanics of

Overthrust Faulting .1. Mechanics of Fluid-Filled Porous Solids and Its Application to Overthrust Faulting: Geological Society of America Bulletin, v. 70, no. 2, p. 115–166.

Incel, S., Nadege, H., Labrousse, L., John, T., Deldicque, D., Ferrand, T., Wang, Y., Renner, J., Morales, L., and Schubnel, A., 2017, Laboratory earthquakes triggered during eclogitization of lawsonite-bearing blueschist: Earth and Planetary Science Letters, v. 459, p. 320–331, doi: 10.1016/j.epsl.2016.11.047.

Issen, K.A., and Rudnicki, J.W., 2000, Conditions for compaction bands in porous rock: Journal of Geophysical Research: Solid Earth, v. 105, no. B9, p. 21529–21536, doi: 10.1029/2000jb900185.

Joesten, R., and Fisher, G., 1988, Kinetics of diffusion-controlled mineral growth in the Christmas Mountains (Texas) contact aureole: Bulletin of the Geological Society of America, v. 100, no. 5, p. 714–732, doi: 10.1130/0016-7606(1988)100<0714:KODCMG>2.3.CO;2.

Jonas, L., Müller, T., Dohmen, R., Baumgartner, L., and Putlitz, B., 2015, Transport-controlled hydrothermal replacement of calcite by Mg-carbonates: Geology, v. 43, no. 9, p. 779–782, doi: 10.1130/g36934.1.

Jordan, P., and Nuesch, R., 1989, Deformation Structures in the Muschelkalk Anhydrites of the Schafisheim-Well (Jura Overthrust, Northern Switzerland): Eclogae Geologicae Helvetiae, v. 82, no. 2, p. 429–454.

Jung, H., Green, H.W., and Dobrzhinetskaya, L.F., 2004, Intermediate-depth earthquake faulting by dehydration embrittlement with negative volume change: Nature, v. 428, no. 6982, p. 545–549, doi: 10.1038/nature02412.

Kirby, S., Engdahl, R.E., and Denlinger, R., 1996, Intermediate-Depth Intraslab Earthquakes and Arc Volcanism as Physical Expressions of Crustal and Uppermost Mantle Metamorphism in Subducting Slabs, *in* Subduction Top to Bottom, American Geophysical Union, p. 195–214.

Kita, S., Okada, T., Nakajima, J., Matsuzawa, T., and Hasegawa, A., 2006, Existence of a seismic belt in the upper plane of the double seismic zone extending in the along-

arc direction at depths of 70-100 km beneath NE Japan: Geophysical Research Letters, v. 33, no. 24, doi: 10.1029/2006gl028239.

Ko, S.C., Olgaard, D.L., and Briegel, U., 1995, The Transition from Weakening to Strengthening in Dehydrating Gypsum - Evolution of Excess Pore Pressures: Geophysical Research Letters, v. 22, no. 9, p. 1009–1012, doi: Doi 10.1029/95gl00886.

Ko, S.C., Olgaard, D.L., and Wong, T.F., 1997, Generation and maintenance of pore pressure excess in a dehydrating system .1. Experimental and microstructural observations: Journal of Geophysical Research-Solid Earth, v. 102, no. B1, p. 825–839, doi: 10.1029/96jb02485.

Kohlstedt, D.L., Evans, B., and Mackwell, S.J., 1995, Strength of the Lithosphere - Constraints Imposed by Laboratory Experiments: Journal of Geophysical Research-Solid Earth, v. 100, no. B9, p. 17587–17602, doi: Doi 10.1029/95jb01460.

Kranz, R.L., Saltzman, J.S., and Blacic, J.D., 1990, Hydraulic diffusivity measurements on laboratory rock samples using an oscillating pore pressure method: International Journal of Rock Mechanics and Mining Sciences and Geomechanics Abstracts, v. 27, no. 5, p. 345–352, doi: 10.1016/0148-9062(90)92709-N.

Lachenbruch, A.H., and Sass, J.H., 1980, Heat flow and energetics of the San Andreas Fault Zone: Journal of Geophysical Research: Solid Earth, v. 85, no. B11, p. 6185–6222, doi: 10.1029/JB085iB11p06185.

Lasaga, A.C., 1997, Kinetic theory in the Earth sciences : Princeton University Press.

Lasaga, A.C., 1986, Metamorphic Reaction Rate Laws and Development of Isograds: Mineralogical Magazine, v. 50, no. 357, p. 359–373, doi: 10.1180/minmag.1986.050.357.02.

Lasaga, A.C., and Rye, D.M., 1993, Fluid flow and chemical reaction kinetics in metamorphic systems: American Journal of Science, v. 293, no. 5, p. 361–404, doi: 10.2475/ajs.293.5.361.

Laubscher, H.P., 1975, Viscous Components in Jura Folding: Tectonophysics, v. 27, no. 3, p. 239–254, doi: Doi 10.1016/0040-1951(75)90019-0.

Leclère, H., Faulkner, D., Wheeler, J., and Mariani, E., 2016, Permeability control on transient slip weakening during gypsum dehydration: Implications for earthquakes in subduction zones: Earth and Planetary Science Letters, v. 442, p. 1–12, doi: 10.1016/j.epsl.2016.02.015.

Llana-Funez, S., Brodie, K.H., Rutter, E.H., and Arkwright, J.C., 2007, Experimental dehydration kinetics of serpentinite using pore volumometry: Journal of Metamorphic Geology, v. 25, no. 4, p. 423–438, doi: 10.1111/j.1525-1314.2007.00703.x.

Llana-Funez, S., Wheeler, J., and Faulkner, D.R., 2012, Metamorphic reaction rate controlled by fluid pressure not confining pressure: implications of dehydration experiments with gypsum: Contributions to Mineralogy and Petrology, v. 164, no. 1, p. 69–79, doi: 10.1007/s00410-012-0726-8.

Louis, L., Baud, P., and Wong, T., 2009, Microstructural Inhomogeneity and Mechanical Anisotropy Associated with Bedding in Rothbach Sandstone: Pure and Applied Geophysics, v. 166, no. 5–7, p. 1063–1087, doi: 10.1007/s00024-009-0486-1.

Lucier, A., Zoback, M., Gupta, N., and Ramakrishnan, T.S., 2006, Geomechanical aspects of CO2 sequestration in a deep saline reservoir in the Ohio River Valley region: Environmental Geosciences, v. 13, no. 2, p. 85–103, doi: 10.1306/eg.11230505010.

Mair, K., Main, I., and Elphick, S., 2000, Sequential growth of deformation bands in the laboratory: Journal of Structural Geology, v. 22, no. 1, p. 25–42, doi: 10.1016/s0191-8141(99)00124-8.

Makowitz, A., and Milliken, K.L., 2003, Quantification of brittle deformation in burial compaction, Frio and Mount Simon Formation sandstones: Journal of Sedimentary Research, v. 73, no. 6, p. 1007–1021, doi: 10.1306/051003731007.

Marcoux, J., Brun, J.P., Burg, J.P., and Ricou, L.E., 1987, Shear Structures in Anhydrite at the Base of Thrust Sheets (Antalya, Southern Turkey): Journal of Structural

Geology, v. 9, no. 5–6, p. 555–561, doi: Doi 10.1016/0191-8141(87)90140-4.

McConnell, J.D.C., Astill, D.M., and Hall, P.L., 1987, The pressure dependence of the dehydration of gypsum to bassanite: Mineralogical Magazine, v. 51, no. 361, p. 453–457, doi: 10.1180/minmag.1987.051.361.12.

Menéndez, B., Zhu, W., and Wong, T.-F., 1996, Micromechanics of brittle faulting and cataclastic flow in Berea sandstone: Journal of Structural Geology, v. 18, no. 1, p. 1–16, doi: http://dx.doi.org/10.1016/0191-8141(95)00076-P.

Milsch, H., Priegnitz, M., and Blöcher, G., 2011, Permeability of gypsum samples dehydrated in air: Geophysical Research Letters, v. 38, no. 18, doi: 10.1029/2011GL048797.

Milsch, H.H., and Scholz, C.H., 2005, Dehydration-induced weakening and fault slip in gypsum: Implications for the faulting process at intermediate depth in subduction zones: Journal of Geophysical Research B: Solid Earth, v. 110, no. 4, p. 1–16, doi: 10.1029/2004JB003324.

Mirwald, P.W., 2008, Experimental study of the dehydration reactions gypsum-bassanite and bassanite-anhydrite at high pressure: Indication of anomalous behavior of H2O at high pressure in the temperature range of 50–300 °C: Journal of Chemical Physics, v. 128, no. 7, p. 74502, doi: 10.1063/1.2826321.

Mitchell, T.M., and Faulkner, D.R., 2008, Experimental measurements of permeability evolution during triaxial compression of initially intact crystalline rocks and implications for fluid flow in fault zones: Journal of Geophysical Research-Solid Earth, v. 113, no. B11, doi: 10.1029/2008jb005588.

Miura, N., Murata, H., and Yasufuku, N., 1984, Stress-strain characteristics of sand in a particle-crushing region: Soils and Foundations, v. 24, no. 1, p. 77–89, doi: 10.3208/sandf1972.24.77.

Mollema, P.N., and Antonellini, M.A., 1996, Compaction bands: a structural analog for anti-mode I cracks in aeolian sandstone: Tectonophysics, v. 267, no. 1–4, p. 209–228, doi: 10.1016/s0040-1951(96)00098-4.

Murray, R.C., 1964, Origin and diagenesis of gypsum and anhydrite: Journal of Sedimentary Research, v. 34, no. 3, p. 512–523, doi: 10.1306/74D710D2-2B21-11D7-8648000102C1865D.

Murrell, S.A.F., and Ismail, I.A.H., 1976, Effect of Decomposition of Hydrous Minerals on Mechanical-Properties of Rocks at High-Pressures and Temperatures: Tectonophysics, v. 31, no. 3–4, p. 207–258, doi: Doi 10.1016/0040-1951(76)90120-7.

Nagel, N.B., 2001, Compaction and subsidence issues within the petroleum industry: From Wilmington to Ekofisk and beyond: Physics and Chemistry of the Earth, Part A: Solid Earth and Geodesy, v. 26, no. 1–2, p. 3–14, doi: 10.1016/S1464-1895(01)00015-1.

Nakajima, J., Tsuji, Y., Hasegawa, A., Kita, S., Okada, T., and Matsuzawa, T., 2009, Tomographic imaging of hydrated crust and mantle in the subducting Pacific slab beneath Hokkaido, Japan: Evidence for dehydration embrittlement as a cause of intraslab earthquakes: Gondwana Research, v. 16, no. 3–4, p. 470–481, doi: 10.1016/j.gr.2008.12.010.

Nguyen, V.H., Gland, N., Dautriat, J., David, C., Wassermann, J., and Guélard, J., 2014, Compaction, permeability evolution and stress path effects in unconsolidated sand and weakly consolidated sandstone: International Journal of Rock Mechanics and Mining Sciences, v. 67, p. 226–239, doi: 10.1016/j.ijrmms.2013.07.001.

Okazaki, K., and Hirth, G., 2016, Dehydration of lawsonite could directly trigger earthquakes in subducting oceanic crust: Nature, v. 530, no. 7588, p. 81–84, doi: 10.1038/nature16501.

Olgaard, D.L., Ko, S., and Wong, T., 1995, Deformation and pore pressure in dehydrating gypsum under transiently drained conditions: Tectonophysics, v. 245, no. 3–4, p. 237–248, doi: 10.1016/0040-1951(94)00237-4.

Olsson, W.A., and Holcomb, D.J., 2000, Compaction localization in porous rock: Geophysical Research Letters, v. 27, no. 21, p. 3537–3540, doi: 10.1029/2000gl011723.

Paterson, M., and Wong, T., 2005, Experimental Rock Deformation — The Brittle Field:

Paukert, A.N., Matter, J.M., Kelemen, P.B., Shock, E.L., and Havig, J.R., 2012, Reaction path modeling of enhanced in situ $CO_2$ mineralization for carbon sequestration in the peridotite of the Samail Ophiolite, Sultanate of Oman: Chemical Geology, v. 330–331, p. 86–100, doi: 10.1016/j.chemgeo.2012.08.013.

Peacock, S.M., 2001, Are the lower planes of double seismic zones caused by serpentine dehydration in subducting oceanic mantle? Geology, v. 29, no. 4, p. 299–302, doi: 10.1130/0091-7613(2001)029<0299:atlpod>2.0.co;2.

Peacock, S.A., 1990, Fluid Processes in subduction zones: Science, v. 248, no. 4953, p. 329–337, doi: 10.1126/science.248.4953.329.

Philpotts, A.R., and Ague, J.J., 2009, Principles of igneous and metamorphic petrology: Cambridge University Press, Cambridge, UK.

Plümper, O., John, T., Podladchikov, Y.Y., Vrijmoed, J.C., and Scambelluri, M., 2016, Fluid escape from subduction zones controlled by channel-forming reactive porosity: Nature Geoscience, v. 10, no. December, p. 150–156, doi: 10.1038/NGEO2865.

Pluymakers, A.M.H., Peach, C.J., and Spiers, C.J., 2014, Diagenetic compaction experiments on simulated anhydrite fault gouge under static conditions: Journal of Geophysical Research-Solid Earth, v. 119, no. 5, p. 4123–4148, doi: 10.1002/2014jb011073.

Powell, R., and Holland, T., 2010, Using equilibrium thermodynamics to understand metamorphism and metamorphic rocks: Elements, v. 6, no. 5, p. 309–314, doi: 10.2113/gselements.6.5.309.

Proctor, B., and Hirth, G., 2015, Role of pore fluid pressure on transient strength changes and fabric development during serpentine dehydration at mantle conditions: Implications for subduction-zone seismicity: Earth and Planetary Science Letters, v. 421, p. 1–12, doi: 10.1016/j.epsl.2015.03.040.

Raleigh, C.B., and Paterson, M.S., 1965, Experimental Deformation of Serpentinite and Its Tectonic Implications: Journal of Geophysical Research, v. 70, no. 16, p. 3965–

3985, doi: DOI 10.1029/JZ070i016p03965.

Rhett, D.W., and Teufel, L.W., 1992, Effect of Reservoir Stress Path on Compressibility and Permeability of Sandstones: Proceedings of SPE Annual Technical Conference and Exhibition, p. 965–972, doi: 10.2523/24756-MS.

Rubey, W.W., and Hubbert, M.K., 1959, Role of Fluid Pressure in Mechanics of Overthrust Faulting .2. Overthrust Belt in Geosynclinal Area of Western Wyoming in Light of Fluid-Pressure Hypothesis: Geological Society of America Bulletin, v. 70, no. 2, p. 167–205, doi: Doi 10.1130/0016-7606(1959)70[167:Rofpim]2.0.Co;2.

Rubie, D.C., and Thompson, A.B., 1985, Kinetics of metamorphic reactions at elevated temperatures and pressures: An appraisal of available experimental data, *in* Thompson, A.B. and Rubie, D.C. eds., Metamorphic reactions: Kinetics, textures and deformation, Springer-Verlag, New York, p. 27–79.

Rudnicki, J.W., and Rice, J.R., 1975, Conditions for the localization of deformation in pressure-sensitive dilatant materials: Journal of the Mechanics and Physics of Solids, v. 23, no. 6, p. 371–394, doi: 10.1016/0022-5096(75)90001-0.

Rutter, E.H., 1976, The kinetics of rock deformation by pressure solution: Philosophical Transactions of the Royal Society of London. Series A, v. 283, p. 203–219, doi: 10.1098/rspa.1952.0029.

Rutter, E.H., and Brodie, K.H., 1988, Experimental syntectonic dehydration of serpentinite under conditions of controlled pore water-pressure: Journal of Geophysical Research-Solid Earth and Planets, v. 93, no. B5, p. 4907–4932, doi: 10.1029/JB093iB05p04907.

Rutter, E.H., and Brodie, K.H., 1995, Mechanistic interactions between deformation and metamorphism: Geological Journal, v. 30, no. 3–4, p. 227–240, doi: 10.1002/gj.3350300304.

Rutter, E.H., and Glover, C.T., 2012, The deformation of porous sandstones; are Byerlee friction and the critical state line equivalent? Journal of Structural Geology, v. 44, p. 129–140, doi: 10.1016/j.jsg.2012.08.014.

Rutter, E.H., and Hadizadeh, J., 1991, On the influence of porosity on the low-temperature brittle—ductile transition in siliciclastic rocks: Journal of Structural Geology, v. 13, no. 5, p. 609–614, doi: 10.1016/0191-8141(91)90047-m.

Rutter, E.H., Llana-Fúnez, S., and Brodie, K.H., 2009, Dehydration and deformation of intact cylinders of serpentinite: Journal of Structural Geology, v. 31, no. 1, p. 29–43, doi: 10.1016/j.jsg.2008.09.008.

Schindelin, J., Arganda-Carreras, I., Frise, E., Kaynig, V., Longair, M., Pietzsch, T., Preibisch, S., Rueden, C., Saalfeld, S., Schmid, B., Tinevez, J.-Y., White, D.J., Hartenstein, V., Eliceiri, K., et al., 2012, Fiji: an open source platform for biological image analysis: Nature Methods, v. 9, no. 7, p. 676–682, doi: 10.1038/nmeth.2019.

Schofield, A., and Wroth, P., 1968, Critical state soil mechanics: McGraw-Hill.

Seno, T., Zhao, D.P., Kobayashi, Y., and Nakamura, M., 2001, Dehydration of serpentinized slab mantle: Seismic evidence from southwest Japan: Earth Planets and Space, v. 53, no. 9, p. 861–871.

Singh, N.B., and Middendorf, B., 2007, Calcium sulphate hemihydrate hydration leading to gypsum crystallization: Progress in Crystal Growth and Characterization of Materials, v. 53, no. 1, p. 57–77, doi: 10.1016/j.pcrysgrow.2007.01.002.

Sulak, R.M., 1991, Ekofisk Field: The First 20 Years: Journal of Petroleum Technology, v. 43, no. 10, p. 1265–1271, doi: 10.2118/20773-pa.

Sulem, J., and Famin, V., 2009, Thermal decomposition of carbonates in fault zones: Slip-weakening and temperature-limiting effects: Journal of Geophysical Research: Solid Earth, v. 114, no. B3, p. B03309, doi: 10.1029/2008JB006004.

Takahashi, M., Uehara, S.-I., Mizoguchi, K., Shimizu, I., Okazaki, K., and Masuda, K., 2011, On the transient response of serpentine (antigorite) gouge to stepwise changes in slip velocity under high-temperature conditions: Journal of Geophysical Research: Solid Earth, v. 116, no. B10, doi: 10.1029/2010JB008062.

Tatsuoka, F., and Ishihara, K., 1974, Yielding of sand in triaxial compression: Soils and Foundations, v. 14, no. 2, p. 63–76, doi: 10.3208/sandf1972.14.2_63.

Tembe, S., Baud, P., and Wong, T., 2008, Stress conditions for the propagation of discrete compaction bands in porous sandstone: Journal of Geophysical Research-Solid Earth, v. 113, no. B9, doi: 10.1029/2007jb005439.

Tembe, S., Vajdova, V., Baud, P., Zhu, W., and Wong, T., 2007, A new methodology to delineate the compactive yield cap of two porous sandstones under undrained condition: Mechanics of Materials, v. 39, no. 5, p. 513–523, doi: 10.1016/j.mechmat.2006.08.005.

Teufel, L.W., Rhett, D.W., and Farrell, H.E., 1991, Effect of Reservoir Depletion And Pore Pressure Drawdown On In Situ Stress And Deformation In the Ekofisk Field, North Sea: The 32nd U.S. Symposium on Rock Mechanics (USRMS), v. 32, p. 63–72.

Vajdova, V., Baud, P., and Wong, T., 2004, Compaction, dilatancy, and failure in porous carbonate rocks: Journal of Geophysical Research: Solid Earth, v. 109, no. B5, doi: 10.1029/2003jb002508.

Vajdova, V., Baud, P., Wu, L., and Wong, T., 2012, Micromechanics of inelastic compaction in two allochemical limestones: Journal of Structural Geology, v. 43, p. 100–117, doi: 10.1016/j.jsg.2012.07.006.

Walther, J. V, and Wood, B.J., 1984, Rate and mechanism in prograde metamorphism: Contributions to Mineralogy and Petrology, v. 88, no. 3, p. 246–259, doi: 10.1007/bf00380169.

Wang, W.H., and Wong, T.F., 2003, Effects of reaction kinetics and fluid drainage on the development of pore pressure excess in a dehydrating system: Tectonophysics, v. 370, no. 1–4, p. 227–239, doi: 10.1016/s0040-1951(03)00188-4.

Wheeler, J., 1991, A view of texture dynamics: Terra Nova, v. 3, no. 2, p. 123–136, doi: 10.1111/j.1365-3121.1991.tb00864.x.

Wheeler, J., 2014, Dramatic effects of stress on metamorphic reactions: Geology, v. 42, no. 8, p. 647–650, doi: 10.1130/G35718.1.

Wheeler, J., 1987, The significance of grain-scale stresses in the kinetics of metamorphism: Contributions to Mineralogy and Petrology, v. 97, no. 3, p. 397–

404, doi: 10.1007/BF00372002.

Wheeler, J., Mangan, L.S., and Prior, D.J., 2004, Disequilibrium in the Ross of Mull contact metamorphic aureole, Scotland: a consequence of polymetamorphism: Journal of Petrology, v. 45, no. 4, p. 835–853, doi: 10.1093/petrology/egg113.

Wong, T., and Baud, P., 2012, The brittle-ductile transition in porous rock: A review: Journal of Structural Geology, v. 44, p. 25–53, doi: 10.1016/j.jsg.2012.07.010.

Wong, T., Baud, P., and Klein, E., 2001, Localized failure modes in a compactant porous rock: Geophysical Research Letters, v. 28, no. 13, p. 2521–2524, doi: 10.1029/2001gl012960.

Wong, T., David, C., and Zhu, W., 1997a, The transition from brittle faulting to cataclastic flow in porous sandstones: Mechanical deformation: Journal of Geophysical Research: Solid Earth, v. 102, no. B2, p. 3009–3025, doi: 10.1029/96jb03281.

Wong, T., Ko, S., and Olgaard, D.L., 1997b, Generation and maintenance of pore pressure excess in a dehydrating system 2. Theoretical analysis: Journal of Geophysical Research: Solid Earth, v. 102, no. B1, p. 841–852, doi: 10.1029/96jb02484.

Wong, T., Szeto, H., and Zhang, J., 1992, Effect of loading path and porosity on the failure mode of porous rocks: Applied Mechanics Reviews, v. 45, no. 8, p. 281–293.

Wood, D.M., 1991, Soil Behaviour and Critical State Soil Mechanics: Cambridge university press.

Wood, B.J., and Fraser, D.G., 1976, Elementary thermodynamics for geologists: Oxford University Press, Oxford.

Wood, D.M., and Maeda, K., 2008, Changing grading of soil: Effect on critical states: Acta Geotechnica, v. 3, no. 1, p. 3–14, doi: 10.1007/s11440-007-0041-0.

Wu, X.Y., Baud, P., and Wong, T., 2000, Micromechanics of compressive failure and spatial evolution of anisotropic damage in Darley Dale sandstone: International Journal of Rock Mechanics and Mining Sciences, v. 37, no. 1–2, p. 143–160, doi: 10.1016/S1365-1609(99)00093-3.

Yuan-Hui, L., and Gregory, S., 1974, Diffusion of ions in sea water and in deep-sea sediments: Geochimica Et Cosmochimica Acta, v. 38, no. 5, p. 703–714, doi: 10.1016/0016-7037(74)90145-8.

Yund, R.A., 1997, Rates of grain boundary diffusion through enstatite and forsterite reaction rims: Contributions to Mineralogy and Petrology, v. 126, no. 3, p. 224–236, doi: 10.1007/s004100050246.

Zhang, J., Rai, C.S., and Sondergeld, C.H., 2000, Mechanical strength of reservoir materials: key information for sand prediction: SPE Reservoir Evaluation & Engineering, v. 3, no. 2, p. 127–131.

Zhang, J., Wong, T.F., and Davis, D.M., 1990a, High pressure embrittlement and shear-enhanced compaction of Berea sandstone: Acoustic emission measurement and microstructural observation, *in* The 31th US Symposium on Rock Mechanics (USRMS), American Rock Mechanics Association.

Zhang, J., Wong, T.-F., and Davis, D.M., 1990b, Micromechanics of pressure-induced grain crushing in porous rocks: Journal of Geophysical Research, v. 95, no. B1, p. 341–352, doi: 10.1029/JB095iB01p00341.

Zhang, J., Wong, T.-F., Yanagidani, T., and Davis, D.M., 1990c, Pressure-induced microcracking and grain crushing in Berea and Boise sandstones: acoustic emission and quantitative microscopy measurements: Mechanics of Materials, v. 9, no. 1, p. 1–15, doi: 10.1016/0167-6636(90)90026-c.

Zhu, W., Baud, P., Vinciguerra, S., and Wong, T., 2011, Micromechanics of brittle faulting and cataclastic flow in Alban Hills tuff: Journal of Geophysical Research, v. 116, no. B06209, doi: 10.1029/2010jb008046.

Zhu, W., and Wong, T., 1997, The transition from brittle faulting to cataclastic flow: Permeability evolution: Journal of Geophysical Research, v. 102, no. B2, p. 3027–3041, doi: 10.1029/96JB03282.

Zoback, M.D., 2010, Reservoir Geomechanics: Cambridge University Press.

# Appendix I

## Experimental calibrations.

Calibrations are for the triaxial experimental apparatus described in section 2.3. The following calibrations were performed by John Bedford:

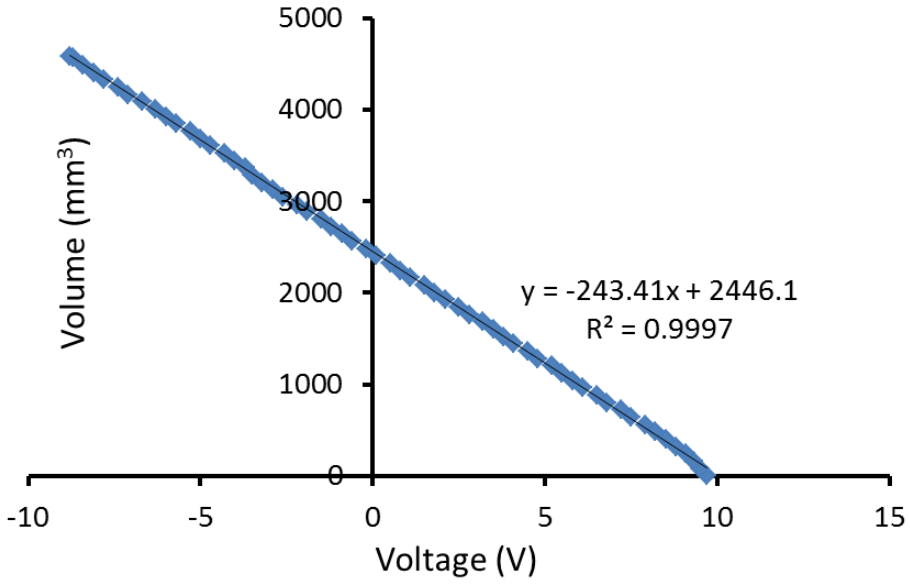


*LVDT calibration for the pore pressure control pump (Fig. 2.11).*

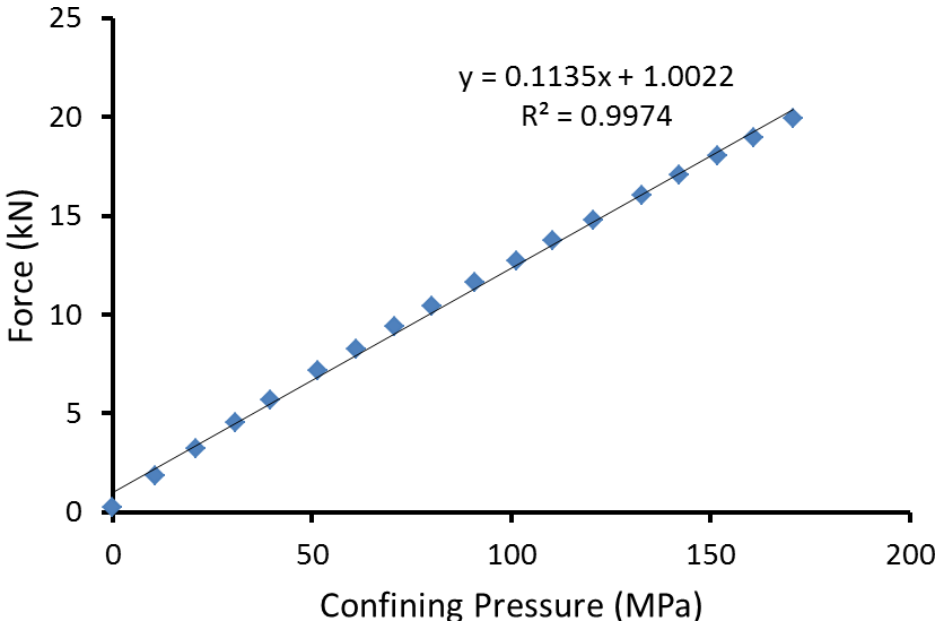


*Load applied to force gauge by confining pressure.*

The following calibrations were performed by other rig users:

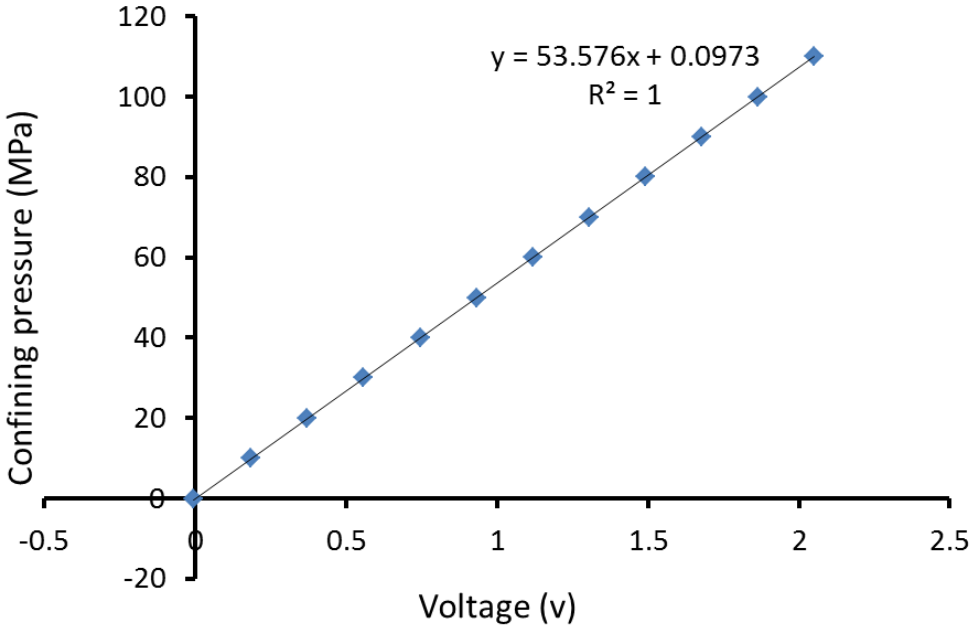


*Confining pressure transducer calibration.*

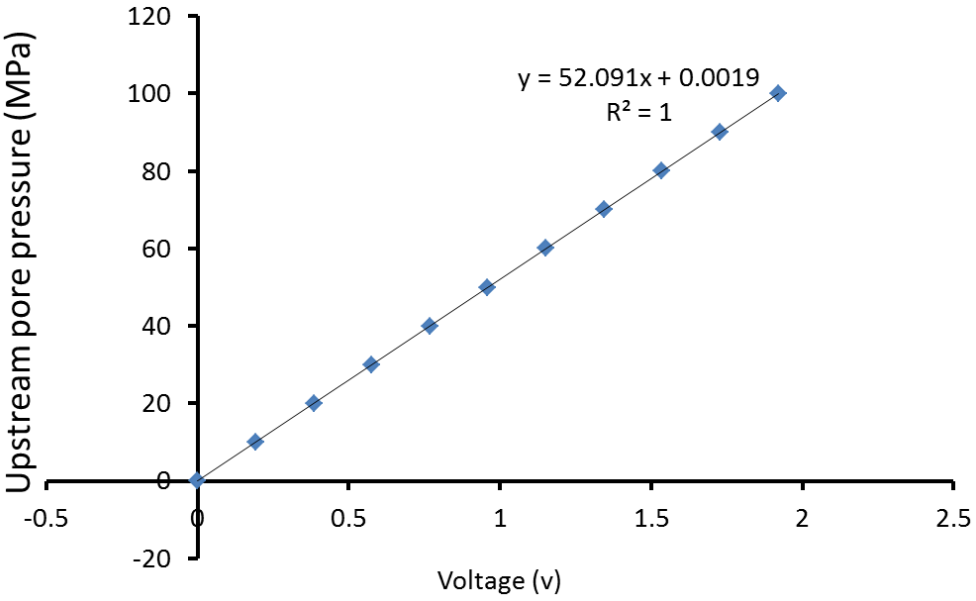


*Upstream pore pressure transducer calibration.*

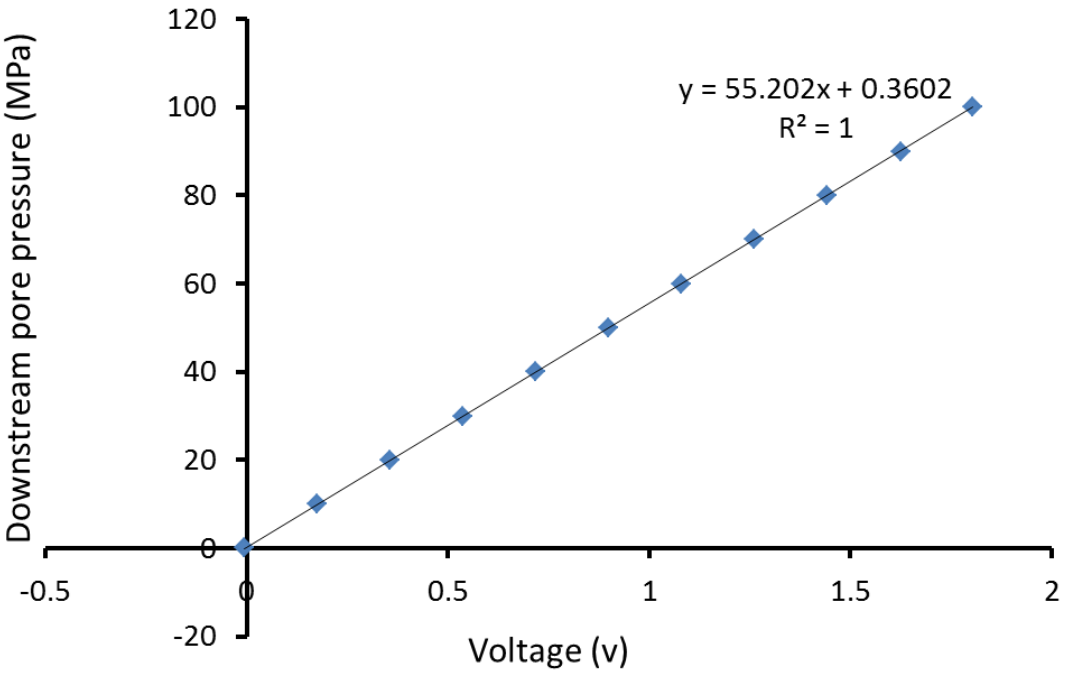


*Downstream pore pressure transducer calibration.*

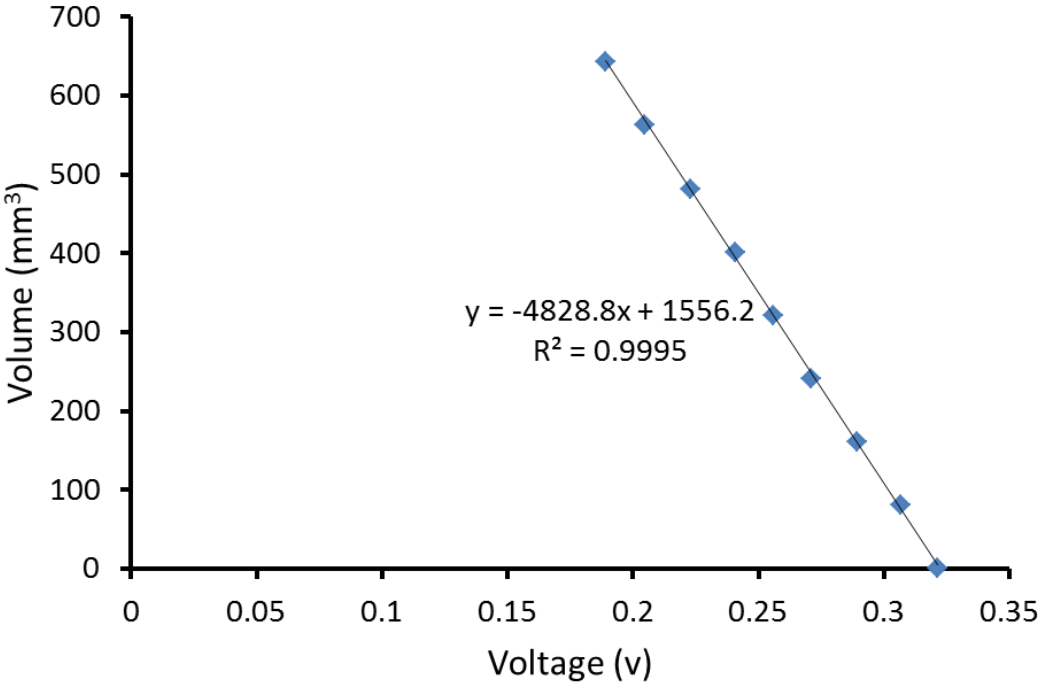


*LVDT for the confining pressure control pump (Fig. 2.9).*

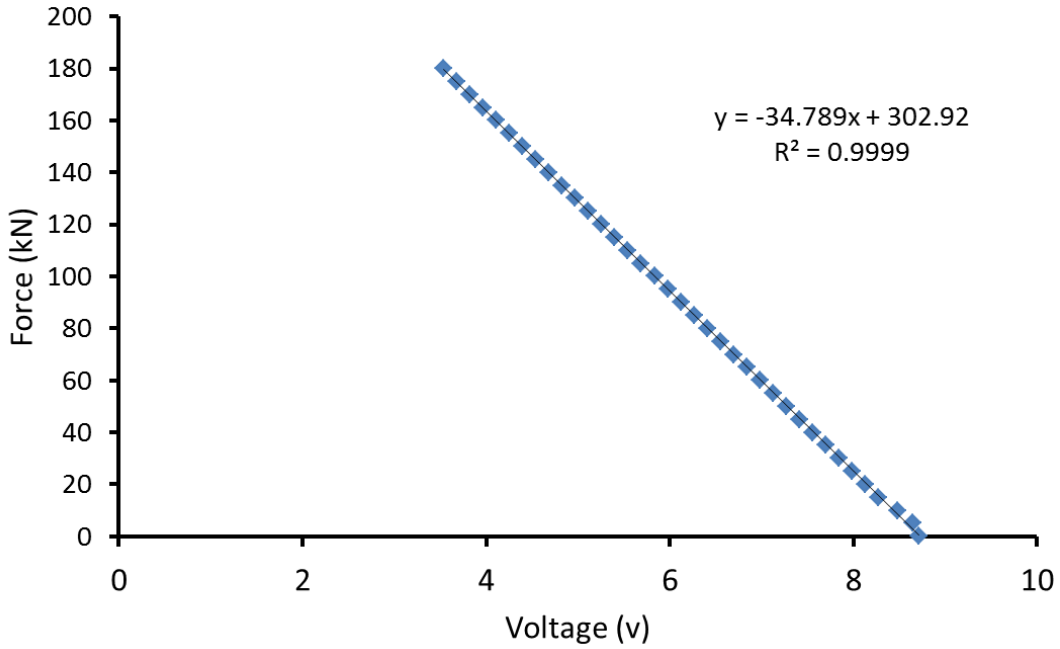


*Force gauge LVDT calibration.*

# Appendix II

## Porosity, permeability and seismic wave velocities

Porosity, permeability and seismic wave velocity data were collected for fully dehydrated samples of bassanite and γ-anhydrite (soluble anhydrite). γ-anhydrite is formed in an oven by the dehydration of bassanite at 125 °C. The porosity, permeability and seismic wave velocity data was collected as the effective pressure was cyclically increased and decreased. Relative changes in pore volume were tracked using the pore volumometer. Permeability was measured used the pulse transient decay method (Brace et al., 1968). Seismic wave velocities were measured using a seismic sample assembly which has piezoelectric crystals attached to the top and bottom platens. A pulser/receiver causes the top crystals to oscillate, generating P- and S-waves which travel through the sample and are received by the bottom crystals. The received pulse is displayed on an oscilloscope with received energy along the vertical axis and elapsed time along the horizontal axis. The seismic wave velocities can then be calculated from travel time of the first arrival of this pulse.

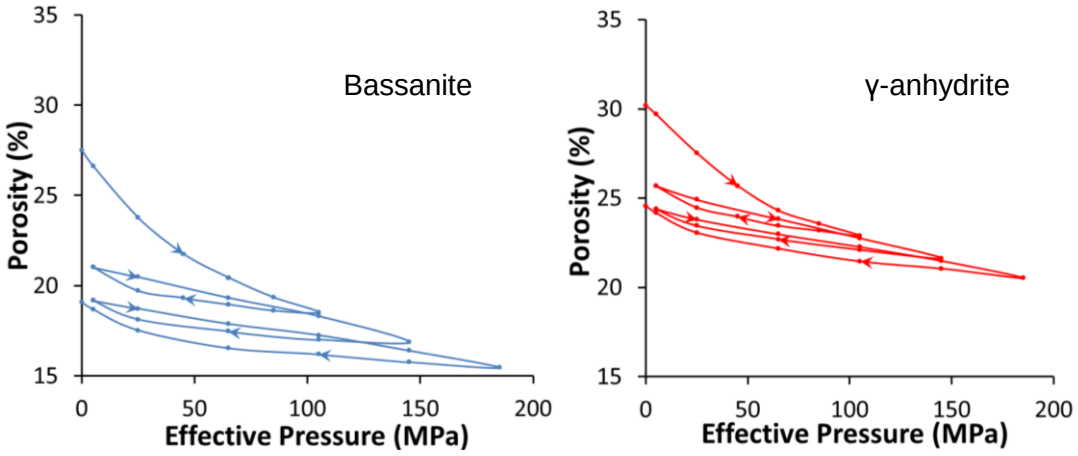


*Porosity evolution with increasing/decreasing effective pressure for bassanite (blue) and γ-anhydrite (red).*

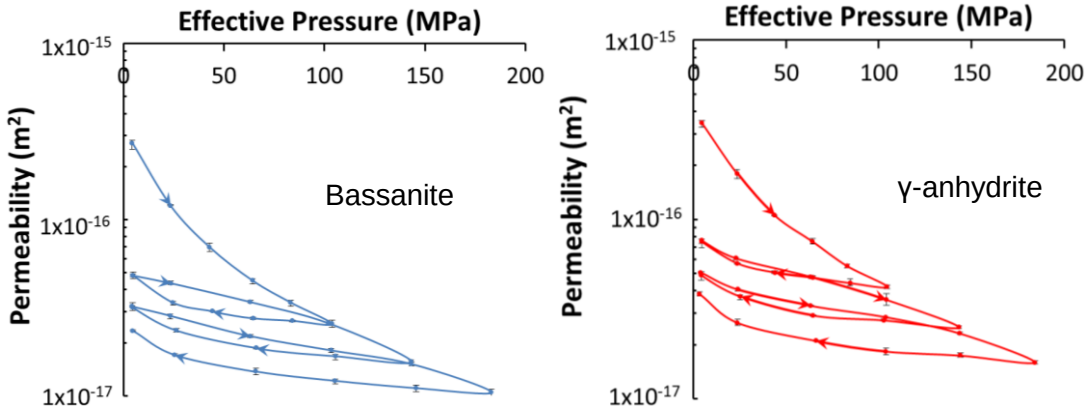


*Permeability evolution with increasing/decreasing effective pressure for bassanite (blue) and γ-anhydrite (red).*

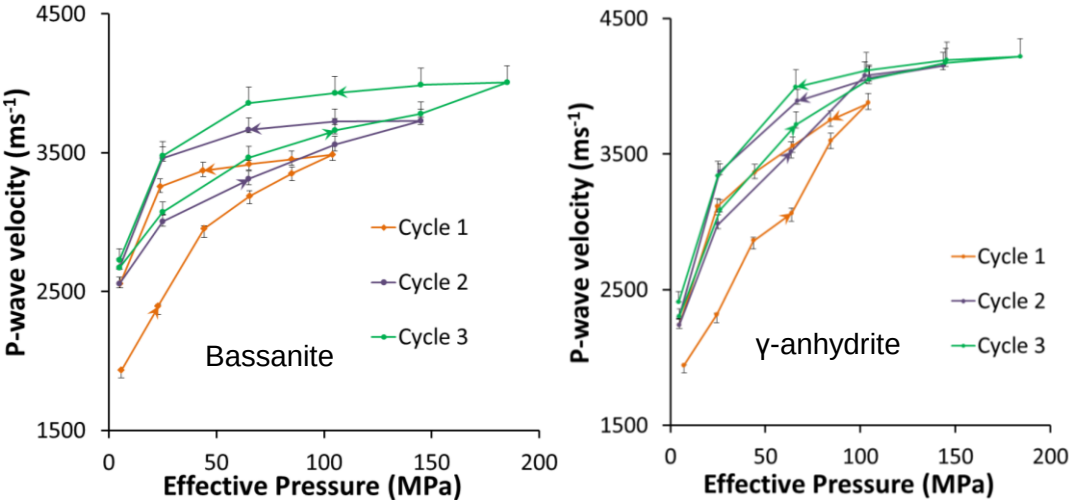


*P-wave velocity evolution with increasing/decreasing effective pressure for bassanite (left) and γ-anhydrite (right).*

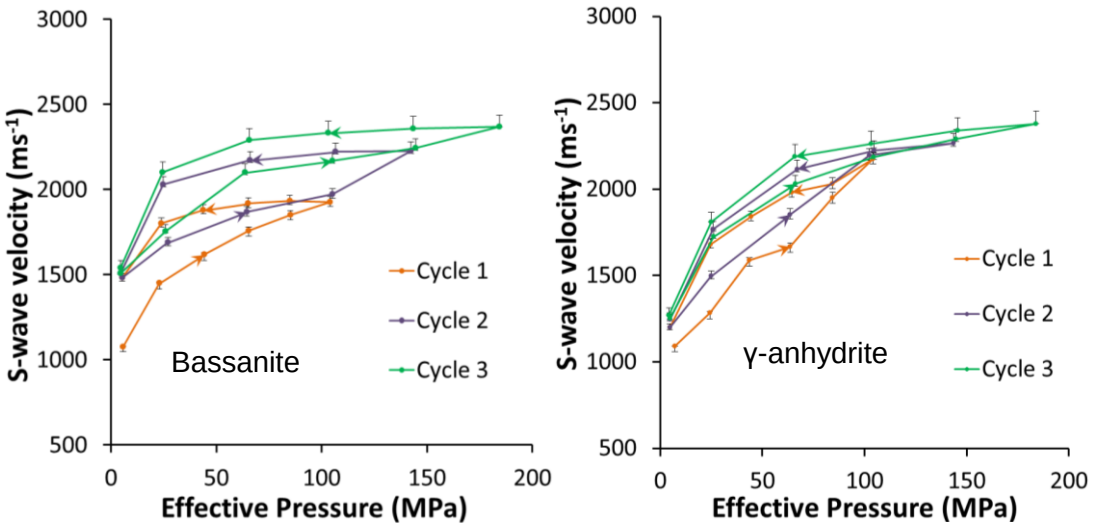


*S-wave velocity evolution with increasing/decreasing effective pressure for bassanite (left) and γ-anhydrite (right).*

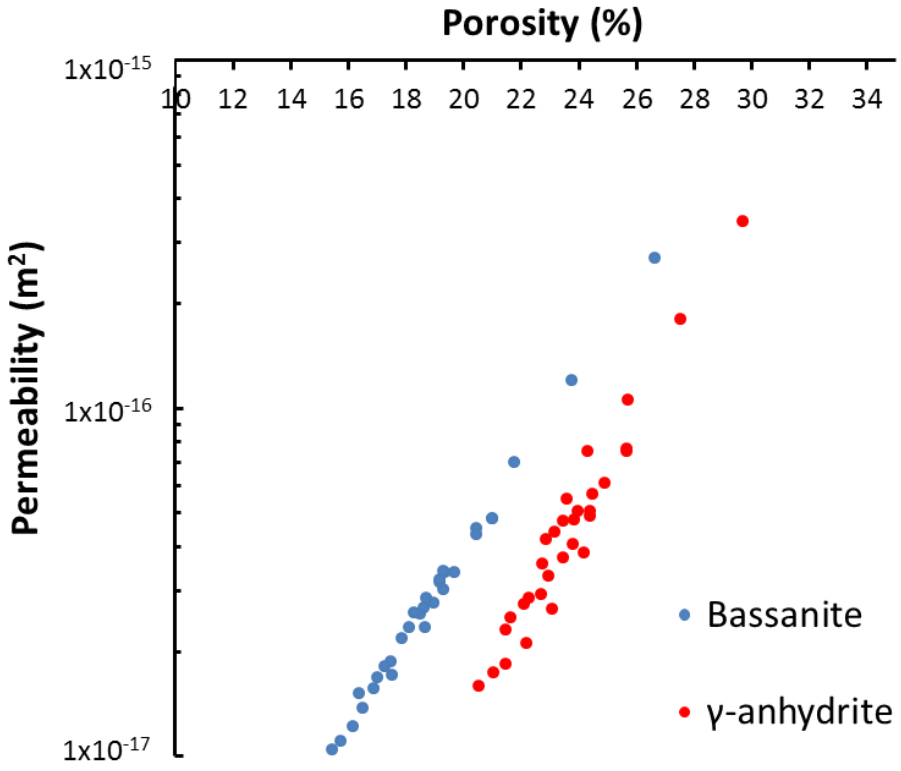


*Porosity-permeability relationship for bassanite and γ-anhydrite. The data fit a power-law relationship with an exponent (n) of 5.77 for bassanite and 8.23 for γ-anhydrite.* Wang and Wong (2003) *suggest an exponent of n=9 for porosities greater than 1.5% during gypsum dehydration.*

# Appendix III

## QEMSCAN mineralogy maps of the porous sandstones

QEMSCAN was used to calculate the modal abundance of different minerals in the two sandstones studied in chapter 5. Thanks to James Utley for assistance with the QEMSCAN. Below are the mineralogy maps that were acquired.

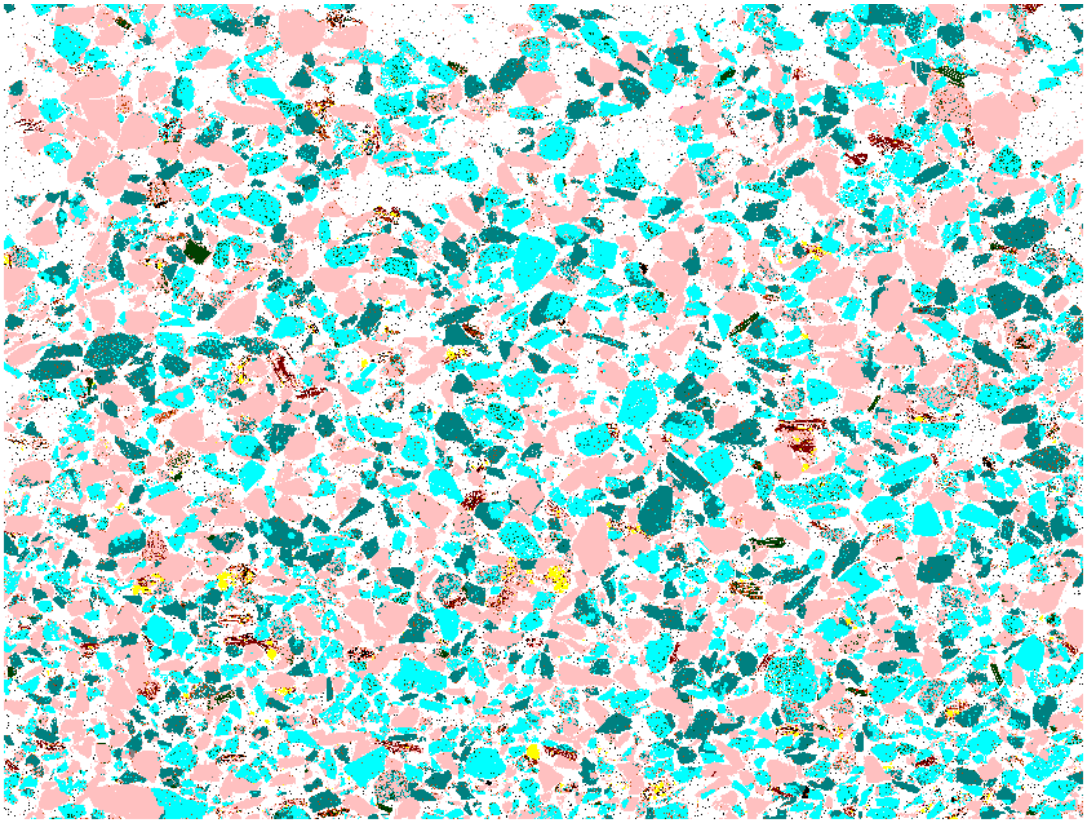

**Mineral Name**

- Porosity
- Quartz
- K-Feldspar
- Plagioclase
- Fe-Oxides and carbonates
- Muscovite
- Biotite
- Clays
- Pyrite
- Rutile
- Apatite
- Zircon
- Al Oxide
- Unclassified
- Others

*QEMSCAN map of Boise sandstone.*

*Horizontal scan length is 17mm.*

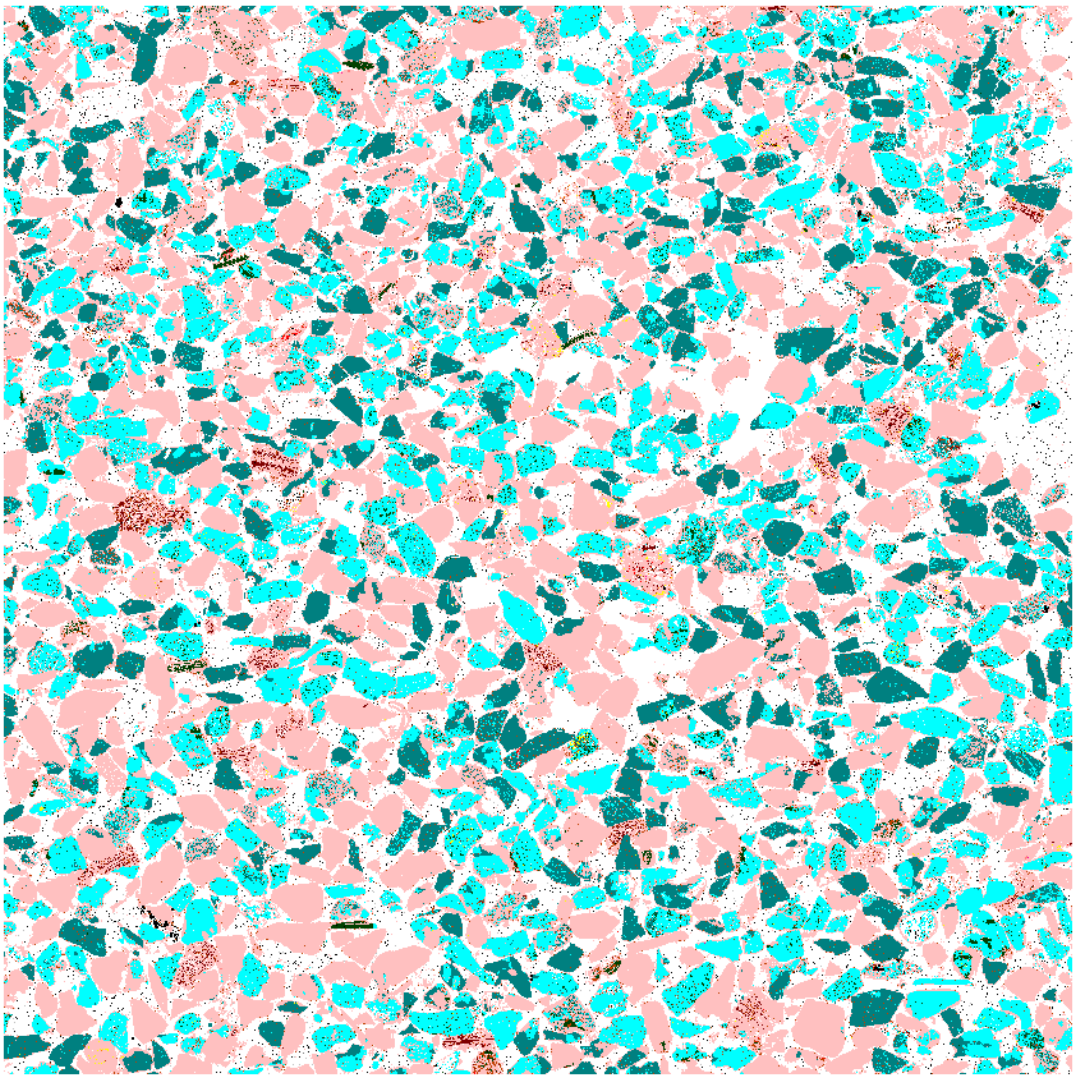

**Mineral Name**

- Porosity
- Quartz
- K-Feldspar
- Plagioclase
- Fe-Oxides and carbonates
- Muscovite
- Biotite
- Clays
- Pyrite
- Rutile
- Apatite
- Zircon
- Al Oxide
- Unclassified
- Others

*QEMSCAN map of Idaho Gray sandstone.*

*Horizontal scan length is 17mm.*

# Appendix IV

## Electronic appendix (see CD)

Included in Appendix IV are:

1. Supplementary movies
2. Conference presentations
3. PDF copy of the thesis

Figure captions for supplementary movies:

***Supplementary Movie 1 -*** *A complete time series movie of the microtomographic reconstructions. The movie is of an individual 2D slice though the cylindrical sample. Sample diameter = 2 mm.*

***Supplementary Movie 2 -*** *A 3D time series movie of the largest pore cluster. The analysed subvolume is a cube with a length of 975 µm. The pore cluster incorporates the majority of individual pores into sample-scale drainage architecture after 255 minutes.*